

# Static and dynamic properties of non-collinear quantum antiferromagnets explored by neutron scattering

Présentée le 25 juin 2021

Faculté des sciences de base  
Laboratoire de magnétisme quantique  
Programme doctoral en physique

pour l'obtention du grade de Docteur ès Sciences

par

**Luc TESTA**

Acceptée sur proposition du jury

Prof. V. Savona, président du jury  
Prof. H. M. Rønnow, directeur de thèse  
Prof. M. Kenzelmann, rapporteur  
Dr N. Bech, rapporteur  
Prof. F. Mila, rapporteur



# Acknowledgements

The *end-of-thesis* rush is now behind me and I am staring at this blank page, trying to figure out the best way to start writing this section, which will probably be the most read of my thesis – if not the only one. Carrying out a PhD thesis undoubtedly represents a great challenge, and I am proud to summarise in this manuscript the result of four years of literature reading, experiments, analysis and writing. What is not reported in this document is all the time and energy invested, the sacrifices made, the tears shed when nothing would work as well as the total relief when it finally does. During these past few years, I've faced a fair share of ups and downs and I would like to take this opportunity to thank everyone around me who helped me go through them, and distracted me from my work.

First and foremost I would like to express my most sincere gratitude to my supervisor, Prof. Henrik Rønnow for guiding me through the world of quantum magnetism. My deepest thanks also goes to Peter the Mighty without whom not much of this would have been possible. I know I grew up so fast, let's see how far I can follow in your footsteps! Thanks also to Bruce, who, besides being so helpful during my final year, is the living example that it is possible – and sometimes necessary – to fully live one's many passions. Thanks to Ivica for managing the lab, driving the RV and playing squash; Caroline for being so helpful whenever I'd be facing bureaucratic issues and for nice chats; Minki for knowing everything and inviting me to B'ham for my first stage performance. Thanks to all members of the LQM – past, present and future. May you enjoy your time here as much as I did! Special thanks to the SCBO group, Ellen, Gaétan and Jana. Hopefully our bike-coffee-pastry-music-bar dream will come true! Je suis sincèrement reconnaissant envers Anh pour m'avoir donné la motivation d'aller jusqu'au bout lorsque ça allait un peu moins bien.

The neutron scattering world forms a very close-knit community, and I am really happy to have made such friends through experiments, conferences and schools. Thanks in particular to Victor *de Propagación*, Irina, Jakob and Stas. It's really nice to know that you will not be alone in beamtime, wherever it takes places, and I will truly miss this community. I am especially grateful to Aga for everything we shared. From the bottom of my heart, dziękuję (and sklep).

I also wish to thank my friends from Trieste who were my true source of inspiration throughout this PhD. I am really grateful for all those chats, trips, thoughts and laughs.

## Acknowledgements

---

J'aimerais profondément remercier tous ceux qui ont partagé un bout de chemin avec moi pendant ces 10 ans d'EPFL, de près ou de loin. Merci en particulier à Loïc, Justin, Vilain, Meyrat, Muth, Cyril et Gayouf. On aurait certainement pu trouver plus intelligents comme potes, mais aussi franchement moins marrants. Justin et Mathias, on s'en est plutôt bien sorti tous les trois, non? Malgré ça, je resterai toujours Luchoong Testang Mendes pour vous et c'est un honneur! Merci d'être de si bons amis pour moi, *pop goes my heart*. Massive thanks to Greg and Alex with whom I spent so much time and shared so many outdoors activities before COVID hit (heh, I had to mention it at least once here). I am proud to have you as my really close friends. Merci également à l'équipe des repas-de-midi-procrastinatifs, sans bien sûr vouloir vous réduire à cela. Merci Francis, Samuel (d'ailleurs, on se fait le mont Rognieux demain?), Samy, Justin et Virgile. C'est pas peu dire que vous avez grandement contribué à ma santé d'esprit dans ce monde de fous. En parlant de Virgile, *je voudrais te remercier Virgile* d'avoir été un si bon collègue mais surtout ami pendant ces quatre dernières années. Tu sais, je ne peux qu'admirer ton savoir faire en tant que *data analyst* ainsi que ta passion pour la compréhension des phénomènes naturels. Merci pour ta disponibilité sans faille, je ne compte plus les heures passées à discuter dans ton bureau ou le mien. Vive le Marsala et les abricots. *Abricooooots!* Marie, presque-voisine-de-bureau, merci pour toutes ces pauses café, ces balades au bord du lac et en montagne, les conversations qu'on a pues avoir, et ces bières de fin de journée. C'est encore mieux quand ça se finit en ski-shot à Grimentz! Merci Valérie d'élargir ma vision très scientifique de la vie (encore que..), et de m'aider à la remettre en question quand cela s'impose. Merci aux Chacals pour ces heures passées à, hum, s'évader.

J'aimerais remercier mes deux coloc Fred et Patrick pour m'avoir supporté pendant ces quatre ans. Maintenant, bouge toi de finir ce doctorat Patrick, vieux frère, pour qu'on puisse ouvrir notre roulotte à pizzas et burgers! Les FloReLuMa (ou Marelluf ou Flarmeul ou autre Fler Maul), je pourrais vous remercier de tellement de choses que j'ai beau y réfléchir, rien de spécial ne me vient en tête. Merci d'être vous et de m'avoir gardé dans un (grand) coin de votre tête lorsque je faisais mon ermite. *Ruby!*

Jen, chaque page de cette thèse porte ton empreinte, directe ou indirecte. Merci de faire de moi une meilleure version de moi-même. Thank you for everything.

Mes derniers remerciements, simples mais si sincères, vont tout naturellement à ma famille. Merci Papa et Maman d'avoir su éveiller ma curiosité pour tout ce qui nous entoure et de m'avoir donné les moyens de réussir. Merci Laura de réussir à me faire rire en toute circonstance. Votre soutien à tous les trois a été plus qu'essentiel au quotidien. Et Louve, puisse le monde qui t'entoure t'émerveiller autant que ton parrain.

*Lausanne, Février 2021*

Luc.



# Abstract

This thesis is devoted to the investigation of static and dynamic properties of two different sets of quantum magnets with neutron scattering techniques and the help of linear spin wave theory. Both systems are copper-based with spin  $S = 1/2$ , which makes them ideal to study the interplay between purely quantum and semi-classical effects.

I start with the analysis of the antiferromagnet  $\text{SeCuO}_3$ , which has a canted spins magnetic structure. Through careful inelastic neutron scattering experiments on thermal and cold triple-axis spectrometers, I demonstrate that this compound exhibits three primary types of excitations that are intrinsically opposite : spin waves (*magnons*), singlet-triplet excitations (*triplons*), and fractional spins excitations (*spinons*). Such a strong coexistence and interdependence of these collective excitations has not been observed yet, thereby the quantification and description of the excitations in  $\text{SeCuO}_3$  leads the way to further theoretical work on multi-excitation spin systems, as well as the existence of quantum effects in high dimensional systems.

My second project is on the extraction of the magnetic structure of three members of the  $A(\text{BO})\text{Cu}_4(\text{PO}_4)_4$  chiral family, namely  $(A;B) = (\text{Ba}; \text{Ti})$ ,  $(\text{Sr}; \text{Ti})$  and  $(\text{Pb}; \text{Ti})$ , from spherical neutron polarimetry measurements. I prove that the first two compounds exhibit a highly non-collinear magnetic structure, with the  $\text{Cu}^{2+}$  spins forming clusters of 'two-in-two-out' arrangements on each structural unit. This structure is stabilised by the presence of a strong Dzyaloshinskii-Moriya interaction, and explains the observation of magnetoelectric effects as emerging from quadrupole moments. The analysis of the latter compound did not lead to the confirmation of its magnetic structure due to strong nuclear-magnetic interference.

I conclude this thesis by the investigation of the magnetic excitation spectrum of some members of the  $(A; B)$  family, probed by inelastic neutron scattering measurements. Indeed, its particular crystallographic structure makes it an ideal playground to study tetramerisation effects on the two dimensional square lattice. Additionally, the aforementioned Dzyaloshinskii-Moriya interaction ensures the presence of a structural gap, which competes with the quantum one emerging from tetramerisation effects. Using linear spin wave theory, I describe  $(\text{Ba}; \text{Ti})$  as a chequerboard system with almost

## Abstract

---

equal intra- and inter-plaquette couplings, with weak quantum effects. I also provide a qualitative description of (Pb; Ti), which exhibits similar physics, and conclude by presenting the first results on the highly symmetric compound (K; Nb), which shows hints of a strong quantum behaviour.

**Keywords :** quantum magnetism, neutron scattering, spinons, triplons, magnons, spin waves, polarisation analysis, magnetic structure, Dzyaloshinskii-Moriya interaction, neutron diffraction, square-lattice, antiferromagnet, inelastic neutron scattering, excitation spectrum, tetramerisation, long ranger order.

# Résumé

Cette thèse est dédiée à l'étude des propriétés statiques et dynamiques de deux différentes classes d'aimants quantiques, à l'aide de la technique dite de diffusion de neutrons ainsi que la théorie linéaire des ondes de spin. Dans le cas des deux systèmes considérés, le magnétisme provient des atomes de cuivre ( $\text{Cu}^{2+}$ ) possédant un spin-1/2. Cette faible valeur de spin en font d'excellents candidats pour étudier aussi bien les effets semi-classiques que ceux purement quantiques.

Je commence par une étude systématique des excitations magnétiques présentes dans l'antiferro-aimant  $\text{SeCuO}_3$  à l'aide d'expériences de diffusion inélastique de neutrons sur des spectromètres à trois axes thermiques et froids. Je démontre que ce système présente trois types d'excitations intrinsèquement opposées coexistent dans ce système : des ondes de spin (*magnons*), des transitions de l'état singulet à l'état triplet (*triplons*), ainsi que des excitations fractionnelles de spins (*spinons*). Cette coexistence, et interdépendance, de ces excitations n'avait jamais été observée sur un matériau réel. Ainsi, ce travail ouvre la voie à d'autres études plus poussées sur la présence d'excitations de spin de différentes natures dans un seul système, ainsi que leur unification dans une même théorie. De plus, la présence de spinons motive la compréhension d'un comportement quantique dans un système à haute dimension.

Mon second projet porte sur la détermination de la structure magnétique de trois membres de la famille d'aimants quantiques chiraux  $A(\text{BO})\text{Cu}_4(\text{PO}_4)_4$ , avec  $(A;B) = (\text{Ba}; \text{Ti}), (\text{Sr}; \text{Ti})$  et  $(\text{Pb}; \text{Ti})$ , à l'aide de la technique de polarimétrie neutronique sphérique. Je démontre que les deux premiers composés possèdent une configuration de spin hautement non-colinéaire, dans laquelle les moments magnétiques associés aux atomes de  $\text{Cu}^{2+}$  forment un arrangement dit 'deux-dedans-deux-dehors' sur chaque unité structurale formée de quatre atomes de spin. Cette structure magnétique est stabilisée par la présence d'une interaction de Dzyaloshinskii-Moriya sur les liens reliant deux atomes plus proches voisins de la dite unité. De plus, elle explique l'observation d'un effet magnéto-électrique comme provenant de moments quadrupolaires. Finalement, l'analyse du dernier composé  $(\text{Pb}; \text{Ti})$  n'a pas conduit à la confirmation de sa structure magnétique à cause de la présence de forts termes d'interférence nucléomagnétique.

## Résumé

---

Je conclus cette thèse par l'étude du spectre d'excitations magnétiques de quelques membres de la famille d'aimants quantiques ( $A$  ;  $B$ ) susmentionnée, mesuré au travers d'expériences de diffusion neutronique inélastique. En effet, la structure atomique de cette classe de composés en fait un excellent terrain de jeu pour étudier les effets de tétramérisation magnétique sur un réseau carré à deux dimensions. De plus, la présence d'une interaction de Dzyaloshinskii-Moriya induit l'existence d'un gap structural qui entre en concurrence avec le gap quantique prédit pour un système fortement localisé. Avec l'aide de la théorie d'ondes de spin linéaire, je décris ( $Ba$  ;  $Ti$ ) comme un système dit de 'plateau d'échec', possédant des interactions inter- et intra- plaquettes de quasi même force. Je propose également une description qualitative des excitations dans ( $Pb$  ;  $Ti$ ) qui présente une physique extrêmement semblable, et conclus par la présentation des premières mesures du spectre d'excitations magnétiques de ( $K$  ;  $Nb$ ), qui montre des signes d'un comportement quantique marqué.

**Mots-clés :** magnétisme quantique, diffusion de neutrons, spinons, triplons, magnons, ondes de spin, analyse de polarisation, structure magnétique, interaction de Dzyaloshinskii-Moriya, diffraction de neutron, réseau carré, antiferroaimant, diffusion inélastique de neutrons, spectre d'excitations, tétramérisation, ordre à longue distance.

# Sommario

Questa tesi è dedicata all'indagine, mediante tecniche sperimentali di dispersione di neutroni e attraverso lo studio teorico con l'ausilio della teoria linearizzata delle onde di spin, delle proprietà statiche e dinamiche di due diversi sistemi di magneti quantistici a base di rame, con spin  $S = 1/2$ , il che li rende ideali per studiare le transizioni tra gli effetti puramente quantistici e quelli semi-classici.

Il primo sistema che ho analizzato è il composto antiferromagnetico  $\text{SeCuO}_3$ . Attraverso accurati esperimenti di spettrometria a tre assi (TAS) con scattering inelastico di neutroni termici e freddi, dimostro che questo composto presenta tre tipi primari di eccitazioni che sono intrinsecamente opposte: onde di spin (*magnoni*), eccitazioni singoletto-tripletto (*triploni*), e eccitazioni frazionarie (*spinoni*). La chiara e forte coesistenza e interdipendenza di queste eccitazioni collettive non era stata osservata finora, queste misure delle eccitazioni nel  $\text{SeCuO}_3$  aprono perciò la strada ad ulteriori lavori teorici sui sistemi di spin a eccitazioni multiple, che manifestano effetti quantistici in sistemi bi e tri-dimensionali.

Il mio secondo progetto riguarda la determinazione per mezzo di misure di polarimetria neutronica sferica (SNP) della struttura magnetica di tre membri della famiglia chirale  $A(\text{BO})\text{Cu}_4(\text{PO}_4)_4$ , ovvero  $(A; B) = (\text{Ba}; \text{Ti})$ ,  $(\text{Sr}; \text{Ti})$  e  $(\text{Pb}; \text{Ti})$ . Dimostro che i primi due composti presentano una struttura magnetica altamente non collineare, in cui i momenti magnetici associati agli atomi di  $\text{Cu}^{2+}$  formano una disposizione detta "due-dentro-due-fuori" per ogni unità strutturale di quattro atomi con spin. Questa struttura è stabilizzata dalla presenza di una forte interazione Dzyaloshinskii-Moriya, e spiega l'osservazione degli effetti magnetoelettrici che emergono dai momenti di quadrupolo. L'analisi di quest'ultimo composto non ha portato alla conferma della sua struttura magnetica a causa di forti interferenze magnetiche nucleari.

Concludo questa tesi con l'indagine dello spettro di eccitazione magnetica di alcuni membri della famiglia  $(A; B)$ , sondati con misure di dispersione dei neutroni inelastici. Questa particolare struttura cristallografica è ideale per lo studio effetti di tetramerizzazione sul reticolo quadrato bidimensionale. Inoltre, la già citata interazione Dzyaloshinskii-Moriya provoca un gap legato alla struttura atomica, che compete con quello che emerge dagli effetti quantistici legati alla tetramerizzazione.

Usando la teoria linearizzata delle onde di spin, descrivo (Ba; Ti) come un sistema a scacchiera con accoppiamenti quasi uguali intra- e inter-placchette e con deboli effetti quantistici. Fornisco anche una descrizione qualitativa di (Pb; Ti) che mostra un comportamento fisico simile, e concludo presentando i primi risultati sul composto altamente simmetrico (K; Nb), che mostra accenni di un forte comportamento quantistico.

**Parole chiave :** magnetismo quantistico, dispersioni di neutroni, spinoni, triploni, magnoni, onde di spin, analisi di polarizzazione, struttura magnetica, interazione di Dzyaloshinskii-Moriya, reticolo quadrato, antiferromagnetico, diffrazione di neutroni inelastici, spettro di eccitazione, tetramerizzazione, ordine a lungo raggio

# Contents

<b>Acknowledgements</b>	<b>i</b>
<b>Abstract (English/Français/Italiano)</b>	<b>iii</b>
<b>1 Introduction</b>	<b>1</b>
1.1 Elements of quantum magnetism . . . . .	3
1.1.1 Origin of magnetism . . . . .	3
1.1.2 Magnetic model . . . . .	4
1.2 Work presented in this thesis . . . . .	7
<b>2 Welcome to the world of neutrons</b>	<b>9</b>
2.1 Introduction to Neutron Scattering . . . . .	10
2.1.1 Scattering cross-section . . . . .	12
2.1.2 Nuclear scattering . . . . .	14
2.1.3 Magnetic scattering . . . . .	15
2.1.4 Polarised neutrons . . . . .	17
2.2 Instrumentation . . . . .	21
2.2.1 Time-of-Flight instruments . . . . .	22
2.2.2 Triple-Axis Spectrometers . . . . .	23
2.2.3 Polarisation analysis with TAS . . . . .	26
2.3 Linear Spin Wave theory . . . . .	27
2.3.1 Square antiferromagnet . . . . .	27
2.3.2 Generalisation and applications to neutrons . . . . .	29
<b>3 Coexistence of multi-type excitations in <math>\text{SeCuO}_3</math></b>	<b>31</b>
3.1 Introduction . . . . .	32
3.1.1 Magnetic excitations . . . . .	33
3.1.2 Crystal structure and magnetic properties . . . . .	36
3.1.3 Experimental setup . . . . .	38
3.2 Localised magnetic dimers . . . . .	39
3.3 Three dimensional long-range order . . . . .	42
3.3.1 Interpretation of the effective couplings . . . . .	46
3.4 A spinon-like continuum . . . . .	49
	ix

## Contents

---

3.5	Summary . . . . .	52
<b>4</b>	<b>Spherical Neutron Polarimetry as a tool for magnetic structure determination</b>	<b>53</b>
4.1	Introduction . . . . .	55
4.1.1	Crystal structure and magnetic properties . . . . .	56
4.1.2	Theoretical elements of symmetry analysis . . . . .	58
4.1.3	Previous neutron powder diffraction experiments . . . . .	61
4.2	The simple case of magnetic scattering processes only . . . . .	66
4.2.1	Combined ND and SNP analysis of $\text{Ba}(\text{TiO})\text{Cu}_4(\text{PO}_4)_4$ . . . . .	68
4.2.2	Spherical Neutron Polarimetry on $\text{Sr}(\text{TiO})\text{Cu}_4(\text{PO}_4)_4$ . . . . .	74
4.2.3	The importance of the Dzyaloshinskii-Moriya interaction . . . . .	77
4.3	Combining nuclear and magnetic scattering processes . . . . .	79
4.3.1	The unsolved case of $\text{Pb}(\text{TiO})\text{Cu}_4(\text{PO}_4)_4$ . . . . .	80
4.4	Summary . . . . .	85
<b>5</b>	<b>Variation on the square lattice – the <math>A(\text{BO})\text{Cu}_4(\text{PO}_4)_4</math> cupola family</b>	<b>87</b>
5.1	Introduction . . . . .	88
5.2	Excitation spectrum of $\text{Ba}(\text{TiO})\text{Cu}_4(\text{PO}_4)_4$ . . . . .	90
5.2.1	Experimental setups . . . . .	91
5.2.2	Spin dynamics . . . . .	92
5.2.3	Derivation of the magnetic Hamiltonian . . . . .	99
5.2.4	Comparison with high-field magnetisation measurements . . . . .	103
5.2.5	Future dedicated work . . . . .	105
5.3	Qualitative description of $\text{Pb}(\text{TiO})\text{Cu}_4(\text{PO}_4)_4$ . . . . .	107
5.3.1	Experimental setups . . . . .	107
5.3.2	Excitation spectrum in zero field . . . . .	108
5.3.3	Excitation spectrum in a vertical magnetic field . . . . .	111
5.4	$\text{K}(\text{NbO})\text{Cu}_4(\text{PO}_4)_4$ as a strongly quantum system . . . . .	113
5.4.1	Powder spectrum of (K; Nb) . . . . .	114
5.5	Summary . . . . .	117
<b>6</b>	<b>Conclusion and outlook</b>	<b>119</b>
	<b>Bibliography</b>	<b>123</b>
	<b>Curriculum Vitae</b>	<b>135</b>



# 1 Introduction

## Contents

<b>1.1 Elements of quantum magnetism . . . . .</b>	<b>3</b>
1.1.1 Origin of magnetism . . . . .	3
1.1.2 Magnetic model . . . . .	4
<b>1.2 Work presented in this thesis . . . . .</b>	<b>7</b>

I remember my first day at university as a physics student, sitting at the back of the auditorium. The professor started his first lecture by stating that *physics does not explain why things work – it is rather about building a deep understanding of how they work*. To this, I would like to add that beauty in physics does not lie in the simple observation and description of a phenomenon, but rather in its contextualisation. What are the conditions necessary in order to observe it? And to recreate it? And then some engineers could ask – how can I exploit it? The beauty lies in connecting the dots.

Magnetism provides a perfect example of how the understanding of a phenomenon is built, and results in the creation of tools now commonly used. The first recordings of magnetism are by the Chinese writer Guanzhong (645 BC), and the Greek philosopher Thales (545 BC). Both mention a stone, lodestone, capable of attracting iron. It is only much later, around the 12<sup>th</sup> century, that pieces of lodestone floating on water were found to align along the same direction, pointing towards the south, this helping realise the first magnetic compass for navigation [1]. Further investigations on magnetic properties resulted in the theoretical description of electromagnetism by Maxwell [2]. However, it is only with the development of quantum mechanics – a true revolution in the world of physics – that the microscopic origin of magnetism was discovered. Magnetism is a quantum effect, strongly associated with electrons, and leads to macroscopic realisations.

A big step forward in the understanding of quantum matter is associated with the discovery of collective effects. Indeed, it is thought that metals are described by free

electrons, which are contrarily bound to atoms in the case of insulators. However, there is an intermediate region in which all electrons in the solid interact in a cooperative way, opening a field of physics yet unexplored – the study of *strongly correlated electron systems*. Probably the most famous associated phenomenon is superconductivity, which is a state of matter where electrons can travel in a solid with no electrical resistance. Engineering superconductive materials would naturally have direct applications to industry, and significantly improve energy storage, transport and bring tremendous help in facing pressing challenges such as climate change. Nevertheless, this quantum state only emerges at low temperature or under extreme, some would even say absurd, experimental conditions [3], and the hunt for room temperature superconductivity is perhaps the most closely watched axis of research in solid state physics presently.

All of the above highlights the great importance of fundamental research in science. Engineering new materials, and integrating them into new technologies in medicine, energy storage or informatics is only possible after a long process that could run over decades, in which the underlying nature of a phenomenon is explored and observations are associated with the structure of magnetic features. Naturally, the exploration of magnetic systems was only possible thanks to the progress of experimental techniques and instrumentation over the last century, which notably saw the developments of neutron and x-ray scattering methods. Furthermore, experimental and theoretical physics evolving hand in hand, the past 50 years witnessed the rise of computational physics [4], which allows for the study – and direct comparison with experiments – of increasingly complex systems.

Throughout my thesis, I studied quantum effects closely associated with a quantity that is the cornerstone of magnetism : the spin. Under certain conditions, such as low temperature or high pressure, real materials found in nature or synthesised in laboratories can reach an ordered magnetic phase. This phase is defined by a particular, and periodic, arrangement of the magnetic moments, mainly driven by the interactions between the spins. This defines the ground state of the system, which minimises the total energy of the system, and is a static property. Furthermore, as some energy is provided to the system, it may reach an excited state. The resulting excitation might then be distributed on all spins of the lattice, or localised... or both, simultaneously. This defines the dynamics of the system.

As the title of my thesis might suggest, I used neutron scattering techniques to in a first instance describe these two properties on two different types of quantum magnets. I then complemented my observations with results extracted from numerical methods applied on the same systems in order to understand the origin of these static and dynamic properties, and place them in a bigger picture. This is my humble contribution towards a better understanding of quantum magnetism.

## 1.1 Elements of quantum magnetism

The forthcoming text is not meant to provide an in-depth introduction to quantum magnetism, which can already be found in many dedicated textbooks [5, 6, 7, 8, 9]. I begin with a quick, and rather qualitative, description of quantum effects in ordered matter, which should provide the new reader with the necessary elements in order to understand this thesis.

### 1.1.1 Origin of magnetism

Magnetism effects have a microscopic origin, which is closely related to the behaviour of electrons. Being fermions, they must obey Fermi-Dirac statistics and are ruled by Pauli exclusion principle. The magnetic properties of an atom then depend on their electronic configuration, which is given in terms of four quantum numbers. The principal quantum number  $n$  defines the energy level of the orbital. The orbital quantum number  $l$  ( $l = 0 \dots n - 1$ ) gives the total angular momentum of the orbital and defines  $s$ ,  $p$ ,  $d$  and  $f$  electrons. The magnetic quantum number  $m_l$  defines the projection of the orbital angular momentum along the quantisation axis ( $-l < m_l < l$ ). Having defined  $s$  as the spin angular momentum (or just spin), which takes a value  $s = 1/2$  for electrons, the last quantum number is  $m_s = \pm s$ , and represents the projection of the spin along the quantisation axis.

There are two distinctive contributions to magnetism. The first one is given by the motion of electrons around the nucleus, and defines the angular momentum  $L$  such that  $L = \sum_i l_i$ . The second contribution is present regardless of the orbital motion, and is an intrinsic property of the electron, namely the spin  $s$ . A set of electrons then has a total spin given by  $S = \sum_i s_i$ . In a first order approximation, only unfilled shells contribute to the angular momenta, and the electronic structure can be derived using Hund rules :

- (i) Maximise the total spin  $S$ ,
- (ii) Maximise the total orbital moment  $L$ ,
- (iii) Choose the angular momentum  $J$  that minimises the energy. This gives  $J = |L - S|$  for less than half full shells and  $J = |L + S|$  above half filling. This rule couples both contributions to magnetism.

In this thesis, I worked with Cu atoms. They are usually most stable as  $\text{Cu}^{2+}$  ions, with the electronic structure  $[\text{Ar}]3d^9$ , and are classified as transition metal ions. They correspond to  $S = 1/2$  and  $L = 2$ , which gives  $J = 5/2$ . However, for real compounds, the effect of the environment should not be neglected. Indeed, as Fig.1.1(a) shows, the shape of the surrounding orbitals, usually from oxygen or phosphorus atoms,

models the local electronic environment. They produce what is called a crystal field surrounding the magnetic ion, and that is related to the Coulomb repulsion between electrons in different orbitals [Fig.1.1(b) and Fig.1.1(c)]. Instead of following Hund's rules, the electrons will tend to occupy the lowest-lying energy level first. This effect is more pronounced for transition metals, which have a rather large orbital distribution, and becomes stronger than spin-orbit coupling. Effectively, this results in what is known as orbital quenching, and in an effective quantum number  $\tilde{L} = 0$ , such that  $J = S$ . The crystal field naturally depends on the neighbouring atoms' positions, and explains why the same magnetic ion can have different effective spin values depending on its surrounding environment.

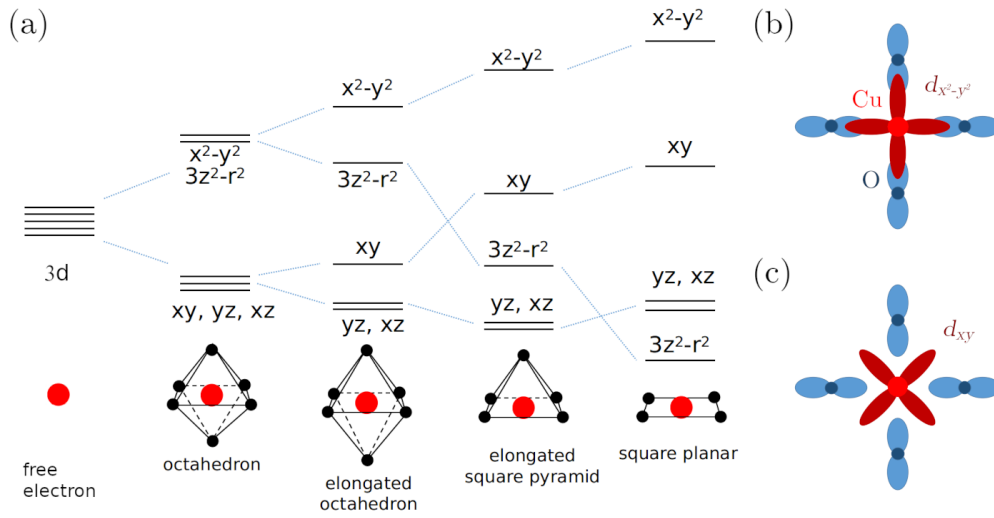


Figure 1.1 – **Crystal field effects and origin.** (a) Energy level splitting of the 3d orbital of a transition metal (in red), applied to  $\text{Cu}^{2+}$ . (b) and (c) Electronic configuration of a Cu atom surrounded by four O atoms. The  $p$  orbitals of the O atoms are represented in blue, while the (b)  $d_{x^2-y^2}$  and (c)  $d_{xy}$  orbitals of the  $\text{Cu}^{2+}$  are drawn in red. The latter minimises the orbital overlap and then has lower energy than the former. Figure adapted from a private conversation with K. Kimura.

### 1.1.2 Magnetic model

Crystals are defined by a periodic arrangement of atoms, forming a crystallographic lattice. Due to the competing interactions, it is sometimes energetically favourable for a system to have all its (free) electrons delocalised over the whole lattice, thereby minimising its kinetic energy. However, this competes with the on-site Coulomb repulsion. The physics of most strongly correlated electron systems is well-described in second quantisation by the so-called Hubbard Hamiltonian

$$\hat{H}_{\text{Hub}} = -t \sum_{\langle i,j \rangle} \sum_{\sigma} c_{i\sigma}^{\dagger} c_{j\sigma} + U \sum_i n_{i\uparrow} n_{i\downarrow}, \quad (1.1)$$

where  $\sigma$  denotes the spin state of the electron. The first term relates to the hopping of one electron from site  $i$  to site  $j$ , and the second term describes the Coulomb repulsion if more than one atom is placed on site  $i$ . However, when the electron wavefunction is smaller than the interatomic distance, the Coulomb term  $U$  dominates. The system is then likely to be described by a Mott insulator, which acts as an insulator even though it should be a metal according to band theory. Remarkably, they exhibit low-lying energy magnetic excitations, hence the popular saying – *a good magnet is a bad metal*. Their formalism can be described by a perturbation analysis on the Hamiltonian 1.1, assuming a small kinetic term,  $t/U \ll 1$ . It can be proven that the effective Hamiltonian reads

$$\hat{\mathcal{H}}_{\text{eff}} = \frac{4t^2}{U} \sum_{\langle i,j \rangle} \left( \hat{\mathbf{S}}_i \cdot \hat{\mathbf{S}}_j - \frac{1}{4} \right) \quad (1.2)$$

where I introduce the vectorial spin operator  $\hat{\mathbf{S}}$ . This effective Hamiltonian is, up to the constant term, similar to the Heisenberg Hamiltonian with interaction  $J = 4t^2/U$ , which I generalise here as :

$$\hat{\mathcal{H}}_{\text{Heis}} = \sum_{i,j} \mathbf{J}_{ij} \hat{\mathbf{S}}_i \cdot \hat{\mathbf{S}}_j. \quad (1.3)$$

This Hamiltonian is probably the most commonly used in solid state physics, and quantum magnetism. Furthermore, it defines a new lattice connecting several spins according to a geometry defined by the hierarchy of the interactions  $\mathbf{J}$ . This lattice is then not structural, but magnetic. The excitations of a system described by it are then given by spin fluctuations around their average value. A few comments can be made on this simple yet extremely rich model.

In magnetic systems, the coupling constant  $\mathbf{J}$  is not necessarily positive, and its strength is usually related to the overlap between orbitals in the case of direct exchange. The separation between atoms being rather large, this situation occurs infrequently for insulators. On the other hand, the interaction between two atoms can be mediated through several non-magnetic ions, such as O, where electrons are allowed to hop via a superexchange process. In both instances, the coupling constant  $\mathbf{J}$  can be negative or positive, which defines the ferromagnetic ( $J < 0$ ), and the antiferromagnetic ( $J > 0$ ) states respectively. In the former, the energy is minimised by a parallel spin configuration, while the latter favours an antiparallel spin arrangement [Figs. 1.2(a) and 1.2(b)]. However, some systems can be geometrically frustrated, as Fig. 1.2(c) shows. Indeed, the last spin cannot satisfy both antiferromagnetic couplings simultaneously, which results in the frustration of one of them. The system is then dominated by quantum fluctuations.

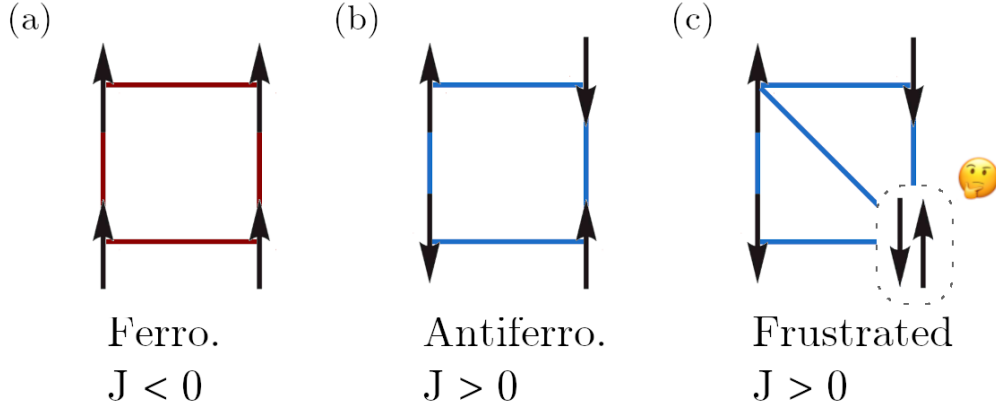


Figure 1.2 – **Magnetic interactions and geometrical frustration.** (a) Ferromagnetic state corresponding to  $J < 0$  [red]. (b) Antiferromagnetic state with  $J > 0$  [blue]. (c) Geometrical frustration induced by the diagonal antiferromagnetic coupling.

These different coupling types naturally introduce my next comment. Although restricted to nearest-neighbour sites in the Hubbard model, couplings involving longer distances also exist in real materials, under the assumption of a reasonable superexchange path. This can lead to frustration, as reported in Fig. 1.2(c). Furthermore, the physics of the system strongly depends on its dimensionality. Notably, Mermin-Wagner theorem states that there is no magnetic order at finite temperature for one- or two-dimensional systems in the absence of anisotropy, while it can emerge in three dimensions [10].

In the simplest case the coupling  $J$  between two magnetic ions is isotropic, which means that the components  $J^x$ ,  $J^y$  and  $J^z$  are equal. However, in many situations, the environment is such that it favours a certain alignment of the spin. We then talk about an easy axis. This behaviour is reported in the exchanges by anisotropic interactions. The most famous case is probably the Ising model ( $J^x = J^y = 0$ ). Furthermore, the interaction could be antisymmetric due to spin-orbit coupling. This is the case of the Dzyaloshinskii-Moriya interaction, which is represented by a matrix  $D$  such that  $D_{ij} = -D_{ji}$ .

Finally, since the energy scales of these magnetic systems are relatively small, there is constant competition between quantum and thermal fluctuations. The former tends to induce a quantum ordered phase, while the latter would destroy it. Quantum properties then strongly depend on the value of the spin  $S$ . In general, a system exhibits a stronger quantum behaviour for low spins, the minimal value being naturally  $S = 1/2$ . On the other hand, the classical limit corresponds to  $S \rightarrow \infty$ . Additionally, the quantum behaviour of a system is quantified by its quantum fluctuations, which are strongest for frustrated or low-dimensional systems.

## 1.2 Work presented in this thesis

This thesis is dedicated to the study of ground state properties, as well as magnetic excitations of  $\text{Cu}^{2+}$  quantum magnets with the use of neutron scattering techniques. It is divided in five chapters that can be read independently. Additionally, I was partially involved in several side projects, which I did not report in this manuscript. The main ones are the investigation of the two-dimensional antiferromagnet  $\text{CoPS}_3$  which may lead to Kitaev-Heisenberg physics, the commissioning of the multiplexing spectrometer CAMEA (PSI), first inelastic measurements on the quantum spin liquid candidate  $\text{K}_2\text{Ni}_2(\text{SO}_4)_3$ , and the investigation of magnetic properties of chiral Tellurium [11].

In **Chapter 2**, I present a brief review of neutron scattering techniques, as well as the main numerical method that I used, which is the linear spin wave approximation.

**Chapter 3** presents my work on the excitation spectrum of  $\text{SeCuO}_3$ . It was initially thought based on its crystallographic structure that this system exhibits localised states, which evolve into long range order at low temperature. I demonstrate that this vision is slightly incomplete, and that magnetic excitations in this system emerge from two weakly coupled sublattices, namely dimer units and weakly coupled chains. This system gives rise to triplons, magnons and finally spinons-like excitations which have not been observed in a purely three-dimensional system before.

**Chapter 4** introduces the core of my thesis, which consists of an in-depth investigation of the chiral quantum magnet family  $A(\text{BO})\text{Cu}_4(\text{PO}_4)_4$ . This study is motivated by two objectives. First, this series of compound is known to exhibit magnetoelectric effects, and further knowledge of the spin's configuration is necessary in order to understand the origin of this property. Secondly, the nuclear structure of these magnets makes it a good realisation of the two dimensional square lattice antiferromagnet. This chiral family thus forms a nice playground to study tetramerised effects on a square model. I present how spherical neutron polarimetry was used in order to extract the magnetic structure of a series of members of this family, and how this ground state is supported by magnetic anisotropies. I conclude by showing the limitations of this method.

I pursue the study of the  $(A; B)$  family in **Chapter 5**, which presents a complete description of the magnetic excitations in  $(\text{Ba}; \text{Ti})$ , both at zero magnetic field and under a finite vertical field. This quantum magnet can be modelled by a network of weakly tetramerised coupled plaquettes. I also present qualitative results on other members of this family, and notably highlight the quantum effects of the highly-symmetric  $(\text{K}; \text{Nb})$  compound. I finally perform a first attempt to place these results in the more general context of the study of plaquettisation effects on the two dimensional square lattice antiferromagnet with a structural gap.

My work is summarised in **Chapter 6**, which concludes this thesis.





## 2 Welcome to the world of neutrons

### Contents

<b>2.1 Introduction to Neutron Scattering . . . . .</b>	<b>10</b>
2.1.1 Scattering cross-section . . . . .	12
2.1.2 Nuclear scattering . . . . .	14
2.1.3 Magnetic scattering . . . . .	15
2.1.4 Polarised neutrons . . . . .	17
<b>2.2 Instrumentation . . . . .</b>	<b>21</b>
2.2.1 Time-of-Flight instruments . . . . .	22
2.2.2 Triple-Axis Spectrometers . . . . .	23
2.2.3 Polarisation analysis with TAS . . . . .	26
<b>2.3 Linear Spin Wave theory . . . . .</b>	<b>27</b>
2.3.1 Square antiferromagnet . . . . .	27
2.3.2 Generalisation and applications to neutrons . . . . .	29

All the work presented in this thesis relies on neutron scattering measurements. It is then necessary to present the underlying principles and physics, which explain why neutron scattering is such a powerful tool for the investigation of static and dynamic properties of crystals. This chapter is not meant to serve as a lecture book, as rigorous treatment can be found in many dedicated textbooks [12, 13, 14, 15, 16] that those interested are invited to read. Rather, my goal is to familiarise the reader with the main concepts that will be used in the rest of this text. I start by presenting the neutrons properties. Then, the magnetic and nuclear cross-sections are introduced as the main concepts in neutron scattering theory. I briefly cover the instrumentation, and conclude by deriving key elements of the Linear Spin Wave theory. This chapter is strongly based on the textbooks referenced. If the reader is already familiar with the neutron world, they are welcome to go directly to Chapter 3.

### 2.1 Introduction to Neutron Scattering

The history of the neutron is closely related to Nobel Prizes. Based on the predictions of Rutherford who modelled the modern atom as made of a massive positive nucleus surrounded by negative charges [17] and predicted the existence of a neutral particle in the nucleus, Bothe [18] and Becker [19], who observed some unexplained radiation when hitting light elements with alpha particles; and Majorana, who stated that this radiation should be associated to a new neutral particle, James Chadwick discovered the neutron in 1932 [20]. He received the Nobel Prize in Physics for this discovery in 1935. Due to their chargeless behaviour, neutrons were almost immediately thought to be used for probing the properties of nuclei. Indeed, scientists used to work with alpha particles before, which have a charge of +2, making it complicated to overcome the Coulomb potential of the orbiting electrons and to reach the nucleus of an atom. Enrico Fermi then bombarded a series of heavy elements with neutrons, discovering new radioactive elements and investigating nuclear reactions induced by slow neutrons [21]. He received the Nobel Prize in Physics in 1938 for his work. Intrigued by this new physics, Otto Hahn and Lise Meitner bombarded Uranium atoms with neutrons and observed their splitting into lighter elements [22], releasing extra neutrons in the process as well as a tremendous amount of energy (more than 200 MeV!). Otto Hahn obtained the Nobel Prize in Chemistry for the discovery of nuclear fission, a honour that should have been shared with Lise Meitner. The potential destructive applications of Uranium nuclear fission are sadly well-known, but fortunately did not deter the emerging the use of neutrons to probe matter.

A key property of neutrons is their electric neutral charge, allowing them to penetrate travel much deeper inside matter, to make possible the use of extreme sample environments such as pressure cells, magnets and cryostats. Additionally, since neutrons interact with nuclei via the strong force which is very short-ranged, it allows the study of bulkier samples – to the order of the centimetre – and an accurate description of physical phenomena. Another consequence of the strong force interaction is that neutrons provide weak perturbations to the system, easily exciting magnetic transitions, but without modifying the nature of the states. This simplifies a lot the underlying scattering theory. Furthermore, neutrons have a wavelength to the order of the inter-atomic distance (around 1.8 Å) and an energy of 25 meV, similar to the excitations bandwidth in a crystal. They are then ideal for probing both static and dynamic properties of the matter. Another reason to chose neutrons over X-rays is the scattering cross-section which is isotope dependent to allow study of very light elements such as (deuterised) Hydrogen. Moreover, the neutron is then sensitive to the isotope which allows the study of biological systems by deuterisation. Finally, neutrons possess an intrinsic magnetic moment which makes them ideal for the study of static and dynamic magnetic properties such as excitations, magnetic interactions and structures.

## 2.1. Introduction to Neutron Scattering

Based on these criteria, Ernest Wollan and Clifford Shull performed one of the first neutron diffraction experiments [23]. They discovered the presence of diffraction peaks at unexpected positions as the very first evidence of the Néel state, predicted in 1948 by Louis Néel [24] for which he obtained the Nobel Prize in Physics in 1970. These results have defined the basis of modern quantum magnetism. The properties of neutrons are now well known and are summarised in Table 2.1. Neutron scattering techniques are also much more advanced, with the development of very specific instruments and the creation of dedicated facilities around the globe. They are now widely used, complementary to in-lab bulk measurements, to shed light on physical behaviours of systems. Having mentioned Nobel Prize laureates, the list grows longer with Flory (1974), Bednorz and Muller (1987), de Gennes (1991), Shull and Brockhouse (1994), whose research could not have been conducted without the use of neutron scattering techniques. And there will be more to come ...

In the frame of any work with neutrons, it is convenient to introduce the following equivalences :

$$\hbar\omega = E = 81.81 \cdot \frac{1}{\lambda^2} = 2.072 \cdot k^2 = 5.227 \cdot v^2 = 0.08617 \cdot T \quad (2.1)$$

and

$$1 \text{ meV} = 8.07 \text{ cm}^{-1} = 11.6 \text{ K} = 17.3 \text{ T}. \quad (2.2)$$

As for any experimental technique, it is necessary to start by introducing theoretical elements. In the next paragraphs, elements of the scattering theory, as it has been derived for neutrons, are provided.

Table 2.1 – Physical properties of neutrons, inspired by [12]

Property	Value
Charge	0 C
Mass	$1.674928(1) \cdot 10^{-24} \text{ g}$
Spin	1/2
Cold neutrons	0 – 10 meV
Thermal neutrons	10 – 100 meV
Hot neutrons	100 – 500 meV
Magnetic moments	$-1.9130427(5) \mu_N$

### 2.1.1 Scattering cross-section

In all neutron scattering experiments, incoming neutrons of wavevector  $\mathbf{k}_i$  are scattered by a crystalline sample, modelled by a periodic Bravais lattice, into outgoing neutrons of wavevector  $\mathbf{k}_f$  with an angle  $\Psi$ . The interaction between the neutrons and the sample will thus change the energy and the momentum of the neutrons and can be pictured as in Fig. 2.1. As for all collisions, these changes are described by the momentum and energy transfers,  $\hbar\mathbf{Q}$  and  $\hbar\omega$  such that

$$\mathbf{Q} = \mathbf{k}_i - \mathbf{k}_f \quad (2.3)$$

$$\hbar\omega = \hbar(\omega_i - \omega_f) = \frac{\hbar^2}{2m} (\mathbf{k}_i^2 - \mathbf{k}_f^2) . \quad (2.4)$$

From here, one can already distinguish two types of scattering processes. Elastic scattering is defined by an energy transfer  $\hbar\omega = 0$  and thus  $\mathbf{k}_i - \mathbf{k}_f = \mathbf{G}$ , where  $\mathbf{G}$  is a reciprocal lattice vector. This condition is equivalent to Bragg's law  $\lambda = 2d_{hkl} \sin \theta_{hkl}$ , in which case  $\Psi$  is the Bragg angle  $2\theta$ . If this condition is not fulfilled, the scattering vector can be decomposed into  $\mathbf{Q} = \mathbf{G} + \mathbf{q}$ . The dispersion relation  $\hbar\omega(\mathbf{Q})$  of magnetic crystals can then be obtained with inelastic neutron scattering measurements by scanning over multiple points in the reciprocal space. In this thesis, I will use Miller's notation, such that a point in the reciprocal space is denoted by  $\mathbf{Q} = h \mathbf{a}^* + k \mathbf{b}^* + l \mathbf{c}^*$  with

$$\mathbf{a}^* = \frac{\mathbf{b} \wedge \mathbf{c}}{V_0}, \quad \mathbf{b}^* = \frac{\mathbf{c} \wedge \mathbf{a}}{V_0}, \quad \mathbf{c}^* = \frac{\mathbf{a} \wedge \mathbf{b}}{V_0}, \quad (2.5)$$

where  $\mathbf{a}^*$ ,  $\mathbf{b}^*$  and  $\mathbf{c}^*$  are the lattice parameters of the crystal and  $V_0 = \mathbf{a} \cdot (\mathbf{b} \wedge \mathbf{c})$  is the volume of the structural unit cell.

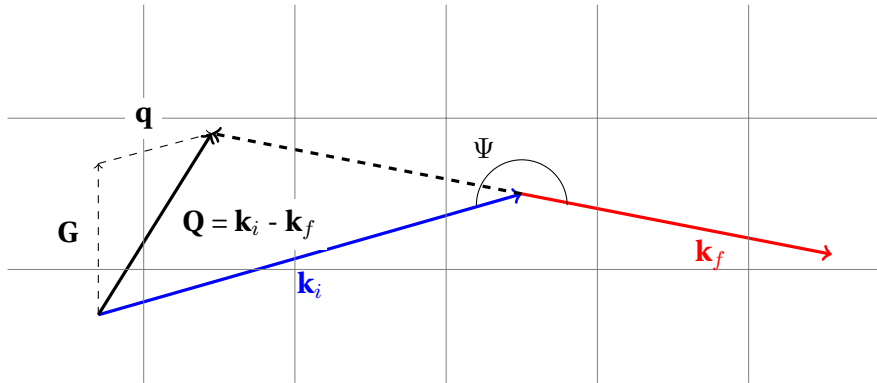


Figure 2.1 – **Illustration of a scattering process.** The vector  $\mathbf{Q} = \mathbf{G} + \mathbf{q}$  closes the triangle formed by  $\mathbf{k}_i$  and  $\mathbf{k}_f$ . The Brillouin zone boundaries are represented by the grid. Here is then an inelastic process,  $\mathbf{k}_i \neq \mathbf{k}_f + \mathbf{G}$ .

## 2.1. Introduction to Neutron Scattering

Outgoing neutrons are then measured by  $^3\text{He}$  detectors of efficiency  $\eta$ , covering a solid angle  $\Delta\Omega$  and an energy range of  $\Delta E$ , leading to the neutron count rate

$$C = \Psi_0 \eta \left( \frac{d\sigma^2}{dE d\Omega} \right) \Delta\Omega \Delta E, \quad (2.6)$$

where  $\Psi_0$  is the initial neutron flux. This expression naturally introduces the *partial differential cross-section*, defined as the probability that an incident neutron of wavevector  $\mathbf{k}_i$  is scattered into a solid angle  $d\Omega$  orthogonal to the wavevector  $\mathbf{k}_f$  and reaches a final energy between  $E_f$  and  $E_f + dE$ .

An expression of this quantity can be derived from first principles using the formalism of many-body interacting systems, based on the Born approximation [25]. Because of their energy range, neutrons can excite a transition between two quantum states but without modifying the nature of these states. The formalism of such weakly perturbed systems is well-described by Fermi's Golden Rule stating that

$$\frac{d\sigma^2}{dE d\Omega} = \left( \frac{m}{2\pi\hbar} \right)^2 \frac{k_f}{k_i} \sum_{\lambda_f, \sigma_f} \sum_{\lambda_i, \sigma_i} p_{\lambda_i} p_{\sigma_i} \left| \langle \mathbf{k}_f, \lambda_f, \sigma_f | \hat{V}(\mathbf{Q}) | \mathbf{k}_i, \lambda_i, \sigma_i \rangle \right|^2 \cdot \delta(\hbar\omega + E_i - E_f), \quad (2.7)$$

where  $\lambda_i$  ( $\lambda_f$ ) is the initial (final) state of the scattering system with corresponding energy  $E_i$  ( $E_f$ ) and statistical population  $p_{\lambda_i}$  ( $p_{\lambda_f}$ ); and  $\sigma_i$  ( $\sigma_f$ ) is the initial (final) spin state of the neutron, with polarisation probability  $p_{\sigma_i}$ ;  $m$  is the mass of the neutron. The delta function ensures the conservation of energy, and  $\hat{V}(\mathbf{Q})$  is the Fourier transform of the interaction potential. This expression is known as the *master formula* because it describes every neutron scattering process. For an unpolarised neutron beam, as for most neutron experiments, Eq. 2.7 can be rewritten as follows

$$\frac{d\sigma^2}{dE d\Omega} = \frac{k_f}{k_i} S(\mathbf{Q}, \omega), \quad (2.8)$$

where  $S(\mathbf{Q}, \omega)$  is called the *response function* and contains information about the quantum system only. This is the key quantity in neutron scattering experiments since it provides all necessary information on the system, with the appropriate choice of interaction potential  $V$ . By expressing the delta function with integrals, Eq. 2.8 can be rewritten as

$$\frac{d\sigma^2}{dE d\Omega} = \left( \frac{m}{2\pi\hbar} \right)^2 \frac{k_f}{k_i} \frac{1}{2\pi\hbar} \int dt e^{-i\omega t} \langle V^\dagger(\mathbf{Q}, 0) V(\mathbf{Q}, t) \rangle. \quad (2.9)$$

The notation  $\langle \dots \rangle$  denotes the average over initial states. This expression highlights the fact that neutrons probe the time correlations in the system.

### 2.1.2 Nuclear scattering

The main elastic scattering process emerges from the ordered crystal structure. Neutrons interact with atoms' nuclei at positions  $\mathbf{R}_j$  via the strong force at very short distance, typically to the order of  $10^{-12}$  cm. The potential  $V$  can thus be modelled by a Fermi pseudopotential

$$\hat{V}_N(\mathbf{r}) = \frac{2\pi\hbar^2}{m_n} \sum_j b_j \delta(\mathbf{r} - \mathbf{R}_j), \quad \hat{V}_N(\mathbf{Q}) = \frac{2\pi\hbar^2}{m_n} \sum_j b_j e^{i\mathbf{Q} \cdot \mathbf{R}_j}. \quad (2.10)$$

We introduced the scattering length  $b_j$  of the nucleus on site  $\mathbf{R}_j$ . Their values have been experimentally determined in [26] and are now tabulated. At this point, one must distinguish coherent scattering from incoherent scattering. Assuming that the sites are not correlated, the two associated cross-sections read

$$\left( \frac{d\sigma^2}{dE d\Omega} \right) \Big|_{\text{coh}} = \frac{k_f}{k_i} \frac{1}{2\pi\hbar} \int dt e^{-i\omega t} \sum_{j,j'} \bar{b}_j \bar{b}_{j'} \langle e^{i\mathbf{Q} \cdot (\mathbf{R}_j(t) - \mathbf{R}_{j'}(0))} \rangle \quad (2.11)$$

$$\left( \frac{d\sigma^2}{dE d\Omega} \right) \Big|_{\text{inc}} = \frac{k_f}{k_i} \frac{1}{2\pi\hbar} \int dt e^{-i\omega t} \sum_j \left( \bar{b}_j^2 - (\bar{b}_j)^2 \right) \langle e^{i\mathbf{Q} \cdot (\mathbf{R}_j(t) - \mathbf{R}_j(0))} \rangle. \quad (2.12)$$

The former emerges from the average scattering length on each site, giving rise to interference effects which makes it a collective phenomenon among atoms. This results in the appearance of Bragg peaks at positions determined by the static structure factor  $F_N(\mathbf{Q}) = \sum_j \langle b_j \rangle e^{i\mathbf{Q} \cdot \mathbf{R}_j} e^{W_j}$ , where  $W_j$  is the Debye-Waller factor, accounting for fluctuations of the atoms about their equilibrium position due to thermal effects. Equation 2.11 can be rewritten, with  $n$  being the number of unit cells, as

$$\left( \frac{d\sigma^2}{dE d\Omega} \right) \Big|_{\text{coh}} = n \frac{(2\pi)^3}{V_0} |F_N(\mathbf{Q})|^2 \delta(\mathbf{Q} - \mathbf{G}) \delta(\hbar\omega). \quad (2.13)$$

The latter comes from time fluctuations of the scattering length of an isotope. As an example, let us consider Hydrogen atoms. The scattering length varies a lot depending on the quantum state of the atom, jumping from  $b_{|t\rangle} = 1.085 \cdot 10^{-12}$  cm in the triplet state to  $b_{|s\rangle} = -4.750 \cdot 10^{-12}$  cm in the singlet state. This leads to a very large incoherent cross-section and explains why one generally does not want to study systems containing Hydrogen, but rather replaced by Deuterium. In the frame of this thesis, incoherent effects will be considered as background and disregarded.

### 2.1.3 Magnetic scattering

In a similar way, a magnetic potential emerges from the interaction between the dipole moments of the neutrons and the internal magnetic field  $\hat{B}(\mathbf{r})$  of the crystal generated by both the magnetic moments of unpaired electrons and their orbital motion. The magnetic potential reads

$$\hat{V}_M(\mathbf{r}) = -\hat{\boldsymbol{\mu}}_n \cdot \hat{\mathbf{B}}(\mathbf{r}) \quad (2.14)$$

where  $\boldsymbol{\mu}_n = -\gamma\mu_N\hat{\boldsymbol{\sigma}}$  is the magnetic dipole moment of the neutron,  $\gamma = 1.913$  is the gyromagnetic ratio,  $\mu_N = \frac{e\hbar}{2m}$  is the nuclear magneton and  $\hat{\boldsymbol{\sigma}}$  is the Pauli spin operator. Thus, the spin's contribution to the interaction magnetic field has a pure quantum origin. The spin's angular momentum  $\hat{\mathbf{s}}$  and the Pauli operators for neutrons are related by a factor of two such that  $\hat{\boldsymbol{\sigma}} = 2\hat{\mathbf{s}}$ . Another contribution to this field  $\mathbf{B}(\mathbf{r})$  comes from the classical orbital motion of the spins. The magnetic field emerging from a magnetic dipole and a single electron with velocity  $\mathbf{v}_e$  is given by

$$\hat{\mathbf{B}}(\mathbf{r}) = \hat{\mathbf{B}}_s(\mathbf{r}) + \mathbf{B}_L(\mathbf{r}) = \frac{\mu_0}{4\pi r^2} \left( \nabla \wedge \hat{\boldsymbol{\mu}}_e \wedge \mathbf{r} - \frac{2\mu_B}{\hbar} \mathbf{p} \wedge \mathbf{R} \right), \quad (2.15)$$

where  $\hat{\boldsymbol{\mu}}_e = -2\mu_B\hat{\mathbf{s}}$  is the magnetic moment operator of an unpaired electron and  $\hat{\mathbf{s}}$  is the spin angular momentum operator. The first term corresponds to the magnetic vector potential of a dipolar field due to the electron spin moment, and the second is a reformulation of Biot-Savart law for a single electron with linear momentum  $\mathbf{p}$ . For simplicity, the case of identical magnetic ions and a non polarised beam is considered. Assuming a periodic configuration of magnetic moments, it can be proven that the Fourier transform of 2.14 is

$$\hat{V}_M(\mathbf{Q}) = -\mu_0\boldsymbol{\mu}_n \cdot \mathbf{M}_\perp(\mathbf{Q}). \quad (2.16)$$

We introduced the Fourier transform of the magnetic moments in real space  $\mathbf{S}_i$  as  $\mathbf{M}(\mathbf{Q}) = \sum_i \mathbf{S}_i e^{i\mathbf{Q} \cdot \mathbf{R}_i}$  and the so-called magnetic selection rule  $\mathbf{M}_\perp(\mathbf{Q}) = \hat{\mathbf{Q}} \wedge (\mathbf{M}(\mathbf{Q}) \wedge \hat{\mathbf{Q}})$ . After insertion of the potential 2.16 in the master formula 2.7, the scattering cross-section reads

$$\left( \frac{d\sigma^2}{dE d\Omega} \right) \Big|_{\text{mag}} = \frac{k_f}{k_i} (\gamma r_0)^2 |f(\mathbf{Q})|^2 e^{-2W(\mathbf{Q})} \sum_{\alpha, \beta} \left( \delta_{\alpha, \beta} - \frac{\mathbf{Q}_\alpha \mathbf{Q}_\beta}{Q^2} \right) S^{\alpha\beta}(\mathbf{Q}, \omega), \quad (2.17)$$

where  $r_0 = \mu_0 e^2 / (4\pi m)$  is the classical radius of the electron, and  $S^{\alpha\beta}$  is the dynamic structure factor  $(\alpha, \beta = x, y, z)$ , covering the time dependent spin-spin correlations

$$S^{\alpha\beta}(\mathbf{Q}, \omega) = \frac{1}{2\pi\hbar} \sum_{j, j'} e^{i\mathbf{Q} \cdot (\mathbf{R}_j - \mathbf{R}_{j'})} \int dt e^{-i\omega t} \langle S_j^\alpha(t) S_{j'}^\beta(0) \rangle. \quad (2.18)$$

This value is equal – up to a constant factor – to the response function derived in Eq. 2.9. The magnetic form factor  $f(\mathbf{Q})$  corresponds to the Fourier transform of the

## Chapter 2. Welcome to the world of neutrons

---

magnetisation density of a single atom in space. It usually decreases with increasing modulus of  $\mathbf{Q}$ . Its value for each magnetic atom has been tabulated in [27]. Another important feature in 2.17 is the polarisation factor  $\left(\delta_{\alpha,\beta} - \frac{Q_\alpha Q_\beta}{Q^2}\right)$  which states that neutrons can only probe spin fluctuations that are orthogonal to the scattering vector  $\mathbf{Q}$ . It is interesting to introduce the following notation :

$$\mathcal{S}^{\alpha\beta}(\mathbf{Q}, \omega) = \frac{1}{2\pi\hbar} \int dt e^{-i\omega t} \langle M^{\alpha\dagger}(\mathbf{Q}, 0) M^\beta(\mathbf{Q}, t) \rangle. \quad (2.19)$$

The response function  $\mathcal{S}^{\alpha\beta}$  describes the evolution of a physical averaged quantity under an external perturbation – here, the magnetic field created by an incoming neutron. In the limit of a weak applied force, the response of the system will be linear. In this context, as stated by the fluctuation-dissipation theorem, the response function and the imaginary part of the susceptibility are closely related [28], and the following formula has been derived by Van Hove [29], with  $N_m$  as the total number of magnetic ions

$$\mathcal{S}^{\alpha\beta}(\mathbf{Q}, \omega) = \frac{N_m \hbar}{\pi} \left(1 - e^{-\frac{\hbar\omega}{k_B T}}\right)^{-1} \text{Im} \chi^{\alpha\beta}(\mathbf{Q}, \omega). \quad (2.20)$$

The elastic magnetic cross-section can be extracted from 2.17 by considering the limit  $t \rightarrow \infty$ . In this case, the spin-spin correlations become independent of time and

$$\lim_{t \rightarrow \infty} \langle \hat{S}_j^\alpha(t) \hat{S}_{j'}^\beta(0) \rangle = \langle \hat{S}_j^\alpha \rangle \langle \hat{S}_{j'}^\beta \rangle. \quad (2.21)$$

One derives the elastic differential cross-section by inserting this result in 2.17 and integrating over energy

$$\left( \frac{d\sigma^2}{d\Omega} \right)_{\text{mag}}^{\text{el}} = (\gamma r_0)^2 n \frac{(2\pi)^3}{V_0} \sum_{\mathbf{G}} \delta(\mathbf{Q} - \mathbf{G}) \left| \hat{\mathbf{Q}} \wedge \left( \mathbf{F}_M(\mathbf{Q}) \wedge \hat{\mathbf{Q}} \right) \right|^2, \quad (2.22)$$

which is the relation that governs magnetic Bragg peaks scattering. We have defined the magnetic structure factor as

$$\mathbf{F}_M(\mathbf{Q}) = f(\mathbf{Q}) e^{-W(\mathbf{Q})} \sum_j \langle \mathbf{S}_j \rangle e^{i\mathbf{Q} \cdot \mathbf{R}_j} = f(\mathbf{Q}) e^{W(\mathbf{Q})} \mathbf{M}(\mathbf{Q}). \quad (2.23)$$

Importantly, the matrix elements of Eq. 2.7 corresponding to the spin  $M_s$  and to the orbital motion  $M_L$  contributions defined in Eq. 2.15, between the eigenstates of the atoms expressed through its total angular momentum, must satisfy the dipole selection rules [30] leading to  $\Delta S = 0, \pm 1$  for transition metals ions. Furthermore, since the projection of the total (atom plus neutron) projection on the quantisation axis is a scalar quantity, it must be conserved throughout the scattering process.  $\Delta S^z$  must correspond to the change in the neutron's spin. This leads to the two scattering



selection rules for neutrons :

$$\Delta S = 0, \pm 1, \quad (2.24)$$

$$\Delta S^z = 0, \pm 1. \quad (2.25)$$

### 2.1.4 Polarised neutrons

In the previous section, I decided to describe scattering events from a non-polarised. However, their spin state is also susceptible to change after interacting with the sample as highlighted in 2.7. In the most general state (spherical neutron polarimetry), the scattering cross-section becomes a  $3 \times 3$  matrix, where the basis for each measurement is given by the three different quantisation axis. One can also restrict the polarisation analysis to a single quantisation axis (longitudinal neutron polarimetry, SNP), but this aspect has not been addressed throughout this thesis. Assuming a polarised beam along any direction, and three orthogonal measurement channels corresponding to each quantisation axis, a measurement then provides additional information about the system. A full theoretical derivation of the partial differential cross-section has been performed independently by Blume [31] and Maleev [32], leading to the Blume-Maleev equations. Since neutrons are sensible to the orthogonal fluctuations only – with respect to the scattering vector – we will hereafter work in a new coordinate system called polarisation axis, defined by

$$\begin{cases} x \parallel Q, \\ z \text{ perpendicular to the scattering plane,} \\ y \text{ completing the right-handed coordinates system.} \end{cases} \quad (2.26)$$

in such a coordinate system, the component of the magnetisation along  $x$  cannot be probed, which might already give significant insights on the direction of the magnetic moments. Assuming an initial polarisation  $P_i$  of the neutron beam and elastic events only, the total cross-section reads

$$\sigma = NN^* + M_{\perp} \cdot M_{\perp}^* + P_i \cdot (M_{\perp} N^* + M_{\perp}^* N) + i P_i \cdot (M_{\perp}^* \wedge M_{\perp}), \quad (2.27)$$

where we omitted of the  $Q$  dependencies in order to simplify the notation, as for the rest of this section. The final polarisation of the beam  $P_f$  can be written as follows [33]

$$P_f \sigma = P_f \sigma|_N + P_f \sigma|_M + P_f \sigma|_C + P_f \sigma|_I. \quad (2.28)$$

A change in the neutron's spin state can have various origins : nuclear, magnetic, chiral and nuclear-magnetic interference. A detailed description of each contribution can be found in Table 2.2.

## Chapter 2. Welcome to the world of neutrons

Table 2.2 – Description of each scattering contribution, presented in Eq. 2.28, heavily inspired by [34].

Type	Contribution	Effects
<u>N</u> uclear	$P_i N N^*$	The polarisation remains unchanged when considering interactions with the nuclear structure
<u>M</u> agnetic	$-P_i (M_{\perp} \cdot M_{\perp}^*)$ $+ M_{\perp} (P_i \cdot M_{\perp}^*)$ $+ M_{\perp}^* (P_i \cdot M_{\perp})$	Purely magnetic scattering leads to a spin-flip unless $P_i \parallel M_{\perp}$
<u>C</u> hiral <u>m</u> agnetic	$-i M_{\perp}^* \wedge M_{\perp}$	For certain types of magnetic structures (e.g. helicoidal), $M_{\perp}^*$ is not parallel to $M_{\perp}$ , giving rise to chiral terms
<u>N-M-</u> <u>I</u> nterference	$N M_{\perp}^* + N^* M_{\perp} -$ $i [(N M_{\perp}^* - N^* M_{\perp}) \wedge P_i]$	If nuclear and magnetic Bragg peaks coincide (e.g. $k = 0$ ), the contribution from nuclear and magnetic scattering interfere, creating some polarisation along $M_{\perp}$ and inducing a precession of the polarisation around $M_{\perp}$ .

With these definitions, Blume-Maleev equations can be written in a tensor form as

$$P_f = \mathcal{P} P_i + P_c, \quad (2.29)$$

where  $P_c$  is the polarisation created during the process and  $\mathcal{P}$  is the polarisation tensor whose components can be deduced from Table 2.2. An explicit expression for  $\mathcal{P}$  will not be given here, but is expanded upon in the aforementioned literature, such as [35]. Blume introduced a quantity that can be deduced from observables, the polarisation matrix  $P^{\alpha\beta}$ . It is related to the polarisation tensor as

$$P^{\alpha\beta} = \left\langle \frac{\mathcal{P}^{\alpha\beta} P_i^{\beta} + P_c^{\alpha}}{P_i^{\beta}} \right\rangle_{\text{dom.}}, \quad (2.30)$$

where  $\langle \dots \rangle$  denotes an average over the magnetic domains. For a single magnetic domain, the polarisation matrix can also directly be extracted from measurements. Considering neutrons initially with a state  $|\beta\rangle$  scattered into a final spin state  $|\alpha\rangle$ , it

reads

$$P^{\alpha\beta} = \frac{|\langle\alpha|\hat{\mathbf{V}}(\mathbf{Q})|\beta\rangle|^2 - |\langle\alpha|\hat{\mathbf{V}}(\mathbf{Q})|\bar{\beta}\rangle|^2}{|\langle\alpha|\hat{\mathbf{V}}(\mathbf{Q})|\beta\rangle|^2 + |\langle\alpha|\hat{\mathbf{V}}(\mathbf{Q})|\bar{\beta}\rangle|^2} = \frac{\sigma_{\alpha\beta} - \sigma_{\alpha\bar{\beta}}}{\sigma_{\alpha\beta} + \sigma_{\alpha\bar{\beta}}}. \quad (2.31)$$

The cross-sections are then measured in the spin-flip and non-spin-flip channels. Since the polarisation matrix is accessible both experimentally and theoretically, a simple comparison can provide great insight on the orientation of the magnetic moments in the system. It has been previously established that the interaction potential takes the form  $\hat{\mathbf{V}}(\mathbf{Q}) = \hat{\mathbf{V}}_N(\mathbf{Q}) + \hat{\mathbf{V}}_M(\mathbf{Q})$ , where each component has been defined in Eqs. 2.10 and 2.16. If there is no magnetic contribution, the spins of the neutrons are not affected by the scattering process and the polarisation matrix simply reads  $P^{\alpha\beta} = \delta_{\alpha\beta}$ .

When working with polarised neutrons, the most effective approach is to measure peaks which provide a magnetic contribution only to the interaction potential, which is the case when the propagation vector is not a reciprocal lattice vector, or on structurally forbidden positions. In such a case, the cross-section reads, up to a proportionality factor,  $\sigma_{\alpha\beta} = |\langle\beta|\sigma_y M_y + \sigma_z M_z|\alpha\rangle|^2$ , where  $\sigma_i$  are the Pauli matrices. Assuming a single magnetic domain, the polarisation matrix can be written as follows

$$P^{\alpha\beta} = \begin{pmatrix} -1 & 0 & 0 \\ H & -K & L \\ H & L & K \end{pmatrix}. \quad (2.32)$$

where the matrix components are defined by

$$\begin{cases} H D = i (M_y M_z^* - M_y^* M_z) \\ K D = |M_z|^2 - |M_y|^2 \\ L D = M_y M_z^* + M_y^* M_z \\ D = |M_y|^2 + |M_z|^2. \end{cases} \quad (2.33)$$

Importantly, in the msot general case,  $P^{xx}$  gives great insight on the type of scattering process occurring. A value of  $P^{xx}$  close to -1 means that most of the spins have been flipped, which is the case when magnetic scattering occurs. If  $P^{xx}$  is close to 1, then nuclear scattering dominates. However, sometimes both scattering events emerge at the same positions. This case is more complicated and will be considered in detail in the last section of Chapter 4. Additionally, one must account for imperfect beam polarisation such that, experimentally,  $|P^{xx}| < 1$ . This will result in some neutrons naturally scattering into the wrong channel which must be accounted when comparing measured and computed matrices. It is useful to introduce the spin-flip ratio  $R$ , commonly extracted from a purely nuclear reflection, defined as

$$R = \frac{\sigma_{\alpha\alpha}}{\sigma_{\alpha\bar{\alpha}}}\bigg|_N = \frac{1}{2\eta(1-\eta)} - 1, \quad (2.34)$$

## Chapter 2. Welcome to the world of neutrons

---

which naturally introduces the neutron beam polarisation efficiency  $\eta$ . Consequently,  $\eta$  neutrons will have the correct polarisation  $|\alpha\rangle$ , and  $(1 - \eta)$  neutrons will have the wrong polarisation  $|\bar{\alpha}\rangle$ . Note that nuclear incoherent scattering might flip the spin and be measured in all channels, slightly changing the effective spin-flip ratio value.

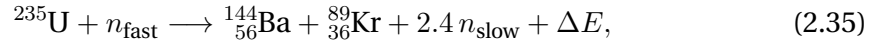
In a typical SNP diffraction experiment, one would measure as many inequivalent reflections as possible, ideally with a strong magnetic to nuclear contribution ratio. The comparison between experimentally extracted polarisation matrices and simulated ones based on Eq. 2.31 will lead to the determination of the magnetic vector direction with great accuracy. Note that polarised neutrons can also be used in inelastic measurements, allowing separation of phonon signals from magnetic features, but this has not been used in the scope of this thesis.

## 2.2 Instrumentation

Although neutron scattering techniques are among the most powerful tools for structure determination and dynamic properties studies, they incur a cost. Neutrons are hard to produce owing to the high energy scale needed to create them, and hence need the construction of dedicated neutron scattering facilities all around the globe. All the experiments performed in this thesis have been performed at PSI (CH), ILL and LLB (FR), ISIS (UK), HZB and HML (GER), and finally NIST (USA).

There are two ways to produce neutrons: either with spallation or nuclear sources. In the first method, protons are accelerated to very high energies (to the order of GeV) and projected onto heavy metal targets (usually Ta or W). Collisions will take place with nuclides which will hit other nuclides inside the same nucleus, inducing in a chain reaction. The resulting excited – and unstable – nuclei will then evaporate protons, mesons and, more importantly, neutrons. The latter will have a similar energy range to the incident particle. Spallation processes are usually pulsed, with a frequency in the range 10 to 100 Hz.

Neutrons can also be produced from fission processes. In this case, slow neutrons are sent onto Uranium-235 atoms which will, in turn, break into fast neutrons and other elements. Since this reaction is exothermal and releases more neutrons ( $n_{\text{fast}} = 2.4 n_{\text{slow}}$ ) than was required to be triggered, it is then self-sustaining. As an example of reaction that describe a fission process:



where  $\Delta E$  usually is of the order of 200 MeV. The resulting fast neutrons energy follows a Maxwell distribution. Fission processes continuously produce neutrons.

As stated, scattering experiments require neutrons in the eV range maximum whereas their energy can go up to 1 GeV just after creation. It is then necessary to drastically cool them down, which can be achieved by colliding them with light elements such as  $\text{H}_2\text{O}$  or  $\text{D}_2\text{O}$ . The choice of the moderator will depend on the type of incoming neutron beam. If it is pulsed, one wants to cool them down in the shortest amount of time. If it is continuous, one then needs to slow as many neutrons as possible.

Neutrons are then distributed to the instruments through neutron guides which greatly improve loss reduction of the flux with distance. Indeed, the flux decreases as  $r^{-2}$  for isotropic radiation whereas the use of optimised neutron guides enable a loss not higher than 2% per 10 m. Neutron guides are based on the total reflection principle, which occurs when the scattering angle is smaller than a critical angle which depends on the composition of the guide. Furthermore, constructing layers of variable thickness with alternating positive and negative length results in so-called supermirrors which dramatically increase the transmission of neutron beams. An example of a neutron

## Chapter 2. Welcome to the world of neutrons

experimental hall can be found in Fig. 2.2.

There are many ways of closing the scattering triangle defined in Fig. 2.1. In the following, I present two types of instruments which can reach such a geometry and that I used throughout this thesis.

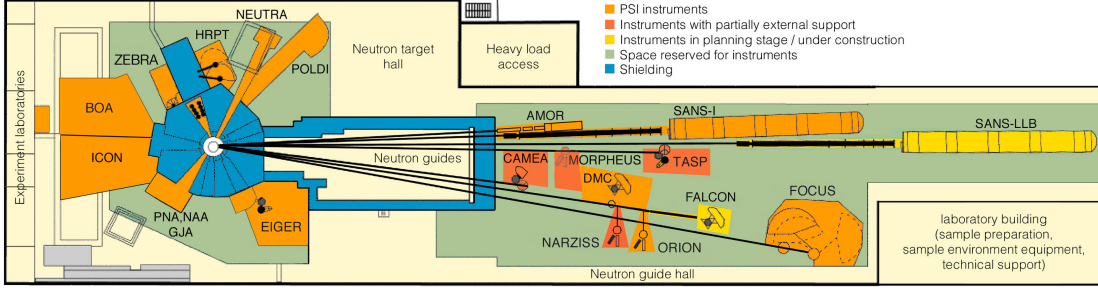


Figure 2.2 – **SINQ neutron guide hall**, at PSI (CH). Neutrons are produced and then distributed to the instruments via neutron guides. Figure taken from [www.psi.ch](http://www.psi.ch)

### 2.2.1 Time-of-Flight instruments

Time-of-Flight (ToF) instruments work on a very simple principle. Assuming that neutrons are point-like particles and using position sensitive detectors, the energy of the neutrons can be easily determined from their time-of-flight, *i.e.* between the selection of a neutron by a chopper and its observation by a detector. This implies the existence of a very large circular bank of detectors, such that they all lie at the same distance from the sample. For inelastic scattering events, there exist two types of scattering geometry. In the direct ToF configuration, the incident energy  $E_i$  is fixed, usually by a chopper or a crystal, and the time of flight gives the final energy  $E_f$ . If the spectrometer is in an indirect configuration, the sample is illuminated by a white (polychromatic) beam and the final energy is determined by a crystal. The initial energy is then obtained by the time-of-flight. Most ToF spectrometers work in a direct configuration. A good instrument will reach an energy resolution to the order of 1% of the incoming energy. In the case of diffraction, inelastic scattering processes are neglected since their intensity usually lies several orders of magnitude below elastic scattering on Bragg peaks. A white pulse of neutrons is sent towards the crystal and is scattered at different wavelengths and angles. From the time of flight, one easily extracts the wavelength of the neutron as  $\tau_{\text{ToF}} = \alpha(L_1 + L_2)\lambda$ , where  $\alpha = 252.7 \mu\text{s}/\text{m}/\text{\AA}$ , and  $L_{1,2}$  are the distances before and after the sample defined on Fig. 2.3. If the detector coverage is big enough, one can measure a large portion of the reciprocal space in a single sustained measurement to retrieve good statistics.

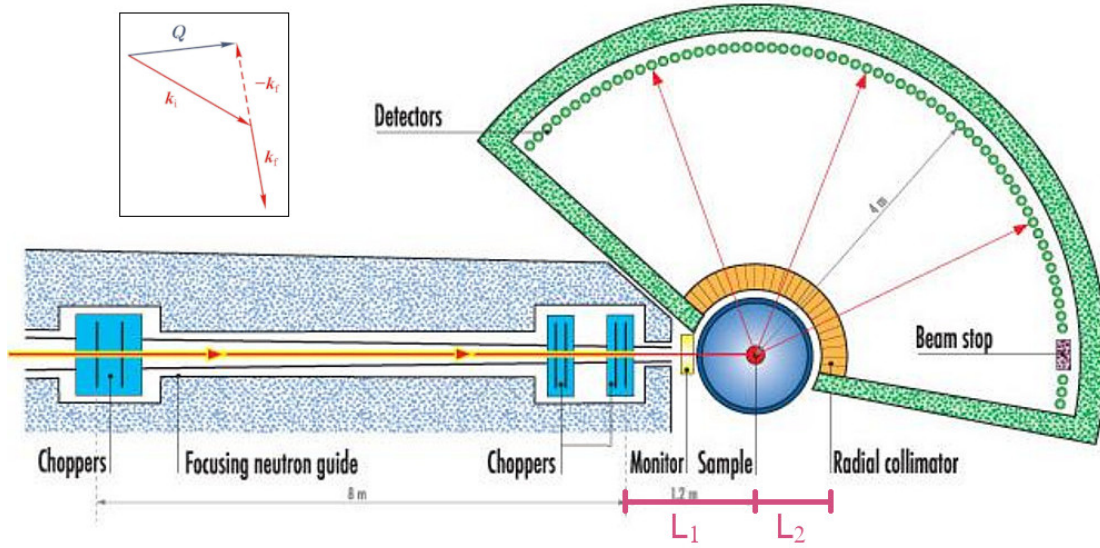


Figure 2.3 – **Schematic representation of the IN5 direct TOF spectrometer (ILL).** Six choppers select the initial neutron wavelength and tune the resolution of the instrument. After a distance  $L_1$ , the incoming neutrons are scattered in all directions. Those whose energy satisfies the scattering condition shown inset are detected by the detectors placed at a distance  $L_2$  from the sample. Adapted from [www.ill.eu](http://www.ill.eu)

### 2.2.2 Triple-Axis Spectrometers

Triple-Axis Spectrometers (TAS) work in a slightly different way. The main difference is that the energy selection takes place both before and after the sample, to ensure there is only one configuration that satisfies the scattering condition 2.1 for a given incoming and outgoing energy, achieved by rotating the arms of the spectrometer around its three axis, hence the name. A polychromatic beam of neutrons reaches to the monochromator (typically made of pyrolytic graphite PG or Si) that, due to Bragg scattering, will select only one wavelength by changing the scattering angle  $2\theta_M$ . A similar process occurs at the analyser, where the outgoing energy is selected by a rotation of the angle  $2\theta_A$ . All the angles are defined in Fig. 2.4. Since the neutron flux drastically varies with  $k_i$  (examples can be found in [16]), a typical TAS experiment will fix  $k_i$  to an optimal value and then allow  $k_f$  to vary. The 4-dimensional resolution depends strongly on the position in reciprocal space where the measurement is taken from. It then takes the form of an ellipsoid and must be accounted for in the data analysis. A full investigation on TAS data will then involve scans along all directions at the elastic line level. It has been described theoretically [36, 37] and implemented in some packages like ResLib, which can be found online.

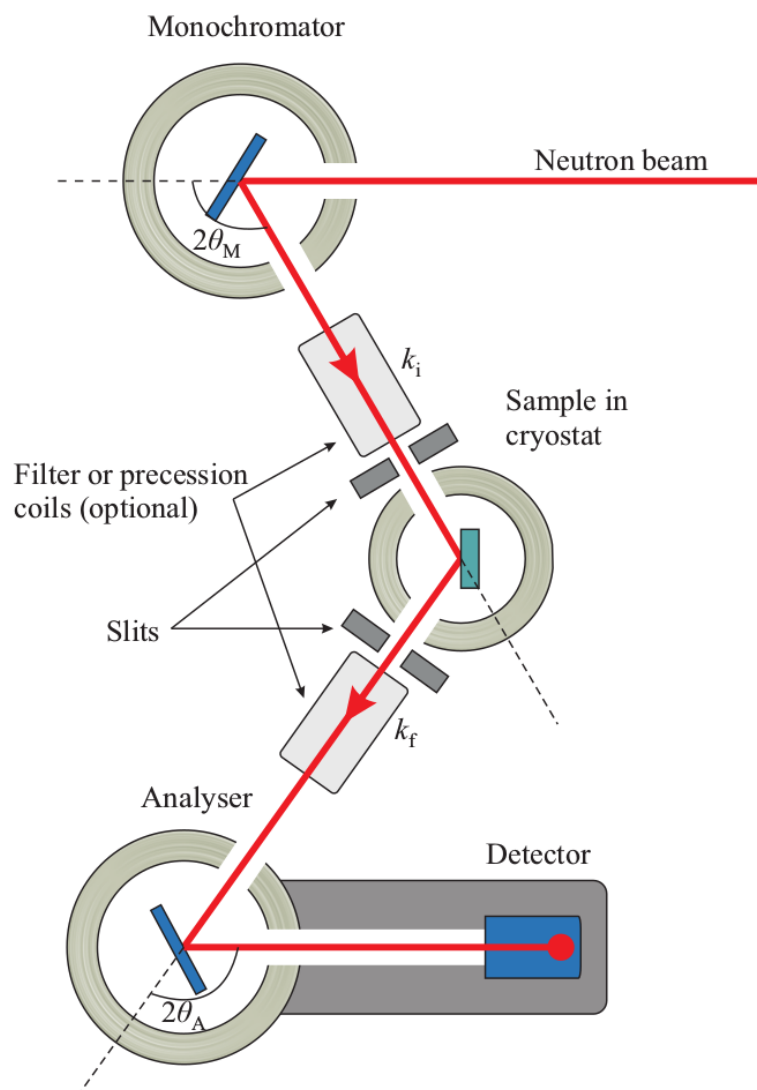


Figure 2.4 – **Schematic representation of a Triple-Axis Spectrometer.** The setup is described in the paragraph above. Collimators are usually placed both before and after the sample. Slits are used in order to remove any signal which does not emerge from the sample. Beryllium (BE) or Graphite (PG) filters are added before and after the sample to remove higher order wave vectors. Finally, monitors are placed along the monochromator – sample, or the sample – analyser paths in order to normalise the neutron flux. Figure taken from [38]



### Multiplex analysers

The last decade has witnessed the birth of a whole new generation of analysers, called multiplex analysers. So far, in order to study low-energy excitations, one has to compromise between the large coverage but low flux of a ToF instrument, and the high flux but very limited coverage of a TAS. Indeed, in a standard TAS experiment, only one final wavevector is being measured at a time, which means that a significant amount of scattering processes are not considered. By allowing neutrons to be scattered vertically instead of horizontally, individual or 2D detectors can be placed at different altitude scattering angles  $2\theta$  which are associated to sets of analysers, each of them scattering a single wave vector with the angle  $2\theta_A$ , as represented in Fig. 2.5. Such analyser systems can be fixed on the third axis of a TAS and are meant to compete with TOF spectrometers. Here can be cited FlatCone (ILL) [39], MultiFLEXX (HZB) [40] and more recently CAMEA (PSI) [41, 42, 43] on which I worked for a couple of months during its commissioning phase. The near future will see the development of MARMOT which is part of ILL's endurance plan and should be operational in 2023, and BIFROST (ESS) which will use the prismatic concept developed on CAMEA and that will lead the creation of a whole new generation of neutron spectrometers.

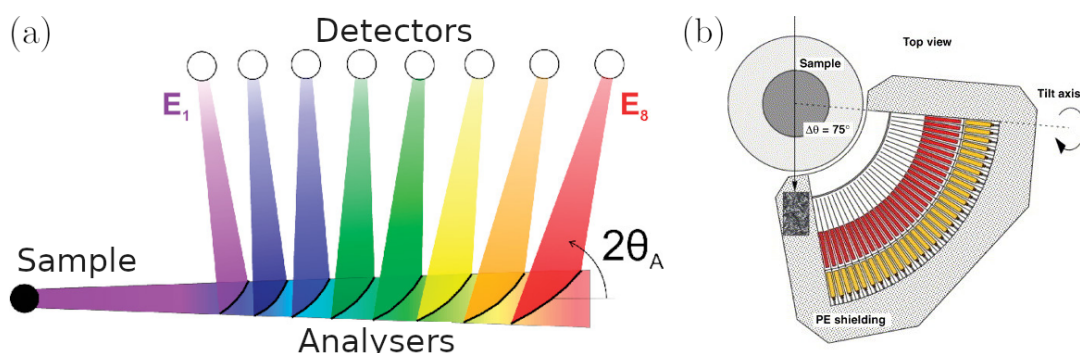


Figure 2.5 – **Multiplex analysers.** (left) Array of analysers. Each of them vertically scatters one wavelength only such that several final energies are being measured at the same time. (right) Detectors bank of FlatCone, with internal shielding to avoid cross-talking. Each detector measures neutrons with a different outgoing wave vector  $k_f$ , covering a huge part of the reciprocal space. Figures taken from [42] and [39].

### 2.2.3 Polarisation analysis with TAS

Section 2.1.4 mentioned the possibility to integrate the neutron's spin in the analysis by tracking changes in its spin state during the scattering process. This is the basis of Spherical Neutron Polarimetry (SNP). It is among the most challenging neutron techniques in term of engineering, because one has to completely isolate the sample space from any external source of magnetic field, including the Earth's, in order to control the orientation of the spin at all time. This is typically done on CryoPAD (ILL) [33, 34, 44, 45] by shielding the region around the sample with superconducting Nb, resulting in a Meissner effect, or by using highly permeable mu-metals which will reduce any external field by a factor of 1000, as is the case for MuPAD (PSI) [46]. This shielding unit will then sit around the sample place of a TAS, as described in detail in Fig. 2.6. Although this configuration can be used to study inelastic processes in order to separate the magnetic signal from phonon contributions, we will restrain ourselves to the case of elastic scattering in the frame of this thesis. We used both CryoPAD and MuPAD in order to determine the magnetic structure of antiferromagnets. Indeed, since this technique relies on the absence of any magnetic field inside the sample chamber, it excludes the investigation of compounds whose magnetic moments have a ferromagnetic component. Another drawback is that although powerful, this method implies a drastically reduced count rate because of the extra shielding and selection of the outgoing polarisation.

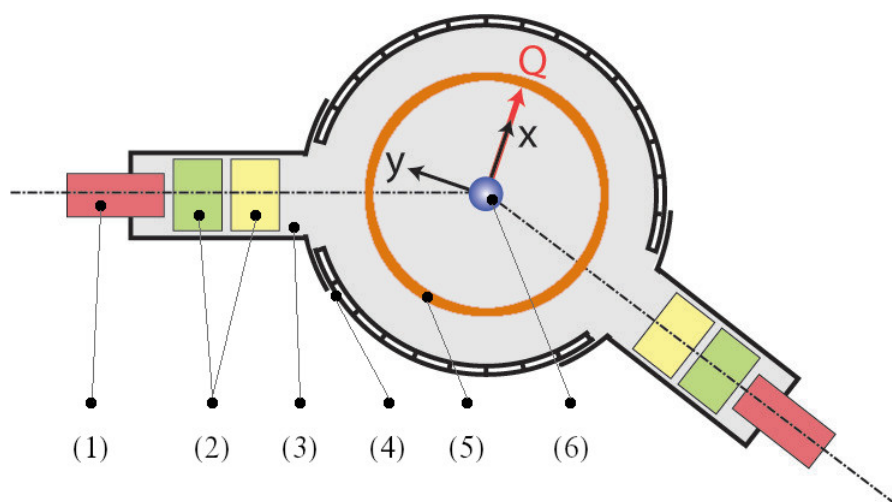


Figure 2.6 – **Spherical Neutron Polarimetry on MuPAD (PSI)**. The incoming beam is polarised by super-mirrors or single crystal polarisers, along the arm of the TAS (3). Guide-fields (1) are used to maintain the polarisation of the neutron. In the shielded region (grey area), Helmholtz coils (2) control the orientation of the polarisation with magnetic fields. Neutrons are then scattered onto the sample (6) which lies in a cryostat (5) and a beam shield (4), as for any TAS. The same elements are present on the other arm of the spectrometer. The  $(x, y, z)$  coordinate system specific to polarised neutrons is also highlighted. Figure adapted from [www.psi.ch](http://www.psi.ch)

## 2.3 Linear Spin Wave theory

The Linear Spin Wave (LSW) approximation is widely used in studies of systems described by a Heisenberg Hamiltonian in order to derive an upper estimate to the ground state energy, and extract ground state and low-lying energy states properties. It is a very powerful tool, both for its simplicity and for its accuracy and has been extensively adapted for the analysis of inelastic neutron scattering experiments. This semi-classical method consists of introducing quantum fluctuations on top of a highly degenerated classical ground state, which provides a reasonable estimate for the quantum ground state of the system.

### 2.3.1 Square antiferromagnet

As a gentle introduction, let us start with the simple case of a square antiferromagnet, as investigated by Kubo [47] and Anderson [48]. We consider the following Heisenberg Hamiltonian, with  $J > 0$  and  $\langle i, j \rangle$  denotes a sum restricted to nearest-neighbour sites

$$\hat{\mathcal{H}} = J \sum_{\langle i, j \rangle} \hat{\mathbf{S}}_i \cdot \hat{\mathbf{S}}_j. \quad (2.36)$$

Assuming a Néel state  $|N\rangle = |\uparrow\downarrow \dots \uparrow\downarrow\rangle$ , the lattice can be decomposed into two sublattices,  $A$  and  $B$  with only spins up, and down respectively. We assume a quantisation along the  $z$  axis. Although the Néel state is well-suited to describe the classical ground state properties of the system, it does not correspond to its quantum ground state. In fact, it is not even an eigenstate of the Hamiltonian. Nevertheless, it can act as a reference state in order to get a reasonable approximate of the quantum ground state. Indeed, local quantum fluctuations can be added on site  $i \in A$  ( $j \in B$ ) through the bosonic operators  $\hat{a}$  and  $\hat{a}^\dagger$ , as proposed by Holstein and Primakoff [49].

$$\text{A: } \begin{cases} \hat{\mathbf{S}}_i^z = S - \hat{n}_i \\ \hat{\mathbf{S}}_i^+ = \sqrt{2S} \sqrt{1 - \frac{\hat{n}_i}{2S}} \hat{a}_i \\ \hat{\mathbf{S}}_i^- = \sqrt{2S} \hat{a}_i^\dagger \sqrt{1 - \frac{\hat{n}_i}{2S}} \end{cases}, \quad \text{B: } \begin{cases} \hat{\mathbf{S}}_j^z = -S + \hat{n}_j \\ \hat{\mathbf{S}}_j^+ = \sqrt{2S} \hat{a}_j^\dagger \sqrt{1 - \frac{\hat{n}_j}{2S}} \\ \hat{\mathbf{S}}_j^- = \sqrt{2S} \sqrt{1 - \frac{\hat{n}_j}{2S}} \hat{a}_j \end{cases} \quad (2.37)$$

The term  $\hat{n}_i = \hat{a}_i^\dagger \hat{a}_i$  represents the magnon occupation number on site  $i$ . Assuming  $\hat{n}_i \ll 2S$  allows us to keep the linear terms in  $S$  only in Eq. 2.37. This hypothesis is justified for spin- $\frac{1}{2}$  antiferromagnets by the low amount of quantum corrections  $\langle \hat{a}_i^\dagger \hat{a}_i \rangle \sim 0.196$  [50]. The Hamiltonian 2.36 reads :

$$\hat{\mathcal{H}} = J \sum_i \sum_{j(i)} \left( S^2 - S \hat{a}_i^\dagger \hat{a}_i - S \hat{a}_j^\dagger \hat{a}_j - \frac{2S}{2} (\hat{a}_i \hat{a}_j + \hat{a}_i^\dagger \hat{a}_j^\dagger) \right) \quad (2.38)$$

$$= JS^2 \frac{Nz}{2} - \frac{JS}{2} \sum_{\tau} \sum_{\mathbf{k}} \left( 2 \hat{a}_{\mathbf{k}}^\dagger \hat{a}_{\mathbf{k}} + \hat{a}_{\mathbf{k}} \hat{a}_{-\mathbf{k}} e^{-i\mathbf{k}\cdot\boldsymbol{\tau}} + \hat{a}_{\mathbf{k}}^\dagger \hat{a}_{-\mathbf{k}}^\dagger e^{i\mathbf{k}\cdot\boldsymbol{\tau}} \right), \quad (2.39)$$

where  $j(i)$  denotes the sites  $j$  interacting with a fixed site  $i$ ,  $\boldsymbol{\tau} = \mathbf{r}_j - \mathbf{r}_i$  and  $z$  is the coordination number. We also used the Fourier transform of the ladder operators  $\hat{a}_{\mathbf{k}} = \frac{1}{\sqrt{N}} \sum_i \hat{a}_i e^{-i\mathbf{k}\cdot\mathbf{r}_i}$ . This Hamiltonian can be rewritten as sum of harmonic oscillators with the appropriate unitary coordinate transformation, as proposed by Bogoliubov [51].

$$\hat{a}_{\mathbf{k}} = u_{\mathbf{k}} \hat{b}_{\mathbf{k}} + v_{\mathbf{k}} \hat{b}_{-\mathbf{k}}^\dagger \quad (2.40)$$

The old magnon ladder operators  $\hat{a}$  are now expressed as linear combination of bosonic operators  $\hat{b}$  which preserve the commutation rules  $[\hat{b}_{\mathbf{k}}, \hat{b}_{\mathbf{k}'}^\dagger] = \delta_{\mathbf{k}, \mathbf{k}'}$ , with real coefficients  $u_{\mathbf{k}}$  and  $v_{\mathbf{k}}$  which respect the relation  $u_{\mathbf{k}}^2 - v_{\mathbf{k}}^2 = 1$ . In this new basis, the Hamiltonian can be rewritten as  $\hat{\mathcal{H}} = \mathcal{E}_0 + \hat{\mathcal{H}}_2$ , where

$$\mathcal{E}_0 = \frac{JS^2 Nz}{2} \quad (2.41)$$

$$\hat{\mathcal{H}}_2 = \sum_{\mathbf{k}} \omega_{\mathbf{k}} \hat{b}_{\mathbf{k}}^\dagger \hat{b}_{\mathbf{k}} + \varepsilon_0. \quad (2.42)$$

This quadratic Hamiltonian introduces a new type of excitations, called *spin waves*. Their expression  $\omega_{\mathbf{k}}$  can be derived from the commutation relation  $[\hat{\mathcal{H}}, \hat{b}_{\mathbf{k}}] = \omega_{\mathbf{k}} \hat{b}_{\mathbf{k}}$  which, for a square antiferromagnet, yields  $\omega_{\mathbf{k}} = -JSz\sqrt{1 - \gamma_{\mathbf{k}}^2}$  where  $\gamma_{\mathbf{k}} = \frac{\sum_{\boldsymbol{\tau}} \cos(\mathbf{k}\cdot\boldsymbol{\tau})}{z}$  depends on the dimensionality of the system. The constant term  $\mathcal{E}_0$  is the classical energy of the system, and  $\varepsilon_0$  is the so-called zero point energy of the system, associated to the quantum fluctuations of the ground state. It represents the energy of the unperturbed state  $|0\rangle$ , in the magnon representation such that  $\hat{a}|0\rangle = 0$ . An analytical form can be deduced from the condition  $\langle 0 | \hat{\mathcal{H}}_2 | 0 \rangle = 0$ , which yields  $\varepsilon_0 = \frac{JSz}{2} \sum_{\mathbf{k}} (\omega_{\mathbf{k}} - 1)$ . It has been proven that these spin waves provide a good description of the magnetic excitations in many quantum system, assuming that quantum fluctuations are not too important ( $\Delta S \ll S$ ).

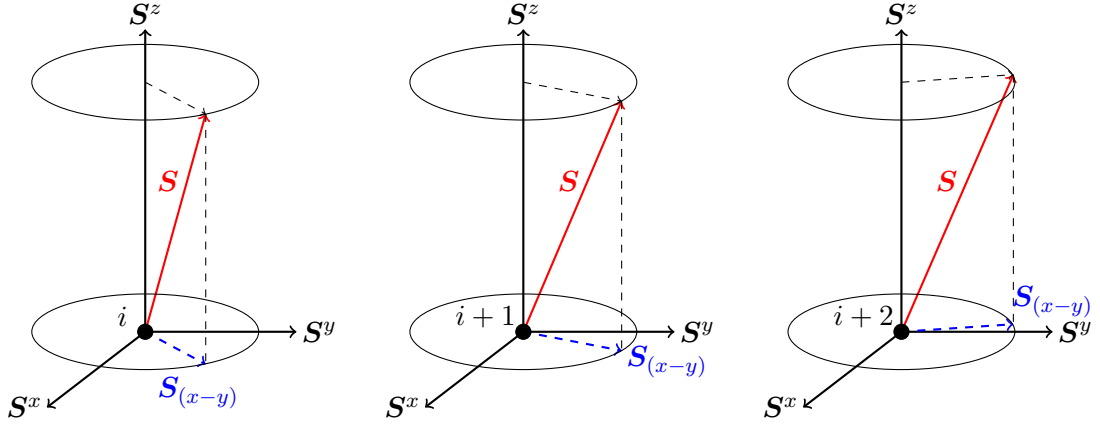


Figure 2.7 – **Representation of a spin wave** in real space created by a single local spin deviation defined by  $k$ . The fluctuations perpendicular to the quantisation axis  $z$  form a cosine of period  $\sim 1/k$ . In the LSW formalism, many different spin deviations can be created on the same site

### 2.3.2 Generalisation and applications to neutrons

In the case of real compounds, their nuclear structure and magnetic interactions between the atoms make such that all spins are not necessarily collinear. To deal with these more realistic cases, it becomes necessary to introduce local spin transformations on each site which will leave the Hamiltonian invariant. First of all, LSW theory assumes that there is long range order. This means that the classical spins of a magnetic cell at position  $r_m$  are built relatively to the ones in the original magnetic cell by rotating all moments by  $\phi_m = \mathbf{k} \cdot \mathbf{r}_m$ , where  $\mathbf{k}$  is the propagation vector. In order to recover a ferromagnetic state which is easy to work with because of the single choice of quantisation axis, it is necessary to use a rotating frame defined by two rotations. The first one will make such that all magnetic cells will be identical by defining new operators  $\hat{\mathbf{S}}'_{m,i}$  for each site  $i$  belonging to the  $m^{\text{th}}$  unit cell.

$$\hat{\mathbf{S}}_{m,i} = \mathcal{R}_m \hat{\mathbf{S}}'_{m,i}. \quad (2.43)$$

The rotation matrix  $\mathcal{R}_m$  depends on the angle  $\phi_m$  defined above. The second transformation ensures that all spins within the same magnetic unit cell are oriented ferromagnetically

$$\hat{\mathbf{S}}'_{m,i} = \mathcal{R}'_i \hat{\mathbf{S}}''_{m,i}. \quad (2.44)$$

As mentioned previously, the Hamiltonian is invariant under these transformations. In the most general case, it reads:

$$\hat{\mathcal{H}} = \sum_{m,i} \sum_{n,j} \hat{\mathbf{S}}_{m,i}^\dagger \mathcal{J}_{m,i;n,j} \hat{\mathbf{S}}_{n,j} + \sum_{m,i} \hat{\mathbf{S}}_{m,i}^\dagger \mathcal{A}_{m,i} \hat{\mathbf{S}}_{m,i} + \mu_B \mathbf{H} \sum_{m,i} \mathbf{g}_i \hat{\mathbf{S}}_{m,i}, \quad (2.45)$$

where  $\mathcal{J}$  is the interaction matrix coupling site  $i$  to site  $j$ , including asymmetric exchanges such as the Dzyaloshinskii-Moriya interaction. The matrix  $\mathcal{A}$  represents any local anisotropy, such as the single ion anisotropy, and  $\mathbf{H}$  accounts for an external magnetic field. Substituting the spin operators for their approximate expressions defined in Eq. 2.37 provides the dispersion relation of this system. Another measurable quantity is the dynamic structure factor introduced in Eq. 2.18. The same approximation can be used in this expression, allowing for direct comparisons with experiments.

Of course, an analytical solution cannot always be obtained for more structurally complex systems. Hence the development of softwares that would diagonalise large bosonic Hamiltonians in their Hilbert space using an optimisation method proposed by Colpa [52]. The Matlab package SpinW [53] has been developed in the past few years and has rapidly become the most powerful software for a spin wave analysis of real compounds. It has been widely used in the frame of this doctoral thesis. Being a semiclassical theory, assuming  $\langle \hat{a}_i^\dagger \hat{a}_i \rangle \ll 2S$ , this theory does not cover strong quantum effects, nor cluster systems, but is extremely simple and powerful for the description of long range ordered quantum magnets.

### Beyond the LSWT

Some extensions to the LSWT have been developed throughout the years. The first natural improvement is to include higher order terms in Eq. 2.37 which is necessary to describe phenomena with symmetry breaking or vanishing order parameters as for the Ginzburg-Landau so-called mexican hat potential [54]. Similarly, novel excitations could be described with quartic terms, but the literature about this is, to the best of my knowledge, very poor. A second improvement to the LSWT can be achieved by assuming the existence of many condensates, each of them describing a quantum state. This is the essence of the multi-boson spin wave theory which has been widely used in the case of quantum systems with  $S > \frac{1}{2}$  that exhibit clustered long range order such as tetrahedra based systems [55]. New bosonic operators are then introduced in a similar fashion, probing higher order spin states. Finally, although not directly related to the LSWT, one can present mean field bonds operators which are ideal in systems that lie close to a quantum critical point [56, 57, 58]. It consists in the introduction of new operators corresponding to clustered quantum states, for example triplets  $|t\rangle$  and singlets  $|s\rangle$  in the Hamiltonian describing the system.

# 3 Coexistence of multi-type excitations in $\text{SeCuO}_3$

## Contents

<b>3.1 Introduction</b>	<b>32</b>
3.1.1 Magnetic excitations	33
3.1.2 Crystal structure and magnetic properties	36
3.1.3 Experimental setup	38
<b>3.2 Localised magnetic dimers</b>	<b>39</b>
<b>3.3 Three dimensional long-range order</b>	<b>42</b>
3.3.1 Interpretation of the effective couplings	46
<b>3.4 A spinon-like continuum</b>	<b>49</b>
<b>3.5 Summary</b>	<b>52</b>

In this chapter, I present a complete review of the magnetic excitations in the quantum magnet  $\text{SeCuO}_3$ . Prior susceptibility measurements suggested the existence of localised quantum states at high temperature forming non-magnetic singlets [59]. The system exhibits a long range ordered magnetic behaviour at low temperature but nevertheless retains features of its quantum ancestry.  $\text{SeCuO}_3$  forms an interesting arena to study how localised effects evolve into, or coexist with, collective states. I will demonstrate that three different types of excitations are present simultaneously in  $\text{SeCuO}_3$ , and, more importantly, that they show a high degree of entanglement. These excitations are associated with two magnetic sublattices, one of which forms strongly bound dimers resulting in triplonic excitations. The second one is responsible for long range antiferromagnetic order, forming a network of interacting spin chains. Remarkably, the small amount of frustration in this system contributes to the presence of spinon continua at energies above the magnon band. The coexistence of all three types of excitations in a single quantum magnet and the presence of a spinon continuum different from the traditional one-dimensional form open the door to a consistent and combined theoretical treatment of multi-type excitations. Additionally, it calls for further investigation on the criteria for the presence of a spinon continuum. The work

presented in this chapter has been summarised in a paper published as a Letter in Physical Review B [60].

### 3.1 Introduction

The most common type of magnetic excitations in a system are spin waves, emerging from robust long range order. They are dominant in systems with weak quantum fluctuations and are well-described by the semi-classical linear spin wave approximation, which is a mastered technique. Thus they do not challenge new fields of quantum physics any more. Real challenges appears when the spin quantum fluctuations drive a system beyond this established long range order as is the case when the system has a lower dimensionality, different geometries leading to exotic magnetic lattices, or when it exhibits magnetic frustration. These scenarios result in new collective excitations, such as triplons arising from spin dimerisation [61, 62, 63] and frustration [64], bond states of magnons [65] or triplons [66, 67, 68], or fractional excitations such as spinons [69, 70] solitons [71, 72] or even Majorana particles [73, 74, 75]. All these systems are traditionally analysed in terms of one type of excitations, and great theories have been developed for in-depth comparisons with experiments.

However, if magnetic order is present, nothing states that the remaining quantum fluctuations are incoherent and should then be disregarded. Much less effort has been put into the understanding of quantum systems in which magnons coexist with more exotic quantum states. In  $\text{TlCuCl}_3$ , the field- [76] and pressure-induced [77] quantum phase transitions show an example of weak antiferromagnetic order on top of a dimer system with triplon excitations. Another example is  $\text{KCuF}_3$ , where a weak coupling of 1D spin chains produces magnetic order superposed to spinonic excitations, which is revealed at high energy [78]. It is also known that spinons coexist with square lattice antiferromagnetism [79] and some metal-organic systems offer the possibility to of tuning their coexistence [80]. Similarly, in the tetrahedron material  $\text{Cu}_2\text{Te}_2\text{O}_5\text{X}_2$  ( $\text{X} = \text{Cl}, \text{Br}$ ) [81], theoretical studies predicted a non-ordered ground state [82], which was subsequently confirmed experimentally [83]. Incommensurate magnetism [84] coexists with coupled-clusters excitations [85] – a behaviour that has been observed in other cluser materials [86, 87, 88]. More recently, another study pointed out the coexistence and interaction of spinons and magnons [89], emerging from weakly coupled antiferromagnetic and ferromagnetic chains.



### 3.1.1 Magnetic excitations

As presented in the introduction of this thesis, quantum magnets can be seen as sets of interacting particles defining a magnetic lattice, and characterised by a ground state and a spectrum of excited states. These features depend mainly on the magnetic interactions between the spins of interacting magnetic ions. Knowledge of the energy spectrum  $E_n$  and the corresponding wave functions  $|\psi_n\rangle$  is crucial, since both are used in the computation of observables  $\langle O \rangle = \sum_n p_n \langle \psi_n | \hat{O} | \psi_n \rangle$ . There exists a whole series of excitations, semi-classical or purely quantum, that can be divided in two categories – local or global. They are all very well captured by inelastic neutron scattering assuming that they obey the selection rules  $\Delta S = 1$ . Here, I propose a brief review of the main types of excitations observed in  $\text{SeCuO}_3$ .

#### Triplons

The simplest magnetic system is formed by two identical spins- $\frac{1}{2}$ , 1 and 2, whose interaction strength is given by  $J_D > 0$ . This is called a dimer. The total spin is given by  $S = S_1 + S_2$ , and forms a new quantum number. The Hamiltonian of such a system is given by

$$\hat{\mathcal{H}}_D = J_D \hat{\mathbf{S}}_1 \cdot \hat{\mathbf{S}}_2. \quad (3.1)$$

The spectrum is easily obtained after diagonalisation of the Hamiltonian, and is given by the ground state  $E_0 = -\frac{3J_D}{4}$ , with a total spin  $S = 0$ , and the three times degenerated energy level  $E_1 = \frac{J_D}{4}$  associated with  $S = 1$  states, described by the wave functions

$$\begin{aligned} |\psi_0\rangle &= \frac{1}{\sqrt{2}} (|\uparrow\downarrow\rangle - |\downarrow\uparrow\rangle) \\ |\psi_{1,\bar{1}}\rangle &= |\downarrow\downarrow\rangle \\ |\psi_{1,0}\rangle &= \frac{1}{\sqrt{2}} (|\uparrow\downarrow\rangle + |\downarrow\uparrow\rangle) \\ |\psi_{1,1}\rangle &= |\uparrow\uparrow\rangle. \end{aligned} \quad (3.2)$$

Triplons excitations are, by essence, localised in space. In fact, they can then be considered as a new entity, whose assembly forms a new magnetic lattice, allowing to reach new quantum states. It is a rather common type of excitation, which nevertheless results in interesting quantum states as in the Shastry-Sutherland quantum magnet  $\text{SrCu}_2(\text{BO}_3)_2$  (SCBO) [68, 90, 91]. The structure factor of triplons is not constant in reciprocal space. An expression can be derived by adapting the dynamic structure factor in Eq. 2.7 to the singlet–triplet transition [92]. Of course, there exists similar states for larger sets of atoms which result in doublons, quintuplons, septuplons, etc.

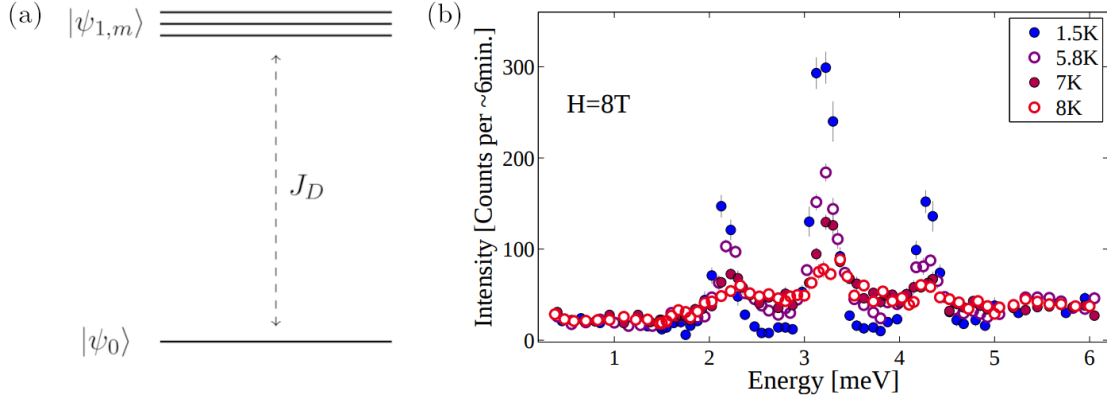


Figure 3.1 – **Triplet states** (a) Energy levels in a magnetic dimer. An energy gap of  $J_D$  separates the non-magnetic ground state  $|\psi_0\rangle$  from the triply degenerated excited states  $|\psi_{1,m}\rangle$ . (b) Splitting of the triplet states ( $S^z = 0, \pm 1$ ) in  $\text{SrCu}_2(\text{BO}_3)_2$  due to Zeeman effect induced by a 8 T vertical magnetic field. Figure taken from [90]

### Magnons

The most common type of excitation in a magnetically ordered quantum magnet is a magnon, also called a spin wave. Unlike in the previous section, it is a collective – or delocalised – spin-1 excitation that can be seen as a periodic rotation of the magnetic moments around their average direction. The existence of spin waves is theoretically predicted by Golstone’s theorem [93], which states that new excitations emerge when a continuous symmetry is spontaneously broken. In the present case, this continuous symmetry is the  $\text{SO}(3)$  rotation of the magnetic moments. Magnons are intrinsically dispersive and well described by the linear spin wave theory derived in Sec. 2.3. In the case of a ferromagnetic system, the dispersion is given by  $\varepsilon(\mathbf{Q}) = JS \sum_{\tau} (1 - e^{i\mathbf{Q} \cdot \tau})$ , where  $\tau$  is the nearest neighbour distance. This expression resumes to  $\varepsilon(Q) = 2JS (1 - \cos(Q \cdot a))$  in the case of a one dimensional problem, with  $a$  the interatomic distance. Similarly, in the most general case of  $m$  atoms per magnetic unit cell, one needs to describe the excitations with  $m$  magnetic sublattices. This implies the existence of  $m$  potentially degenerated magnon modes in the excitation spectrum.

### Spinons

It is known that fundamental excitations in a ferromagnetic quantum chain take the form spin waves. However, the situation is different for antiferromagnetic spin-1/2 chains. The exact solution for the ground state has been derived by Bethe [94]. The excitation spectrum has been calculated by Des Cloizeaux and Pearson [95] and later Faddeev [96], and consists of a macroscopic triplet such that  $S_{\text{tot}} = 1$ . It can be seen as a localised spin-flip, and requires the introduction of two domain walls separating a spin-flip region and a non-spin-flip region [Fig. 3.2(b)]. Additionally, separation of the walls do not cost energy. These domain walls represent fractional excitations, which are called spinons. Since they describe a spin-1 excitation (spin-flip), each of them carries a spin-1/2. A spinon pair can then be observed by neutrons. While each of them has a momentum  $Q_i$  and energy  $\varepsilon(Q_i)$ , an excitation at a given  $Q = Q_1 + Q_2$  can then be formed by an infinity of free spinon pairs and then results in a continuum of scattering intensity at this position, such that  $\varepsilon(Q_1 + Q_2) = \varepsilon(Q_1) + \varepsilon(Q_2)$ . An approximate [97] and exact [98] solution for the two-spinon dynamic structure factor has been proposed based on the Bethe ansatz, while tabulated values are given by Caux [99]. An example is given in Fig. 3.2. An exact excitation spectrum has been theoretically predicted by Haldane [100] and was observed for the first time in the  $S = 1/2$  chain  $\text{KCuF}_3$  [101] a few years later.

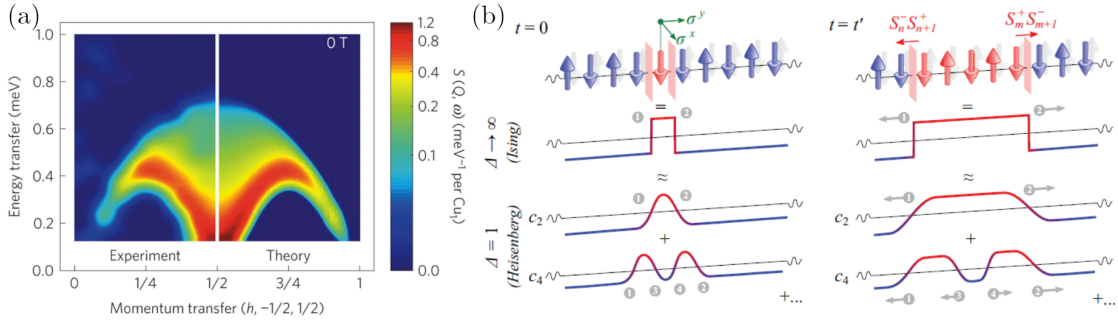


**Figure 3.2 – Spinon excitations.** (a) Spinon continuum measured on the antiferromagnetic Heisenberg chain  $\text{CuSO}_4 \cdot 5\text{D}_2\text{O}$ , and comparison with the two- and four- spinons dynamic structure factor. (b) Sketch of an excitation on the 1D antiferromagnetic chain and its time evolution. A spin-flip is represented by two domain walls, each carrying a spin-1/2. In the Heisenberg limit, it can be written as a sum of an even number of domain walls corresponding to two- four-  $2m$ - spinon processes. Figures taken from [70]

### 3.1.2 Crystal structure and magnetic properties

The  $S = 1/2$  quantum magnet  $\text{SeCuO}_3$  crystallises in a monoclinic unit cell described by the space group  $P2_1/n$  with lattice parameters  $a = 7.71 \text{ \AA}$ ,  $b = 8.24 \text{ \AA}$ ,  $c = 8.50 \text{ \AA}$ , and  $\beta = 99.12^\circ$  [102]. There are two crystallographically inequivalent Cu sites in the unit cell. Each are surrounded by six O atoms, forming  $\text{CuO}_4$  plaquettes and the remaining two Cu atoms form elongated octahedra, as represented in Fig. 3.3. The crystal field generated by the position of the O ligands breaks the degeneracy of the energy levels, favouring a  $d_{x^2-y^2}$  orbital state for the Cu spins. This structural configuration suggested the presence of  $\text{Cu}_1$  dimer units of edge-sharing plaquettes with  $\text{Cu}_1\text{--O--Cu}_1$  angles of  $101.9^\circ$ , highlighted in orange.  $\text{SeO}_4$  tetrahedra serve as ligands between different  $\text{Cu}_2$  sites.

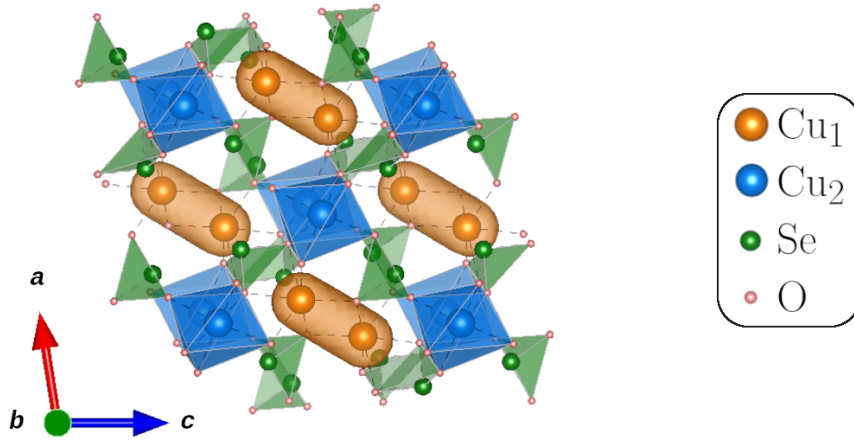


Figure 3.3 – **Nuclear structure of  $\text{SeCuO}_3$**  projected on the  $ac$  plane, showing  $\text{Cu}_1$  (orange),  $\text{Cu}_2$ , Se (green) and O (pink) atoms. Dimer units are highlighted in orange while  $\text{CuO}_6$  octahedra are in blue.

Due to the elongation of the octahedra, free electrons are more likely to lie in the  $d_{x^2-y^2}$  orbital. Superexchange processes  $\text{Cu--O--Cu}$  between two neighbouring Cu sites will then follow the path  $d_{x^2-y^2}\text{--}p_{x(y)}\text{--}d_{x^2-y^2}$ . This led to the initial proposal that  $\text{SeCuO}_3$  consists of a weakly coupled network of  $\text{Cu}_2\text{--Cu}_1\text{--Cu}_1\text{--Cu}_2$  linear tetramers, with a singlet ground state [103]. Magnetic susceptibility ( $\chi = M/H$ ) and specific heat measurements have been performed in the same previous study. The low temperature regime of the former shows a hint of an easy axis along [101] due to the low value of the susceptibility, with a field along this direction compared to the other orthogonal directions, and a narrow maximum around 18 K typical of three dimensional antiferromagnetic order. However, I note the presence of two distinctive energy scales. The first one at  $T_N = 8 \text{ K}$  is associated with the emergence of long range order, as confirmed by the sharp peak in the specific heat curve. The second one subsists until  $\sim 90 \text{ K}$ . The behaviour of the susceptibility is well explained at higher temperature by a tetramer model from thermodynamics considerations [104].

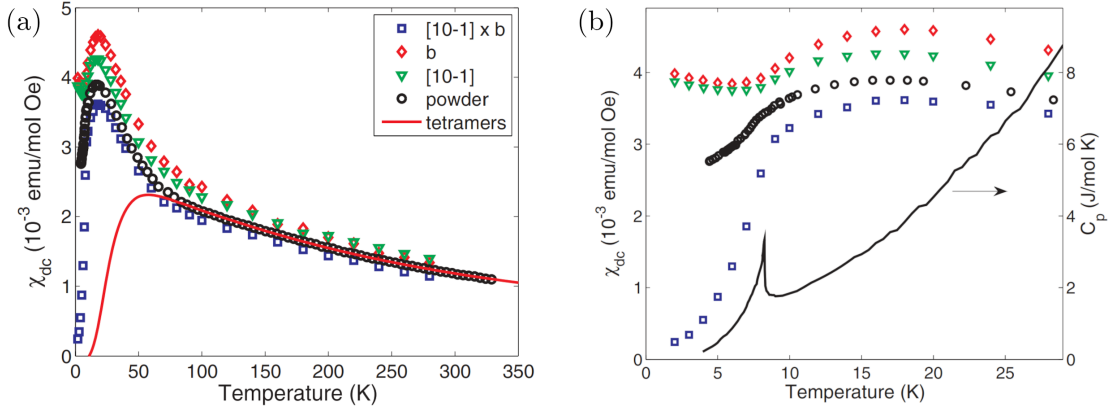


Figure 3.4 – **Magnetic susceptibility and specific heat measurements.** (a) Susceptibility measurements along three orthogonal directions on a single crystal, and on powder. The red line corresponds to a fit to a high temperature tetramer model. (b) Close up on the low temperature of the susceptibility, and specific heat measurements (black line). Figure adapted from [103].

However, the tetramer picture could not completely explain the overall behaviour of magnetic susceptibility below 90 K, as reported in Fig. 3.4. On the other hand, nuclear quadrupole resonance (NQR) indicated the formation of singlet states at temperatures below  $T \lesssim 200$  K, emphasising the existence of a strong bond  $J_D$  connecting two  $\text{Cu}_1$  atoms. Recent nuclear magnetic resonance (NMR), electron spin resonance (ESR) and magnetic torque magnetometry experiments suggested [105, 106] a formation of two decoupled subsystems, consisting of strongly interacting local  $\text{Cu}_1$  dimers and weakly coupled  $\text{Cu}_2$  spins. This deduction is also supported by neutron diffraction measurements performed on DMC (PSI). Indeed, despite the low statistics, a description of the diffraction pattern has been proposed with non collinear spins on both sublattices and site-dependent quantum correlations [107].

### 3.1.3 Experimental setup

In order to reveal the magnetic excitations in  $\text{SeCuO}_3$ , a standard chemical vapour transport method has been used to grow single crystals, resulting in a 1 g elongated and hollow single crystal shown in Fig. 3.5 that proved to be of high quality. It has been mounted on an Al sample holder and aligned using Laue x-ray backscattering at EPFL. Neutron scattering experiments have been carried out by previous members and collaborators of the laboratory. To access high-energy dynamics, the sample has been oriented in the  $(hkh)$  scattering plane and put in the thermal spectrometer IN8 (ILL) [108] with an incident wave vector of  $2.66 \text{ \AA}^{-1}$ , resulting in a resolution of  $1.8(2) \text{ meV}$  (FWHM) at  $\omega = 27 \text{ meV}$ . Low-energy magnetic properties have been probed on the cold spectrometer IN14 (ILL) [109], still in the  $(hkh)$  scattering plane, and 4F1 (LLB) in the  $(hk\bar{h})$  scattering plane. In both cases, the incident neutron wave vector was  $1.55 \text{ \AA}^{-1}$ , allowing for a resolution at  $\omega = 5 \text{ meV}$  of  $0.19(5) \text{ meV}$ . PG(002) monochromators and analysers have been used, as well as a Be filter placed between the sample and the analyser to remove higher order scattering processes. On IN8, counting times were 4 minutes per  $Q$ -point for  $\omega$  scans directly above of below the transition temperature, and 30 s per measurement for the temperature dependence study. On IN14 and 4F1, each  $Q$ -point was measured for 5 and 3 minutes, respectively.



Figure 3.5 – **Single crystal of  $\text{SeCuO}_3$**  used for neutron scattering experiments. The dimensions are approximatively 1.5 cm long by 0.5 cm wide for a mass of 1 g.

### 3.2 Localised magnetic dimers

As mentioned in Sec. 3.1.2, there are two energy scales in  $\text{SeCuO}_3$ . Local states are expected below  $T \lesssim 200$  K, and long range order emerges at  $T_N = 8$  K. In order to probe the physics in the higher energy scale, thermal neutron scattering has been performed on IN8. Two sets of measurements have been made. The first one focuses on low temperature properties by measuring  $I(\omega)$  at constant  $Q$  positions in the high-symmetry  $[0, k, 0]$  and  $[h, 3, h]$  directions. An example measurement is shown in Fig. 3.6(a).

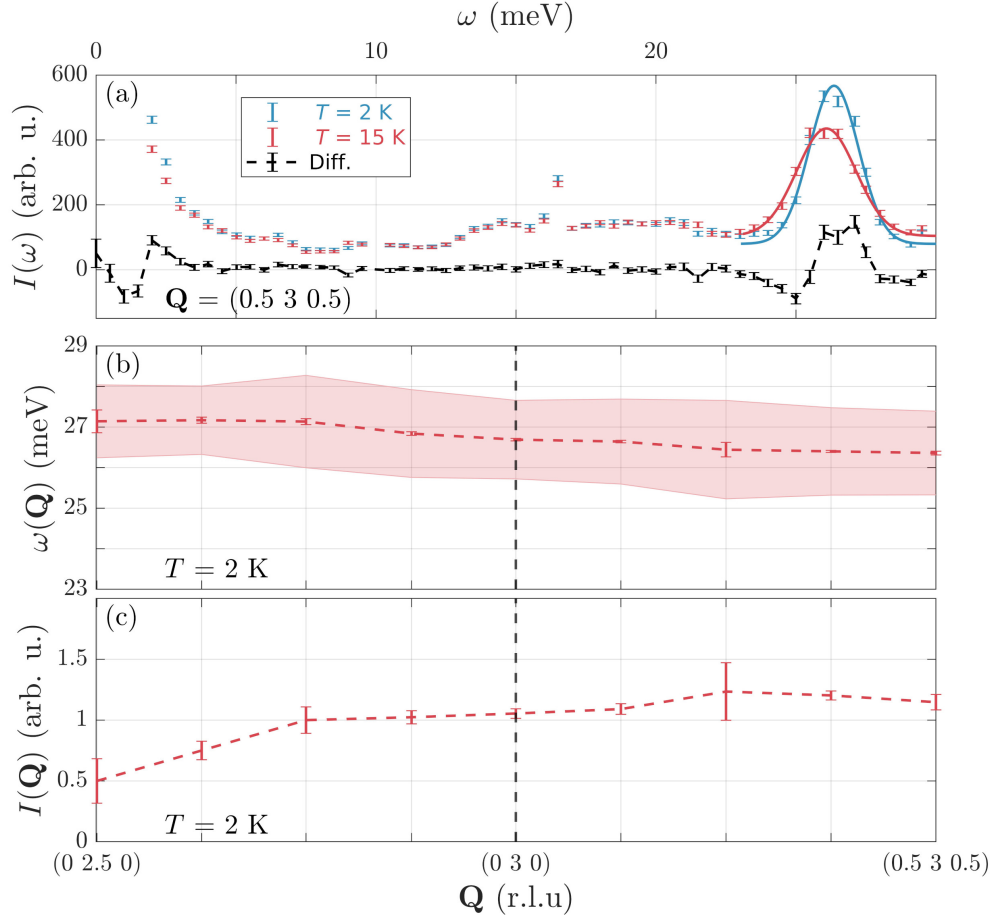


Figure 3.6 – **Low temperature high-energy dynamics of  $\text{SeCuO}_3$ .** (a) Representative  $\omega$  scan measured at low (blue) and intermediate (red) temperature. The difference is drawn in black. (b) Dispersion  $\omega(Q)$  of the mode at low temperature along two high-symmetry directions. The shaded red area represents the extracted width (FWHM) of the mode at each point in reciprocal space. (c) Corresponding integrated intensity  $I(Q)$ .

Each scan at  $T = 2$  K exhibits a sharp peak fitted with a Gaussian distribution. At 15 K, the peak shows a minimal downward shift and a slight broadening. The centres and integrated intensities for each  $Q$ -point are extracted and show a weakly dispersive behaviour around 26.5 meV [Fig. 3.6(b)]. This very weak  $Q$  dependence indicates that

the nature of this mode corresponds to a singlet to triplet transition, associated with a triplon quasiparticle, in the  $\text{Cu}_1$  dimers represented in orange in Fig. 3.3, with an energy gap of  $J_D$ . The weak dispersion is also a sign of a weak coupling between the dimers and the rest of the magnetic lattice, hypothetically formed by  $\text{Cu}_2$  ions. This dispersion has a smooth variation in intensity [Fig. 3.6(c)], whose line shape is different from the standard dimer structure factor [92] (not shown here), even though the portion of the reciprocal space I measured is too limited to reach a definitive conclusion. The difference can also be explained by the weak coupling to the other sub-lattice.

In the second set of measurements, I probe the temperature dependence of the excitation by performing similar  $\omega$ -scans at different temperatures, at  $\mathbf{Q} = (0\ 3\ 0)$ .

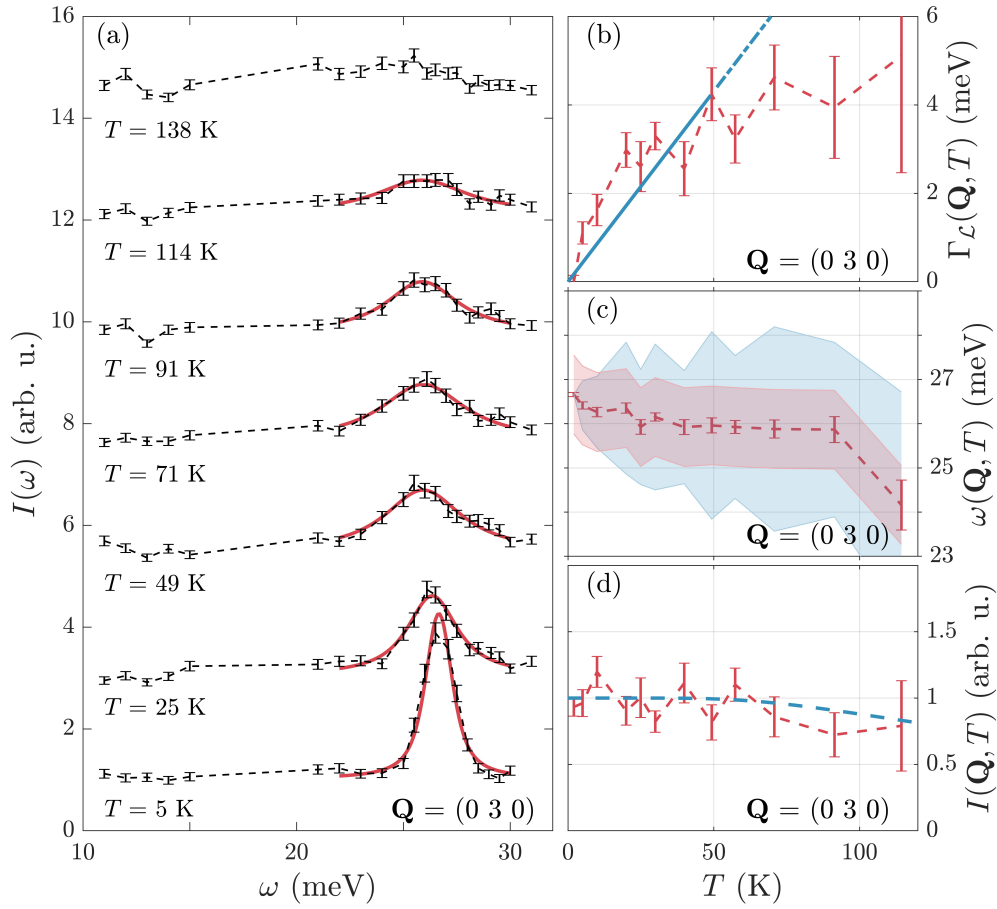


Figure 3.7 – **Temperature evolution of  $\text{SeCuO}_3$**  measured at  $\mathbf{Q} = (0\ 3\ 0)$ . (a) Representative  $\omega$ -scans (black) and Voigt profiles at different temperatures. (b)–(d) Thermal evolution. (b) Extracted Lorentzian width (red) compared to  $k_B T$  (blue). (c)  $\omega(T)$ ; shading accounts for the instrumental resolution of 0.75(8) meV (red) and for the Lorentzian profile (blue). (d) Normalised integrated intensity  $I(T)$  (red) and thermal singlet population (blue).



Each measurement up to 114 K shows a clear peak with a Voigt line shape [Fig. 3.7(a)], confirming the persistence of the mode far above  $T_N$ . The Gaussian component is ruled by the instrumental resolution, and the Lorentzian part accounts for thermal effects. The Lorentzian width reported in Fig. 3.7(b) increases linearly with temperature until a value of  $\sim 4$  meV which, as we will see in the next section, reflects the coupling to the excitations of the  $\text{Cu}_2$  subsystem. More importantly, the mode amplitude is comparable to the statistical thermal population of a singlet state given by  $1/Z = [1 + 3 \exp(-J_D/k_B T)]^{-1}$ , where  $Z$  is the partition function of the dimer system [Fig. 3.7(d)].

To summarise the results presented in this section, I have observed a set of features that confirm the triplon nature of the high-energy excitations in  $\text{SeCuO}_3$ .  $\text{Cu}_1$  dimer units form strong clusters that are weakly coupled to the  $\text{Cu}_2$  subsystem. Their magnetic behaviour is well described by the two sites Hamiltonian

$$\hat{\mathcal{H}}_D = J_D \sum_{\langle i_1, j_1 \rangle} \hat{\mathbf{S}}_{i_1} \cdot \hat{\mathbf{S}}_{j_1}, \quad (3.3)$$

where  $\langle i_1, j_1 \rangle$  denotes a sum over nearest-neighbour  $\text{Cu}_1$  atoms only, and  $J_D$  is the energy gap between the singlet and triplet states,  $J_D = 26.5$  meV.

### 3.3 Three dimensional long-range order

We now turn to the low-energy dynamics of  $\text{SeCuO}_3$ , where magnetic excitations emerge from long range order below  $T_N$ . A total of 74 line scans have been performed at 2 K on the cold spectrometers ThALES and 4F1, and representative  $\omega$  scans are shown in Fig. 3.8 for different positions in reciprocal space.

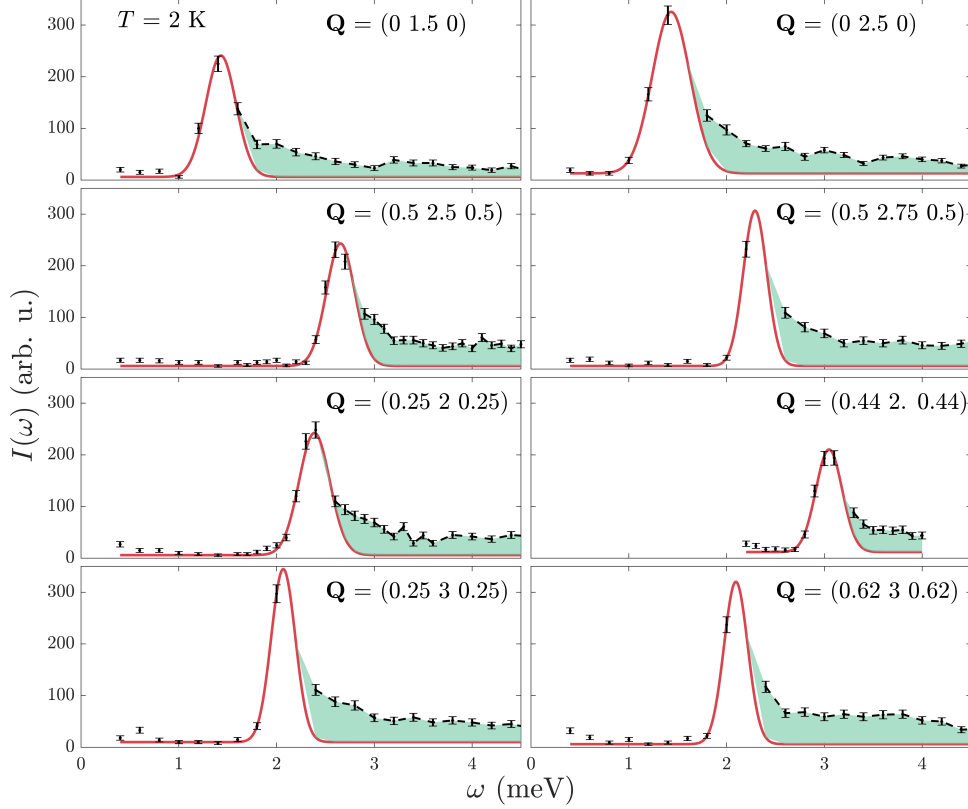


Figure 3.8 – **Magnonic excitations** at eight different  $Q$ -points measured on ThALES at 2 K. The measured intensity  $I(\omega)$  (black) shows a clear peak that is fitted by a Gaussian (red) in the low-energy edge. A scattering continuum (light green) is present at higher energies in all directions.

It is clear that a strong low-energy mode is present at all  $Q$ . Surprisingly, some scattering intensity persists above the magnon peak and at least up to 4.5 meV, along all measured directions. This continuum cannot be explained by the instrumental resolution and must have a different origin. For a better visualisation of this feature, I gather the measured  $\omega$ -scans in a colour plot representation in Fig. 3.9. A deeper analysis of this three dimensional continuum will be addressed in Sec. 3.4.

Similarly, I extracted the spin wave intensity  $I_p(Q)$  by performing Gaussian fits at the magnon peaks. The remaining intensity at higher energies is the contribution from the continuum  $I_c(Q)$ . The results are summarised in Fig. 3.9. The lower panel shows a well-

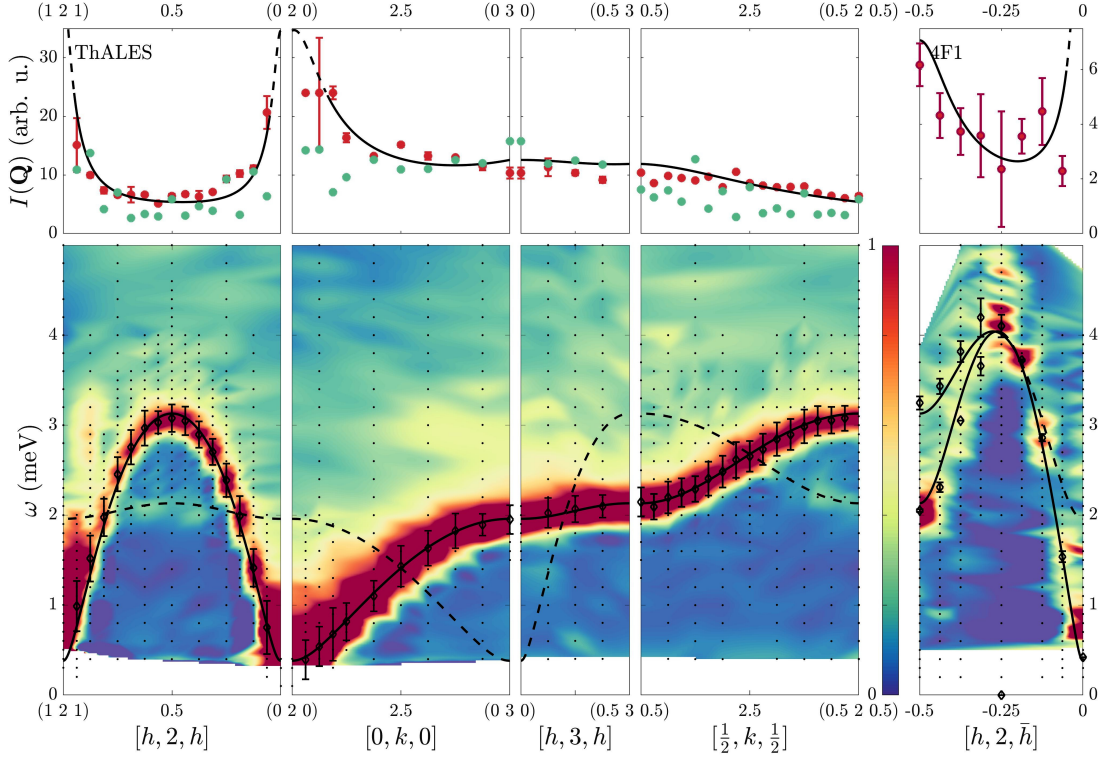


Figure 3.9 – **Low-energy dynamics.** Coloured panels show the scattering intensity  $I(\mathbf{Q}, \omega)$  along five different directions. Black lines show the simulated spin waves extracted from a fit to the magnon peaks in Fig. 3.8, the dashed line has vanishing intensity. Upper panels show the magnon ( $I_p(\mathbf{Q})$ , red) and continuum ( $I_c(\mathbf{Q})$ , light green) integrated intensities, also taken from Fig. 3.8. Black lines correspond to modelled spin waves intensities. The contribution of two modes is considered in the panel at right.

defined band, which disperses in all five measured directions. I also note footprints of a second mode, with much weaker intensity. These features are also well-defined along  $[h, 2, h]$ , despite the lower statistics of the measurements. The system has a small measured gap of  $\Delta = 0.42(3)$  meV, probably emerging from a weak magnetic anisotropy [110]. The two contributions to the scattering intensity are reported in the upper panel. As expected, the value of  $I_p(\mathbf{Q})$  increases around the gap due to magnetic order.

I expect the low-energy physics of the system to be described by a minimal Hamiltonian containing Heisenberg interactions in all three dimensions, which takes the form

$$\hat{\mathcal{H}}_m = \sum_{[i_2, j_2]_m} J_m \hat{\mathbf{S}}_{i_2} \cdot \hat{\mathbf{S}}_{j_2}. \quad (3.4)$$

Here,  $i_2$  and  $j_2$  correspond to  $\text{Cu}_2$  sites, and  $[\dots]_m$  denotes a sum over bonds in the

set  $\{J_m\}$ , defined in Fig. 3.10. The set of interactions I propose then includes near-neighbour couplings  $J_l$  ( $l = \parallel, \perp, b$ ), as well as long-distance effective ones  $\mathcal{J}_\gamma$  with  $\gamma = \alpha, \beta$ , which will be discussed in detail in Sec. 3.3.1. Together, they form the set  $\{J_m\}$ . In the same spirit of previous studies [105] and according to the outcome of the analysis of the higher-energy excitation, I consider atoms that belong to the  $\text{Cu}_2$  subsystem only, resulting in an effective magnetic decoupling between the two lattices. I fit  $\omega(\mathbf{q})$  extracted from the magnon peaks using linear spin wave (LSW) theory as implemented in the `Matlab` package `SpinW`, mentioned in Sec. 2.3. As black lines from Fig. 3.9 show, the extracted set of parameters reported in Table 3.1 delivers a very accurate description of the low-lying energy excitations of the system. The modelled spectrum contains two magnon branches, one of which has more than 90% of the measured intensity in the magnon peak. The second one matches remarkably with the aforementioned hints of neutron scattering intensity in dispersion. Moreover, this set of parameters also delivers an accurate account of  $I_p(\mathbf{Q})$  in the first branch with no further fitting, even though it slightly overestimates the contribution of the weak mode to the total scattering intensity. Indeed, its intensity is of the order of  $\mathcal{O}(0.1\%)$ , whereas the measured values lie between 1–5% of the first branch, rising to 10% at few  $\mathbf{Q}$  points. The low intensity in the second branch could be explained by the presence of two identical quasi-independent  $\text{Cu}_2$  subsystems. The discrepancy in the intensity would then emerge from weak magnetic interactions connecting both sublattices that have not been considered, or cannot be captured by LSW theory. Finally, the magnon gap can be reproduced by including a small exchange anisotropy of less than 1% on the  $J_\parallel$  bond,  $\delta J_\parallel = 0.018$  meV. As this weak Ising behaviour has only limited influence on the magnon dynamics away from the zone centre, I will then treat it as a marginal feature in the system.

Table 3.1 – **Strengths of the magnetic interactions**, in meV, in the  $\text{Cu}_2$  subsystem. These values were obtained by fitting the magnon peak positions from Fig. 3.8. The geometry of the interactions is shown in Fig. 3.10.

$J_\parallel$	$J_\perp$	$J_b$	$\mathcal{J}_\alpha$	$\mathcal{J}_\beta$
3.39(13)	0.39(3)	−0.19(2)	0.34(2)	0.35(2)

### 3.3. Three dimensional long-range order

The interactions presented in Table 3.1 form an effective  $\text{Cu}_2$  magnetic lattice made of parallel chains along the  $[10\bar{1}]$  direction, defined by  $J_{||}$ . Its intrinsic energy scale is on the order of 10 times greater than all inter-chain couplings in all three dimensional directions. Figure 3.10 then emphasises the presence of the two orthogonal chains,  $J_{||}$  and  $J_{\perp}$ , forming corrugated planes which are connected by  $J_b$  on any second site and by  $\mathcal{J}_{\alpha}$  and  $\mathcal{J}_{\beta}$  on all  $\text{Cu}_1$  dimer unit positions. These interactions ensure the three dimensionality of the system and result in a weak inter-chains frustration. While it is clear from Fig. 3.10(c) that  $J_b$  is mediated by the edge-sharing  $\text{CuO}_6$  octahedra, the exchange paths responsible for the two chain-like interactions,  $J_{||}$  and  $J_{\perp}$  are less obvious.  $\text{Cu}_2$  spins are connected through the  $\text{SeO}_3$  tetrahedra, an exchange path that has not been considered in previous studies. Notably, their surprisingly large magnitude was not expected, and any deeper understanding would require further orbital chemistry analysis. Finally, it is crucial to mention that the superexchange paths defining both  $\mathcal{J}_{\alpha}$  and  $\mathcal{J}_{\beta}$  are directly mediated by the central  $\text{Cu}_1$  dimer units, as can be seen on Fig. 3.10(c). These interactions are naturally effective, and reveal an interesting phenomenon. The central  $\text{Cu}_1$  dimer is treated by the system as a non-magnetic singlet that provides additional exchange paths, without directly contributing to the magnetic lattice. It this allows the presence of longer interaction paths. I will provide a detailed description of this phenomenon in the next section.

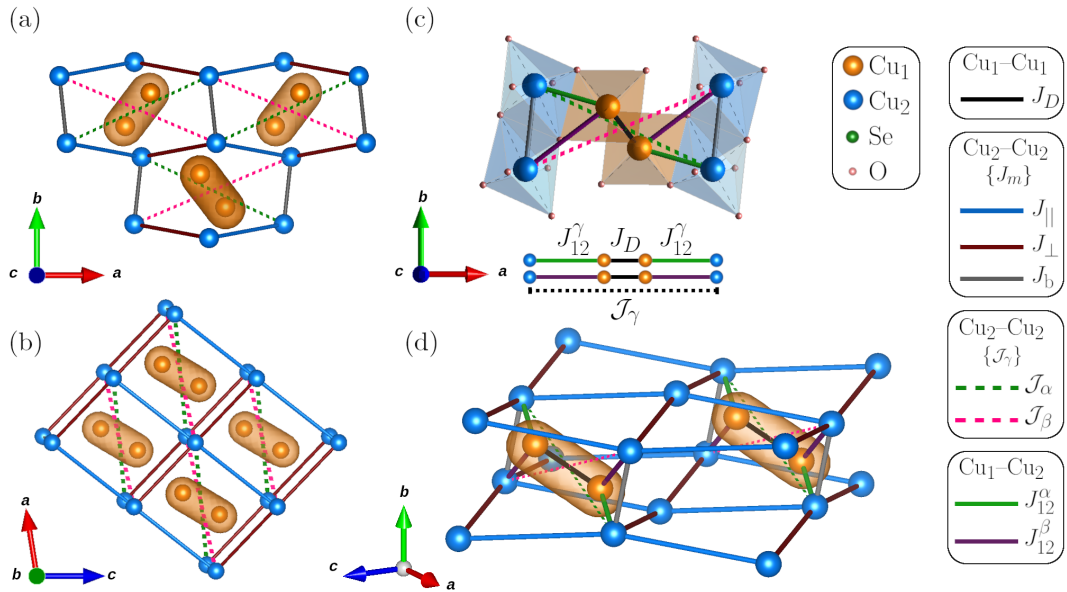


Figure 3.10 – **Magnetic interactions in  $\text{SeCuO}_3$**  defined in the Hamiltonian 3.4. (a) Projection on the  $ab$  and (b) on the  $ac$  planes, indicating the interactions of Table 3.1. (c) Focus around a dimer unit, the effective interactions  $\mathcal{J}_{\gamma}$  between  $\text{Cu}_2$  atoms are described in terms of dimer couplings given by  $J_D$  and  $\text{Cu}_1$ - $\text{Cu}_2$  interactions  $J_{12}^{\gamma}$  (green and purple) defined in Sec. 3.3.1. (d) Perspective view highlighting the  $\text{Cu}_2$  chains given by  $J_{||}$  and the interactions connecting them into coupled, buckled planes.

### 3.3.1 Interpretation of the effective couplings

The dispersive behaviour of the triplon mode and the particular exchange path of what I will hereafter denote as effective couplings  $\mathcal{J}_\gamma$  ( $\gamma = \alpha, \beta$ ) indicate a weak coupling between the two magnetic subsystems. These long paths involve the plaquette O atoms (and hence the  $d_{x^2-y^2}$   $\text{Cu}_2$  orbitals) for  $\mathcal{J}_\alpha$ , but an apical O atom for  $\mathcal{J}_\beta$ . In order to restore crossed-effects, it is necessary to build a self-consistent model where the effective couplings  $\mathcal{J}_\gamma$  are reproduced from  $J_D$  and two coupling parameters  $J_{12}^\gamma$  [Fig. 3.10(d) and Fig. 3.11]. For this, I replace the set  $\{\mathcal{J}_\gamma\}$  terms in Eq. 3.4 by the following coupling Hamiltonian

$$\hat{\mathcal{H}}_c = \sum_{\langle i_1, i_2 \rangle_\gamma} J_{12}^\gamma \hat{\mathbf{S}}_{i_1} \cdot \hat{\mathbf{S}}_{i_2}, \quad (3.5)$$

where  $i_1$  ( $i_2$ ) are  $\text{Cu}_1$  ( $\text{Cu}_2$ ) sites and  $\langle \dots \rangle_\gamma$  is a sum restricted to nearest-neighbouring spins that, together with  $J_D$  form the effective path  $\mathcal{J}_\gamma$ . The interactions  $J_{12}^\gamma$  are defined in Fig. 3.11.

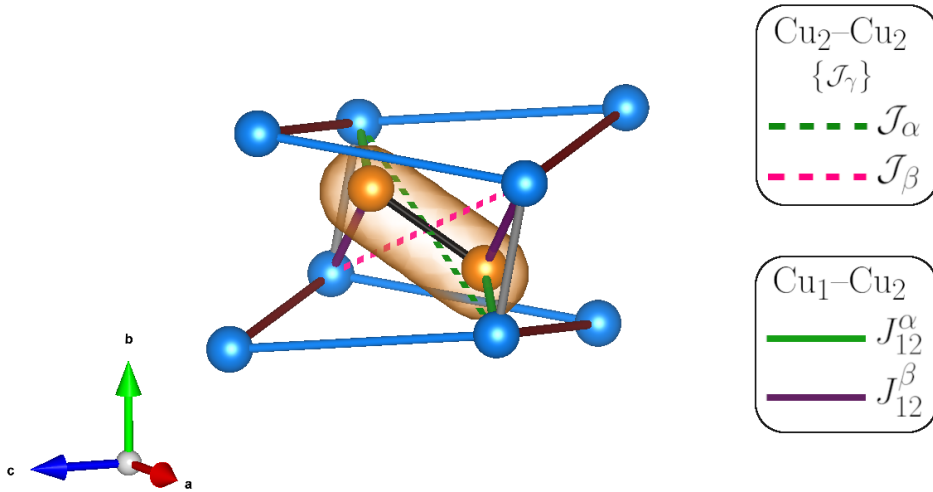


Figure 3.11 – **Focus on a six sites unit** defined by two  $\text{Cu}_2\text{--Cu}_1\text{--Cu}_1\text{--Cu}_2$  tetramers sharing the central  $\text{Cu}_1$  dimer. The two effective couplings  $\mathcal{J}_\gamma$  are described in term of dimer couplings  $J_D$  and inter sublattices interaction  $J_{12}^\gamma$ .

To get a good estimate of  $J_{12}^\gamma$ , I will consider the four Cu atoms that contribute to the effective interaction paths only. Accounting for real interactions only, this four-sites system is described by the following tetramer Heisenberg Hamiltonian

$$\hat{\mathcal{H}}_t = J_{12}^\gamma (\hat{\mathbf{S}}_{1_2} \cdot \hat{\mathbf{S}}_{2_1} + \hat{\mathbf{S}}_{3_1} \cdot \hat{\mathbf{S}}_{4_2}) + J_D \hat{\mathbf{S}}_{2_1} \cdot \hat{\mathbf{S}}_{3_1}, \quad (3.6)$$

where the sites and couplings are defined in Figs. 3.10(c) and 3.11. The ground-state and lowest-lying excited energies are obtained by diagonalising the Hamiltonian in the

16 × 16 Hilbert space,

$$\begin{aligned} E_0 &= \frac{1}{4} \left( -J_D - 2J_{12}^\gamma - 2\sqrt{J_D^2 - 2J_D J_{12}^\gamma + 4(J_{12}^\gamma)^2} \right), \\ E_1 &= \frac{1}{4} \left( -J_D - 2\sqrt{J_D^2 + (J_{12}^\gamma)^2} \right), \end{aligned} \quad (3.7)$$

with corresponding eigenstates

$$\begin{aligned} |\Phi_0\rangle &= |\uparrow\uparrow\downarrow\downarrow\rangle - A|\uparrow\downarrow\uparrow\downarrow\rangle + B|\uparrow\downarrow\downarrow\uparrow\rangle + B|\downarrow\uparrow\uparrow\downarrow\rangle - A|\downarrow\uparrow\downarrow\uparrow\rangle + |\downarrow\downarrow\uparrow\uparrow\rangle, \\ |\Phi_1^-\rangle &= -|\uparrow\downarrow\downarrow\uparrow\rangle + C|\downarrow\uparrow\downarrow\downarrow\rangle - C|\downarrow\downarrow\uparrow\downarrow\rangle + |\downarrow\downarrow\uparrow\uparrow\rangle, \\ |\Phi_1^0\rangle &= -|\uparrow\uparrow\downarrow\downarrow\rangle + D|\uparrow\downarrow\uparrow\downarrow\rangle - D|\downarrow\uparrow\downarrow\uparrow\rangle + |\downarrow\downarrow\uparrow\uparrow\rangle, \\ |\Phi_1^+\rangle &= -|\uparrow\uparrow\downarrow\uparrow\rangle + C|\uparrow\uparrow\downarrow\downarrow\rangle - C|\uparrow\downarrow\uparrow\uparrow\rangle + |\downarrow\uparrow\uparrow\uparrow\rangle, \end{aligned} \quad (3.8)$$

in which the coefficients are given by

$$\begin{aligned} A &= \frac{2J_{12}^\gamma + \sqrt{J_D^2 - 2J_D J_{12}^\gamma + 4(J_{12}^\gamma)^2}}{J_D}, \\ B &= \frac{2J_{12}^\gamma (2J_{12}^\gamma + \sqrt{J_D^2 - 2J_D J_{12}^\gamma + 4(J_{12}^\gamma)^2})}{J_D (J_D + \sqrt{J_D^2 - 2J_D J_{12}^\gamma + 4(J_{12}^\gamma)^2})}, \\ C &= \frac{J_D + \sqrt{J_D^2 + (J_{12}^\gamma)^2}}{J_{12}}, \\ D &= \frac{J_{12}^\gamma + \sqrt{J_D^2 + (J_{12}^\gamma)^2}}{J_D}. \end{aligned} \quad (3.9)$$

In the limit of a strong dimer coupling given by  $J_D \gg J_{12}^\gamma$ , the coefficients become  $A, D \rightarrow 1$ ,  $B \rightarrow 0$ , and  $C \gg 1$ . The eigenstates may then be re-expressed as

$$\begin{aligned} |\Phi_0\rangle &= |\uparrow\uparrow\downarrow\downarrow\rangle - |\uparrow\downarrow\uparrow\downarrow\rangle + |\downarrow\downarrow\uparrow\uparrow\rangle - |\downarrow\uparrow\downarrow\uparrow\rangle = |s_1\rangle \otimes |s_2\rangle, \\ |\Phi_1^-\rangle &= |\downarrow\downarrow\uparrow\uparrow\rangle - |\uparrow\downarrow\downarrow\uparrow\rangle + C(|\downarrow\uparrow\downarrow\downarrow\rangle - |\downarrow\downarrow\uparrow\downarrow\rangle) = C|s_1\rangle \otimes |t_2^-\rangle - |s_2\rangle \otimes |t_1^-\rangle, \\ |\Phi_1^0\rangle &= |\uparrow\downarrow\uparrow\downarrow\rangle - |\uparrow\uparrow\downarrow\downarrow\rangle + |\downarrow\downarrow\uparrow\uparrow\rangle - |\downarrow\uparrow\downarrow\uparrow\rangle = -|s_1\rangle \otimes |t_2^0\rangle, \\ |\Phi_1^+\rangle &= |\downarrow\uparrow\uparrow\uparrow\rangle - |\uparrow\uparrow\downarrow\uparrow\rangle + C(|\uparrow\uparrow\downarrow\downarrow\rangle - |\uparrow\downarrow\uparrow\uparrow\rangle) = C|s_1\rangle \otimes |t_2^+\rangle - |t_1^+\rangle \otimes |s_2\rangle, \end{aligned} \quad (3.10)$$

where I introduced the familiar singlet-triplet notation. The ground state is then the product of two singlets on each pair of Cu<sub>1</sub> and Cu<sub>2</sub> atoms, and the lowest excited states correspond to a singlet state on the dimer, and a triplet  $|t_2^k\rangle$ , with  $k = +, 0, -$  on the outer Cu<sub>2</sub> sites. From Eq. 3.7, I deduce the energy gap of the first excited states which corresponds to the effective coupling between the two Cu<sub>2</sub> atoms. For each path  $\gamma$ , we have

$$\mathcal{J}_\gamma = \frac{J_{12}^\gamma}{2} + \frac{1}{4} \frac{[3(J_{12}^\gamma)^2 - 2J_D J_{12}^\gamma]}{\sqrt{J_D^2 + (J_{12}^\gamma)^2}} \xrightarrow{J_D \gg J_{12}^\gamma} \frac{3}{4} \frac{(J_{12}^\gamma)^2}{J_D}. \quad (3.11)$$

Inserting the fitted values of the effective couplings from Table 3.1 in this expression gives the values of the microscopic interlattice coupling parameters

$$J_{12}^\alpha = 3.47 \text{ meV} \quad \text{and} \quad J_{12}^\beta = 3.52 \text{ meV}. \quad (3.12)$$

Both values are of the same order as the leading interaction of this system,  $J_{||}$ . Although they are large compared to the other couplings in the  $\text{Cu}_2$  subsystem, their effects on the spin dynamics is strongly suppressed by the dimer interaction  $J_D$  as extracted from Eq. 3.11. Furthermore, these values are consistent with the width of the triplon at high temperature reported in Fig. 3.6, indicating its coupling to incoherent excitations. The perturbative treatment of Eq. 3.11 is the opposite limit to the LSW approach, providing then upper bounds for the  $J_{12}^\gamma$  values; using them in a LSW description of the complete system of  $\text{Cu}_1$  and  $\text{Cu}_2$  atoms is then meaningless. Nevertheless, the two approaches indicate the range of normalisation effects due to quantum fluctuations. To gauge the quantum behaviour of both subsystems, I refer to the value of the magnetic moment on the  $\text{Cu}_1$  subsystem  $\mu_1 \approx 0.35 \mu_B$  [107], which is much weaker than the one on the other sublattice  $\mu_2 < 0.8 \mu_B$ , meaning a significantly stronger quantum behaviour. The interactions  $J_{12}^\gamma$  then only induce weak order on the  $\text{Cu}_1$  subsystem which provides additional evidence that LSW theory cannot be used in a coupled analysis. Finally, I comment that the microscopic interactions  $J_{12}^\gamma$  could explain the intensity transfer to the weak magnon branch in Fig. 3.9. Furthermore, it could carry a symmetrically allowed Dzyaloshinskii–Moriya interaction which explains the relative canting of the  $\mu_1$  and  $\mu_2$  moment direction observed in neutron diffraction experiments [103] and can contribute to the observed magnon gap  $\Delta$ , as already proposed in a previous study [110].



### 3.4 A spinon-like continuum

I now return to the strongest, and most exotic, feature of Figs. 3.8 and 3.9 yet to be explained – the continuum of scattering intensity above the one-magnon peak, along several measured directions. This continuum could possibly emerge from two different origins : multi-magnon processes or spinon quasiparticles.

In a scattering process, neutrons are generally scattered by single magnons, resulting in excitations *transverse* to the ordered moment direction,  $\delta S^{xx} + \delta S^{yy}$ . However, there are situations where the spin waves interfere, and a neutron would then be scattered by a pair of magnons, or two independent spin waves. They are called two-magnons scattering processes [111], and are allowed no matter the dimensionality of the system [111, 112, 113]. Physically, they correspond to situations where two magnons are created with opposite spins  $S^z = \pm 1$  due the selection rule, which results in a total  $\Delta S^z = 0$  process. Each process being associated to a transverse excitation, the resulting scattering events correspond to *longitudinal* excitations  $\delta S^{zz}$  [114]. Each magnon would conserve its independent behaviour, so that its momentum and energy does not change throughout the process. The new quasi-particles are then defined by

$$\mathbf{Q} = \mathbf{Q}_1 + \mathbf{Q}_2, \quad \text{and} \quad \omega(\mathbf{Q}) = \omega(\mathbf{Q}_1) + \omega(\mathbf{Q}_2). \quad (3.13)$$

This results in the formation of a scattering continuum above the one magnon line. Since the origin of those processes is understood, one can compute the expected intensities both in the longitudinal and transverse directions from the sum rules [115]. Similarly to the work on the  $S = 5/2$  antiferromagnet  $\text{Rb}_2\text{MnF}_4$  [113], I compare the integrated intensity associated with one- ( $I_p$ ) and potentially two-magnons ( $I_c$ ) scattering events whose ratio  $\kappa = I_c/I_p$  cannot exceed a certain limit  $\kappa_M$ . In Table 3.2, I average these quantities along all meaningful directions in reciprocal space, obtaining a lower bound to the ratio  $\kappa_{\min}$  because our measurements were experimentally limited in energy [Fig. 3.8] and may not capture the upper edge of the continuum.

Table 3.2 – Integrated peak intensity,  $I_p$ , and continuum intensity,  $I_c$ , averaged along four high-symmetry directions. The lower row presents the LSW theoretical result for the spin reduction,  $\Delta S_2 = 0.13$ , on the  $\text{Cu}_2$  sublattice [107].

Direction	$I_p$	$I_c$	$\kappa_{\min}$
$[0, k, 0]$	133(5)	99	0.85(4)
$[\frac{1}{2}, k, \frac{1}{2}]$	85(4)	56	0.65(4)
$[h, 2, h]$	90(4)	61	0.69(4)
$[h, 3, h]$	98(4)	125	1.28(4)
Theory	$(S - \Delta S)(2\Delta S + 1)$	$\Delta S(\Delta S + 1)$	$\kappa_M$
$\Delta S_2 = 0.13$	0.47	0.15	0.32

Here,  $I_c$  is of the same order of  $I_p$ . Their ratio then far exceeds typical values found in previous multimagnon scattering studies [111, 113]. I also computed the prediction from LSW theory, based on the measured reduced magnetic moment on the  $\text{Cu}_2$  sublattice [107]. As Table. 3.2 shows, these values are incompatible with multi-magnon processes. Furthermore, from Eq. 3.13, the existence of a magnon gap implies the existence of another gap between the magnon branch and the continuum, as observed in Ref. [113]. However, Figs. 3.8 and 3.9 exclude the existence of such a gap – as small as it could be – which is perhaps the most conclusive evidence that the observed continuum in  $\text{SeCuO}_3$  cannot be explained by multi-magnon scattering events.

The second plausible explanation of the scattering intensity continuum is that it originates from spin-1/2 fractionalised excitations, or spinons, which have been introduced in Sec. 3.1.1. Spinons were originally thought to exist in one dimensional systems only, since are solutions of Bethe Ansatz. However, their presence has been observed in the two dimensional material  $\text{Cs}_2\text{CuCl}_4$  [116, 117], an interpretation mostly due to the functional form of the measured excitation spectrum. Spinons were thought to be bound by an attractive potential and to be *deconfined* at energies above the threshold given by the one-magnon band. More recently, a weak continuum of intensity has been observed in the square lattice  $J_1$ – $J_2$  antiferromagnet  $\text{Cu}(\text{DCOO})_2 \cdot 4\text{D}_2\text{O}$  at the zone boundary  $\mathbf{Q} = (0, \pi)$ , explained by the coexistence of spinons and magnons [79, 118, 119]. I also comment on another, and more conventional, interpretation of the presence of spinons in non one-dimensional systems. The existence of spinons in both  $\text{Cs}_2\text{CuCl}_4$  [120] and, much more recently,  $\text{Cu}_2(\text{OH})_3\text{Br}$  [89] has been explained by the quasi-1D behaviour of those chain-like systems. I comment that this picture is only realistic in the presence of frustration which would add strong quantum fluctuations to the system, while it is known that coupled spin chains form a square lattice that develops long range order in the presence of interchain couplings [121]. Recent studies on frustrated two-dimensional lattices [122, 123, 124, 125, 126] predicted the presence of partially confined spinons with a lower spectral weight than on a 1D chain where it accounts for 71 % of the total scattered intensity [70, 98, 99].

The quantum system  $\text{SeCuO}_3$  is, to my knowledge, the first purely three-dimensional compound in which fractionalised spinonic excitations are present. As shown in the previous sections, significant couplings exist in all three dimensions even though some of them ( $J_{12}^\gamma$ ) are renormalised downwards by the presence of the singlet states. Furthermore, as Fig. 3.9 shows, the continuum follows the established one-magnon line that is well-described by LSW theory and, importantly, is present throughout the 3D Brillouin zone, unlike the familiar 1D case [70, 99]. Similarly to previous references, I motivate its existence by the deconfinement of  $S = 1$  magnons into  $S = \frac{1}{2}$  fractional excitations above their binding energy given by the one-magnon band.

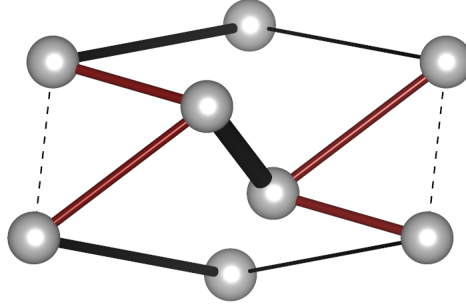


Figure 3.12 – **Frustration in  $\text{SeCuO}_3$** , present on two five-sites loops  $\text{Cu}_2\text{--Cu}_2\text{--Cu}_2\text{--Cu}_1\text{--Cu}_1$ , defined in Fig. 3.10(a) and 3.10(c). Dashed lines indicate ferromagnetic couplings, while plain lines represent antiferromagnetic ones. The size of the bonds is related to their strength, and coloured ones indicate the interactions frustrating the system.

Indeed, in the case of a non frustrated three-dimensional antiferromagnet, the magnetic interactions stabilise a robust semi-classical long range ordered state, with weak quantum fluctuations. However, the presence of frustration on the  $J_{12}^\gamma$  bonds induced both by the upper and lower five-site loops [Fig. 3.12], as well as the possible Dzyaloshinskii–Moriya interaction, provides the system with enough quantum fluctuations to allow the presence of fractionalised excitations. At lower energies, their most energetically favourable configuration is achieved by turning bound spinons pairs into magnons, and being delocalised. This binding potential corresponds to the one-magnon band. At higher energy, these fractionalised excitations are deconfined and free to form new pairs resulting in the high-energy intensity continuum that I observed in the INS spectrum. Since this paradigm is yet to be explored, my hope is that the values of Tab. 3.2 as well as the position and functional form of the continua will provide essential input for advanced experimental and theoretical studies of spinons in high dimensional systems.

### 3.5 Summary

In this project, I analysed INS measurements of  $\text{SeCuO}_3$  which led to a complete description of its magnetic dynamic spectrum. I first described it at the level of two independent subsystems. In the first,  $\text{Cu}_1$  dimer units are in a non-magnetic singlet ground state, and their first excited state is characterised by a triplon band whose energy scale is given by  $J_D$ . The second subsystem forms an *effective* 3D frustrated network of interacting  $\text{Cu}_2$  chains, whose excitations are well-described at the level of the LSW theory by the set of parameters reported in Tab. 3.1. In this picture, the effective Hamiltonian of the system would be

$$\hat{\mathcal{H}}_{\text{eff}} = \hat{\mathcal{H}}_D + \hat{\mathcal{H}}_m, \quad (3.14)$$

where the terms are defined in Eqs. 3.3 and 3.4. Nevertheless, two features prove that the two subsystems are not decoupled. First, the triplon band is weakly but sensitively dispersive, which would not have been the case in the reverse scenario. Since dimer units lie too far from each other to interact, I concluded that the only possible coupling that would explain the dispersion connects to the  $\text{Cu}_2$  sublattice. Second, in the frame of the LSW description of the system, I introduced the couplings  $\mathcal{J}_\gamma$  whose exchange paths pass through  $\text{Cu}_1$  dimer units. Of course, such a situation is physically impossible, and in a self-consistent model they should be described by a combination of  $J_D$  and two  $\text{Cu}_1$ – $\text{Cu}_2$  couplings  $J_{12}^\gamma$ . Using a perturbative approach on  $\text{Cu}_2$ – $\text{Cu}_1$ – $\text{Cu}_1$ – $\text{Cu}_2$  tetramers, I proposed upper bounds for the value of those inter-subsystems interactions. The self-consistent Hamiltonian of the system then reads

$$\hat{\mathcal{H}} = J_D \sum_{\langle i_1, j_1 \rangle} \hat{\mathbf{S}}_{i_1} \cdot \hat{\mathbf{S}}_{j_1} + \sum_{[i_2, j_2]_{m'}} J_{m'} \hat{\mathbf{S}}_{i_2} \cdot \hat{\mathbf{S}}_{j_2} + \sum_{\langle i_1, i_2 \rangle_\gamma} J_{12}^\gamma \hat{\mathbf{S}}_{i_1} \cdot \hat{\mathbf{S}}_{i_2}, \quad (3.15)$$

where  $\langle \dots \rangle$  denotes a sum restricted to nearest-neighbours bonds;  $i_1, i_2$  and  $i_2, j_2$  denote  $\text{Cu}_1$  and  $\text{Cu}_2$  sites;  $\langle \dots \rangle_\gamma$  a sum on bonds corresponding to inter-sublattices interactions  $J_{12}^\gamma$ ; and  $[i_2, j_2]_{m'}$  corresponds to a sum over the bonds in the set  $\{J_m\}$  where we removed all the couplings already covered in the third term of the Hamiltonian.

Finally, I observed a continuum of scattering intensity above the one-magnon line along all directions. A multi-magnon origin having been ruled out, these energy continua are strong evidence for the presence of fractionalised excitations which are closely associated with spin waves. I explained the presence of spinons by the deconfinement of magnons at energies higher than the one-magnon band.  $\text{SeCuO}_3$  provides the first quantified observation of spinons in a purely 3D magnetic network. Due to the coexistence of these three excitations,  $\text{SeCuO}_3$  is an excellent candidate for the understanding of systems at a higher level than an independent subsystems interpretation, and is likely to mandate further theoretical treatments of similar systems where the magnetic excitations show such a high degree of entanglement.

# 4 Spherical Neutron Polarimetry as a tool for magnetic structure determination

## Contents

<b>4.1 Introduction . . . . .</b>	<b>55</b>
4.1.1 Crystal structure and magnetic properties . . . . .	56
4.1.2 Theoretical elements of symmetry analysis . . . . .	58
4.1.3 Previous neutron powder diffraction experiments . . . . .	61
<b>4.2 The simple case of magnetic scattering processes only . . . . .</b>	<b>66</b>
4.2.1 Combined ND and SNP analysis of $\text{Ba}(\text{TiO})\text{Cu}_4(\text{PO}_4)_4$ . . . . .	68
4.2.2 Spherical Neutron Polarimetry on $\text{Sr}(\text{TiO})\text{Cu}_4(\text{PO}_4)_4$ . . . . .	74
4.2.3 The importance of the Dzyaloshinskii-Moriya interaction . . . . .	77
<b>4.3 Combining nuclear and magnetic scattering processes . . . . .</b>	<b>79</b>
4.3.1 The unsolved case of $\text{Pb}(\text{TiO})\text{Cu}_4(\text{PO}_4)_4$ . . . . .	80
<b>4.4 Summary . . . . .</b>	<b>85</b>

A large part of this thesis is devoted to the analysis of the quantum chiral magnet family  $A(\text{BO})\text{Cu}_4(\text{PO}_4)_4$ , where  $(A; B) = (\text{Ba}, \text{Pb}, \text{Sr}; \text{Ti})$  and  $(\text{K}; \text{Nb})$ . In a systematic study of a magnetic compound, the first step is to understand its static properties. While specific heat and magnetic susceptibility measurements provide great insight on the behaviour of the system, the most precise way to determine the magnetic structure of a quantum magnet is through neutron diffraction (ND) measurements. As explained in Chapter. 2, magnetic scattering of neutrons emerges when the system possesses a periodic configuration of magnetic moments, and thus an appropriate experiment can lead to the quantification of its magnetic order. It can be achieved in two ways. First, assuming a non-polarised neutron beam, a direct comparison of the measured diffraction pattern with simulations based on the magnetic structure factor of a spin configuration is usually sufficient to derive its magnetic structure. This technique is extensively used and many softwares have been developed in order to facilitate the analysis. The most practised are the FullProf [127] suite, or Jana [128]. However, there are situations in which a diffraction pattern can be equally well described by several

## Chapter 4. SNP as a tool for magnetic structure determination

---

inequivalent magnetic structures. Probably the best way to cope with such a situation is to use polarised neutrons and measure the incoming and outgoing neutron flux in three orthogonal channels corresponding to the polarisation axis. For each Bragg peak, one can then build the so-called polarisation matrix, which is much more sensitive to the orientation of the moments, and compare it with numerical calculations based on the scattering cross section. This allows for a much accurate determination of the magnetic structure of the system.

In this chapter, I present the outcome of Spherical Neutron Polarimetry (SNP) measurements on three members of the  $A(BO)Cu_4(PO_4)_4$  family : (Ba; Ti), (Sr; Ti) and (Pb; Ti). Prior neutron diffraction experiments have been performed on all three compounds, which resulted in two candidates for their magnetic structure. I will demonstrate that SNP is extremely powerful if the propagation vector has non-integer Miller indices, but has some serious limitations if it corresponds to a reciprocal lattice vector because of nuclear magnetic interference. Furthermore, my conclusions are consistent with the presence of a strong Dzyaloshinskii-Moriya interaction which is directly responsible for the unusual highly non-collinear magnetic structure that I extracted. I comment that preliminary neutron diffraction results have been analysed by Peter Babkevich before I started my thesis. The SNP results on (Ba; Ti) have been presented in a paper published in Physical Review B [129].

## 4.1 Introduction

The chiral quantum magnets family  $A(BO)Cu_4(PO_4)_4$  forms a really interesting playground to study quantum effects. Indeed, it has been proven that cation ( $A^{2+}$ ) substitution changes the static magnetic properties of the system [130]. This behaviour is naturally also expected in its dynamic properties, which makes this family ideal to build a deeper understanding of quantum paradigms. I will expand this point in Chapter 5. However, the series of compounds forming the ( $A$ ;  $B$ ) family have initially been extensively studied for the presence of a linear magnetoelectric effect, which describes the coupling between magnetism and ferroelectricity. The material's magnetisation can then be tuned using an external electric field, and reciprocally the polarisation of the compound can be controlled using a magnetic field. Such an effect emerges when both the time reversal and the spatial inversion symmetry are broken. The associated interaction energy can be written as a multipole expansion containing monopole, toroid, and quadrupole moments, which all change sign under time reversal or space inversion.

There are two motivations behind this study. First, the magnetoelectric effect is directly related to the moments configuration in a spin cluster. In the case of ( $A$ ;  $B$ ), it is believed that it originates from magnetic quadrupole moments [131], which would make it the first experimental realisation of such systems. Secondly, before any dynamic study of a quantum system, it is necessary to begin by building a solid understanding of the static properties. Indeed, magnetic excitations naturally emerge from the ground state. As the analytical expression of the inelastic neutron scattering cross section clearly states, an accurate description of the dynamic structure factor of a system, which will be the core of Chapter 5, cannot be made without prior knowledge of the ordered ground state.

As mentioned in the previous paragraph, diffraction patterns could be equally well-described by two spin configurations. However, the analysis was limited by (i) the small magnetic moment on Cu ions which resulted in weak magnetic Bragg reflections and (ii) the assumption of an isotropic magnetic form factor which is not always the case due to the nature of electronic orbitals. Even though SNP is a challenging technique, it does not directly suffer these limitations when the system shows magnetic scattering events only. Indeed, the weak signal can be counterbalanced by long counting times. This technique is then an ideal tool to solve this problem.

### 4.1.1 Crystal structure and magnetic properties

The crystal structure of the cupola family  $A(BO)Cu_4(PO_4)_4$  is rather complicated, and shown in detail in Fig. 4.1. There are eight equivalent Cu magnetic atoms in the unit cell ( $S = \frac{1}{2}$ ). Groups of four corner-sharing  $CuO_4$  square planes form  $Cu_4O_{12}$  cupolas shown in blue in Fig. 4.1(b). These clusters are connected by  $PO_4$  tetrahedra into square-lattice like layers in the  $(ab)$  plane where their  $c$ -orientation alternates, resulting in an assembly of up- and down-pointing cupolas. Together with  $BO_5$  pyramids, the  $PO_4$  structures form a non-magnetic layer separating two cupolas planes as shown in Fig. 4.1(a), and ensuring a strongly two-dimensional magnetic behaviour. This compound crystallises in a tetragonal chiral structure that is well-described by the tetragonal  $P42_12$  spacegroup with  $a = 9.60 \text{ \AA}$  and  $c = 7.12 \text{ \AA}$  lattice parameters.

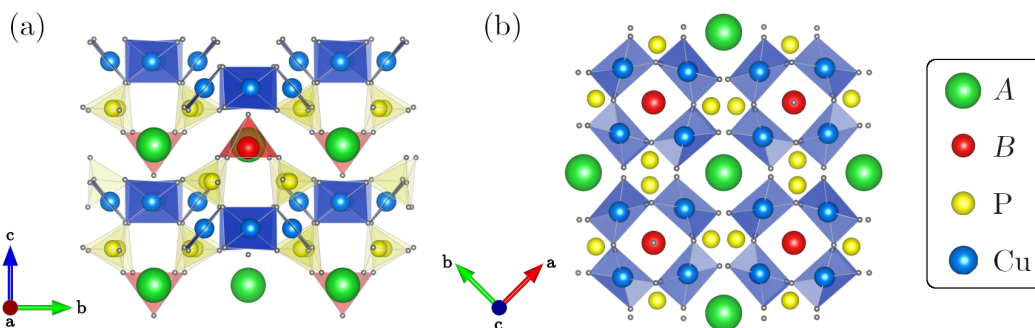


Figure 4.1 – **Schematic representation of the nuclear structure of the cupola family members**, showing Cu (blue), A (green), B (red), P (yellow) and O (grey) atoms, together with the associated coordination polyhedra. (a) Side view, projection on the  $(bc)$  plane showing buckled layers of  $CuO_4$  cupolas with alternating orientation along the  $c$ -axis, and separated by non magnetic layers. (b) Top view, projection on the  $(ab)$  plane, highlighting the square cupola structures as made of four connected  $CuO_4$  planes.

Interestingly, it was shown using polarised-light microscopy and x-ray diffraction [130] that not only the direction of the cupolas changes every second unit in the  $(ab)$  plane, but also that they have an alternating rotation about the  $c$ -axis quantified by the angle  $\varphi$ , shown in Fig. 4.2(a). Furthermore, substitution of the  $A^{2+}$  cation controls the strength of this structural chirality. While the plaquettes in (Sr, Pb, Ba; Ti) are tilted by a finite angle, (K; Nb) reaches a highly symmetrical configuration and is then achiral [Fig. 4.2(b)]. The latter compound has not been studied in the frame of this chapter, and focus is on the chiral ones. Finally, polarised light microscopy also highlighted the coexistence of multiple domains in a single crystal, related by spatial inversion symmetry and sample dependent. Thus, they also differ by the sign of the chiral angle  $\varphi$ . I will denote these domains as *dextro* for a positive rotation, and *levo* for a negative one. A previous study concluded that (Ba; Ti) was less likely to be mono-domained than (Sr; Ti) which has been proven to be mainly *dextro*, due to its smaller chirality strength. The reader is invited to consult this reference [130] for further considerations



on the crystal structure.

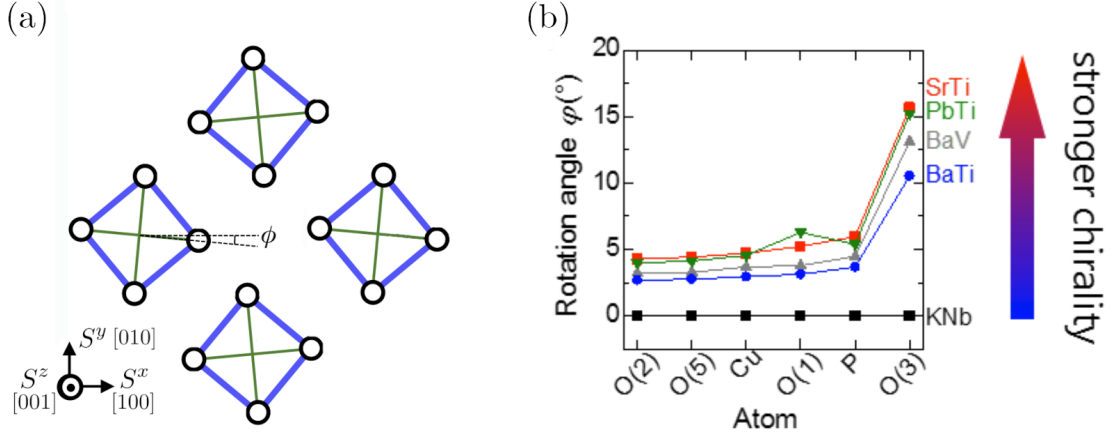


Figure 4.2 – **Quantification of the chirality strength.** (a) Focus on a set of four cupola units (blue bonds), with  $\phi$  being defined as the angle between the  $a$ -axis and the associated diagonal (green). (b) Representation of the chirality strength, where O(3) denotes the oxygen atom binding the  $\text{CuO}_4$  planes together to form cupola units.

It has been proven through magnetic susceptibility measurements that structural chirality has an effect on the magnetic properties of the system, as shown in Fig. 4.3. The Curie-Weiss temperature  $\Theta_{\text{CW}}$  has been extracted from a linear fit to the inverse susceptibility in the paramagnetic phase, and is negative for all three compounds. The values are reported in Table 4.1. This is a sign of a leading antiferromagnetic coupling since in a first order approximation the Curie-Weiss temperature is given by the sum of all couplings of a given site  $i$  to its neighbours  $j$ ,  $\Theta_{\text{CW}} \sim \sum_j J_{ij}$ . A peak appears in the susceptibility data around  $\sim 10$  K. Its large width is a direct evidence of low-dimensional interactions, a hypothesis also supported by the layered structure of these materials. The ordering temperature  $T_N$  corresponds to the change of regime and is highlighted by a kink in specific heat measurements (not shown here) [130]. Finally, the finite value of the low-temperature susceptibility for all directions of applied field is a strong hint of a non-collinear structure.

Table 4.1 – Weiss temperature  $\Theta_{\text{CW}}$  and Néel temperature  $T_N$  of the (A; B) compounds studied in this chapter, as extracted from magnetic susceptibility measurements.

	(Sr; Ti)	(Pb; Ti)	(Ba; Ti)
$\Theta_{\text{CW}} (K)$	-21	-21.3	-31.4
$T_N (K)$	6.5	7.0	9.5

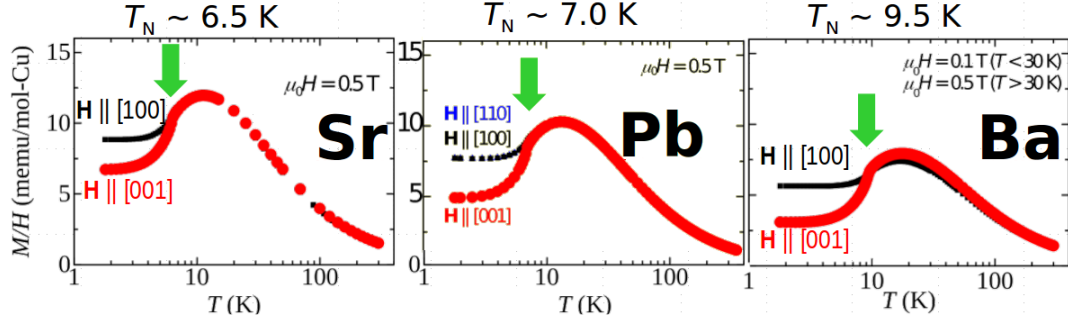


Figure 4.3 – **Susceptibility curves** of (Sr, Pb, Ba; Ti) for a field along the [100] (black), [001] (red) and [110] (blue) direction. Figure obtained from a private conversation with K. Kimura, used with his permission.

To conclude this section, I comment that the nuclear structure of the (*A*; *B*) family symmetrically allows for the existence of an anisotropic Dzyaloshinskii–Moriya interaction [132, 133] on the bond connecting two neighbouring Cu atoms from the same cupola unit (blue bonds in Fig. 4.2). It takes the form of an antisymmetric matrix  $\mathcal{D}$  such that  $\mathcal{D}_{\alpha\beta} = -\mathcal{D}_{\beta\alpha}$ . Effectively, this interaction is defined by a vector  $\mathbf{D}_{ij}$  orthogonal to the segment connecting two neighbouring  $\text{Cu}^{2+}$  ions. In the present case, its direction is given by  $\mathbf{D}_{ij} \propto \mathbf{d}_i \wedge \mathbf{d}_j$ , where  $\mathbf{d}_{i,j}$  are the vectors connecting the ligand oxygen atom to the Cu at position  $\mathbf{r}_{i,j}$ . The DM Hamiltonian then reads  $\mathcal{D} = -\sum_{\langle i,j \rangle} \mathbf{D}_{ij} \cdot (\hat{\mathbf{S}}_i \wedge \hat{\mathbf{S}}_j)$ .

#### 4.1.2 Theoretical elements of symmetry analysis

Crystallographic structures can be seen as sets of atoms that are placed in a very particular way. They are based on two properties : periodicity and symmetry. I propose here a quick summary of basic operations in a solid and introduce some symmetry properties that will be used in the rest of the chapter in order to reduce the complexity of the system. For further understanding, the reader is referred to the following textbooks [134, 135].

The most important property in physics is probably symmetry. Indeed, with the appropriate symmetry considerations, most complex systems can be simplified and solvable. The same applies to the investigation of ground state properties of quantum magnets. Let us start with a single unit cell given by a set of atoms at positions  $\mathbf{r}_i$ . There is a set of rotation and reflection operations that leaves the nuclear structure unchanged. For example, in the case of a cubic unit cell, a  $\pi/2$  rotation around the axis orthogonal to a face and intersecting it at its centre will leave the position of the atoms unchanged. Mathematically, this operation reads  $\mathbf{r}_j = \mathcal{R} \cdot \mathbf{r}_i$ , where  $\mathcal{R}$  is the matrix corresponding to a symmetry operation. Accounting for the crystallographic restriction, there is a total of 32 inequivalent symmetry operations that are commonly called *point groups*.

Table 4.2 – List of the possible symmetry operations on a unit cell giving rise to the 32 point groups.

Symmetry operation	Symmetry element	Symbol
Identity	–	$E$
Rotation by $2\pi/n$	$n$ -fold axis	$C_n$
Reflection	Mirror plane	$\sigma_i$
Inversion	Centre of inv.	$i$
Rotation by $2\pi/n$ and inv.	$n$ -fold axis + centre of inv.	$S_n$

Such a definition can be extended to a periodic assembly of unit cells, which then form a crystal. In this case, translation operations are also possible, which can be combined with the elements reported in Table 4.2 to form a total of 230 *space groups*, which are commonly represented by the variable  $G_0$ . There exist different notations to describe a space group, but the most widely used was proposed by Hermann–Mauguin. In their notation, the space group is defined by a letter followed by a series of numbers, each of them corresponding to a symmetry operation. For example, members of the  $(A, B)$  family are described by the space group  $P4_21_2$  (# 90). The "P" stands for the type of Bravais lattice, here it is a primitive one where the lattice points lie on the cell corners. For a tetragonal structure, the first "4" indicates a four-fold rotation along the higher-order (or primary) axis, here  $c$ . The " $2_1$ " in third position describes a screw operation along the secondary axis, orthogonal to the primary one. It is formed by a rotation of  $\pi$  followed by a translation of  $1/2$  of the lattice vector. Finally, the last "2" indicates a two-fold rotation around the tertiary axis.

The symmetry analysis becomes really interesting when the magnetic properties of the system are also considered. These properties are given by the moments on each site  $S_i$  and associated to the propagation vector  $\mathbf{k}$ , which describes how a spin configuration propagates throughout the crystallographic structure. Among all the set of operations described in the space group  $G_0$ , only a subset of symmetry elements will leave the propagation vector unchanged ( $\mathbf{k} = \mathcal{R} \cdot \mathbf{k}$ ) by the associated elementary operations  $\mathcal{R}$ . Here, I comment that only the rotational part of the transformation is likely to change the propagation vector. This new set defines the *little group* denoted by  $G_{\mathbf{k}}$ . Each symmetry operation defines an element of this set and is given by  $g_n$ . All the operations of a little group can be written as a large block diagonal matrix  $\Gamma_{\text{mag}}$  under the appropriate basis transformation. Each block corresponds to an irreducible representation  $\Gamma_{\nu}^{(\mu)}$  of dimension  $\mu$ , which I hereafter denote *irrep*. It is now important to distinguish the effects of a symmetry operation on an atom's position (polar) and on its magnetic moment (axial). The effect of an operation on the nuclear structure is simply to change the atom's position such that  $\mathbf{r}_j = g_n \mathbf{r}_i$ , which results in an effective permutation of two atoms in the unit cell. However, its effect on the magnetic moment must account for the fact that it is a vectorial quantity, and must then remain invariant under inversion. The associated transformation is then given by  $S' = \mathcal{R} S \det(\mathcal{R})$ . The

## Chapter 4. SNP as a tool for magnetic structure determination

---

determinant is here to ensure that the moment vector is not reversed by the inversion operation. At this point, it is convenient to introduce the *character*  $\chi$  of a symmetry operation, which corresponds to the trace of the associated transformation matrix. Thus, the magnetic representation is a direct product of the two independent polar and axial representations such that

$$\Gamma_{\text{mag}} = \Gamma_{\text{perm}} \otimes \Gamma_{\text{axial}}, \quad (4.1)$$

$$\chi_{\text{mag}} = \chi_{\text{perm}} \cdot \chi_{\text{axial}}. \quad (4.2)$$

In this orthogonal form, the magnetic representation can be written as a linear combination of *irreps*, where I introduce  $n_\nu$  as the number of basis vectors of  $\Gamma_\nu$ . This quantity practically corresponds to the degree of freedom of the magnetic structure. For instance, if  $n_\nu = 1$ , then the only variable would be the angle of the moment, or its length.

$$\Gamma_{\text{mag}} = \sum_{\nu} n_{\nu} \Gamma_{\nu}^{(\mu)} \quad (4.3)$$

$$n_{\nu} = \frac{1}{n(G_{\mathbf{k}})} \sum_{g \in G_{\mathbf{k}}} \chi_{\text{mag}}(g) \chi_{\Gamma_{\nu}}(g)^*. \quad (4.4)$$

Here,  $\chi_{\text{mag}}(g)$  is the character of the magnetic representation, and  $\chi_{\Gamma_{\nu}}(g)^*$  is the complex conjugate of the character of the *irrep* with index  $\nu$  and element  $g$ . The basis vectors  $\psi$  can be computed with the help of test functions along the crystallographic axis  $\phi_a = (1, 0, 0)$ ,  $\phi_b = (0, 1, 0)$  and  $\phi_c = (0, 0, 1)$ , which often is the most sensible choice, and using the projector operator technique. The basis vector  $\psi_{\alpha,\nu}^{\lambda}$  for the *irrep*  $\Gamma_{\nu}$  and using the test basis vector  $\phi_{\alpha}$  is then given by

$$\psi_{\alpha,\nu}^{\lambda} = \sum_{g \in G_{\mathbf{k}}} \mathcal{D}_{\nu}^{*\lambda}(g) \sum_i \delta_{i,g_i} \det(\mathcal{R}_g) \mathcal{R}_g \phi_{\alpha}, \quad (4.5)$$

where  $\mathcal{D}_{\nu}^{*\lambda}(g)$  is the complex conjugate of  $\lambda^{\text{th}}$  column of the transformation matrix associated with the  $\nu^{\text{th}}$  *irrep* for the symmetry element  $g$ .  $\sum_{g \in G_{\mathbf{k}}}$  ensures that the sum is restricted to the elements of the little group,  $\sum_i \delta_{i,g_i}$  denotes a sum on all sites from the same sub-lattice. Practically, one first chooses an *irrep* of dimension  $\mu$ . Then, one arbitrarily picks a row in the associated matrix, which will be fixed during the investigation of this *irrep*. If the latter is of dimension 1 ( $\mu = 1$ ), the problem is greatly simplified and  $\mathcal{D}_{\nu}^{*\lambda}(g) = \chi_{\nu}^{*}(g)$ . For each element  $\lambda$  of this row, one then projects out the components that correspond to the test basis vector  $\phi_{\alpha}$ , which eventually give us the basis function  $\psi_{\alpha,\nu}^{\lambda}$ . Of course, since three components are projected out for each element  $\lambda$ , there is a total of  $3\mu$  projected components. This number must correspond to the number of basis vectors  $n_{\nu}$  derived in Eq. 4.4. For a better understanding of these last steps, I strongly recommend to use Tables 4.3 and 4.4 as examples.

Having derived the basis vectors of an *irrep*, they can naturally be used to express quantities. In the frame of our analysis, the most useful one is of course the magnetic moment on site  $j$  which is defined as the Fourier transform of a linear combination of basis vectors  $\psi_{\alpha,\nu}^\lambda$  associated to a propagation vector  $\mathbf{k}$  such that

$$\mathbf{S}_j = \sum_{\alpha,\lambda} C_\alpha^\lambda \psi_\alpha^\lambda e^{2\pi i \mathbf{k} \cdot \boldsymbol{\tau}}, \quad (4.6)$$

where  $\boldsymbol{\tau}$  is the translation vector from the reference site  $i$  to the atom at position  $j$ .

The sum contains  $n_\nu \mu$  elements, which correspond to as many coefficients  $C_\alpha^\lambda$  to be refined in the analysis of the data. However, this number is much smaller than if all the spins were considered independently and thus the symmetry analysis is tedious yet necessary, in order to reduce the complexity of the system and make it solvable. Thankfully, dedicated softwares have been developed in order to reduce the dimensionality of the problem and have proven their great efficiency over the years [127, 128, 136, 137].

#### 4.1.3 Previous neutron powder diffraction experiments

A first attempt to determine the magnetic structure of the cupola compounds has been made by Peter Babkevich through neutron diffraction experiments on powder samples at WISH (ISIS) and D20 (ILL). On WISH, a 8.1 g powder sample of (Ba; Ti) has been measured for 25 minutes per temperature step, from 1.5 K to 20 K. Due to the particular detector configuration of WISH, data was simultaneously collected for different ranges of  $d$ -spacing and thus different resolutions. Fits have been made in the  $0.7 < d < 18$  Å range. On D20, a 5.4 g powder sample of (Sr; Ti), a 5.2 g powder sample of (Pb; Ti) and a 6.6 g powder of (Ba; Ti) have been measured at 1.7 K and 12 K for 8 hours per temperature, with an incoming (and outgoing) wavelength of  $\lambda = 2.41$  Å. The resulting diffraction patterns in the magnetically ordered phase are shown in Fig. 4.4.

The diffraction patterns of (Ba; Ti) and (Sr; Ti) show the same features [Figs. 4.4(a) and 4.4(c)]. Indeed, Bragg peaks emerge at the same diffraction angles  $2\theta$ , and only their intensities differ, notably at  $17^\circ$  and  $23^\circ$ . This is a hint that their magnetic structure is similar, with a small difference in the orientation of the moment. In both cases, Bragg peaks could be indexed by the propagation vector  $\mathbf{k} = (0, 0, \frac{1}{2})$ . The diffraction pattern of (Pb; Ti) [Fig. 4.4(b)] is somewhat different and peaks could only be indexed by a magnetic propagation wavevector  $\mathbf{k} = (0, 0, 1)$ , meaning that the cupolas stack ferromagnetically along the  $c$ -axis. The group theory analysis described in Sec. 4.1.2 has been carried using BASIREP [127]. In the case of ( $A$ ;  $B$ ), the little group  $G_{\mathbf{k}}$  contains all elements of  $G_0$ , which are listed in Table. 4.3.

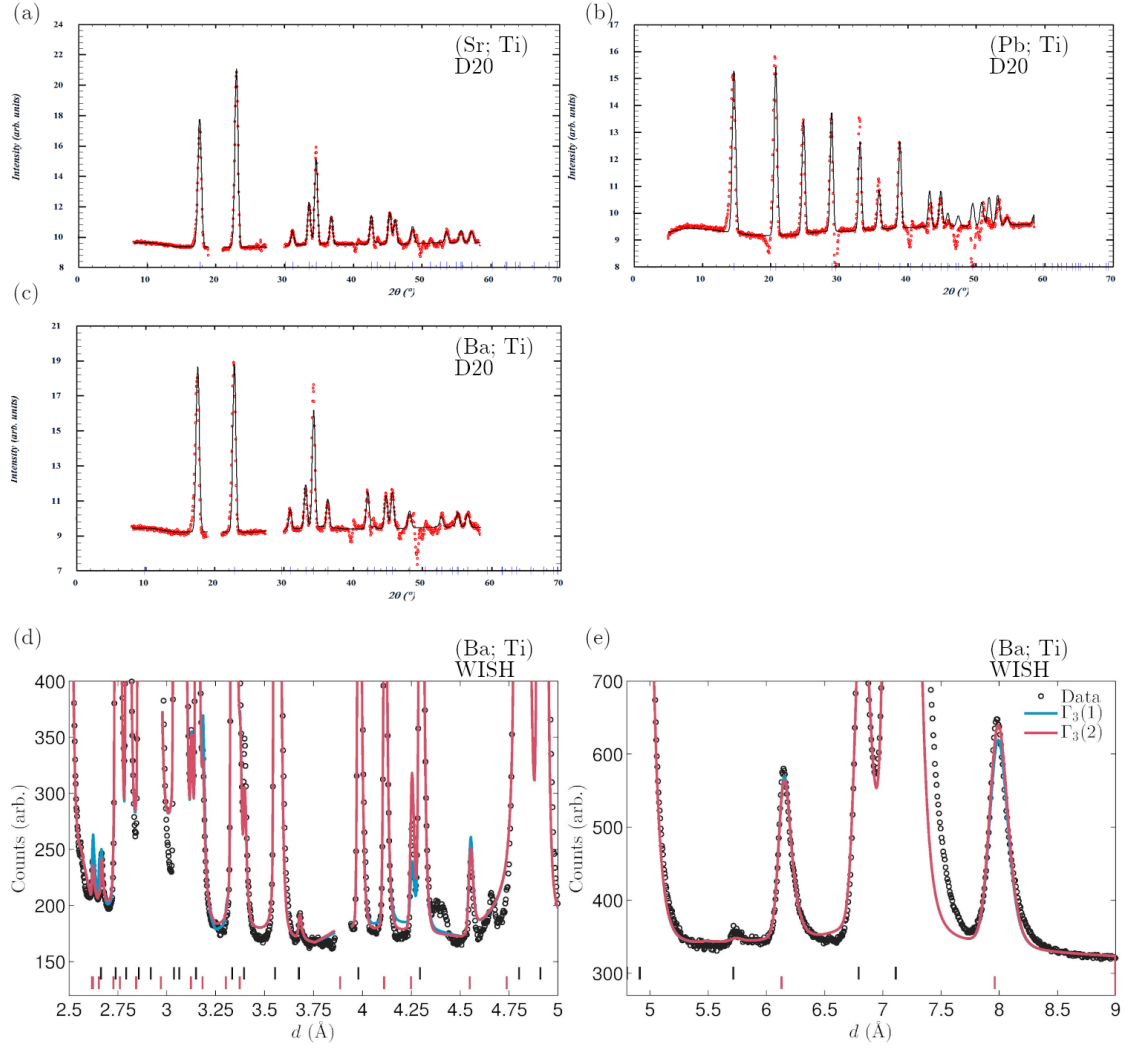


Figure 4.4 – **Neutron diffraction patterns** of (*A*; *B*) measured on (a–c) D20 (ILL) and (c, d) WISH (ISIS). Paramagnetic measurements have been subtracted from the patterns collected in the magnetically ordered phase in (a) (Sr; Ti), (b) (Pb; Ti), and (c) (Ba; Ti). The results have been fitted by a model constrained to respect the  $\Gamma_3$  irrep (black line). (d) and (e) show the high-temperature diffraction patterns of (Ba; Ti) from two detector banks with different  $d$ -coverage, intensity and resolution. Fits based on two different spin configurations in the same irrep  $\Gamma_3(1)$  and  $\Gamma_3(2)$  are proposed.

The magnetic representation of all members of the ( $A$ ;  $B$ ) cupola family can be written as a direct sum of five *irreps* as  $\Gamma_{\text{mag}}(8g) = 3\Gamma_1 + 3\Gamma_2 + 3\Gamma_3 + 3\Gamma_4 + 6\Gamma_5^{(2)}$ , the last one being two-dimensional. The corresponding character table is reported in Table. 4.4. Among those *irreps*, diffractions patterns were best described by  $\Gamma_3$  for (Ba; Ti) and (Sr; Ti), and  $\Gamma_2$  for (Pb; Ti). Both *irreps* are of dimension 1 and are described by three basis vectors. The three Fourier coefficients [ $C_\alpha = (u, v, w)$ ] can be obtained from Eq. 4.6 projected on the crystallographic axis. Even though (Pb; Ti) obeys a different *irrep*, the resulting spin configuration in a single magnetic layer is similar to those of its sister compounds. A recap of all essential results from the symmetry analysis is reported in Table. 4.5.

Table 4.3 – Elements of the little group  $G_k$ , which are equivalent to the symmetry operators of the space group  $P42_12$ . The rotational part  $\mathcal{R}$  is shown, as well as the IT notation as listed in the International Tables of Crystallography, and the Jones representation.

Element $g_n$	Rotation matrix $\mathcal{R}$	IT notation	Jones symbol
$g_1$	$\begin{pmatrix} 1 & 0 & 0 \\ 0 & 1 & 0 \\ 0 & 0 & 1 \end{pmatrix}$	1	$(x, y, z)$
$g_2$	$\begin{pmatrix} \bar{1} & 0 & 0 \\ 0 & \bar{1} & 0 \\ 0 & 0 & 1 \end{pmatrix}$	2 0, 0, $z$	$(-x, -y, z)$
$g_3$	$\begin{pmatrix} 0 & \bar{1} & 0 \\ 1 & 0 & 0 \\ 0 & 0 & 1 \end{pmatrix}$	$4^+ 0, \frac{1}{2}, z$	$(-y + 1/2, x + 1/2, z)$
$g_4$	$\begin{pmatrix} \bar{1} & 0 & 0 \\ 0 & 1 & 0 \\ 0 & 0 & \bar{1} \end{pmatrix}$	$2(0, \frac{1}{2}, 0) \frac{1}{4}, y, 0$	$(-x + 1/2, y + 1/2, -z)$
$g_5$	$\begin{pmatrix} 0 & 1 & 0 \\ \bar{1} & 0 & 0 \\ 0 & 0 & 1 \end{pmatrix}$	$4^- \frac{1}{2}, 0, z$	$(y + 1/2, -x + 1/2, z)$
$g_6$	$\begin{pmatrix} 1 & 0 & 0 \\ 0 & \bar{1} & 0 \\ 0 & 0 & \bar{1} \end{pmatrix}$	$2(\frac{1}{2}, 0, 0) x, \frac{1}{4}, 0$	$(x + 1/2, -y + 1/2, -z)$
$g_7$	$\begin{pmatrix} 0 & \bar{1} & 0 \\ \bar{1} & 0 & 0 \\ 0 & 0 & \bar{1} \end{pmatrix}$	2 $x, \bar{x}, 0$	$(-y, -x, -z)$
$g_8$	$\begin{pmatrix} 0 & 1 & 0 \\ 1 & 0 & 0 \\ 0 & 0 & \bar{1} \end{pmatrix}$	2 $x, x, 0$	$(y, x, -z)$

## Chapter 4. SNP as a tool for magnetic structure determination

Table 4.4 – Character table of the little group  $G_k$  showing how the  $\Gamma_\nu$  *irreps* transform according to symmetry operations  $g_1, \dots, g_8$  from Table 4.3. For  $\nu = 1 \dots 4$ , the element  $g_1 \dots g_8$  corresponds to the character  $\chi$  of the transformation while it corresponds to  $\mathcal{D}_\nu(g)$  for  $\Gamma_5$ .

$\nu$	$g_1$	$g_2$	$g_3$	$g_4$	$g_5$	$g_6$	$g_7$	$g_8$
1	1	1	1	1	1	1	1	1
2	1	1	1	1	$\bar{1}$	$\bar{1}$	$\bar{1}$	$\bar{1}$
3	1	1	$\bar{1}$	$\bar{1}$	1	1	$\bar{1}$	$\bar{1}$
4	1	1	$\bar{1}$	$\bar{1}$	$\bar{1}$	$\bar{1}$	1	1
5	$\begin{pmatrix} 1 & 0 \\ 0 & 1 \end{pmatrix}$	$\begin{pmatrix} \bar{1} & 0 \\ 0 & \bar{1} \end{pmatrix}$	$\begin{pmatrix} 1 & 0 \\ 0 & \bar{1} \end{pmatrix}$	$\begin{pmatrix} \bar{1} & 0 \\ 0 & 1 \end{pmatrix}$	$\begin{pmatrix} 0 & 1 \\ 1 & 0 \end{pmatrix}$	$\begin{pmatrix} 0 & \bar{1} \\ \bar{1} & 0 \end{pmatrix}$	$\begin{pmatrix} 0 & \bar{1} \\ 1 & 0 \end{pmatrix}$	$\begin{pmatrix} 0 & 1 \\ \bar{1} & 0 \end{pmatrix}$

Table 4.5 – Magnetic propagation vector and irreducible representation for (A; B). The magnetic moments  $\mathbf{S}_j$  on site  $j = 1 \dots 8$  are given in terms of the three real Fourier coefficients ( $u, v, w$ ) projected on a basis formed by the three vectors along the crystallographic axes, for the best *irrep*. The extracted strength of the magnetic moments is given by  $m_0$ . Bottom rows show the Wyckoff Cu positions 8g.

(A; B)	$\mathbf{k}$	$\Gamma_{\text{mag}}(8g)$	Best	$\mathbf{S}_j(u, v, w)$	$m_0 (\mu_B)$
(Ba; Ti)	$(0, 0, \frac{1}{2})$	$3\Gamma_1 + 3\Gamma_2 + 3\Gamma_3 + 3\Gamma_4 + 6\Gamma_5^{(2)}$	$\Gamma_3$	1. $(u, v, w)$ ; 2. $(\bar{u}, \bar{v}, w)$ 3. $(v, \bar{u}, \bar{w})$ 4. $(u, \bar{v}, w)$ 5. $(\bar{v}, u, \bar{w})$ ; 6. $(\bar{u}, v, w)$ 7. $(\bar{v}, \bar{u}, \bar{w})$ ; 8. $(v, u, \bar{w})$	0.80(1)
(Sr; Ti)	$(0, 0, \frac{1}{2})$	$3\Gamma_1 + 3\Gamma_2 + 3\Gamma_3 + 3\Gamma_4 + 6\Gamma_5^{(2)}$	$\Gamma_3$	1. $(u, v, w)$ ; 2. $(\bar{u}, \bar{v}, w)$ 3. $(v, \bar{u}, \bar{w})$ 4. $(u, \bar{v}, w)$ 5. $(\bar{v}, u, \bar{w})$ ; 6. $(\bar{u}, v, w)$ 7. $(\bar{v}, \bar{u}, \bar{w})$ ; 8. $(v, u, \bar{w})$	0.74(2)
(Pb; Ti)	$(0, 0, 1)$	$3\Gamma_1 + 3\Gamma_2 + 3\Gamma_3 + 3\Gamma_4 + 6\Gamma_5^{(2)}$	$\Gamma_2$	1. $(u, v, w)$ ; 2. $(\bar{u}, \bar{v}, w)$ 3. $(v, \bar{u}, \bar{w})$ 4. $(\bar{u}, v, \bar{w})$ 5. $(\bar{v}, u, \bar{w})$ ; 6. $(u, \bar{v}, \bar{w})$ 7. $(v, u, w)$ ; 8. $(\bar{v}, \bar{u}, w)$	0.71(6)
Cu atom position					
1. $(x, y, z)$ ; 2. $(-x, -y, z)$ ; 3. $(-y + \frac{1}{2}, x + \frac{1}{2}, z)$ 4. $(-x + \frac{1}{2}, y + \frac{1}{2}, -z)$ ; 5. $(y + \frac{1}{2}, -x + \frac{1}{2}, z)$ ; 6. $(x + \frac{1}{2}, -y + \frac{1}{2}, -z)$ 7. $(-y, -x, -z)$ ; 8. $(y, x, -z)$ .					



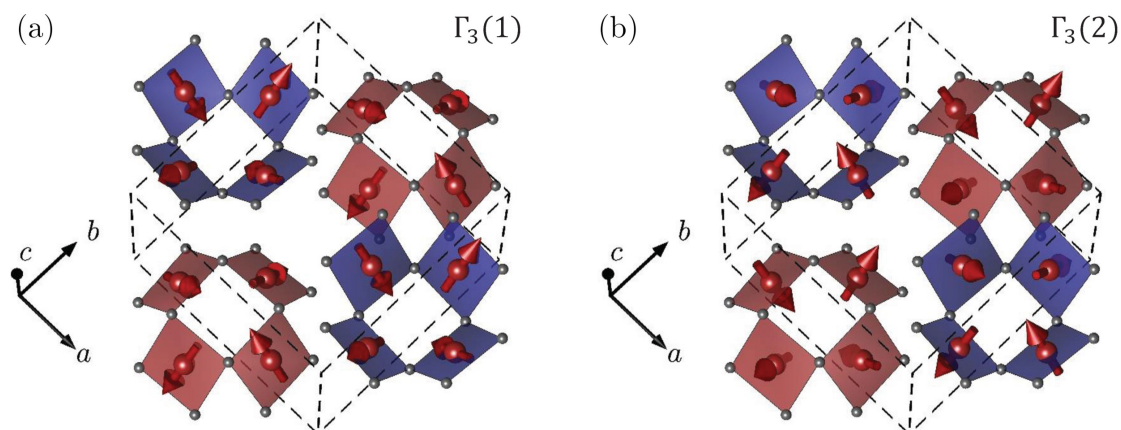


Figure 4.5 – **Proposed spin configurations in the  $\Gamma_3$  *irrep*** that describe the measured spectrum of (Ba; Ti) equally well. In  $\Gamma_3(1)$ , the moments lie approximately in the  $\text{CuO}_4$  plane, whereas they are almost orthogonal to it in the  $\Gamma_3(2)$  spin configuration.

The high-resolution data from the WISH diffractometer allowed for a more accurate analysis of (Ba; Ti). As shown in Figs. 4.4(d) and 4.4(e), two different spin orientations within the  $\Gamma_3$  *irrep* with Fourier coefficients  $(u, v, w) = (0.49(1), 0.36(2), 0.58(2))$  and  $(0.48(1), 0.1(3), -0.64(2))$  give similar quality of fit to the measured diffraction pattern. I shall refer to these spin configurations as  $\Gamma_3(1)$  and  $\Gamma_3(2)$  respectively. The former corresponds to a situation where the spins are lying approximately in the  $\text{CuO}_4$  plane, while in the latter the spins are pointing out of the  $\text{CuO}_4$  plane, forming a two-in-two-out configuration within the  $\text{Cu}_4\text{O}_{12}$  cupola. Both spin configurations are shown in Fig. 4.5. A good metric to evaluate the quality of a fit is the magnetic R-factor,  $R_{\text{mag}} = \frac{\sum_{\mathbf{Q}} |I_{\text{obs},\mathbf{Q}} - I_{\text{calc},\mathbf{Q}}|}{\sum_{\mathbf{Q}} |I_{\text{obs},\mathbf{Q}}|}$ , which is found to be 18.5% for  $\Gamma_3(1)$  and 11.5% for  $\Gamma_3(2)$ . The latter has therefore been proposed for (Ba; Ti) [138]. We did not have such high-resolution data on the sister compounds, but suspect that they follow a similar behaviour. However, since the difference between the two *irreps* is too small to reach a definitive conclusion, I propose in the following to use SNP as an extra tool to derive the magnetic structure of all three sister compounds.

## 4.2 The simple case of magnetic scattering processes only

The analysis of SNP data entirely relies on the computation of one quantity : the polarisation matrix defined in Eq. 2.31 as  $P^{\alpha\beta} = \frac{\sigma_{\alpha\beta} - \sigma_{\alpha\bar{\beta}}}{\sigma_{\alpha\beta} + \sigma_{\alpha\bar{\beta}}}$ . As explained in Sec. 2.1.4, this quantity can be extracted from a total of 18 scattering intensities, measured with an incoming and outgoing beam polarisation projected along the three orthogonal dynamic axes  $(\alpha, \beta)$ . I recall here that these axes depend on the position of the measured Bragg peak  $\mathbf{Q}$ , as defined in Eq. 2.26. In the most general case, but with no consideration of incoherent scattering events, the Fourier transform of the scattering potential for a set of atoms at positions  $\{\mathbf{r}_i\}$  is given by

$$V(\mathbf{Q}) = \sum_i e^{i\mathbf{Q} \cdot \mathbf{r}_i} V(\mathbf{r}_i) = \sum_i e^{i\mathbf{Q} \cdot \mathbf{r}_i} \left[ b_i^{\text{coh}} - p_i \mathbf{S}_{\perp i} \cdot \boldsymbol{\sigma} \right], \quad (4.7)$$

where  $b_i^{\text{coh}}$  is the coherent scattering length of the atom;  $p_i = (\gamma r_0/2) f_i(\mathbf{Q})$  with the gyromagnetic ratio  $\gamma = 1.913$ , the electron radius  $r_0 = 2.82$  fm, and the magnetic form factor  $f_i(\mathbf{Q})$ ; and finally  $\hat{\sigma}$  is the Pauli spin operator. The operator  $\boldsymbol{\sigma}$  is given by the Pauli matrices with the quantisation axis along  $z$ , and  $\mathbf{S}_{\perp i}$  is the orthogonal magnetic interaction vector on site  $i$ . In the case of a propagation vector with non-integer Miller indices, as it for (Ba; Ti) and (Sr; Ti) where  $\mathbf{k} = (0, 0, \frac{1}{2})$  [Table. 4.5], nuclear scattering does not occur at the same positions as magnetic scattering processes, in reciprocal space. The interaction potential is then greatly simplified and resumes to the last term of Eq. 4.7,  $\hat{V}_M(\mathbf{Q})$ , that is equivalently defined in Eq. 2.16. When inserted in the master Eq. 2.7, this potential yields a elastic scattering cross-section similar to Eq. 2.22. The only difference comes from the extra projection on the polarisation states  $|\sigma_{i,f}\rangle$  given by

$$\begin{aligned} |x\rangle &= \frac{1}{\sqrt{2}} \begin{pmatrix} 1 \\ 1 \end{pmatrix}, & |y\rangle &= \frac{1}{\sqrt{2}} \begin{pmatrix} 1 \\ i \end{pmatrix}, & |z\rangle &= \begin{pmatrix} 1 \\ 0 \end{pmatrix} \\ |\bar{x}\rangle &= \frac{1}{\sqrt{2}} \begin{pmatrix} 1 \\ \bar{1} \end{pmatrix}, & |\bar{y}\rangle &= \frac{1}{\sqrt{2}} \begin{pmatrix} 1 \\ \bar{i} \end{pmatrix}, & |\bar{z}\rangle &= \begin{pmatrix} 0 \\ 1 \end{pmatrix}. \end{aligned}$$

With the definition  $\mathbf{M}_{\perp}(\mathbf{Q}) = (0, M_y, M_z)$  in the new coordinates system, the cross section, for magnetic scattering events only, is

$$\sigma_{\alpha\beta} \propto |\langle\beta| \begin{pmatrix} M_z & -iM_y \\ iM_y & -M_z \end{pmatrix} |\alpha\rangle|^2. \quad (4.8)$$

Being a ratio of intensities at a single Bragg peak position, the polarisation matrix is not sensitive to the magnetic form factor, whose behaviour can be strongly influenced by covalency [139] and bias the results of unpolarised neutron diffraction experiments. However, measuring Bragg peaks at large  $|\mathbf{Q}|$  becomes challenging because of the very weak scattering intensity. In the case of a perfectly polarised beam, the polarisation

## 4.2. The simple case of magnetic scattering processes only

---

matrix then resumes to Eq. 2.32, which I recall here

$$P^{\alpha\beta} = \begin{pmatrix} -1 & 0 & 0 \\ H & -K & L \\ H & L & K \end{pmatrix}.$$

Importantly,  $H \propto i(\mathbf{M} \wedge \mathbf{M}^*)$ , also called the chiral term, is a sign of non-collinear magnetic order. When performing and analysing a SNP experiment, one must be aware of the existence of potential domains – both magnetic and structural. Magnetic ones might exist when the symmetry of the ordered phase is lower than that of the paramagnetic phase [15]. As mentioned earlier, in the case of the cupola family, the little group  $G_k$  contains all elements of  $G_0$  and then conserves its symmetry. In other words, translation symmetry is preserved on the application of symmetry operators, and no magnetic domain is expected. However, I mentioned earlier the observed existence of structural *levo* and *dextro* chiral domains in  $(A; B)$  compounds [130]. These two domains are related by spatial inversion such that  $\mathbf{r}_{levo} = -\mathbf{r}_{dextro}$ . In this case, the computation of the polarisation matrices must account for the separate domains. The cross-section then simply reads

$$\sigma_{\alpha\beta} \rightarrow \sum_n f_n \sigma_{\alpha\beta}^n, \quad (4.9)$$

where the fraction of the  $n^{\text{th}}$  domain is given by  $f_n$  and the computation of the polarisation matrix is performed as usual.

### 4.2.1 Combined ND and SNP analysis of $\text{Ba}(\text{TiO})\text{Cu}_4(\text{PO}_4)_4$

The first compound that I studied in my thesis is (Ba; Ti). It is known to have a domain population of roughly 50% *levo* and 50% *dextro* [130]. The eight equivalent Cu ions are sitting at the Wyckoff positions originating from the original position  $r_0 = (0.27, 0.99, 0.40)$ , in crystallographic cell unit.

#### Experimental setting

I have performed Spherical Neutron Polarimetry measurements on the TASP spectrometer using the MuPAD configuration at SINQ (PSI) [46, 140, 141], with an initial neutron wavelength of  $1.97 \text{ \AA}^{-1}$ . A single crystal sample of 0.6 g has been mounted on an Al sample holder which allowed for two scattering geometries. I initially probed the  $(h0l)$  scattering plane and reoriented the crystal in the  $(hhl)$  scattering plane in the second part of the experiment. Measurements of the flipping ratio  $R$  were performed on the  $Q = (2\ 0\ 0)$ ,  $(2\ 2\ 0)$  and  $(0\ 0\ 2)$  nuclear Bragg peaks, giving a ratio of  $R = 13.2$ . It corresponds to a polarisation efficiency of  $\eta = 96.4\%$  [Eq. 2.34], which was accounted for the computation of polarisation matrices. Complete sets of positive  $P^{\alpha\beta}$  and negative  $P^{\bar{\alpha}\bar{\beta}}$  were measured at 1.5 K and 20 K to eliminate scattering contribution from the systematic errors and background. A total of 26 polarisation matrices were measured, for a counting time of one hour per matrix.

#### Results

The main results are reported in Figs. 4.6 and 4.7, which show a representative set of measured and calculated matrices, in the  $\Gamma_3(1)$  and  $\Gamma_3(2)$  *irreps* respectively, for 6 inequivalent positions in reciprocal space. Scattering intensities in the paramagnetic phase at 20 K have been subtracted from low temperature data in order to remove systematic errors. I observe that in our data,  $P^{yx} \neq P^{zx}$ , and that  $P^{xz} \neq 0$  for some of the measured reflections. This emerges from a known feature of MuPAD, where small gaps in the shielding cause systematic errors. To account for these deviations, I also included different equivalent reflections as well as negative matrices in the analysis. I note the presence of weak chiral terms  $H$  for some reflections, meaning that  $M_{\perp}^*(Q)$  is not parallel to  $M_{\perp}(Q)$ , which is naturally the case when the spins are not aligned along the same direction. However, no definitive conclusion can be reached based on the form of these matrices and with no further fitting. The numbers in parentheses are extracted from statistical errors on the total neutron count  $N$  given by  $\sqrt{N}$  for Poisson statistics.

## 4.2. The simple case of magnetic scattering processes only

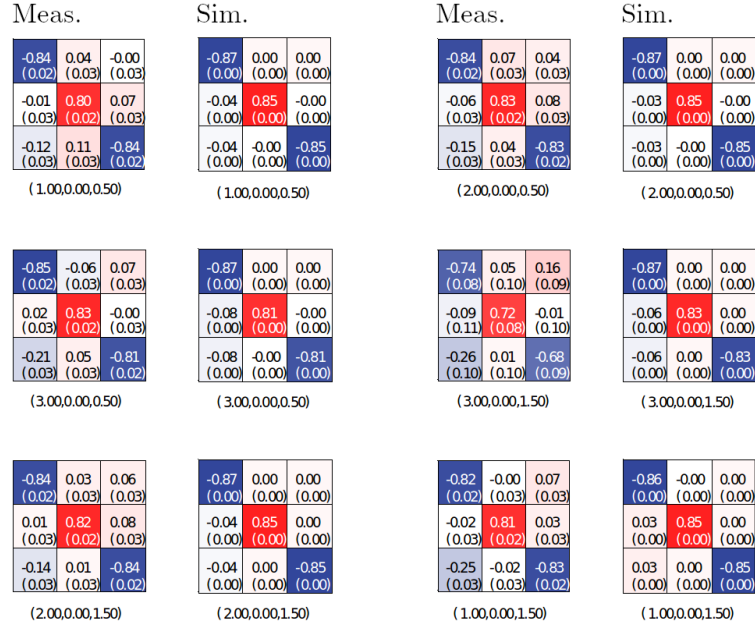


Figure 4.6 – **Representative polarisation matrices** measured (left) and calculated (right, no uncertainties) for different positions. The colour code goes from blue, corresponding to a value of -1, to red (+1). High temperature background measurements have been subtracted from data measured in the antiferromagnetic phase. Uncertainty in the measured matrices are reported in parentheses. Here, the simulated polarisation matrices were calculated for the  $\Gamma_3(1)$  configuration in Table 4.6 and Fig. 4.5.

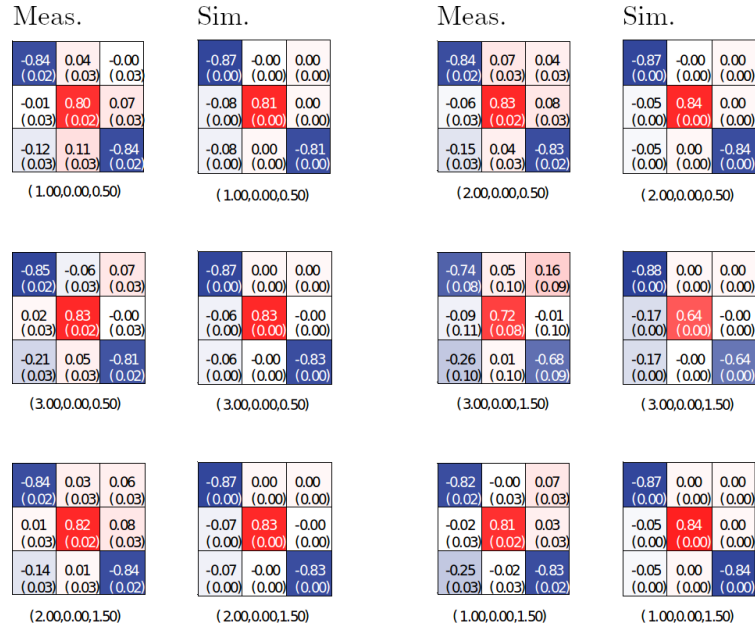


Figure 4.7 – **Representative polarisation matrices**, similar to Fig. 4.6 but the simulations are for the  $\Gamma_3(2)$  configuration.

## Chapter 4. SNP as a tool for magnetic structure determination

To start the discussion, I observe that no magnetic signal was measured for reflections  $Q = (0\ 0\ 0.5) + [0, 0, l]$ , with a typical count rate of two neutrons per minute in the  $\sigma_{x\bar{x}}$  channel, which also explains the large uncertainties reported in Fig. 4.8. Since neutrons only probe the component of the spin perpendicular to the scattering vector  $Q$ , one may believe that the low magnetic signal indicates that moments are pointing along the  $c$  axis. However, this can easily be disproved by examining other reflections, such as  $Q = (1\ 1\ 0.5)$  for example, which then forms an angle of  $46^\circ$  with the  $c$  axis. The diagonal elements  $P^{yy}$  and  $P^{zz}$  have measured values of  $-0.89(1)$  and  $+0.85(1)$ , respectively (not shown here). With a beam polarisation efficiency of  $\eta = 96.4\%$ , and spins pointing along the  $c$  axis, computations of the polarisation matrices give  $P^{yy} = +0.86$  and  $P^{zz} = -0.86$ , which is the exact opposite to our measurements. Furthermore, including the complete set of matrices in the comparison results in a goodness-of-fit of  $\chi^2 = 2000$ , which is extremely poor. This solution being ruled out, it calls for further in-depth analysis of the results.

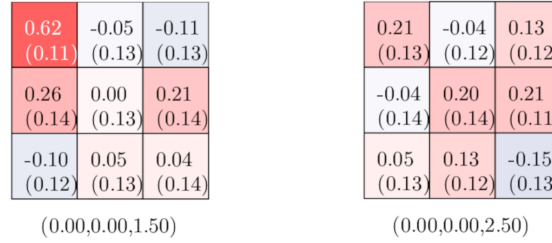


Figure 4.8 – **Polarisation matrices** measured at two magnetic reflections along  $[0, 0, l]$ , indicated below the matrices, and under similar conditions to Fig. 4.5.

Each matrix has a total number of four independent components –  $A, B, C, D$  in Eq. 2.32 – which also correspond to a combination of  $M_{y,z}^{(*)}(Q)$ . The refinement of the moments has been carried using a Levenberg-Marquardt routine [142, 143], which is ideal for non-linear problems as is the case here. As mentioned in the introduction of this chapter, symmetry analysis reduced the number of variational parameters to three: the projection of the magnetic moment vector on the crystallographic basis  $(u, v, w)$ . I recall that the quantities I am interested in here are intensity ratios, which means that the length of the moment cancels out in this expression. I am thus left with two parameters, namely the azimuthal and zenith angles. To this, in the specific case of (Ba; Ti), I must add the domain population which gives, for each *irrep*, a total of three parameters to be refined. I denote *levo* as the domain where all Cu atoms originate from  $r_0 = (0.27, 0.99, 0.40)$ , and *dextro* from  $-r_0$ . I comment that systematic errors are not accounted for in the analysis, which can lead to large values of the chi-squared parameter.

## 4.2. The simple case of magnetic scattering processes only

Table 4.6 – Direction of the magnetic moment on the Cu ions, obtained by fitting the SNP data with the two different spin configurations. The strength of the moment  $m_0$  has been taken from powder diffraction data on WISH. The domain population as well as the fit quality are also shown.

SNP	$\Gamma_3(1)$	$\Gamma_3(2)$
$u$ ( $\mu_B$ )	0.56(2)	0.56(2)
$v$ ( $\mu_B$ )	−0.01(1)	0.03(1)
$w$ ( $\mu_B$ )	0.59(2)	−0.57(2)
$m_0$ ( $\mu_B$ )	0.81(1)	0.80(1)
<i>levo</i> -domain	64(7)%	36(7)%
$\chi^2$	18.9	18.9

Simulated matrices associated with best fits for the complete set of measurements are reported, for each *subirrep*, in the right sub-columns of Figs. 4.6 and 4.7. The refined parameters are reported in Table. 4.6, with the moment normalised to  $m_0$  obtained from WISH refinement. I comment that both configurations  $\Gamma_3(1)$  and  $\Gamma_3(2)$  once again provide an equally good description of the system with a chi-squared of  $\chi^2 = 18.9$ . Interestingly, the values extracted from SNP are slightly different than the previous ones from neutron diffraction. The  $b$  component of the spins is here greatly reduced to nearly 0 compared to  $v_{ND} = 0.36 \mu_B$ . Interestingly, I point out the fact that the contributions from the *levo* [*dextro*] domain population counterbalances the effects of the  $\Gamma_3(1)$  [ $\Gamma_3(2)$ ] *irrep*. Thus, the two sets  $\{\textit{levo}, \Gamma_3(1)\}$  and  $\{\textit{dextro}, \Gamma_3(2)\}$  provide an extremely similar description of the measured data, which then makes an analysis based only on SNP data extremely tedious.

Table 4.7 – Magnetic  $R$ -factors defined in [127] corresponding to magnetic structure refinements based on different models. In the first case, only powder ND measurements are considered and both the moment direction and strength are allowed to vary. The second case, denoted as (SNP + ND), indicates the situation where the direction of the moment has been fixed to the SNP values, but its strength is refined using ND data. The last row corresponds to the case where only the banks covering the largest  $d$ -spacings, resulting in a better resolution, were considered.

	$\Gamma_3(1)$	$\Gamma_3(2)$
ND (D20)	16.4%	11.4%
SNP + ND (D20)	32.6%	18.8%
ND (WISH)	18.5%	11.5%
SNP + ND (WISH)	21.3%	19.4%
SNP + ND (WISH) (4, 5)	(35.5%, 42.9%)	(18.0%, 14.3%)

It is known that SNP has a greater sensitivity to the direction of the magnetic moments than neutron diffraction on powder. In order to solve the magnetic structure of (Ba; Ti), I propose to combine both analyses by refining the powder spectrum with the direction of the moment fixed to the values obtained from SNP, and allowing only the strength to vary. Fits on WISH data were performed on banks 4 and 5, which correspond to the lowest values of  $|Q|$ . Besides having a better resolution, the associated diffraction patterns are also the least affected by a possible anisotropic magnetic form factor that would emerge from covalent bondings. Goodness-of-fits are reported in Table. 4.7. Refinements purely based on neutron diffraction give equivalent results for both models, but the combined analysis results in a clear preference for the  $\Gamma_3(2)$  configuration. The difference is even stronger when the fitted region is restricted to low- $|Q|$  values where the effects of the form factor are minimised. Corresponding fits to the neutron diffraction data from WISH are shown in Fig. 4.9. Even though the quality of the fit is slightly poorer than if considering neutron diffraction data only, these two independent measurements combine to provide solid evidence that  $\Gamma_3(2)$ , shown in Fig. 4.5(b), models the system the best. An additional geometrical argument in favour of this configuration will be given in Sec. 4.2.3.



## 4.2. The simple case of magnetic scattering processes only

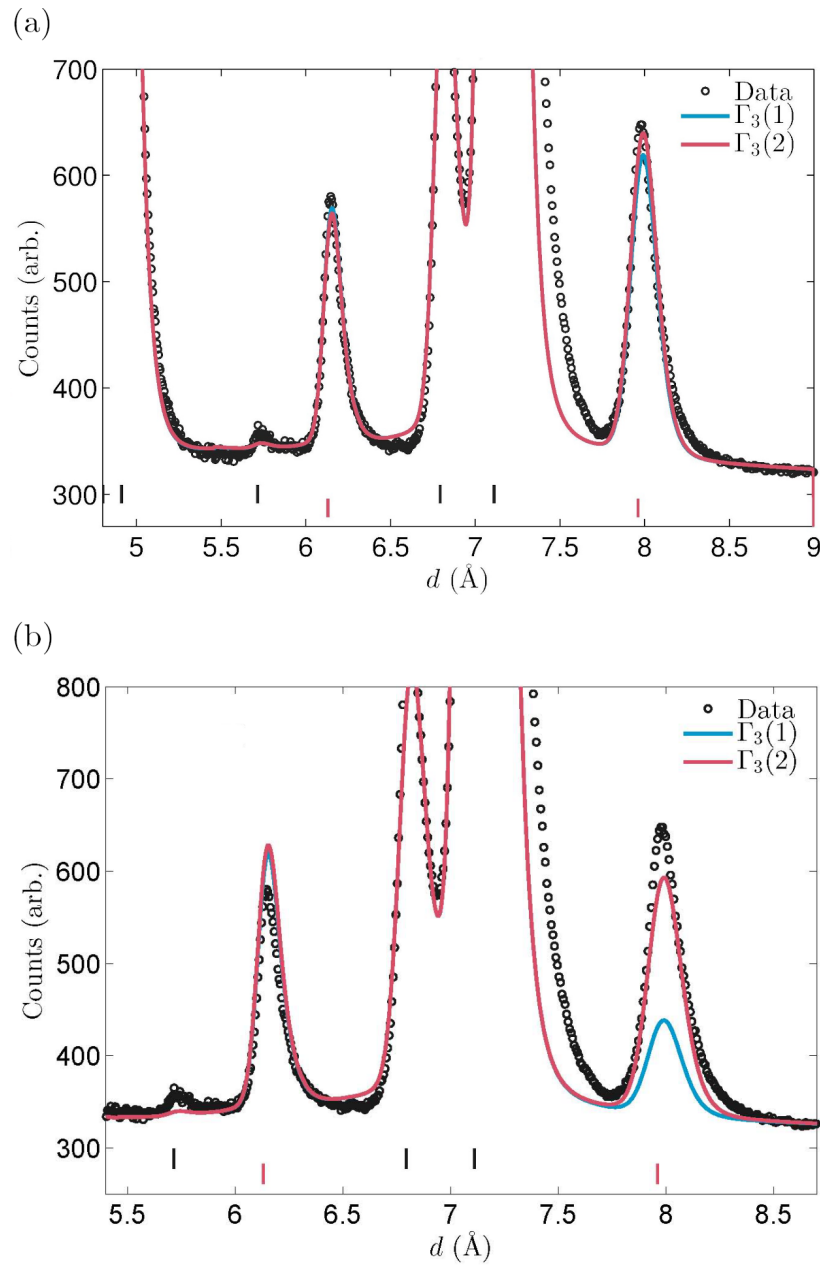


Figure 4.9 – **Fits to the neutron powder diffraction pattern** collected on WISH. (a) Analysis based on ND data only. (b) The moments direction is extracted from SNP data and its strength is allowed to vary. Both cases were refined based on the  $\Gamma_3(1)$  [red] and  $\Gamma_3(2)$  [blue] models.

### 4.2.2 Spherical Neutron Polarimetry on $\text{Sr}(\text{TiO})\text{Cu}_4(\text{PO}_4)_4$

The case of (Sr; Ti) is extremely similar. Neutron powder diffraction patterns could be equally well described by the two aforementioned *subirreps*,  $\Gamma_3(1)$  and  $\Gamma_3(2)$ . However, unlike the previous case, the single crystal that we used is known to be purely *dextro* [144], which reduces the number of fitting parameters to two: the angles in spherical coordinates  $(\varphi, \theta)$ . The Cu positions are generated from the original position  $-\mathbf{r}_0 = (-0.27, -0.98, -0.40)$ .

#### Experimental setup

Spherical Neutron Polarimetry has been performed on the IN20 spectrometer (ILL) in the CRYOPAD configuration [44], with an incoming wavevector  $\mathbf{k}_i = 2.58 \text{ \AA}^{-1}$ . A 0.28 g high-quality single crystal has been mounted on a non-magnetic holder, and oriented in the  $(h0l)$  scattering plane. Collimators have been added to the setup both before and after the sample to reduce diffuse elastic scattering. The flipping ratio  $R$  has been determined from the  $(2\ 0\ 0)$  nuclear Bragg peak, for a polarisation efficiency  $\eta = 98.12\%$ . Both positive and negative polarisation matrices have been collected on a total of 13 matrices for a counting time of two hours each, both at 1.5 K and 20 K to account for systematic errors.

#### Results

Figure 4.10 shows a representative selection of the collected polarisation matrices. Unlike for the previous case of (Ba; Ti), all matrices show strong chiral terms  $P^{yx}$  and  $P^{zx}$ , which is a direct evidence of a non-collinear structure. Since the parameter space is now of dimension 2, given by the angles  $\varphi$  and  $\theta$ , a quick way to start the analysis is to map it out. This will provide direct information on the degeneracy of the optimal candidates. The comparison has been made on the basis of 13 polarisation matrices, and I define the quality criterion as follows

$$\chi^2 = \frac{1}{N} \sum_{i=1}^N \frac{|f(x_i) - y_i|}{|y_i|}, \quad (4.10)$$

where  $N$  is the number of matrix components included in the fitting routine,  $N = 9 \cdot n_{\text{mat}}$ ;  $f(x_i)$  is the predicted value of the matrix component  $x_i$ , which depends on  $\varphi$  and  $\theta$ ; and  $y_i$  is the collected associated value. The result is reported in Fig. 4.11, for two different grid sizes. I immediately note the presence of two minima at positions  $(\varphi_0, \theta_0)$  and  $(\varphi_0 + \pi, -\theta_0)$ , where  $(\varphi_0, \theta_0) \sim (0, -\frac{\pi}{4})$ . These two positions correspond to a spatial inversion of the moment, and are naturally equivalent because of the  $\mathbf{k} = (0, 0, \frac{1}{2})$  propagation vector. I comment that the set  $\sim(\pi, -\frac{\pi}{4})$  that corresponds to  $\Gamma_3(1)$  has a  $\chi^2$  value of almost twice the optimal value (0.96 and 0.54).

## 4.2. The simple case of magnetic scattering processes only

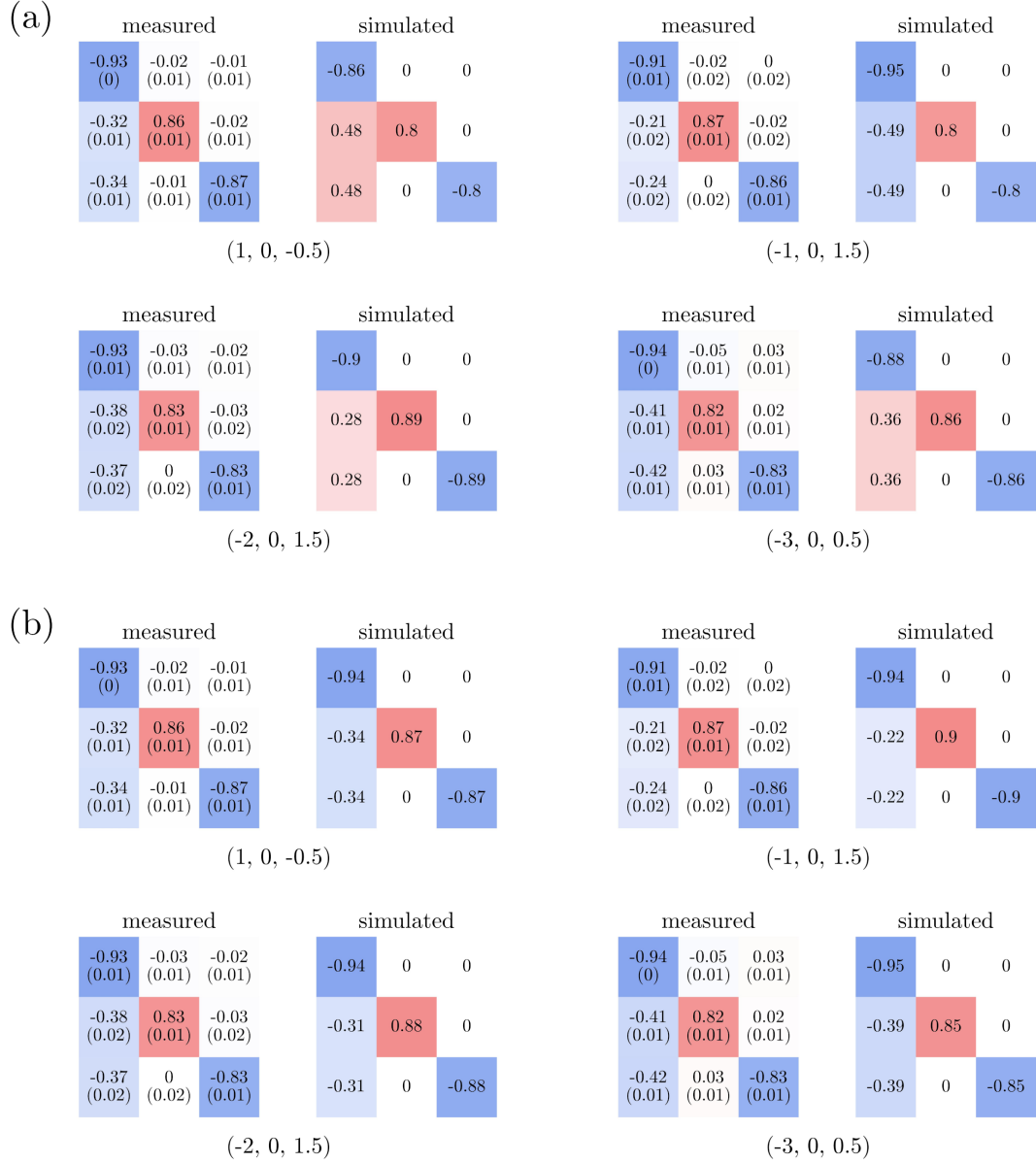


Figure 4.10 – **Selection of polarisation matrices** measured on  $\text{Sr}(\text{TiO})\text{Cu}_4(\text{PO}_4)_4$ . Left columns are measured polarisation matrices while right columns are simulated matrices based on the (a)  $\Gamma_3(1)$  and (b)  $\Gamma_3(2)$  model. The colour code goes from blue (-1) to red (+1). Intensities collected in the paramagnetic phase have been subtracted from low temperature measurements to remove systematic errors and background noise. Statistical errors are shown in parentheses.

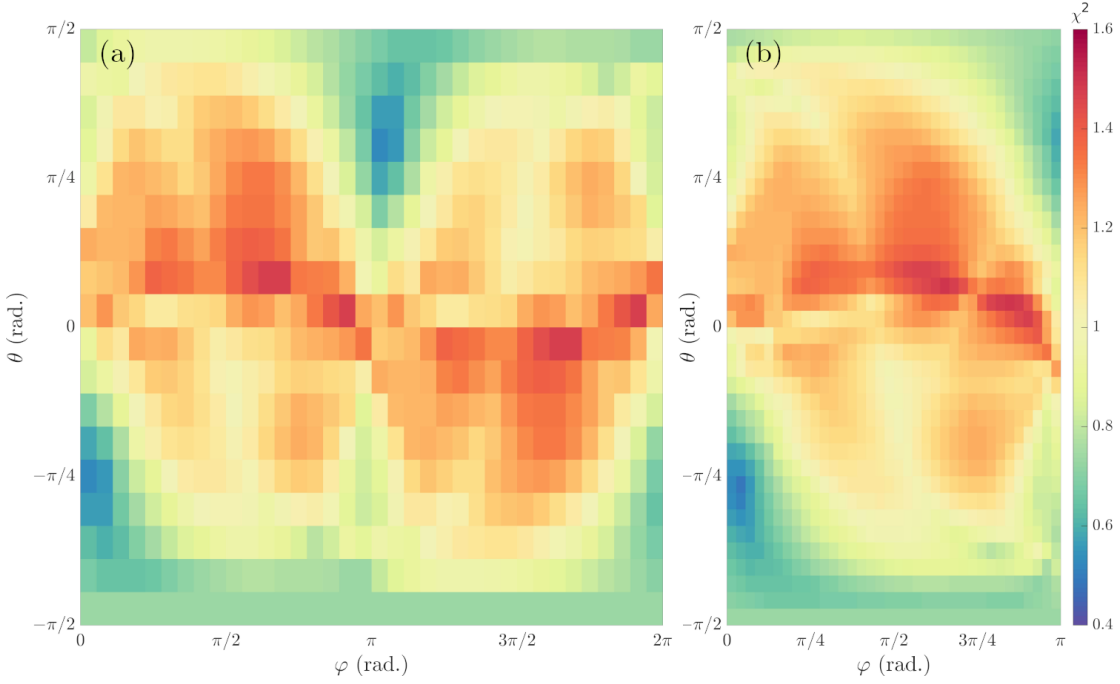


Figure 4.11 – **Colour map of  $\chi^2$  for (Sr; Ti).** The goodness-of-fit defined in Eq. 4.10 is reported for a (a)  $10^\circ \times 10^\circ$  grid and (b)  $5^\circ \times 5^\circ$  grid focused on one unit quadrant, showing two clear equivalent minimum positions.

The second solution being ruled out, I can now refine the angles defining the magnetic moment in a similar way as before, using a Levenberg-Marquardt algorithm. For the sake of consistency with Table. 4.6, I report them in crystallographic basis units. The following solution gives a minimal  $\chi^2$  of 0.49, with

$$u = 0.46(2) \mu_B, \quad v = 0.03(1) \mu_B, \quad w = -0.58(3) \mu_B.$$

The corresponding calculated matrices are reported in the right subcolumns of Fig. 4.10(a), and present a very nice agreement with the collected ones. I also reported in Fig. 4.10(b) the simulated polarisation matrices corresponding to the solution  $(\varphi_0 + \pi, -\theta_0)$  which was a local minimum in (Ba; Ti). Even though diagonal terms are reasonably well-described, the main difference comes from the chiral terms which are completely off – most of them even have the wrong sign. Interestingly, the key to magnetic structure determination came from these off-diagonal chiral terms. In the previous case of (Ba; Ti), the presence of inversion symmetry related domains made the analysis really challenging because of its consequences on the chiral terms. Indeed, I recall that they are defined as  $H \propto i(M(Q) \wedge M^*(Q))$ , where  $M_{D,[L]}(Q) \propto \sum_i M(\mathbf{r}_i) e^{[-]iQ \cdot \mathbf{r}_i}$  and  $D$  [L] correspond to *dextro* [*levo*] domains. As presented in Eq. 4.9, the final scattering cross-section is a weighted sum of the contribution from all domains. For an equal domain population, the Fourier transform of the magnetisation becomes real and the chiral terms  $H$  vanish.

### 4.2.3 The importance of the Dzyaloshinskii-Moriya interaction

As presented in the previous sections, ND and SNP measurements provide clear evidence that the magnetic structures of both  $\text{Ba}(\text{TiO})\text{Cu}_4(\text{PO}_4)_4$  and  $\text{Sr}(\text{TiO})\text{Cu}_4(\text{PO}_4)_4$  are modelled by the  $\Gamma_3(2)$  *irrep*, shown in Fig. 4.12, with angle values reported in Table. 4.8. The spins then form a *two-in-two-out* arrangement, pointing approximately out of the  $\text{CuO}_4$  planes. More importantly, I mentioned previously the presence of a Dzyaloshinskii-Moriya (DM) interaction between two nearest-neighbour Cu atoms within a cupola unit, as shown in Fig. 4.12, such that

$$\mathcal{D} = - \sum_{\langle i,j \rangle} \mathbf{D}_{ij} \cdot (\hat{\mathbf{S}}_i \wedge \hat{\mathbf{S}}_j). \quad (4.11)$$

The shared O atom is responsible for superexchange, but the Cu–O–Cu angle of  $108^\circ$  indicates a rather small coupling value, together with a strong DM interaction. The latter will tend to stabilise a magnetic structure with orthogonal nearest-neighbouring moments, while the former is likely to result in a collinear spin arrangement. The direction of the DM vector is predicted to be  $\mathbf{D}_{ij} \propto \mathbf{d}_i \wedge \mathbf{d}_j$ , where  $\mathbf{d}_{i,j}$  are the vectors connecting the ligand oxygen atom to the Cu atom at position  $\mathbf{r}_{i,j}$ , even though small deviations around this direction are possible.

In the case of (Ba; Ti), a rather strong anisotropy is expected from fits to bulk magnetisation measurements [131], and from the existence of a large gap compared to the bandwidth of the excitations in the powder spectrum [138]. Due to the similar nuclear structure and bulk results, it is reasonable to think that the same holds for (Sr; Ti). In both systems, for the case of the  $\Gamma_3(2)$  model, the spins are found to be almost perpendicular to the  $\text{CuO}_4$  plane, which results in a very small angle between  $\hat{\mathbf{S}}_i \wedge \hat{\mathbf{S}}_j$  and  $\mathbf{D}_{ij}$  [Table 4.8]. This is obviously not the case for the  $\Gamma_3(1)$  spin configuration, where the  $\hat{\mathbf{S}}_i \wedge \hat{\mathbf{S}}_j$  vector lies approximately  $130^\circ$  from  $\mathbf{D}_{ij}$ . The effects of the DM inter-

Table 4.8 – Angles (in degree) defining (top rows) the direction of the magnetic moment on the Cu ions derived from SNP measurements in the  $\Gamma_3(2)$  *irrep*, both on (Ba; Ti) and (Sr; Ti). The angle  $\varphi$  is defined between the crystallographic  $b$  axis and the projection of the moment on the  $(ab)$  plane, while  $\theta$  is the elevation angle. Parentheses indicate the numerical uncertainties on the values. (bottom rows) Angles between the vector orthogonal to two neighbouring spins and the DM vector, as well as between the direction of the moment and the normal to the  $\text{CuO}_4$  planes. The larger uncertainties on the latter account for the fact that  $\text{O}_4$  atoms do not lie exactly in the same plane.

Angles	(Ba; Ti)	(Sr; Ti)
$\varphi$	$3(1)^\circ$	$4(1)^\circ$
$\theta$	$-45(1)^\circ$	$-51(1)^\circ$
$(\hat{\mathbf{S}}_i \wedge \hat{\mathbf{S}}_j), \mathbf{D}_{ij}$	$15(1)^\circ$	$7(1)^\circ$
$\hat{\mathbf{S}}_i, \hat{\mathbf{n}}_{\text{CuO}_4}$	$12(3)^\circ$	$20(4)^\circ$

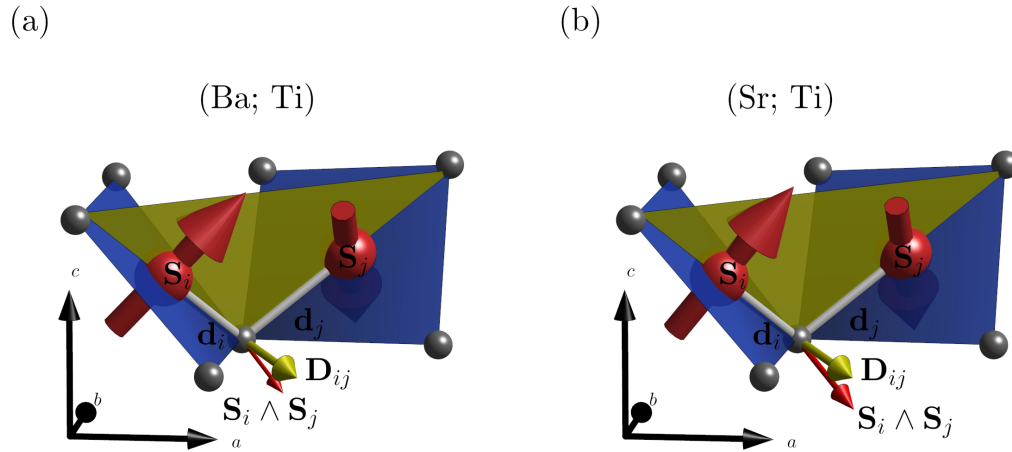


Figure 4.12 – **Direction of the magnetic moments in** (a) [Ba; Ti] and (b) [Sr; Ti]. Half of a cupola unit is reported in each case. The  $D_{ij}$  vector (yellow) defined in Eq. 4.11, as well as the direction orthogonal to both spins  $\hat{S}_i \wedge \hat{S}_j$  (red) are included for each case. The yellow plane is defined by the vectors  $r_i$  and  $r_j$ .

action would then be maximised in the  $\Gamma_3(2)$  spin configuration and naturally stabilise the highly non-collinear magnetic structure that I propose for these two compounds. Furthermore, it is consistent with the large anisotropy gap observed in prior neutron diffraction experiments. I finally comment that the results on (Ba; Ti) have been verified independently by another group with nuclear magnetic resonance techniques [145].

### 4.3 Combining nuclear and magnetic scattering processes

The situation is much more complicated if the propagation vector is equal to a reciprocal lattice vector. Indeed, this implies that nuclear and magnetic scattering events emerge at the same positions in reciprocal space. The cross-section of Eq. 2.28 must consequently be considered, with the terms detailed in Table 2.2. The presence of nuclear scattering events leads to the existence of two extra terms with respect to magnetic scattering events only, which I report here for clarity :

$$\sigma|_N = \mathbf{P}_i \cdot \mathbf{N} \mathbf{N}^*, \quad \sigma|_I = \mathbf{P}_i \cdot (\mathbf{M}_\perp \mathbf{N}^* + \mathbf{M}_\perp^* \mathbf{N}). \quad (4.12)$$

In the polarisation matrix, the former term corresponds to a change in the norm of the polarisation, and adds a correction to diagonal elements, which then go as  $P^{\alpha\alpha} \sim \frac{N^2 - M^2}{N^2 + M^2}$ . The latter term corresponds to a rotation in the polarisation direction, and can be observed in the chiral components  $P^{yx}$  and  $P^{zx}$ , as well as in the creation of so-called nuclear-magnetic-interference (NMI) terms  $P^{xy}$  and  $P^{xz}$ . As can be read from the analytical expression reported in Table 2.2, they are always present when nuclear and magnetic scattering events occur with a phase that is different from 0 or  $\pi$ .

Two remarks can be made out of this. First, nuclear scattering events usually are much stronger than magnetic ones. Thus, the final scattering intensities are less sensitive to any change in the magnetic contribution, which makes the refinement of the magnetic moment much less accurate. It is then naturally recommended to work on reflections that are structurally forbidden, and exhibit magnetism events only, in order to recover the situation described in the previous section. However, the number of inequivalent measured points will surely be lower than in the previous case, which, again, results in a less reliable conclusion. Secondly, the NMI terms mixes the nuclear and magnetic signals. It is thus absolutely impossible to separate both contributions by performing temperature subtraction. The addition of this nuclear term as such adds a clear challenge to the analysis of SNP data from such non-collinear magnetic systems. However, it has recently been proven that similar magnetic structures could be solved under certain conditions, which reduce the complexity of the problem [146].

### 4.3.1 The unsolved case of $\text{Pb}(\text{TiO})\text{Cu}_4(\text{PO}_4)_4$

The chiral compound (Pb; Ti) is known from neutron diffraction measurements [147] to have a propagation wavevector  $\mathbf{k} = (0, 0, 1)$ . Even though it is described by a different *irrep*, its magnetic configuration is thought to be the same as those of its sisters compounds, but with antiferromagnetically stacked plaquettes along the vertical axis. Eight equivalent Cu atoms are generated from the position  $\mathbf{r}_0 = (0.27, 0.99, 0.40)$  in crystallographic units. Unfortunately, the crystal has not been probed by polarised light, thus no information on the domain is known. However, it is believed that a high degree of structural chirality prevents the formation of domains [130], which may imply the existence of a single structural phase in (Pb; Ti).

#### Experimental setup

Spherical Neutron Polarimetry has been performed on the IN20 spectrometer (ILL) in the CRYOPAD configuration [44], with an incoming wavevector  $k_i = 2.58 \text{ \AA}^{-1}$ . A 0.47 g high-quality single crystal has been mounted on a non-magnetic holder, and oriented in the  $(h\bar{h}l)$  scattering plane. Collimators have been added to the setup both before and after the sample to reduce diffuse elastic scattering. The flipping ratio  $R$  has been determined from the  $(0\ 0\ 1)$  nuclear Bragg peak, for a polarisation efficiency  $\eta = 96.67\%$ . Both positive and negative polarisation matrices have been collected on a total of 24 matrices for a counting time of 45 minutes each, both at 1.5 K and 20 K to account for systematic errors.

A second experiment has been performed on the IN22 spectrometer (ILL) also using the CRYOPAD setup. A different sample of 1.68 g, but from the same growing batch, was mounted in the  $(2hkh)$  scattering plane to probe extra reflections with a weak nuclear term. The incident wavevector was  $k_i = 2.662 \text{ \AA}^{-1}$ . Two pyrolytic graphite (PG) filters were added after the sample in order to reduce  $\lambda/2$  scattering processes. Each matrix results from a total counting time of 45 minutes. The flipping ratio has been measured on the nuclear  $(0\ 2\ 0)$  reflection, for a polarisation efficiency  $\eta = 97.26\%$ . The scattering planes chosen in both experiments have been selected in order to maximise the number of weak nuclear reflections that could be probed, based on neutron powder diffraction results. A list is shown in Table. 4.9.



#### Results

A representative set of collected polarisation matrices is shown in Fig. 4.13, on which I can make a few comments. First, I remark that even reflections that are known from ND measurements to give a weak nuclear contribution show a behaviour strongly influenced by nuclear scattering events. This is notably the case of  $(2\bar{2}0)$ , where one measurement gave a total of 257 neutron counts in the non spin-flip channel ( $xx$ ) and 88 in the spin-flip channel ( $x\bar{x}$ ). However, three matrices [at positions  $(1\bar{1}0)$ ,  $(010)$  and  $(030)$ ] show evidence of an important magnetic contribution. I will then mainly elaborate on them. Interestingly, their corresponding NMI terms reported in the  $P^{xy}$  and  $P^{xz}$  components have vanishing intensity. Unfortunately, I comment that the reflections  $(010)$  and  $(030)$  show evidence of nuclear scattering despite the fact they should be structurally forbidden.

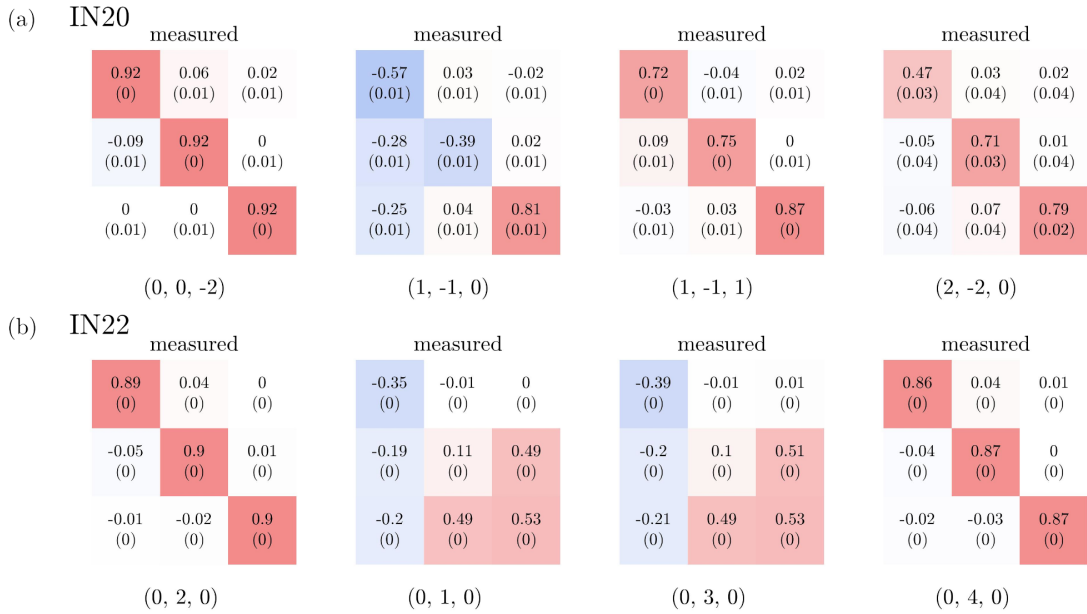


Figure 4.13 – **Selection of collected polarisation matrices** on (Pb; Ti), measured on (a) IN20 and (b) IN22. The colour code goes from blue (-1) to red (+1). Data have been collected at 1.5 K and no A3 subtraction has been performed due to the low background observed. Matrices in the first row correspond to Bragg peaks which are known to give a strong nuclear contribution [Table 4.9].

If both nuclear and magnetic scattering processes occur, the interaction potential must take the form  $\hat{V}(\mathbf{Q}) = \hat{V}_M(\mathbf{Q}) + \hat{V}_N(\mathbf{Q})$  defined in Eqs. 2.10 and 2.22. I made a first attempt to describe the data with this potential on the  $(1\bar{1}0)$  reflection. The corresponding calculated polarisation matrices in the  $\Gamma_2(2)$  *irrep* are shown in Fig. 4.14. Surprisingly, the overall behaviour the collected polarisation matrix was better reproduced in a situation where only the magnetic interaction was accounted for, as Figs. 4.14(b) and 4.14(c) show. Chiral terms are strongly modified by the nuclear poten-

## Chapter 4. SNP as a tool for magnetic structure determination

tial, and more importantly  $P^{xy} \neq P^{xz}$  and  $P^{yx} \neq P^{zx}$ . However, in the purely magnetic representation, the diagonal terms are too strong to describe the measurements accurately. I made another attempt to describe the data by artificially introducing a ratio  $\kappa$  between  $\hat{V}_M$  and  $\hat{V}_N$ , such that  $\hat{V} = \hat{V}_M + \kappa \cdot \hat{V}_N$ . The best description was obtained for  $\kappa = 0$ , which is inconsistent with the physics of the system. Furthermore, I performed a complete mapping of the reduced parameter space, with  $\kappa = 0$ , similar to Fig. 4.11 (not shown here). Unlike for (Sr; Ti), this defined the presence of a very broad minimum region with only little variation from one point to another. I conclude that the problem was badly defined, and decided to stop the analysis here.

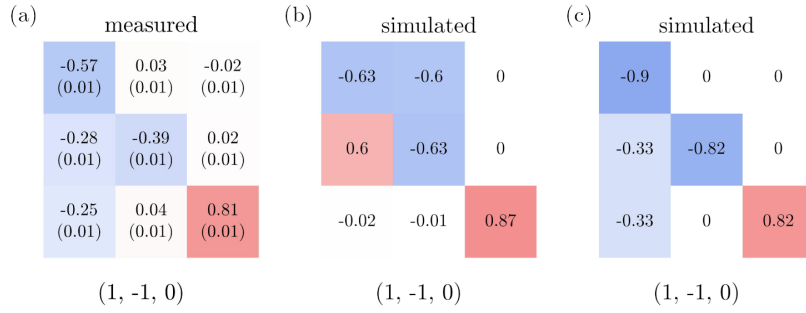


Figure 4.14 – **Polarisation matrices of the most promising reflection.** (a) Measured, (b) simulated with both nuclear and magnetic contributions, and (c) simulated with the magnetic contribution only. Both (a) and (b) are based on the  $\Gamma_2(2)$  irrep.

Table 4.9 – Predicted value of the nuclear structure factor  $|F_N(Q)|^2$  for different reflections in the probed scattering planes, and  $k = 2.662 \text{ \AA}^{-1}$ . Reflections with no scattering intensities are not shown, and a value of 0 caused by rounding effects and is then finite. The multiplicity is indicated by  $m$  and a set of equivalent reflections is shown in the last column.

$h$	$k$	$l$	$d_{hkl}$	$ Q_{hkl} $	$2\theta_{hkl}$	$ F_N _{hkl}^2$	$m$	Reflections
0	0	1	7.014	0.896	19.37	70	2	[0 0 -1],[0 0 1]
1	1	0	6.748	0.931	20.15	0	4	[-1 -1 0],[-1 1 0],...
1	1	1	4.863	1.292	28.09	147	8	[-1 -1 -1],[-1 -1 1],...
2	0	0	4.771	1.317	28.64	270	4	[-2 0 0],[0 -2 0],...
2	0	1	3.945	1.593	34.81	57	8	[-2 0 -1],[-2 0 1],...
2	1	1	3.646	1.723	37.77	1	16	[-2 -1 -1],[-2 -1 1],...
0	0	2	3.507	1.792	39.33	124	2	[0 0 -2],[0 0 2]
2	2	0	3.374	1.862	40.95	1	4	[-2 -2 0],[-2 2 0],...
1	1	2	3.112	2.019	44.57	32	8	[-1 -1 -2],[-1 -1 2],...
2	2	1	3.040	2.067	45.68	481	8	[-2 -2 -1],[-2 -2 1],...
2	2	2	2.431	2.584	58.08	591	8	[-2 -2 -2],[-2 -2 2],...
4	0	0	2.386	2.634	59.30	66	4	[-4 0 0],[0 -4 0],...

#### Discussion

Unfortunately, I was not able to confirm nor deny the proposed magnetic structure of (Pb; Ti). The difficulty that I encountered during the analysis can be explained by a few factors. First, nuclear signals are usually stronger than magnetic ones. Thus, a small variation in the nuclear structure factor with respect to its predicted value will have a big influence on the resulting calculated polarisation matrices. Yet it is known from experimental powder refinements that the measured value is rarely exactly the same as the predicted one. For example, at  $Q = (1 \bar{1} 0)$ , the measured intensity from ND is  $I_{\text{obs}} = 0.3$ , while the value predicted from the structure factor is  $I_{\text{cal}} = 0.1$ . Naturally, the weaker the absolute signal, the bigger the relative difference, which leads to large variations. Furthermore, in typical neutron experiments, the ratio  $\alpha = I_{\text{obs}}/I_{\text{cal}}$  has been shown to be smaller than one, even for small intensities [148], and gets even worse with increasing scattering signal. I made an attempt to include these intensity corrections to the analysis, but the outcome was not very successful. Indeed, correcting the intensities resulted in reduced off-diagonal terms, while diagonal ones were left quasi unchanged. This then produces the opposite effect to expected. I conclude that an analysis based on the predicted value of the structure factor becomes tedious, or even impossible under certain conditions.

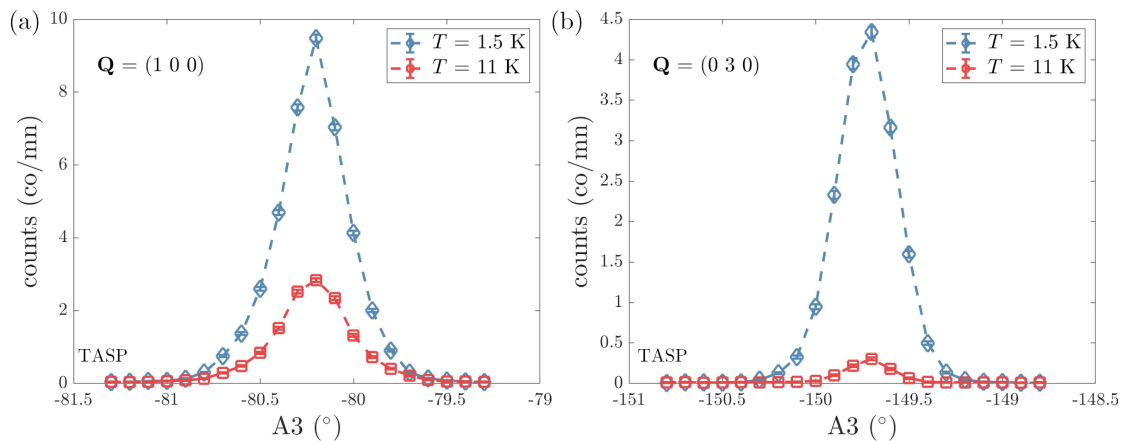


Figure 4.15 – **Rocking curves** measured on the 1.68 g single crystal of (Pb; Ti) both in the antiferromagnetic (blue) and paramagnetic (red) phase, at positions (a)  $Q = (1 \ 0 \ 0)$ , and (b)  $Q = (0 \ 3 \ 0)$ . Both reflections are structurally forbidden, yet some non-negligible nuclear scattering intensity is observed. The measurement has been done on TASP (PSI).

Additionally, as I mentioned earlier, some nuclear scattering intensity has been observed on two Bragg peak positions that are structurally forbidden – (0 1 0) and (0 3 0) [Table 4.9], as reported in Figs. 4.15 and 4.16. This additional intensity could emerge from  $\lambda/2$  scattering events, or multiple scattering, from a change in the nuclear structure, or even by the presence of structural defects. The first possibility is very unlikely due to the presence of PG(002) filters, which drastically reduce multiple order scattering. No clear sign of structural change has been observed on this compound, and neutron powder diffraction showed no sign of nuclear signal emerging from (0 1 0) nor (0 3 0). Unfortunately, this unexpected scattering intensity implied that the two most promising Bragg peaks could not be included in the polarisation analysis. It would be interesting to repeat the experiment on a different crystal, taken from another growing batch.

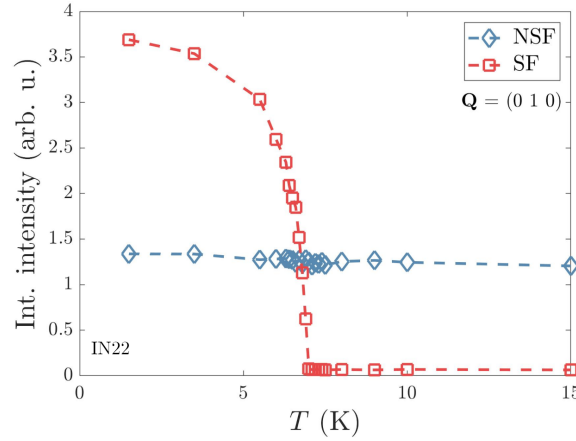


Figure 4.16 – **Temperature evolution** of the (0 1 0) reflection, collected on IN22. Each point corresponds to the integrated intensity of an A3 scan around  $Q = (0\ 1\ 0)$  in the non spin-flip (blue) probing structural effects, and spin-flip (red) probing magnetic effects.

There are two ways to overcome the structure factor issue. The first one is to define it as  $F(Q) = R_Q e^{i\phi_Q}$ , where both the magnitude and the phase depend on  $Q$ . However, this method adds two extra variational parameters per polarisation matrix, and thus cannot be used in the analysis of this experiment. Another method is to base the description of the structure factor on high temperature diffraction data measured on the very same single crystal  $I_{\text{obs}}(Q)$ . Under the assumption that it is a real quantity, which is true under certain circumstances that have to be verified beforehand,  $\hat{V}_N(Q) = (\tau \cdot I_{\text{obs}}(Q))^{1/2}$ . The tuning strength  $\tau$  would then be the only extra variational parameter added to the analysis. Furthermore, the size of the magnetic moment matters when both nuclear and magnetic contributions are considered. The parameter  $\tau$  would also capture this feature. Unfortunately, I have not implemented this method so far.

A second issue that has not been addressed in the case of (Pb; Ti) arises from the chirality of the crystal, and the presence of structural domains. Since I used two different samples for my experiments, including the domain population in the analysis becomes tedious. Furthermore, no solid dedicated experiment on the domain population has been performed to my knowledge. As I observed on both (Ba; Ti) and (Sr; Ti), the domain population is a key element in the description of the magnetic structure. I performed an in-depth investigation on the domain population, which emphasised the significant influence of this factor on the chiral terms, and, to a smaller extent, on the diagonal ones. As I pointed, assuming a vanishing nuclear contribution, a *dextro* crystal described by a  $\Gamma_2(1)$  *irrep* provides an equally good description of the data as  $\Gamma_2(2)$  on a *levo* crystal. Prior knowledge of the domain population is necessary in the analysis of chiral structures, and is missing here.

Additionally, the low number of inequivalent polarisation matrices does not allow me to push the analysis any further as it would result in the description of a system by more parameters than its dimensionality. However, as I mentioned in the introduction of this section, recent work proved that solving  $\mathbf{k} = (0, 0, 0)$  magnetic structures was indeed possible [146]. More effort towards this direction will certainly be done in the next few years. Furthermore, the recent development of the Mag2Po1 [149] analysis tool will certainly be of great use to the neutron scattering community.

## 4.4 Summary

In this chapter, I used the spherical neutron polarimetry technique to extract the magnetic structure of three sister members of the  $A(BO)Cu_4(PO_4)_4$  structurally chiral family – (Ba; Ti), (Sr; Ti) and (Pb; Ti). Prior neutron powder diffraction showed that magnetic peaks in the first two compounds could be indexed by a propagation vector  $\mathbf{k} = (0, 0, \frac{1}{2})$ . Nevertheless, two competing magnetic structures within the same *irrep* described the diffraction pattern equally well, which I denoted  $\Gamma_3(1)$  and  $\Gamma_3(2)$ . Both correspond to non-collinear structures for which SNP is highly sensitive. It is known that magnetic domains must be accounted for in the analysis of SNP data. However, only little can be found in the literature when structural domains coexist. As it can be read from Blume-Maleev equations, I confirmed experimentally that chiral terms are sensitive to the domain population. Furthermore, in the case I was interested in, domains were in direct competition with the magnetic structure, where  $\{\textit{levo}, \Gamma_3(1)\}$  shows similar effects than  $\{\textit{dextro}, \Gamma_3(2)\}$ .

In the case of (Ba; Ti), the full analysis was made possible by the high number of inequivalent collected polarisation matrices, as well as the high-resolution neutron powder diffraction data. They allow for a joint analysis, which, importantly, also included the domain population as a free parameter. For (Sr; Ti), prior knowledge of the existence of a single chiral domain in the crystal greatly simplified the analysis. I

thus comment that it is a key element of the analysis, and should always be considered. Finally, I used the presence of a symmetrically allowed Dzyaloshinskii-Moriya interaction, predicted from inelastic neutron scattering measurements, as a solid argument in favour of a magnetic configuration where the spins would point out of the  $\text{CuO}_4$  planes. The extracted direction of the moments are reported below. I did not include the strength of the moments since this quantity cannot be directly extracted from SNP measurements.

Angles	(Ba; Ti)	(Sr; Ti)
$\varphi$	$3(1)^\circ$	$4(1)^\circ$
$\theta$	$-45(1)^\circ$	$-51(1)^\circ$

I encountered notable complications in the final case of (Pb; Ti), which is known to have a propagation wavevector  $\mathbf{k} = (0, 0, 1)$  resulting in the presence of both magnetic and nuclear scattering events simultaneously. Indeed, these SNP experiments did not lead to a successful determination of its magnetic structure, although a recent study successfully demonstrated the feasibility of such analyses on simpler systems. Several reasons are responsible for this outcome. First, the single crystal that I used showed clear evidence of nuclear scattering at forbidden positions. These scattering processes were not observed on powder diffraction patterns, and point out that a complete description of its nuclear structure is still incomplete. Second, I commented on the huge influence of the static structure factor on the resulting polarisation matrix. The results are also easily biased by the fact that the measured structure factor does not always match its theoretical value. Third, I noted the existence of structural domains whose populations were not exactly known. This ended up being a key point in the analysis of its sister compounds, and showed that prior structural knowledge was needed in order to carry with the analysis. Unfortunately, I did not collect enough reliable polarisation matrices for the dimensionality of the problem. Finally, I would like to highlight the complexity of the system resulting from the non-collinear magnetic order. Efforts are being put towards the understanding of non-simple magnetic structures, and (Pb; Ti) is undoubtedly a great candidate to serve this purpose.

# 5 Variation on the square lattice – the $A(BO)Cu_4(PO_4)_4$ cupola family

## Contents

<b>5.1 Introduction</b>	<b>88</b>
<b>5.2 Excitation spectrum of <math>Ba(TiO)Cu_4(PO_4)_4</math></b>	<b>90</b>
5.2.1 Experimental setups	91
5.2.2 Spin dynamics	92
5.2.3 Derivation of the magnetic Hamiltonian	99
5.2.4 Comparison with high-field magnetisation measurements	103
5.2.5 Future dedicated work	105
<b>5.3 Qualitative description of <math>Pb(TiO)Cu_4(PO_4)_4</math></b>	<b>107</b>
5.3.1 Experimental setups	107
5.3.2 Excitation spectrum in zero field	108
5.3.3 Excitation spectrum in a vertical magnetic field	111
<b>5.4 <math>K(NbO)Cu_4(PO_4)_4</math> as a strongly quantum system</b>	<b>113</b>
5.4.1 Powder spectrum of (K; Nb)	114
<b>5.5 Summary</b>	<b>117</b>

In Chapter 4, I performed an in-depth investigation on the magnetic structure of three compounds of the  $(A; B)$  family, revealing a highly non-collinear spin arrangement reported in Fig. 5.1. However, the most interesting feature of this series of compounds is probably their crystal structure, reported in both Figs. 5.1 and 5.2. I recall here that polarised-light microscopy showed that the cupolas have an alternating rotation about the  $c$ -axis, and that the extent of this structural chirality depends on the  $A^{2+}$  cation [130]. It has been found by a range of thermodynamic measurements [131, 138, 144, 150, 151, 152] that this tunable nuclear structure causes significant changes in the magnetic interactions too. These structural and magnetic considerations make  $A(BO)Cu_4(PO_4)_4$  an ideal playground to study tetramerisation effects on the 2D spin-1/2 square antiferromagnetic magnetic lattice. A significant amount

of dedicated studies have been undertaken in order to characterise static properties [131, 150, 152, 153, 154], and to relate them to the particular structure of the compounds. However, dynamic properties have not been truly investigated for this purpose, yet. Additionally, I pointed out in the last chapter the presence of a strong Dzyaloshinskii-Moriya (DM) interaction explaining the large gap observed in preliminary inelastic neutron scattering experiments on powder samples [138], which was a key element in the determination of the magnetic structure. Yet, the competition between robust long range order and quantum disorder induced by frustration or anisotropies is a frontier research domain in condensed matter physics. The chiral family  $A(BO)Cu_4(PO_4)_4$  then provides a unique arena to understand the dynamics of tetramerised “ $J_1$ - $J'_1$ - $J_2$ - $J'_2$ ” models in extended square-lattice systems.

In this chapter, I present the results of high-resolution inelastic neutron scattering (INS) measurements that I performed on single crystals of two members of the chiral family – (Ba; Ti) and (Pb; Ti) – as well as powder INS on the high-symmetry compound (K; Nb). While an accurate determination of the couplings in the latter two is still ongoing, I propose a definitive set of magnetic interaction parameters that describe the dynamic structure factor of the former to high accuracy.

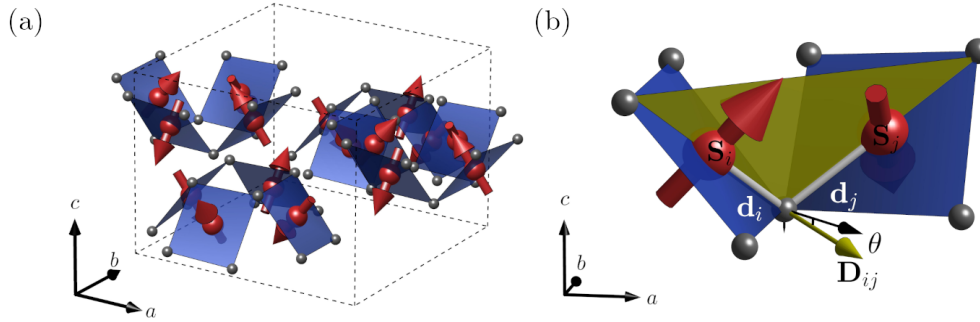


Figure 5.1 – **Schematics of the crystallographic and magnetic structure of  $Ba(TiO)Cu_4(PO_4)_4$ .** (a) Ordered magnetic moments (red) point almost perpendicular to the  $CuO_4$  planes (blue) in a two-in-two-out configuration on each cupola, with the relative directions between upward- and downward-oriented cupolas as shown. (b) The DM vector (yellow) lies in a vertical plane equidistant from the two Cu atoms and forms an angle  $\theta$  with the horizontal  $(ab)$  plane.

## 5.1 Introduction

The antiferromagnetic (AF) spin- $\frac{1}{2}$  Heisenberg model has always shown remarkable physics. While the one-dimensional (1D) chain is exactly solvable and its solution describes a strongly fluctuating spin state with fractionalised excitations [155, 156, 157], its 2D analogue shows spontaneous breaking of the continuous spin symmetry and Néel-type magnetic order [23, 24], albeit with strong quantum renormalisation of the



ordered moment [50]. Additionally, geometrical frustration induced by diagonal next-nearest-neighbour interaction ( $J_2$ ) suppresses long range order (LRO). This system has been extensively studied [158, 159, 160, 161, 162, 163, 164], although no definitive conclusion has been drawn on the nature of the quantum disordered state around  $J_2 = J_1/2$ .

In the frame of this study, two axes of research are of great interest. In the direction of spatial anisotropy, numerical investigation of plaquette-based, or tetramerised, square lattices with no frustration reveal a quantum phase transition (QPT) to a plaquette-singlet state at an inter- to intra-plaquette coupling ratio  $\alpha = 0.55$  [165, 166]. Experimentally, while a certain numbers of compounds are now known to realise the square lattice [116, 167, 168, 169], the most interesting two for my purpose are probably the tetramerised compound  $\text{Na}_{1.5}\text{VOPO}_4\text{F}_{0.5}$  [170], which opens a route towards experimental studies of plaquette-based systems on the frustrated square lattice, and  $\text{La}_2\text{O}_2\text{Fe}_2\text{O}(\text{Se},\text{S})_2$ , which offers a similar possibility for (“double”) checkerboard geometries [171]. However, most studies to date have focused on the static properties of these materials, and the dynamics of such extended models are still unexplored. In the direction of spin anisotropies, the effect of DM interactions remain somewhat mysterious on square-lattice geometries; available studies concern spin ladders [172], tetramer systems with pyrochlore geometry [82], and coupled chains treated by the simplification of staggered magnetic fields [173]. Recent numerical work has explored some of the parameter space for frustrated square lattices with exchange anisotropies [174].

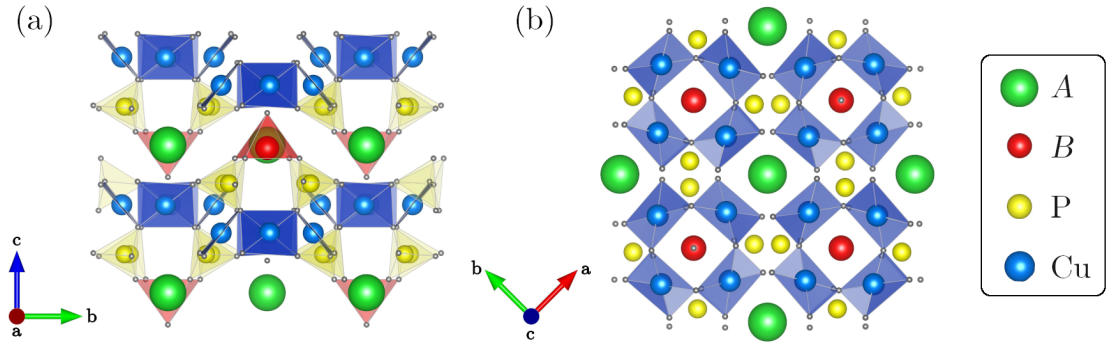


Figure 5.2 – **Schematic representation of the structure of  $A(\text{BO})\text{Cu}_4(\text{PO}_4)_4$** , showing Cu (blue), A (green), B (red), P (yellow), and O (grey) atoms with associated coordination polyhedra. (a) Projection on the  $ac$  plane, providing a side view of the buckled layers. (b) Projection on the  $ab$  plane of the layers, highlighting the square cupola structures as four  $\text{CuO}_4$  squares (blue) connected around a B atom.

Due to its crystallographic structure and bulk magnetic properties, which I will not describe here in detail [see Fig. 5.2 and Sec. 4.1.1], the chiral quantum magnet family  $A(\text{BO})\text{Cu}_4(\text{PO}_4)_4$  forms an ideal proving ground to experimentally study how the excitation spectrum of the extended square lattice evolves throughout the evolution of

the composition series, which can be associated to the ratio between intra- ( $J$ ) and inter- ( $J'$ ) tetramer interactions, as well as the effects of the strong anisotropic gap on the excitation spectrum.

## **5.2 Excitation spectrum of $Ba(TiO)Cu_4(PO_4)_4$**

A first attempt to extract the magnetic exchange parameters has been made on the basis of *ab initio* calculations [138, 150], combined with fitting the high-field magnetisation response for different field directions to a cluster mean field (CMF) approximation [131, 152]. These studies suggest a model with dominant intra-plaquette interactions and a strong DM vector, and provide a good description of the strong magnetoelectric effect. However, despite their success in accounting for the static properties, the proposed interaction parameters do not provide an accurate account of the spin dynamics measured on a powder sample [138]. Indeed, the latter corresponds to an intensity average over constant  $|Q|$  values, and thus does not provide an accurate representation of the excitation spectrum, especially in a region where several modes interfere. The next step is naturally to study the dynamics of this compound with inelastic neutron scattering measurements on a single crystal, in order to extract an accurate set of parameters that describe the magnetic interactions in the system. I performed two distinctive set of measurements on the same sample. In the first, I probe the excitation spectrum at zero magnetic field, which provides data for the extraction of the isotropic exchange parameters in a large part of the reciprocal space. In the second, I include a vertical magnetic field to a TAS setup in order to be able to fine-tune the direction of the DM interactions, build a qualitative understanding of the magnetic excitations, and of course confirm the accuracy of the aforementioned set of magnetic interactions. The results reported in this section were sent for review to PRB, and only minor adjustments have been made to the text.

### 5.2.1 Experimental setups

To probe the dynamics of Ba(TiO)Cu<sub>4</sub>(PO<sub>4</sub>)<sub>4</sub>, three single crystals were grown by the flux method [130], with a total mass of 3.3 g. They were co-aligned on an Al holder to a precision of less than 1° in the (*hk*0) scattering plane using Laue x-ray diffractometry, as shown in Fig. 5.3. The spin dynamics at zero magnetic field were measured on the direct-geometry time-of-flight neutron spectrometer IN5 [175] whose functioning has been explained in Chapter 2. I measured the excitation spectrum at three different temperature to account for systematic errors and background : at 1.5 K in the ordered phase, at 10 K just above  $T_N$ , and deep in the paramagnetic phase at 30 K. Inelastic data were collected by rotating the sample around its *c* axis by a total of 138°, in steps of 1°. Counting times were 20 minutes per angular step at 1.5 K and 30 K, and 13 minutes per step at 10 K, for a total measurement time of 46 hours. I oriented the crystals in order to maximise the accessible range in the (*hk*0) scattering plane, and such that scattering in the orthogonal direction could be measured using the opening of the orange cryostat. The incident energy was set to  $E_i = 7.08$  meV, resulting in a resolution of 0.25 meV (FWHM). I took advantage of the tetragonal symmetry of (Ba; Ti) by summing the intensities from detection pixels corresponding to  $Q$  points that are equivalent under crystal symmetry operations of the point group ( $4/m\bar{m}$ ). Due to the non-dispersive behaviour of the excitations along  $[0, 0, l]$ , I integrated the data over  $\pm 0.6$  in  $l$  for higher statistics. The ToF data were processed exclusively using the Horace software suite [176]. In both experiments, the intensity  $I(Q, \omega)$  measured at each wave-vector transfer  $Q$  and energy transfer  $\omega$  is directly proportional to the dynamic structure factor,  $S(Q, \omega)$ , convolved with a Gaussian distribution that accounts for the finite measurement resolution of the spectrometers.

I probed the spin dynamics of (Ba; Ti) in a magnetic field on the IN12 triple axis spectrometer at ILL [177]. For a direct comparison of both experiments, I used the same crystal as for the zero field experiment, shown in Fig. 5.3. All measurements were made at a base temperature of 2 K, in the antiferromagnetic phase. In order to maximise the resolution, the final wave vector was fixed to  $k_f = 1.3 \text{ \AA}^{-1}$ , giving a resolution of 0.172(5) meV (FWHM). An 80 mm collimator was placed between the monochromator and the sample; the monochromator had both horizontal and vertical focusing, while the analyser was horizontally focused only. The sample was inserted in a 10 T vertical cryomagnet, in which data were collected at field values up to 5 T in 1 T steps. The counting time was 2 minutes per  $(Q, \omega)$  point.

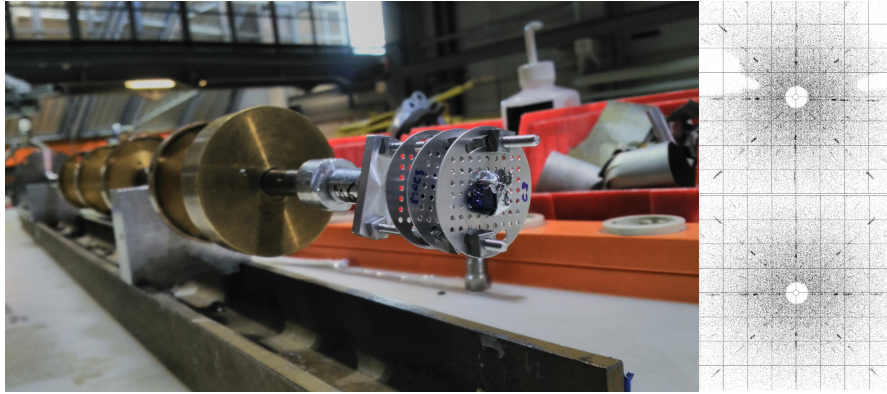


Figure 5.3 – **Co-alignment of three single crystals of (Ba; Ti)** with a total mass of 3.3 g. (left) Sample before insertion in the IN5 spectrometer. (right) Laue diffraction patterns of two crystals, with the  $c$ -axis along the beam. The same sample was probed on IN12 in the field experiment.

### 5.2.2 Spin dynamics

#### Zero field measurements

In Figure 5.4, I report the scattering intensity  $I(\mathbf{Q}, \omega)$  at 2 K as colour maps of the magnetic excitations integrated over selected constant energy ranges at  $\mathbf{Q}$  values throughout the Brillouin zone (BZ). This format highlights the fact that the spectrum has the same fourfold symmetry as the atomic structure, as shown in Fig. 5.4(a), which justifies averaging the measured intensity and discussing a single quadrant in the remaining panels. Additionally, I comment that even though the dispersion relation  $\omega(\mathbf{Q})$  follows a periodic pattern, the intensity does not have the same periodicity, a difference that cannot be explained by the magnetic form factor  $f(\mathbf{Q})$ . As the energy is increased, Fig. 5.4(b) shows that gapped spin excitations appear first at the Bragg peak positions, at an energy of 1.13(3) meV. This branch shows a strong anisotropic dispersion for wave vectors across the BZ [Fig. 5.4(c)], and at approximately 3 meV they begin to merge while a different excitation branch also emerges at the zone centres [Fig. 5.4(d)]. In the energy range up to 4 meV, scattering contributions from several different branches disperse and merge, resulting in complicated patterns in  $\mathbf{Q}$  [Figs. 5.4(e) and 5.4(f)], but always retaining the same periodicity. Finally, above 4.4 meV one only finds weak remnant scattering [Fig. 5.4(g)].

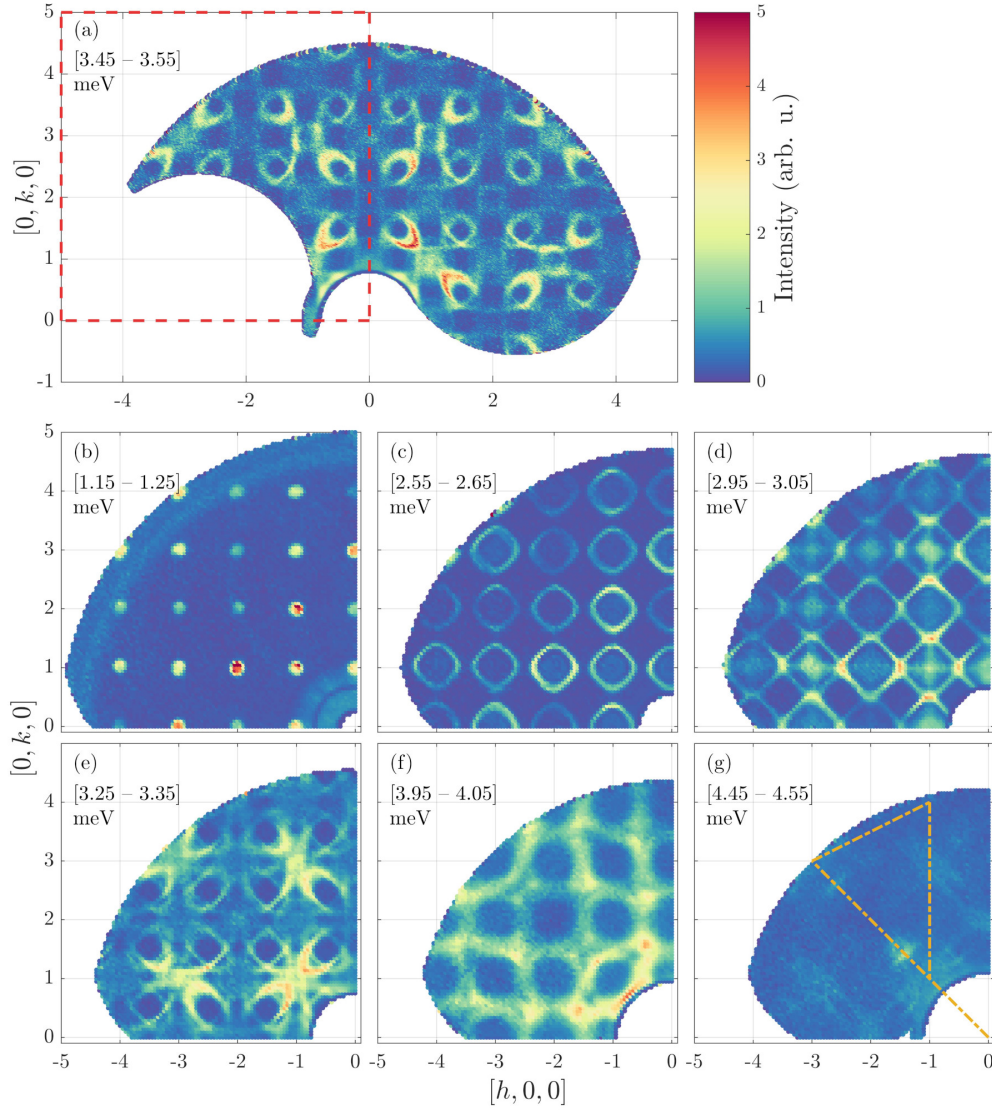


Figure 5.4 – **Mapping of the excitations at constant energies  $\omega$ .** The scattering intensity,  $I(\mathbf{Q}, \omega)$ , is integrated over different  $\omega$  ranges throughout the band width of the excitations and shown as a function of  $\mathbf{Q}$  in the  $(hk0)$  scattering plane. The measurement temperature is 2 K, the momentum step is  $dq = 0.01 \text{ \AA}^{-1}$ , and the energy integration range is indicated in each panel. (a) Unsymmetrised data across the full accessible Brillouin zone, highlighting the fourfold symmetry of the excitations in  $\mathbf{Q}$ . The dashed red box marks the second quadrant, to which the remaining panels should be referred. (b)-(g) Symmetrised data, folded onto the second quadrant, and shown for six selected energy ranges. Orange dashed lines in panel (g) represent the scattering directions reported in Fig. 5.6

An alternative representation of the magnetic excitations is given in Fig. 5.5, where I report the scattering intensity as a function of the energy transfer  $\omega$ , at different  $Q$  points along a single high-symmetry direction in reciprocal space. I observe the presence of multiple shark peaks with various intensities, all of which are well described by a Gaussian line shape, as red lines in Fig. 5.5 show. By extracting peak centres, width and intensities of the multi-Gaussian profiles, I am able to identify a maximum of seven different excitations in some parts of the BZ.

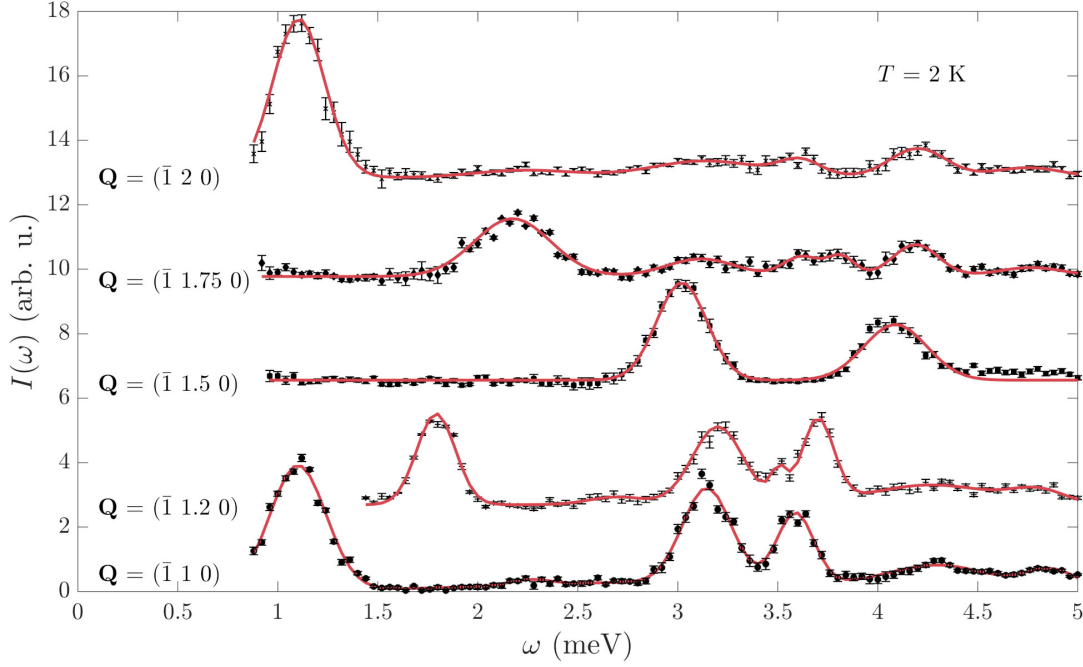
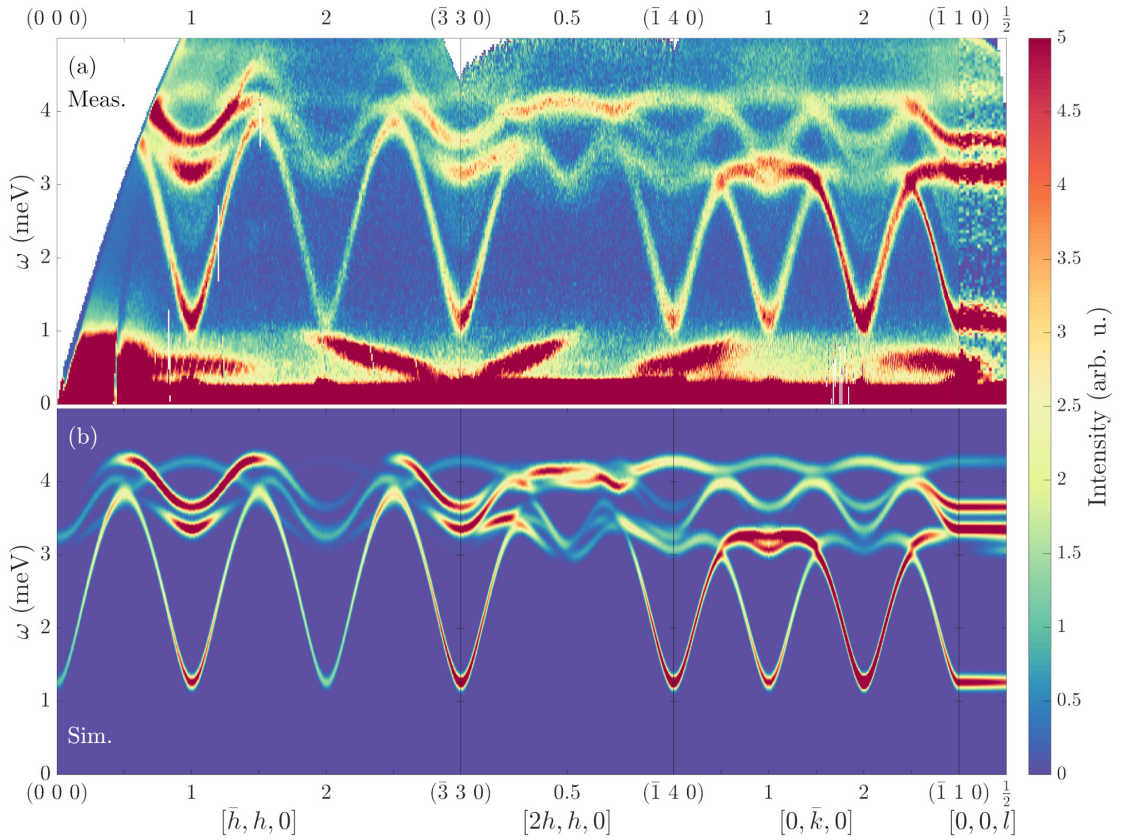


Figure 5.5 – **Constant  $Q$ ,  $\omega$ -scans.**  $I(Q, \omega)$  (black points) collected at 2 K for different  $Q$  points along the  $[\bar{1}, k, 0]$  direction and shown as a function of  $\omega$ . The red lines are an interpolated multi-Gaussian fit, from which the peak centres and widths were extracted.

The greatest advantage of ToF measurements is that they allow for a full mapping of the reciprocal space in only one long measurement by effectively collecting the neutron intensity for each  $(Q, \omega)$  point in the reciprocal space. Figure 5.6(a) collects this information to display the dynamic structure factor,  $S(Q, \omega)$ , along several different high-symmetry  $Q$ -space directions indicated in Fig. 5.4(g). The reported excitation spectrum is extremely rich, much more so than reported from previous studies [138], where it was thought that the spectrum was formed by a highly dispersive low-energy band, and an almost flat high-energy band. To describe the excitation spectrum, I begin by decomposing the observed excitations into three distinct regimes of energy, which I define on the basis of the  $[0, \bar{k}, 0]$  scattering direction (the third panel in Fig. 5.6). First, there is a robust gap,  $\Delta = 1.13(3)$  meV, at the BZ centre, which repeats along all measured directions. Second, a single, sharp excitation branch with a largely cosinusoidal dispersion is present at 1–3 meV, to which I refer henceforth as the low-



energy regime. At the BZ boundaries, this mode flattens in a manner reminiscent of a level-repulsion with the higher-energy excitations. The gradient with which the low-energy mode disperses around the Bragg-peak positions indicates the magnitude of the leading interaction, and the fact that this mode seems to have a periodicity of two BZs [Figs. 5.4 and 5.6] suggests that this interaction corresponds to a potential that covers half of the magnetic unit cell. Third, the high-energy regime at 3–4.5 meV contains three distinct and continuous modes, one of which merges into the low-energy mode at the lower edge of the energy window. I comment again that there are no well-defined magnetic excitations above the upper edge of the high-energy regime [Fig. 5.4(g)].



**Figure 5.6 – Excitation spectrum of (Ba; Ti).** (a) Measured dynamic structure factor,  $S(\mathbf{Q}, \omega)$ , shown along the four high-symmetry  $\mathbf{Q}$  directions indicated in Fig. 5.4(g). The step size in energy is  $dE = 0.04$  meV and in momentum it is  $dq = 0.01$   $\text{\AA}^{-1}$  in the scattering direction for  $\mathbf{Q}$  in the  $(hk0)$  plane and  $dq = 0.03$   $\text{\AA}^{-1}$  for  $\mathbf{Q}$  in the  $[0, 0, l]$  direction. The integration range in the orthogonal direction is  $\pm 0.06$   $\text{\AA}^{-1}$ . No smoothing effect has been added to the data. (b)  $S(\mathbf{Q}, \omega)$  modelled using a spin wave description of the dispersion convolved with Gaussian functions representing the spectrometer resolution.

I also report a number of subtle details in Fig. 5.6(a), which are important for different aspects of fitting the relevant interaction parameters. Above the low-energy mode one may discern the presence of an additional scattering feature with very low intensity; denoting the low-energy mode dispersion by  $E_1(\mathbf{Q})$ , this feature appears above  $E_{2\text{M}}(\mathbf{Q}) = E_1(\mathbf{Q}) + \Delta$ . This information identifies the feature as a two-magnon scattering continuum, which is sharpest at its lower boundary. I obtain further information to confirm this identification in Sec. 5.2.2. Importantly, I observe the splitting of the second most energetic mode at the zone centre, in the high-energy regime, which strongly supports the presence of the DM interactions and, together with the gap, provides the most accurate means of quantifying their strength. This feature at 3.2–3.5 meV is the most visible in the  $[0, k, 0]$  direction. In general the scattering intensity is strongest near the zone centres, and primarily in the low-energy regime, although a clear exception occurs in the second BZ, where the high-energy branches are equally intense. I comment on the particular distribution of scattering intensity along the  $[0, k, 0]$  direction, notably in the 3 meV region, which provides good comparison for a future fit. As expected from the crystallographic structure, where non-magnetic atoms lie between cupola layers [Fig. 5.2(a)], the magnetic excitations are only very weakly dispersive in the direction orthogonal to the magnetic layers [right panel of Fig. 5.6(a)], and thus I have chosen to integrate all of our scattered intensities over the range  $-0.6 < l < 0.6$  for better statistics.

### Vertical magnetic field

I now turn to the spin dynamics of the system in the presence of a magnetic field along the  $c$  axis, *i.e.*  $\mathbf{H}=(0,0,H_z)$ . I exploited the good resolution of a TAS in order to resolve the bands in energy. Physically, the effects of a magnetic field are reflected in an extra term  $\hat{\mathcal{H}}_m$  to the unperturbed Hamiltonian that I will present in Eq. 5.2 such that  $\hat{\mathcal{H}}' = \hat{\mathcal{H}} + \hat{\mathcal{H}}_m$  and

$$\hat{\mathcal{H}}_m = -g\mu_B \sum_i \mathbf{H} \cdot \mathbf{S}_i, \quad (5.1)$$

where the  $g$ -factor is assumed to be isotropic, and  $\mu_B$  is the Bohr magneton. Aside from building a better understanding of the degeneracy of the modes at  $\mathbf{H} = 0$ , which usually split in the presence of  $H_z$ , I expect that including a vertical magnetic field will provide significant insight into the effect of the DM interaction, since  $[\hat{\mathcal{H}}_m, \mathcal{D}] \neq 0$  if the angle between these two is different than  $90^\circ$ , where  $\mathcal{D}$  is the DM Hamiltonian.

Figure 5.7 shows the evolution of the measured scattering intensities  $I(\omega)$ , represented as  $\omega$ -scans performed at constant- $\mathbf{Q} = (1\ 1\ 0)$ , for field values of 0, 1, 2, 3 and 5 T. The four modes observed at zero-field rapidly evolve and split. They are well-resolved at 5 T, represented by six clear peaks, all of which are well described by Gaussian profiles. The lowest two show clear separation into two modes of near equal intensity, which evolve symmetrically in energy with increasing field. Comparatively, the two modes at



higher-energy show a more complex evolution of their energies and intensities. Finally, the highest mode is observed as a wide hump of scattering intensity above 4 meV, which shifts upwards with field. The spectrum evolution also shows an additional feature in the form of a low-intensity excitation around 2.1 meV, which I previously identified as a continuum of two-magnon scattering processes. This magnetic feature is constant as a function of field, which strongly supports this hypothesis. Indeed, as mentioned in Chapter 3, two scattering events are associated with the creation of two spin waves with  $\Delta S^z = 1$  and  $-1$ , such that the effective excitation has  $\Delta S_{\text{tot}}^z = 0$  and therefore does not respond to an external magnetic field. Furthermore, I comment that a weak scattering continuum emerges above this peak. However, I did not quantify it in the frame of this study.

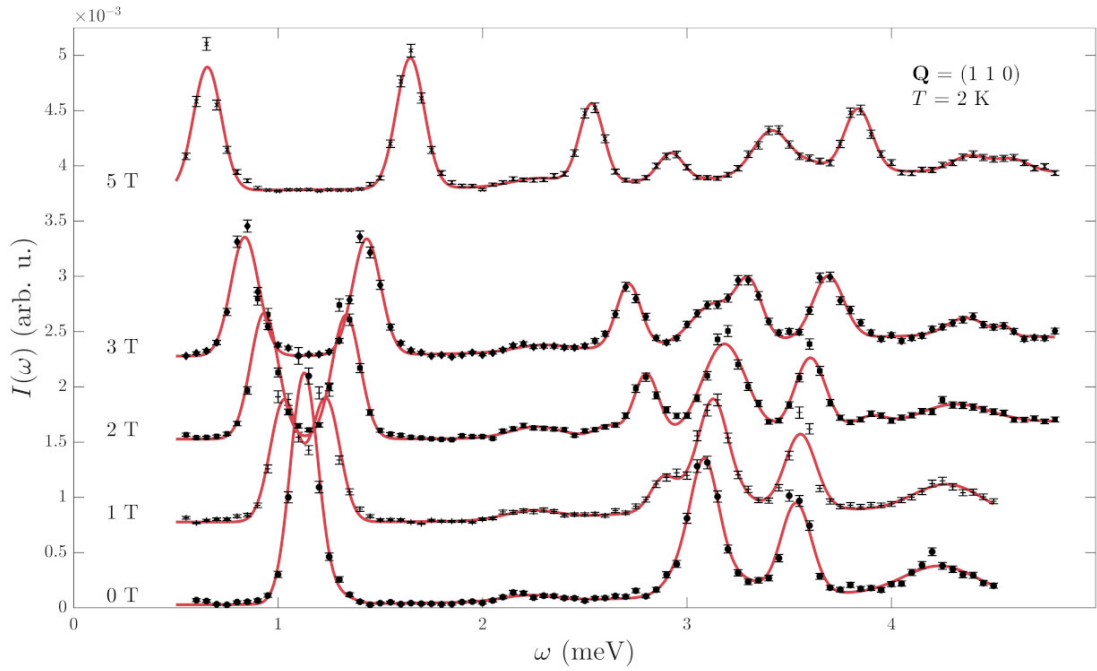


Figure 5.7 – **Scattering intensity**  $I(\omega)$  represented as  $\omega$ -scans measured at  $Q = (1\ 1\ 0)$ , normalised by the monitor counts, and for increasing values of the vertical magnetic field  $H$ . Black points denote measured intensities, and red lines correspond to fits to a multi-Gaussian model.

The field-induced evolution of the modes is alternatively represented in Fig. 5.8(a) as a colour map. A few comments can be made. I observe the clear presence of two different regimes in the field evolution. While the low-energy mode and the broad peak show a near-ideal field dependence, the peak in the intermediate region (2.5–4 meV) remains somewhat flat at low fields ( $H \lesssim 2$  T) before recovering a similar gradient. This separation into two regimes indicates their sensitivity to the in-plane (non-commuting) DM component ( $D_x$ ). However, the particular geometry of the DM interactions, pointing inwards/downwards in each plaquette, makes it difficult to relate the field scale with  $|D|$ . The gradients of the linear evolution beyond 2 T ruled by

Zeeman effects are similar to those of the lowest split excitations, whose peaks centres move by  $-0.09(3)$  meV/T and  $0.10(3)$  meV/T. These slopes are consistent with the value  $g\mu_B = 0.12$  meV/T expected from a spin-1 excitation.

The peak separation shown in Fig. 5.8(a) allows for a better understanding of the origin of the modes in the 2.5–4 meV regime. Of the two peaks apparent at  $H = 0$ , the one centred around 3 meV contains in fact three branches, whilst the one at 3.5 meV is a single mode. They are not degenerate at  $H = 0$  because of the DM interaction, which generates the  $\sim 0.5$  meV separation of the  $\Delta S^z = \pm 1$  branches.

The dynamic structure factor at 5 T is extracted from several  $\omega$ -scans of the type shown in Fig. 5.7, at different positions in the momentum space. I report in Fig. 5.8(b) the corresponding excitation spectrum in half of the BZ. These results verify that the effects of the field on each branch are the same at each  $Q$ . No additional splitting is observed with  $Q$ , indicating that  $[1, k, 0]$  has no special symmetries. I additionally note that the excitations show no evidence of avoided crossing at 5 T, associated with level mixing.

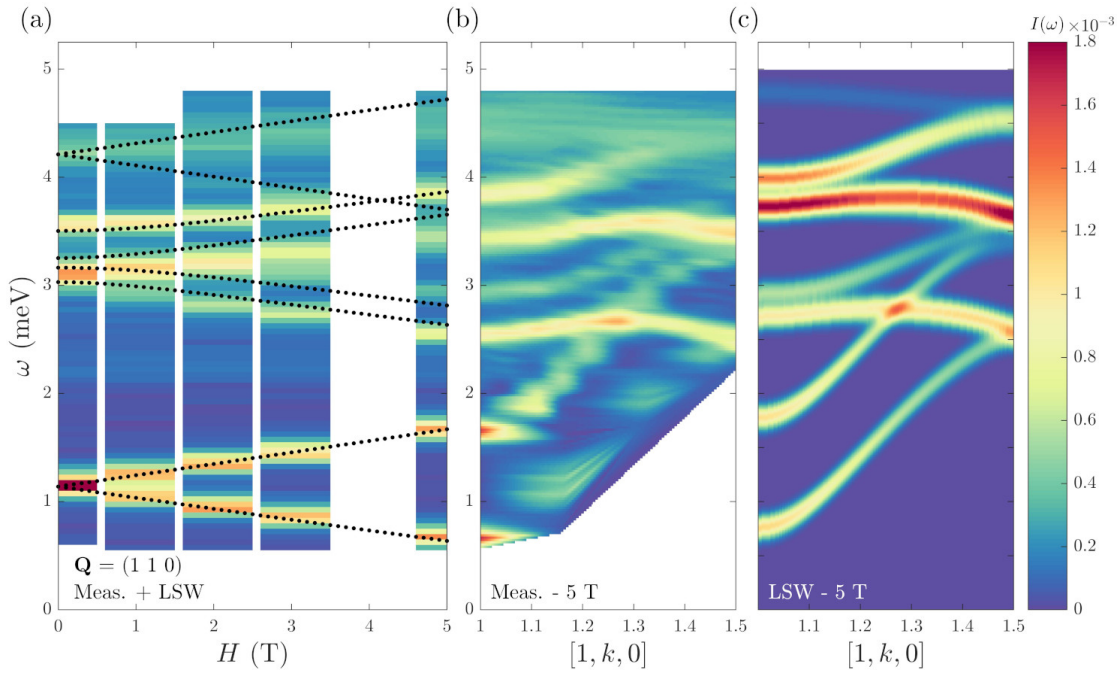


Figure 5.8 – (a) Measured scattering intensities  $I(Q, \omega)$  from Fig. 5.7, normalised by the monitor counts and presented as a colour map. Black dots denote the magnetic excitations extracted from LSW calculations based on the Hamiltonian 5.1 with the parameters from Table 5.1. (b) Measured and (c) modelled excitation spectrum in half a BZ, in the presence of a 5 T vertical magnetic field. For a better visualisation of the data, a linear interpolation has been applied on the measured data reported in panel (a).

### 5.2.3 Derivation of the magnetic Hamiltonian

To model the magnetic excitations, I propose a set of parameters that, when inserted in the following Hamiltonian, describes the dynamic structure factor of the system both in dispersion and in intensity:

$$\hat{\mathcal{H}} = \sum_{[i,j]_m} J_m \mathbf{S}_i \cdot \mathbf{S}_j - \sum_{\langle i,j \rangle} \mathbf{D}_{ij} \cdot (\mathbf{S}_i \wedge \mathbf{S}_j), \quad (5.2)$$

where  $[i, j]_m$  denotes a sum over relevant Cu–Cu bonds with Heisenberg interactions of strength  $J_m$ . From a previous neutron scattering study [138], I have identified the relevant magnetic interactions as those represented in Fig. 5.9(b), forming a 2D magnetic lattice. In addition, any understanding of (Ba; Ti) requires DM interactions, which are most likely to connect pairs of neighbouring Cu sites,  $\langle i, j \rangle$ , within each cupola. By standard structure and symmetry considerations, the DM vectors on the four cupola bonds [Fig. 5.9(c)] are perpendicular to the vector  $\mathbf{r}_i - \mathbf{r}_j$  connecting the two concerned Cu atoms, and are oriented at an angle  $\theta$  to the  $(ab)$  plane, as shown in Fig. 5.1(b). I comment that the DM vector can equivalently be described by  $(|D|, \theta)$ , or  $(D_x, D_z)$ , where  $x$  denotes the direction perpendicular to the aforementioned bond carrying the interaction  $J_1$ , in the  $ab$  plane, and  $z$  is parallel to  $c$ . The presence of a significant  $|D|$  and the importance of the angle  $\theta$  to a detailed understanding of the magnetic order was suggested in the early studies of Ref. [138]. The DM interaction naturally frustrates the Heisenberg interactions on each cupola and stabilises a highly non-collinear spin configuration, best understood as a two-in, two-out structure [Fig. 5.1], as explained in detail in Chapter 4.

In a material with a plaquette-like structure, as it the case for Ba(TiO)Cu<sub>4</sub>(PO<sub>4</sub>)<sub>4</sub>, [Fig. 5.9], there are *a priori* two separate possibilities for opening the observed gap : tetramerisation effects and a strong anisotropy of the form of the DM interaction. Motivated by the relatively large bandwidth of the low-energy excitation [Fig. 5.6(a)] and the parameters estimated on the basis of static measurements [131], I adopt the hypothesis that the system is not strongly tetramerised and that the gap will then arise primarily from the DM term. In addition, the robust ordered moment of (Ba; Ti) of  $\sim 0.8 \mu_B$  suggests that a semi-classical linear spin wave (LSW) theory should provide a good approximation in which to describe the magnetic order and excitations, and thus I employ the SpinW package [53] to extract the coupling strengths.

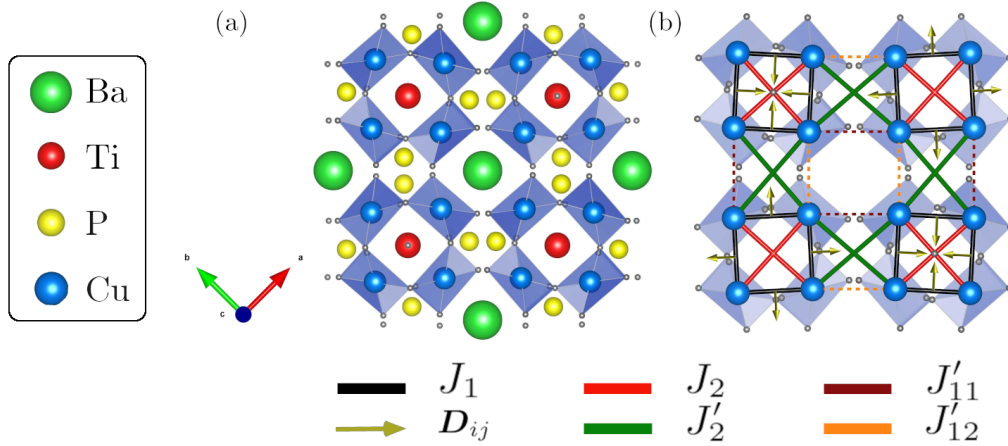


Figure 5.9 – **Magnetic lattice of  $Ba(TiO)Cu_4(PO_4)_4$** , similar to Fig. 5.2. (a) Projection of the nuclear structure on the  $(ab)$  plane. (b) Associated magnetic interactions, defined in Eq. 5.2. Another representation centred on the DM vector is given in Fig. 5.1.

The optimal parameter set is obtained by fitting only the measured dispersions throughout the BZ [Fig. 5.6(a)], with additional information taken from the finite-field dispersion [Fig. 5.8]. They are reported in Table 5.1, and the resulting magnetic lattice is shown in Fig. 5.9(c). The corresponding ordered ground state is very similar to that deduced from SNP measurements [129], with the Cu spins oriented almost normal to the  $CuO_4$  squares and forming a canted *two-in-two-out* arrangement on each cupola. A direct comparison of the elevation angles gives  $45^\circ$  for the SNP extracted ground state [Chapter 4, Fig. 5.1], and  $63^\circ$  for the ground state obtained with the LSW approximation. Thus, two neighbouring spins have a mutual angle of  $37^\circ$  according to LSW. I comment based on Table 5.1 that given the relative values of the Heisenberg couplings, which favour a collinear alignment, and those of the DM interaction, which favours an orthogonal spin configuration, the value of  $37^\circ$  is consistent. Once again, the accurate LSW description confirms the initial hypothesis that the system is weakly tetramerised. The excitation spectrum produced with these model parameters is shown at zero field in Fig. 5.6(b), and in a finite magnetic field in Figs. 5.8(a) and 5.8(c). It is clear that all the primary features of the measured bands are captured with quantitative accuracy in both cases, even though LSW slightly overestimates the gradient of the most energetic mode, in its linear regime [Fig. 5.8(a)]. A strong confirmation of this parameter set is provided by the fact that the scattered intensities are very well reproduced with no further fitting. The level of the remaining discrepancies is extremely small, and concerns mostly details of (anti-)crossing events between rather flat modes in the high-energy regime, although some of these may be a consequence of only low intensities. A small amount of discrepancies is of course expected because of a semi-classical description of a  $S = 1/2$  spin system. I note in particular that the feature  $E_{2M}(Q)$  with onset around 2 meV is not present in the fitted spectrum, consistent with the conclusion that it is not an elementary spin wave but a two-magnon scattering state.

## 5.2. Excitation spectrum of Ba(TiO)Cu<sub>4</sub>(PO<sub>4</sub>)<sub>4</sub>

Table 5.1 – Interaction parameters, in meV, used in the LSW description of the magnetic spectrum of Fig. 5.6. The geometry of these interactions is shown in Fig. 5.9(b) and the two components of the DM vector in Fig. 5.1(b).

$J_1$	$J_2$	$J'_2$	$J'_{11}$	$J'_{12}$	$D_x$	$D_z$	$ D $	$\theta$
2.03	0.52	2.22	0.17	0.17	1.05(3)	0.18	1.07(3)	10°

The Heisenberg interactions of Table 5.1 define a magnetic lattice of square antiferromagnetic plaquettes,  $J_1$ , with a small diagonal intra-plaquette  $J_2$  coupling generating rather weak frustration. The dominant inter-plaquette interaction linking the plaquettes in the  $ab$  plane is the crossed coupling,  $J'_2$ . Surprisingly, this interaction, being slightly stronger than the plaquette couplings, is the leading one in the system. Relatively, the plaquettes have a coupling twice as strong as the value that could be estimated on the basis of static measurements [131]. Finally, the structure of (Ba; Ti) requires two different  $J'_1$  bonds, which I label  $J'_{11}$  and  $J'_{12}$ , and these are similar in value but weak by comparison with  $J'_2$ .

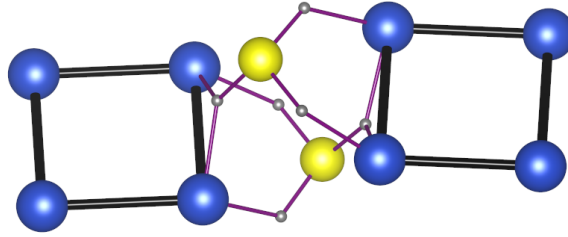


Figure 5.10 – **Illustration of the  $J'_{1i}$  and  $J'_2$  bonds.** Two neighbouring alternated plaquettes formed by Cu ions (blue) are connected by two pairs of both  $J'_{1i}$  (purple, "straight-") and  $J'_2$  (purple, "crossed-") bonds, which use the non-magnetic  $p$  orbitals of the P (yellow) and O (grey) atoms.

One further point of difference between the fitted parameters deduced from static and dynamic measurements emerges from these inter-plaquette  $J'_{11}$  and  $J'_{12}$  crossed-interactions. Two considerations can be made. First, in the spin wave spectrum, these are necessary for an accurate description of the separation between the low- and high-energy regimes, and my fitting quality quickly deteriorates when they are not equal and antiferromagnetic. By contrast, these two parameters were given opposite signs in fitting the magnetisation data [131], suggesting that smaller values in the global fit can be subject to large relative uncertainties. Secondly, one might be surprised by the large strength of the crossed bonds ( $J'_2$ ) with respect to the straight ones ( $J'_{11}$  and  $J'_{12}$ , denoted as  $J'_{1i}$  in the following paragraph). This can be explained structurally in terms of Cu–O–P–O–Cu superexchange paths, which are both represented in Fig. 5.10. Interestingly, the only difference between these interactions comes from the last P–O–

Cu path, which leads to two comments. First, the absence of direct straight Cu-O-Cu exchange path naturally explains the low value of  $J'_{1i}$ . Secondly, due to the shape of the  $p$  orbital, the superexchange path connecting two opposing Cu ions ( $J'_2$ ) is overall rather direct (or *straight*, ironically) with  $\sim 180^\circ$  angles, whereas it forms a  $\sim 90^\circ$  angle in the case of straight bonds ( $J'_{1i}$ ). Additionally, any set of parameters with these two parameter values inverted did not provide a satisfying description of the system at all.

The other strong interaction in Table 5.1 is the DM term. For the sake of coherence with the rest of the thesis, it is represented in Table. 5.1 by both its vector components in the local coordinate system of a bond, such that  $\mathbf{D} = (D_x, 0, D_z)$ , and by its magnitude  $|\mathbf{D}|$  and elevation angle, relative to the  $(ab)$  plane. Naturally, these coordinates systems are related by  $D_x = D \cos \theta$  and  $D_z = D \sin \theta$ . By symmetry, the vector  $\mathbf{D}_{ij}$  lies in the plane orthogonal to the Cu-Cu path of  $J_1$  and its direction alternates between all-in or all-out [Fig. 5.9(c)] with the upward or downward cupola orientation. On structural grounds one would expect this angle to take the value  $\theta_p = 14^\circ$  obtained for a single cupola bond from  $\mathbf{D}_{ij} \propto \mathbf{d}_i \times \mathbf{d}_j$ , where  $\mathbf{d}_i$  is the bond vector connecting two Cu site at positions  $\mathbf{r}_{i,j}$  to the O atom shared by their  $CuO_4$  squares [Fig. 5.1]. My result  $\theta = 10^\circ$  being consistent with this value, which recall does not depend on quantum effect, once again confirm the accuracy of the calculation. The strong  $J'_2$  interaction means that the origin of the gap must lie in the DM term, and thus it is no surprise to find a large magnitude,  $|\mathbf{D}|$ , which is also required to reproduce some of the mode separations in the high-energy regime reported in Fig. 5.6. The direction of the DM vector is also a key parameter in the fitting process, because its in- and out-of-plane components have quite different effects on the eigenstates of the Heisenberg terms in Eq. 5.2.

Describing the data with these couplings ended up being a rather tedious task because of the high number of independent parameters, as well as the high sensitivity of some features to these variables. However, the quantity best described is the gap, mostly due to the DM interaction. In Fig. 5.11, I report the difference between the measured gap  $\Delta_m = 1.13(3)$  meV and the gap extracted from LSW calculation, with the other parameters set to the values reported in Table. 5.1. At low angles, the size of a gap does not depend strongly on the  $D_z$  component until  $D_z \sim 0.8$  meV, but sets some strict boundaries for the  $D_x$  component, such that  $D_x = 1.05(3)$  meV. The second strongest signature of the DM interaction comes from the splitting of the high-energy regime, especially along the  $[0, \bar{k}, 0]$  direction. It opens the gap between the 3.5 meV and 3.2 meV excitations (at the zone centre), which would merge and form only one without it. However, the strongest effect of the  $D_z$  component emerges in a magnetic field. Indeed, I observed in LSW calculations similar to Fig. 5.8 that the 2.5 meV mode splits for values of  $D_z$  greater than 0.18 meV, which sets an upper limit for this quantity.

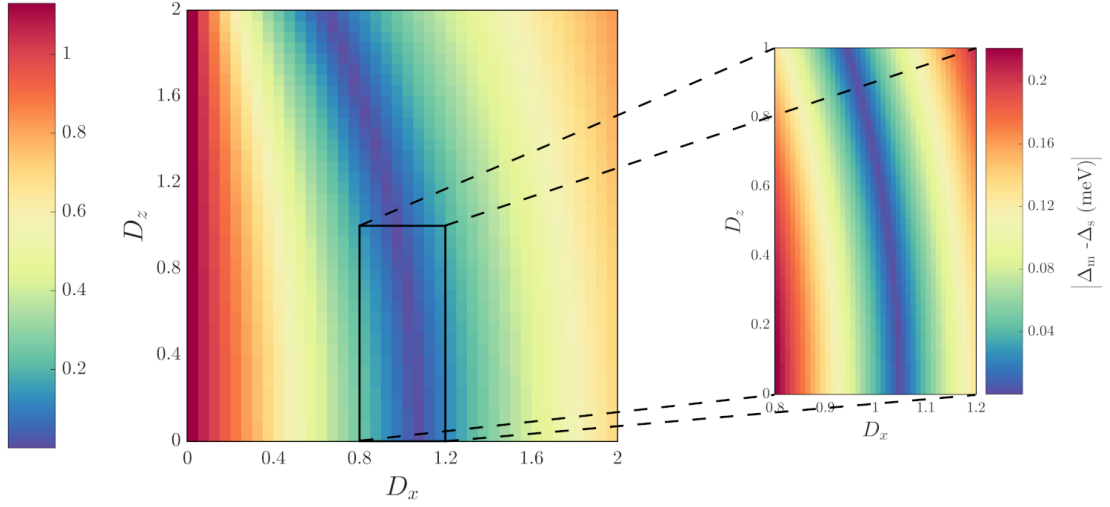


Figure 5.11 – **Evolution of the gap with the DM.** Difference, in absolute value, between the measured  $\Delta_m$  and simulated  $\Delta_s$  gaps, in the frame of the LSW approximation. (inset) Close up on a smaller region in the parameter space, centred around the predicted value of the DM vector in (Ba; Ti).

Finally, I remark that a weak interlayer interaction,  $J_\perp$ , is required to ensure the observed antiferromagnetic order. In principle this parameter could be fitted from the very weakly dispersive behaviour of the low-energy mode for wave vectors orthogonal to the scattering plane. In the present experiment, geometrical and resolution factors were such that my data for the out-of-plane direction are of qualitative value only, and thus I did not attempt to include  $J_\perp$  in our fitting procedure. All of our observations are consistent with the order-of-magnitude estimate  $J_\perp \approx J_1/100$  proposed in previous studies.

#### 5.2.4 Comparison with high-field magnetisation measurements

The higher sensitivity of the dynamic excitations to the coupling parameters of the system allowed for a more accurate account of the magnetic interactions than was possible on the basis of static measurements, primarily of the high-field magnetisation, which were performed up to full saturation [131, 138] around 60 T. As a consistency check, the authors of the previous study repeated their cluster mean-field (CMF) analysis of the system with the derived parameters from Table. 5.1. The results are shown in Fig. 5.12.

The CMF modelled magnetisation curves are in semi-quantitative agreement with the measurements. Both highlight the presence of a field-induced phase transition at values  $B_c$ , where the gap closes, and a saturation at high-fields  $B_{\text{sat}}$ . Qualitatively, this saturation field appears to be overestimated by approximately 20 % with the



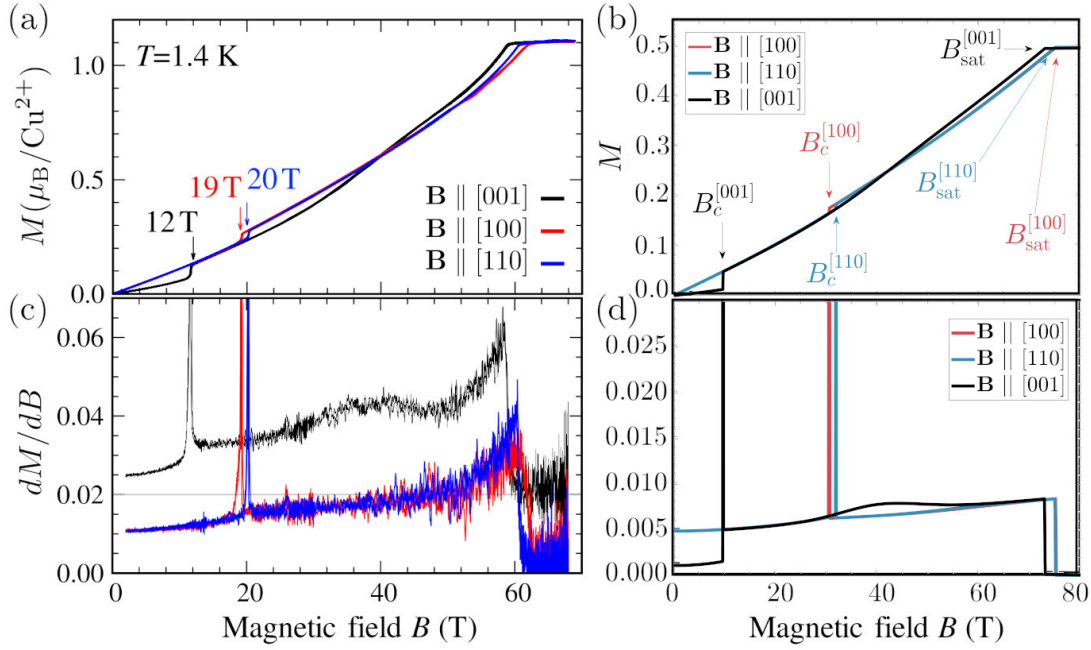


Figure 5.12 – **Magnetisation curves.** (a,b) Magnetisation curves  $M(B)$ , (a) measured and (b) obtained from a CMF analysis using the magnetic interaction parameters from Table 5.1, for magnetic fields applied in the three primary crystallographic directions of the tetragonal structure. (c,d) Magnetisation derivatives  $dM(B)/dB$ , which highlight the discontinuous features in  $M(B)$ . The calculated steps at different fields  $B_c$ , at which the gap is closed, and  $B_{\text{sat}}$ , where saturation is achieved, show semi-quantitative agreement with the measurements, and highlight the presence of two distinct magnetic phases. The left side panels are extracted from Ref. [131], with the permission of the authors.

set of parameters obtained from LSW calculations. However, this saturation field is proportional to the sum of all coupling parameters, which is known to be overestimated by a factor of 1.18 in a pure Heisenberg model described by the LSW theory [118]. This difference is a direct consequence of the fact that quantum corrections are not included in the LSW approximation, and I observe that a qualitative agreement in  $B_{\text{sat}}$  would be reached with the consideration of this correction.

However, an equally good description of the magnetisation curves was previously proposed with an interplaquette interaction  $J'_2$  twice as small, which raises the question of the uniqueness of the set of parameters. To gauge its variability, I comment that the two methods of analysis are intrinsically different. The CMD method assumes weakly coupled plaquette units, whereas LSW theory is based on robust magnetic long range order. However, my set of parameters describes rather well both the magnetisation curves and the excitation spectrum, whilst the previous one gives a poor account of the latter. This sets the parameters from Table 5.1 as the updated benchmark for (Ba; Ti).



### 5.2.5 Future dedicated work

The previous section demonstrates that (Ba; Ti) is well-described by a set of parameters indicating that the system is not strongly tetramerised. However, the intrinsic nature of the modes is not yet understood. I propose here a few directions for future investigation of these systems.

In order to build a deeper understanding of the spectrum, and motivated by the cluster behaviour of the DM interaction, I computed the excitation spectrum at the BZ centre in order to disregard the dispersive effects of the modes, obtained by the diagonalisation of a four sites plaquette with the interactions  $J_1$ ,  $J_2$  and  $D_{ij}$  taken from Table 5.1. The corresponding Hamiltonian reads:

$$\hat{\mathcal{H}}_p = J_1 \sum_{\langle i,j \rangle} \hat{\mathbf{S}}_i \cdot \hat{\mathbf{S}}_j + J_2 \sum_{\langle\langle i,j \rangle\rangle} \hat{\mathbf{S}}_i \cdot \hat{\mathbf{S}}_j - \sum_{\langle i,j \rangle} D_{ij} \cdot (\hat{\mathbf{S}}_i \wedge \hat{\mathbf{S}}_j) , \quad (5.3)$$

where  $\langle \dots \rangle$  denotes a sum over nearest-neighbours only (*e.g.* 1–2) and  $\langle\langle \dots \rangle\rangle$  represent opposite Cu sites (*e.g.* 1–3).

Figure 5.13 shows a direct comparison between the measured field evolution and the excitation spectrum of a four-site plaquette. I observe clear similarities between the two spectra in panels (a) and (b). First, the ED spectrum naturally shows the presence of three distinct energy regions formed by the lowest triplet, followed by the two remaining triplets and the singlet, and finally the high-energy quintuplet. Secondly, the field-induced dependence equivalently shows the presence of the linear (Zeeman) and DM dominated regimes. Interestingly, the triplet modes at 4 meV shows the longest flat regime, similar to what I measured. However, the persistence of this regime could also be due to the strong mode mixing occurring at these energies. I also remark that the DM interaction induces a large energy separation within each of the two intermediate triplet states. This induced gap is equivalent in magnitude to the measured one of  $\sim 0.5$  meV around 3 meV. A direct comparison would imply that the measured 3 meV region of Fig. 5.13(a) is not formed by a set of  $3 + 1$  branches as I claimed in Sec. 5.2.3, but rather by the  $2 + 2$  triplet states, each triplet being naturally split because of the DM interaction. Finally, the gradients of the triplets and  $\Delta S^z = \pm 1$  quintuplets are similar to those of the lowest measured excitation, with a value of  $0.09(2)$  meV/T.

It is tempting to conclude that my INS measurements probed the  $\Delta S^z = \pm 1$  excitations (two pairs of triplets, and one quintuplet) of (Ba; Ti). However, one should be cautious since it requires identification of the modes based on stronger arguments. Furthermore, this implies that  $\Delta S^z = 0$  processes are not probed by neutrons, which opposes the selection rules. Additionally, the alternated geometry of the DM vectors (pointing alternatively inwards and outwards of the plaquette) is not considered in this basic calculation and requires further work.

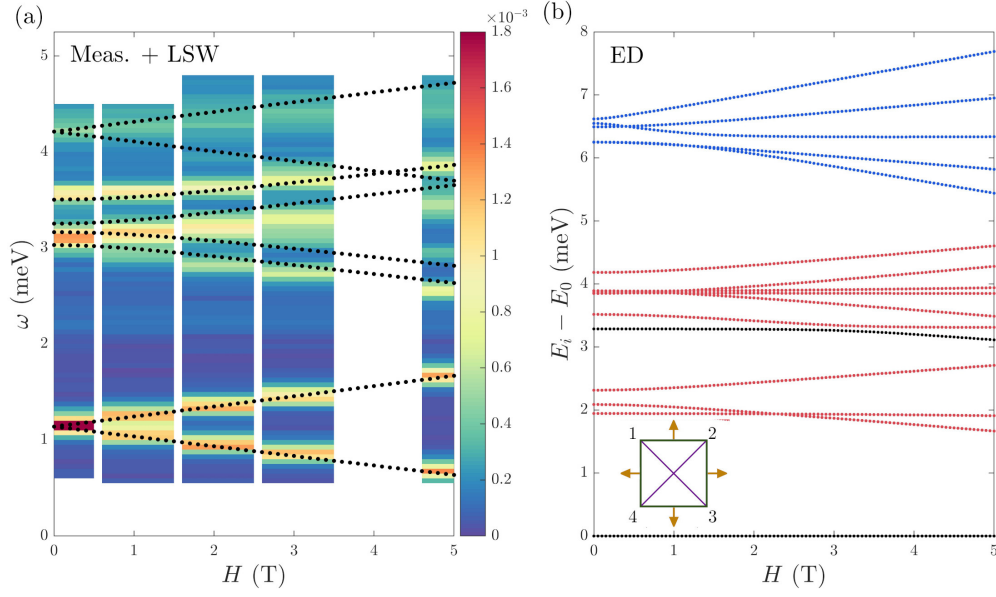


Figure 5.13 – **Comparison of the field-induced evolution of the branches.** (a) Field-induced evolution of the excitations, measured on (Ba; Ti). Same as Fig. 5.8(a). (b) Excited states of the four-sites plaquette unit sketched in the inset at  $Q = 0$ , extracted from an exact diagonalisation (ED) calculation of the Hamiltonian 5.3, with the values of  $J_1$  (green),  $J_2$  (purple) and  $D_{ij}$  (orange) taken from Table 5.1. Black lines represent singlet states  $|s\rangle$ , red ones are triplets  $|t\rangle$ , while blue lines denote quintuplet states  $|q\rangle$ .

Nevertheless, this introduces the next axis of research on which I started working in part. At the beginning of this chapter, I introduced the  $(A; B)$  family as an ideal playground to study the phase diagram of structurally gapped  $J$ – $J'$  plaquettised systems. It is now known that the isotropic  $J_1$ – $J'_1$  model has a quantum phase transition from a gapless magnetically ordered phase to a gapped singlet phase at  $\alpha_c = J'_1/J_1 \approx 0.55$  [165, 166]. Further effort has been put towards the theoretical understanding of plaquette phases [160, 178, 179] on the square lattice, but the presence of an extra anisotropy has not been considered yet. In gapped systems, the critical point  $\alpha_c$  is not as well defined and the question arises whether the gap emerges from an anisotropy, or has a quantum origin.

In similar fashion, future work will be dedicated to building a deeper understanding of the effects of the two-component DM interaction on the quantum states of the system, and of the excitation spectrum. Similarly to what has been done on the dimer system  $\text{Sr}_3\text{Ir}_2\text{O}_7$  [180], or on coupled tetrahedra systems [82], the goal is to build the phase diagram of gapped plaquettised systems based on (Ba; Ti), with a plaquette-operator theory. Indeed, this approach allows for a qualitative description of both the long range ordered and the tetramerised phases. The excitation spectrum derived from the Hamiltonian 5.3 will be used to define the elementary excitations in the frame of the plaquette-operator approach.

### 5.3 Qualitative description of $\text{Pb}(\text{TiO})\text{Cu}_4(\text{PO}_4)_4$

In the frame of this thesis, I also performed neutron scattering measurements on  $\text{Pb}(\text{TiO})\text{Cu}_4(\text{PO}_4)_4$ , both in the presence and absence of a vertical magnetic field. As Fig. 4.2 shows, (Pb; Ti) has a smaller chirality strength than (Ba; Ti), and I expect the magnetic interactions to vary accordingly. Prior neutron diffraction experiments [138] reported in Chapter 4 proved that this compound had an integer propagation wavevector  $\mathbf{k} = (0, 0, 1)$ . However, similarly to (Ba; Ti), I believe that the compound behaves as a 2D system, which means that the difference in the propagation wavevector should not have any influence on the magnetic excitation spectrum.

I comment that the analysis of the results reported in the rest of this section is ongoing. I will then give a qualitative description of the measured excitation spectrum and provide hints for any further investigation.

#### 5.3.1 Experimental setups

I report here the outcome of three experiments performed on different neutron spectrometers. I used the same crystal of 1.68 g for all experiments, oriented in different scattering planes.

In the first experiment, I used the triple axis spectrometer FLEXX (HZB) [181], with the outgoing wavevector  $k_f = 1.48 \text{ \AA}^{-1}$ . The sample was aligned in the  $(hk0)$  scattering plane on a x-ray Laue diffractometer, and set in a 14.8 vertical field cryomagnet. Each  $(\mathbf{Q}, \omega)$  point at 2 K has been measured for  $\sim 3$  minutes. The data were collected at field values up to 13.5 T, above the observed magnetic transition similar to the one shown in Fig. 5.12, in 2 T steps.

On the PANDA TAS (MLZ) [182], the crystal has been oriented in the  $(hhl)$  scattering plane in order to probe the direction orthogonal to the magnetic layers. A final wavevector  $k_f = 1.33 \text{ \AA}^{-1}$  has been used, and each point has been measured for 14 minutes. Both the analyser and monochromator had vertical focusing for higher resolution.

Finally, the same crystal has been set in the multiplexing spectrometer CAMEA (PSI) [42, 43] during its commissioning phase. To cover the full bandwidth of the excitations of  $\sim 4$  meV, I needed to use two different incoming energies given by  $k_i = 1.62 \text{ \AA}^{-1}$  ( $E_i = 5.5$  meV) and  $k_i = 1.85 \text{ \AA}^{-1}$  ( $E_i = 7.1$  meV). Various final energies were analysed simultaneously with wavevector from  $k_f = 1.24 \text{ \AA}^{-1}$  to  $k_f = 1.55 \text{ \AA}^{-1}$  (corresponding to energies from  $E_f = 3.2$  meV to  $E_f = 5$  meV), for an energy range of 1.8 meV. In order to have a full coverage of the reciprocal space, one must also account for dark angles between wedges, which requires the acquisition of A3 scans for different A4 values, which are  $4^\circ$  apart. For each  $(A4, E_i)$  configuration, four A3 scans were then performed from  $0^\circ$  to  $180^\circ$  in  $1^\circ$  steps, for a counting time of 2 minutes per point.

### 5.3.2 Excitation spectrum in zero field

I first report in Fig. 5.14 the results of the zero field experiment as  $\omega$ -scans along the  $[h, 1, 0]$  direction, as measured on FLEXX. Similarly to (Ba; Ti), I comment that the excitation spectrum can also be divided in three energy regions, showing the same behaviour even though its overall bandwidth is smaller than in (Ba; Ti), with no strong feature being observed above 3.5 meV. The observed anisotropy gap is slightly weaker too, with  $\Delta = 0.98(5)$  meV. The lower branch follows a cosinusoidal dispersion from 1 to 2.3 meV. At these energy values it seems to interfere with the high-energy regime, which is not as well defined than on (Ba; Ti), probably due to the lower statistics and to the resolution ellipsoid. Despite having to exclude some high-energy regions in my fit, I managed to extract a maximum of five distinctive Gaussian peaks per  $Q$ -point. As with its sister compound (Ba; Ti), I also comment on the presence of two-magnon scattering events, which are noticeable at the zone centres and at energies given by  $E_{2M}(Q) = E_1(Q) + \Delta$ . This feature appears to be stronger in intensity in (Pb; Ti) than in (Ba; Ti).

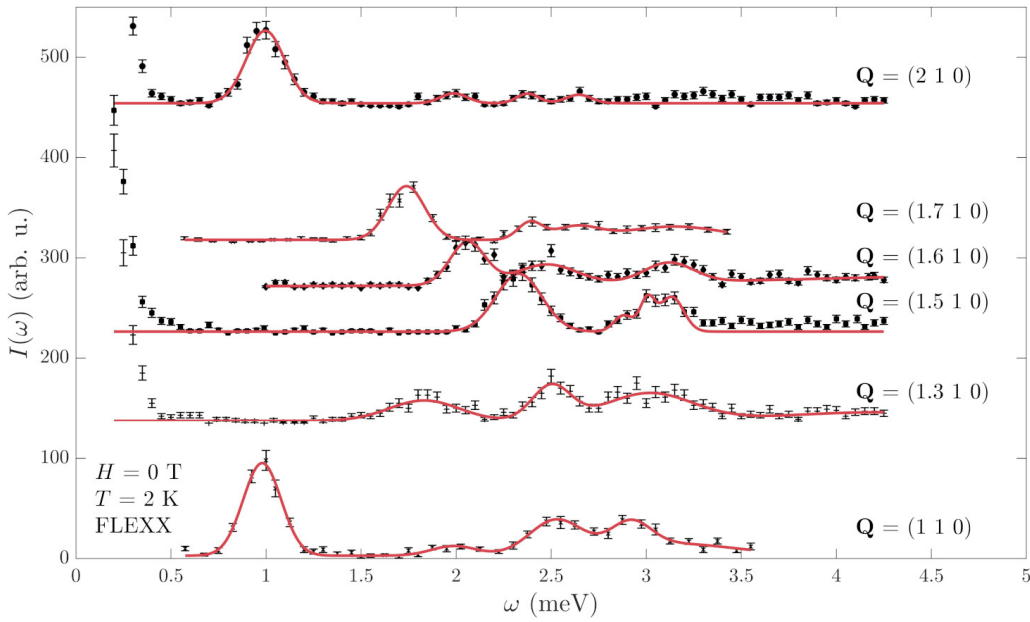


Figure 5.14 – **Constant  $Q$   $\omega$ -scans** measured on FLEXX, on a single crystal of (Pb; Ti). Black dots indicate measured points whilst the red lines represent multi-Gaussian fits to the data.

An alternative representation of the excitation spectrum, this time along the  $[h, h, 0]$  direction, is given in Fig. 5.15(a). It is the result of one of the first measurements performed on the multiplexing spectrometer CAMEA during its commissioning phase in November 2018. Figure 5.15(b) shows  $Q$ -scans taken at constant energy. At the time, numerical constraint did not allow for  $\omega$ -scans. However, excitations are well-resolved in the low-energy regime, while peaks tend to merge at higher energy.

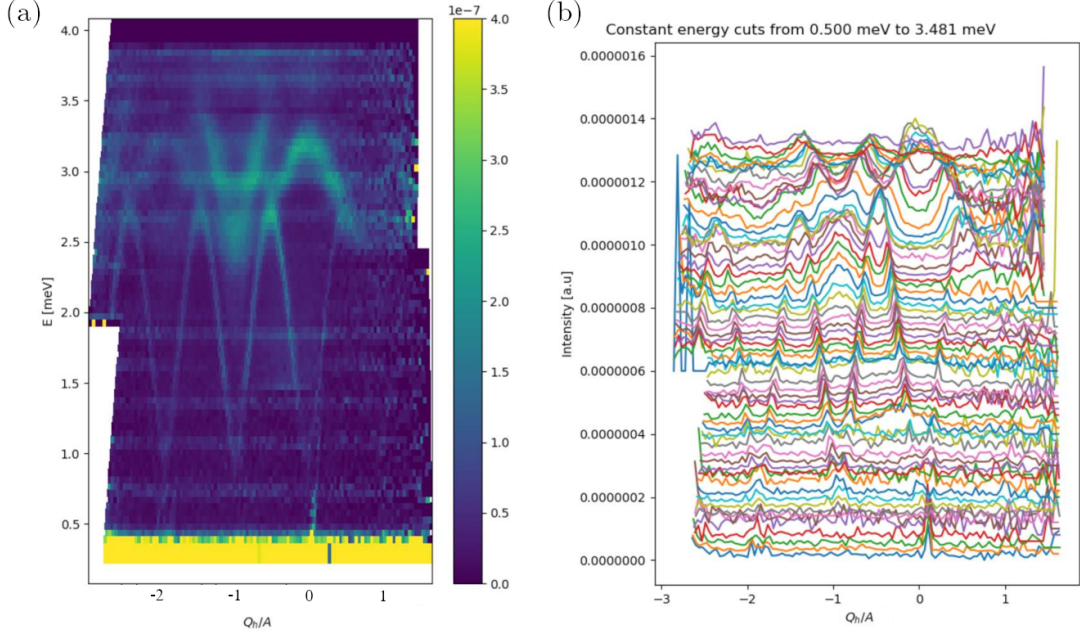


Figure 5.15 – **Results of the CAMEA experiment.** (a) Excitation spectrum of (Pb; Ti) along the  $[h, h, 0]$  direction, measured during the commissioning of the CAMEA (PSI) multiplex spectrometer with  $n_s = 8$ . This figure is the result of 48 h of counting time with two different incident energies  $E_i$ , and integrated over  $-1 < l < -0.35$ . (b)  $Q$ -scans for different values of energy transfer  $\omega$ .

The dynamic structure factor of Fig. 5.15(a) is to be compared with the first direction shown in Fig. 5.6, with  $|Q| \sim 0.98$  corresponding to  $Q = (1\ 1\ 0)$ . A few remarks can be made. First, as I mentioned previously, the energy of the system is downscaled with respect to (Ba; Ti). However, this rescaling is not uniform. Indeed, while the low-energy region is rescaled by a factor  $2/3$  ( $\Delta E = 2$  meV compared to  $\Delta E = 3$  meV), the high-energy regime is more dispersive in (Pb; Ti) than in its sister compound. This could be explained by a weaker leading interaction  $J'_2$ , and changes in the crossed inter-plaquettes terms  $J'_{11}$  and  $J'_{12}$ . However, since the chirality strength has no effect on a single plaquette, I do not expect  $J_1$  and  $J_2$  to vary much.

Secondly, while the intensity distribution does not seem to differ a lot around  $Q = (1\ 1\ 0)$  with two very intense modes between the two energy regimes, the high-energy region looks more intense than in (Ba; Ti) at  $Q = (0\ 0\ 0)$ . Once again, this implies a change in the inter-plaquette interactions, as expected from the nuclear structure shown in Fig. 5.2. Finally, I comment on the anisotropy gap that is weaker than predicted in (Ba; Ti) from LSW calculations, implying a weaker DM interaction. Another hint for it can be found in the  $\omega$ -scans shown in Fig. 5.14, where the modes in the high-energy region are not as well resolved as in (Ba; Ti). This is a direct consequence of a weaker mode splitting, as I explained in Sec. 5.2. Unfortunately, a more in-depth LSW analysis of (Pb; Ti) ended up being rather complicated, due to the low statistics in the high-energy

region. Since this regime is the most affected by structural changes, I believe that high-resolution and high-statistics data are necessary in order to push the analysis further. Additionally, I would recommend collecting data along other directions as well, since an accurate description of (Ba; Ti) would not have been possible without ToF data.

As a side note, I take the opportunity to comment on one of the biggest strength of this spectrometer : the prismatic concept [183]. Indeed, as can be seen in Fig. 5.16(a), the smaller the sample size, the smaller the divergence of the neutron beam that propagates through the instrument. This, with the neutron guide width and the dimension of the detector, defines a set of geometrical constraints denoted as distance collimation. It is known that a fine mosaicity in the analyser means the selection of a very narrow energy range at the cost of a weaker flux, while a coarse mosaicity selects a larger energy range in exchange for a poorer resolution. However, if the sample is small enough, the resulting resolution is not driven by the mosaicity of the analyser, but by the distance collimation [Fig. 5.16(b)]. Relaxing the mosaicity of the analyser then allows for a bigger neutron flux with no concession on the detector resolution. Additionally, CAMEA is constructed with a series of 1D detectors, which are position sensitive. Dividing them in  $n_s$  segments of  $1024/n_s$  pixels each is conceptually equivalent to placing  $n_s$  sub-detectors along the main one. It is then possible to study  $n_s$  times more transfer energies with no change on their resolution since it is governed by the detector distance collimation. As Fig. 5.15(a) shows with  $n_s = 8$ , the results are impressive and this new generation of spectrometers can easily compete with ToF instruments in the near future.

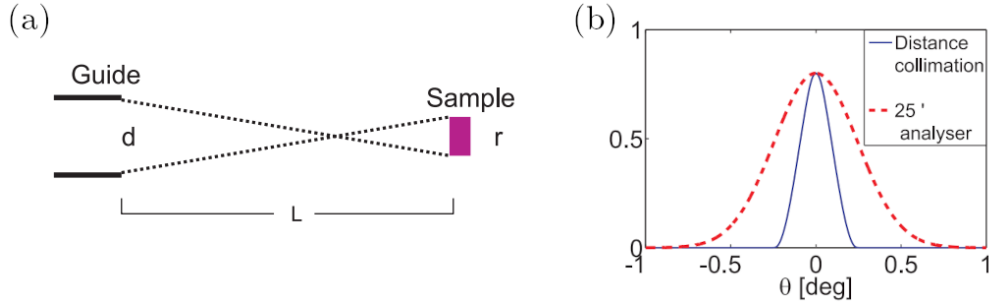


**Figure 5.16 – Resolution effects on CAMEA.** (a) Illustration of the dependence of the beam divergence on geometrical parameters. (b) Comparison of the resolution from distance collimation (blue, numerically calculated) and a typical PG(002) analyser mosaicity (25') (red) for the reference  $E_f = 5$  meV CAMEA analyser. Panels (a) and (b) are taken from [183].

I conclude the description of the zero-field measurements with a quick note on the interlayer dispersion, measured on PANDA. I tracked the value of the anisotropic gap along the  $[0, 0, l]$  direction, and reported the resulting dispersion in Fig. 5.17. A fit to the function  $\omega(q_l) = \sqrt{A^2 \sin^2(\pi q_l) + \Delta^2}$  gave a value for  $\Delta$  similar to that obtained from

FLEXX measurement. Furthermore, for 1D chains, the amplitude of the oscillation is given by  $\Delta\omega \sim 4J$ . In this particular case,  $\Delta\omega = 0.053$  meV which directly gives an interlayer interaction  $J_\perp \sim 0.01$  meV, akin to what has been predicted on (Ba; Ti).

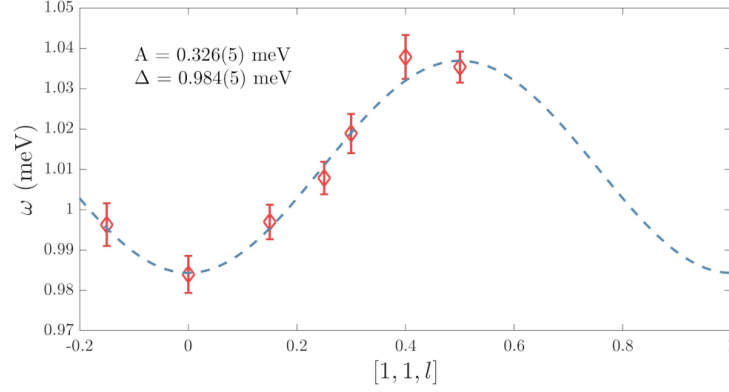


Figure 5.17 – **Dispersion along the interlayer direction.** First excited state (red) extracted from Gaussian fits to  $\omega$ -scans at different positions in reciprocal space, whereby the uncertainties correspond to statistical errors. Fit to the function  $\omega(q_l) = \sqrt{A^2 \sin^2(\pi q_l) + \Delta^2}$  (blue), with the extracted parameters shown in the legend.

### 5.3.3 Excitation spectrum in a vertical magnetic field

I report in Fig. 5.18 the results of  $\omega$ -scans measured on FLEXX at the zone centre and zone boundary for different values of the vertical magnetic field. A few comments can be made. First, this figure confirms that the field dependence of the modes is very similar to (Ba; Ti). However, the poorer resolution does not allow for a precise tracking of the excitations. At  $\mathbf{Q} = (1\ 1\ 0)$ , the two lowest modes have a slope of  $\alpha = -0.09(4)$  meV/T and  $0.08(3)$  meV/T, which is similar to the reported values on its sister compound  $[-0.09(3)$  and  $0.10(3)$  meV/T] and also consistent with spin-1 excitations. I observe the field-induced phase transition between 12 T and 13.5 T, which was predicted from susceptibility measurements at 12.2 T. This transition naturally emerges when the lowest-lying excitation becomes the most energetically favourable (*i.e.* when the field closes the gap). Assuming a purely linear response to the magnetic field with the slope  $\alpha$  defined above, a 12.2 T field transition would correspond to a  $\Delta_H = 1.1(5)$  meV gap. This value gives an indication of the influence of the DM interaction on the low-field dynamics of the system, where the evolution of the excitations is not linear.



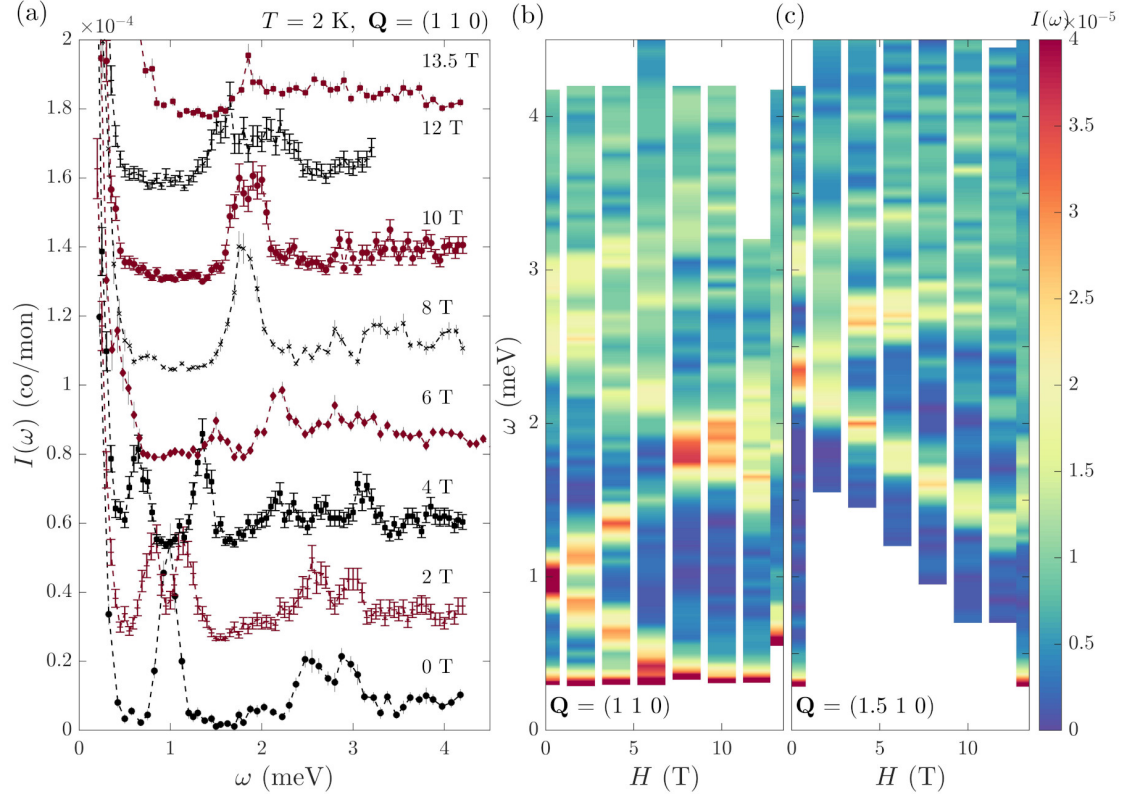


Figure 5.18 – **Field dependence of the magnetic excitations.** (a) Scattering intensity  $I(\omega)$  measured at  $Q = (1\ 1\ 0)$  and  $T = 2$  K, normalised by the monitor counts and for increasing values of the vertical magnetic field  $H$ . (b,c) Colour map representation produced from an assembly of  $\omega$ -scans, measured at (b)  $Q = (1\ 1\ 0)$  and (c)  $Q = (1.5\ 1\ 0)$ . The colour scale goes from blue (low intensity) to red (high intensity).

Unfortunately, the poor resolution of the modes in the high-energy regime does not allow for a more in-depth analysis of the excitation spectrum. However, this series of measurements provides qualitative insight on (Pb; Ti), which can be used in the future for a direct comparison with the excitation spectrum of (Ba; Ti). Additionally, the field dependence can be qualitatively compared with theoretical models such as four-site exact diagonalisation results similar to the ones derived on (Ba; Ti). However, I recommend to collect new high-resolution data in a field up to 6 T with 0.5 T step in order to perform a quantitative analysis of this system.



## 5.4 $\text{K}(\text{NbO})\text{Cu}_4(\text{PO}_4)_4$ as a strongly quantum system

The last member of the  $(A; B)$  that I briefly studied throughout my thesis is the non-chiral compound  $(\text{K}; \text{Nb})$ , which can be described by the space group  $P4/nmm$ . It is probably the most interesting member of the family, but technical difficulties encountered during the growth of single crystals made a consistent analysis of its dynamic properties extremely complicated. Specific heat measurements of  $(\text{K}; \text{Nb})$  report the presence of an ordered phase below  $T_N = 8.6$  K. However, unlike for  $(\text{Ba}, \text{Sr}, \text{Pb}; \text{Ti})$ , little entropy is released during the transition, as Fig. 5.19(a) shows. An upturn in the specific heat around 20 K is a signature of short range interactions. The entropy is then released at higher temperature, where it reaches a stable value of  $R \ln(2)$ , consistent with  $S = 1/2$  systems. It is thought that long-range antiferromagnetism is strongly suppressed and that the ground state of  $(\text{K}; \text{Nb})$  is then very close to a non-magnetic singlet state. Additionally, a Curie-Weiss temperature of  $\theta_{\text{CW}} = -61.5$  K was extracted from magnetic susceptibility curves (not shown here), which is much larger in magnitude than those for the other members [144].

Furthermore, unpublished powder diffraction results measured on D20 [Fig. 5.19(b)] and analysed by P. Babkevich suggested that the spin configuration of  $(\text{K}; \text{Nb})$  is different than the other compounds, with the spins lying approximately in the  $\text{CuO}_4$  plane. Additionally, magnetic peaks were indexed by the propagation vector  $\mathbf{k} = (0, 0, \frac{1}{2})$ . However, strong incoherent scattering from unknown origin has been observed, and the magnetic signal was extremely weak, such that a definitive magnetic structure could not be proposed from the data. On the other hand, the very weak magnetic scattering is a sign of a low ordered moment, which suggests much stronger quantum fluctuations in the system. This is consistent with the presence of a non-magnetic singlet ground state.

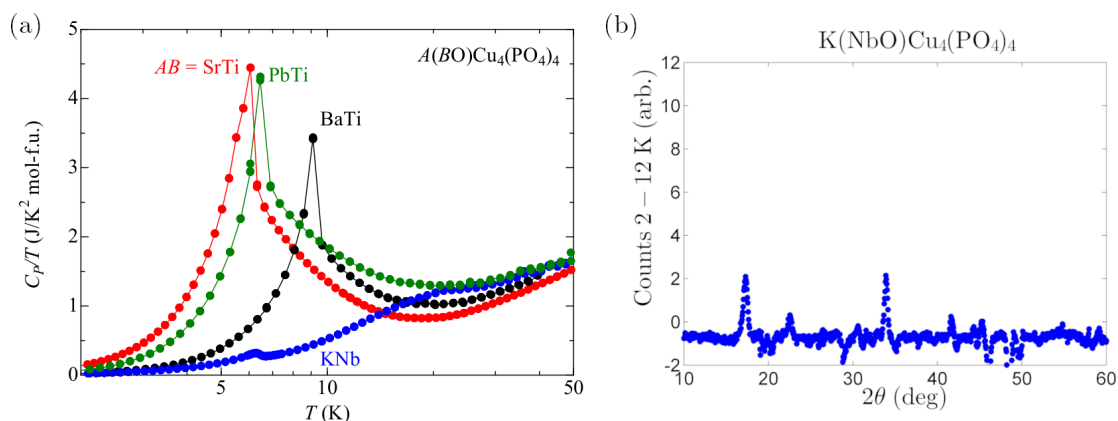


Figure 5.19 – **Previous measurements on  $(\text{K}; \text{Nb})$ .** (a) Specific heat curves of four sister compounds of the  $A(\text{BO})\text{Cu}_4(\text{PO}_4)_4$  family. (b) Magnetic powder neutron diffraction pattern. Data collected in the paramagnetic phase (12 K) has been subtracted from data measured in the ordered phase (at 2 K) to extract magnetic scattering events only.

### 5.4.1 Powder spectrum of (K; Nb)

I report here the first inelastic neutron measurements on (K; Nb), performed on a 5.3 g sample of powder on the ToF spectrometer LET (ISIS). Data have been collected at 1.8 K for 18 h, and for 7 h at 9 K, 30 K and 80 K. The multi-chopper setting at LET is designed to take several non-overlapping measurements from a single neutron pulse of 100 ms [184]. I thus collected data at incident energies  $E_i = 1.03, 1.77, 3.70$  and 12.14 meV. The aim of this experiment is to have a direct comparison with the powder spectrum of (Ba; Ti), previously measured on FOCUS (PSI).

The corresponding spectra are reported in Fig. 5.20. I start by reporting the presence of spurious signal in panels (a–c) emerging at  $|Q| \sim 2.75$  meV and likely due to Al scattering from the can. It should be disregarded in the analysis. As expected from 2D systems, panel (b) shows that some magnetic order is retained slightly above the transition temperature. However, the corresponding excitations vanish at 30 K. The magnetic excitations from panel (d) are extremely sharp and well defined, probably due to the tetragonal symmetry of (K; Nb). Similar to (Ba; Ti), it is composed of three regimes: namely the magnon gap  $\Delta = 0.96$  meV, the low-energy region and the high-energy region. Remarkably, the excitations bandwidth of (K; Nb) is much greater than those of its sister compounds (8 meV compared to  $\sim 4$  meV), as the large value of  $\theta_{CW}$  suggested. However, the gap value does not change accordingly. Measurements with  $E_i = 22$  meV indicated the absence of any magnetic excitation above 8 meV.

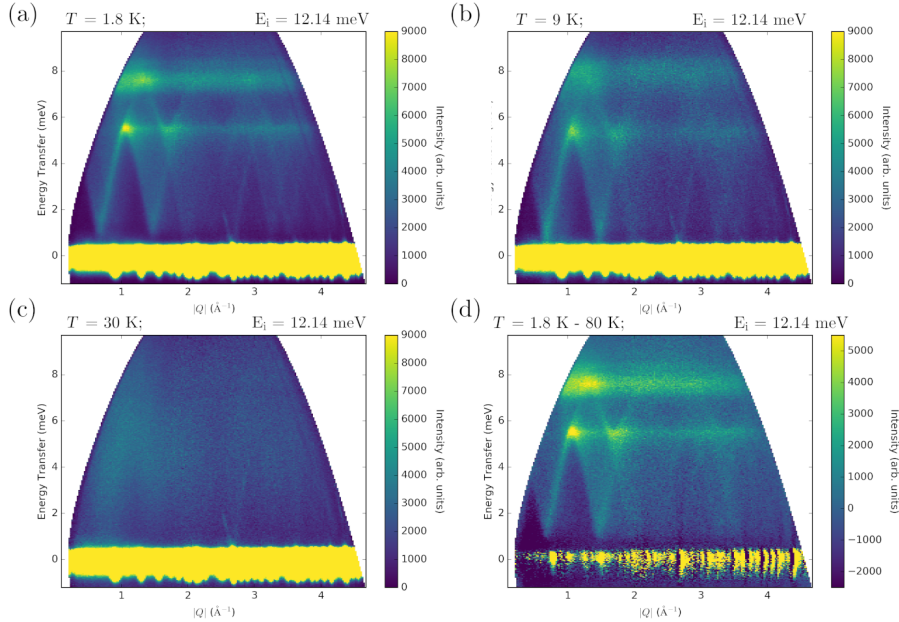


Figure 5.20 – **Powder excitation spectrum of (K; Nb)** (a) 2 K measurements with  $E_i = 12.14$  meV. The whole excitation range is captured. (b) Process repeated at 9 K. The excitations are still present, but are broader. (c) Repeated at 30 K. There is no longer sign of magnetic ordering. (d) Background subtraction

#### 5.4. $\text{K}(\text{NbO})\text{Cu}_4(\text{PO}_4)_4$ as a strongly quantum system

Figure 5.21 provides a direct comparison of the excitation spectrum with the one of (Ba; Ti) measured on FOCUS. As just mentioned, despite the difference in energy range, the overall structure of both spectra is similar. If I denote the first peak as  $P_1$  and the second as  $P_2$ , then their relative position is similar after deduction of the gap, as the first row of Table 5.2 shows. However, the spectral weight distribution differs slightly in two ways. First, in a similar manner, the ratio of intensities indicates that more scattering intensity is present in the low-energy regime of (K; Nb) than in (Ba; Ti), as the second row of Table 5.2 demonstrates. This is also clear from Figs. 5.21(c) and 5.21(d), which clearly show a difference in the scattering intensity in the  $0 - P_1$  region. Additionally, I report that the "intermediate" region between  $P_1$  and  $P_2$  is better defined in (K; Nb) than in (Ba; Ti). Indeed, it is clear from Fig. 5.21(c) that there is as much scattering intensity in this region than in the low-energy one, which results in a stronger decoupling between the low- and high-energy regions. A hypothesis is that this is a sign of a decoupling between two energy scales. The first one is associated to long range order, while the second is related to local effects. Finally, I conclude by noting the presence of three shoulders around the main peak  $P_2$  in the high-energy regime of (K; Nb), which were not observed in (Ba; Ti), perhaps because of the resolution of the instrument. Nevertheless, these peaks indicate that complex physics takes place at these energies.

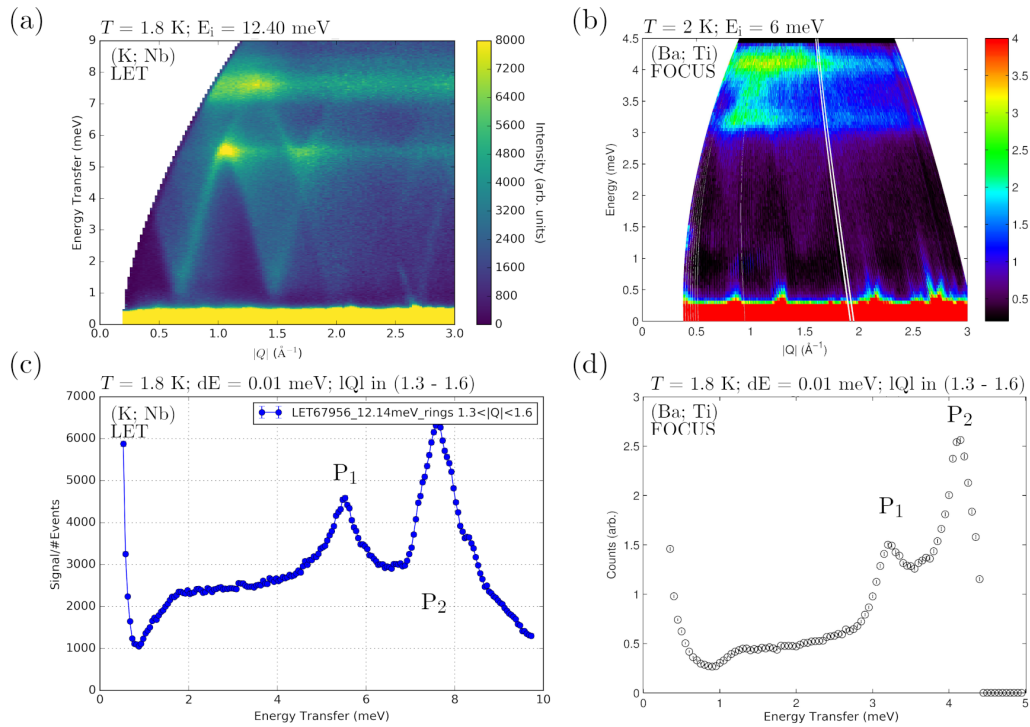


Figure 5.21 – **Direct comparison of (K; Nb) with (Ba; Ti).** (a–b) Powder spectrum of both compounds measured on the two different spectrometers. (c–d) Arbitrary cut through the data, integrated over  $1.3 < |Q| < 1.6$ , and with an energy step  $dE = 0.01$  meV

## Chapter 5. Variation on the square lattice – the $A(BO)Cu_4(PO_4)_4$ cupola family

Table 5.2 – Description of the two energy regimes, defined Fig. 5.21, in terms of amplitude  $I_i$  and centre position  $E_i$  of the peaks  $P_1$  and  $P_2$ .

	(Ba; Ti)	(K; Nb)
$E_2/E_1$	1.42	1.49
$I_2/I_1$	1.67	1.42

The last comment that I would like to make on the excitation spectrum concerns the gap at the zone centres. For this purpose, I report in Fig. 5.22 the spectrum collected with a lower incoming energy  $E_i = 3.70$  meV, which implies a higher resolution. From panel (b), I extract a precise value for the gap  $\Delta = 0.96(3)$  meV. However, I also report the presence of a second peak at  $E_1 = 1.43$  meV that was not observed in the spectrum of (Ba; Ti), nor measured in a powder sample or single crystal. This peak certainly corresponds to the minimal value of an excitation. A hypothesis is that the lowest excited states split in two, and that this mode splitting is reported in the powder data. Unfortunately, it is hard to reach any conclusion without more consistent data from single crystal measurements.

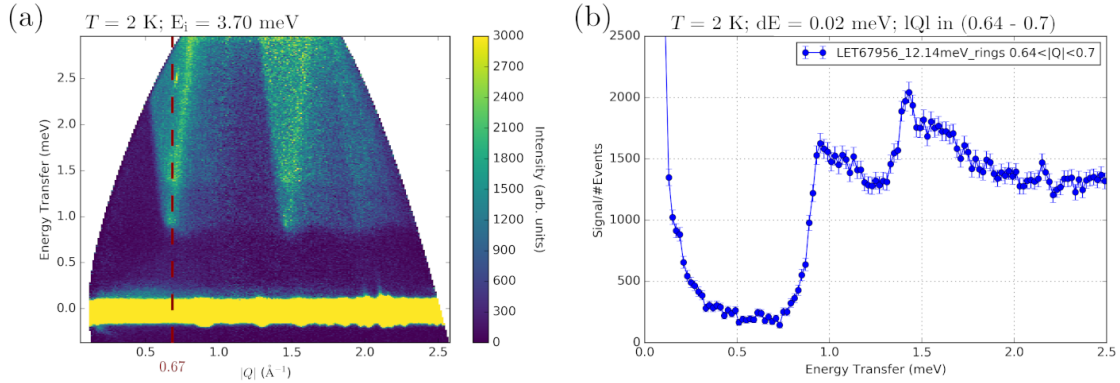


Figure 5.22 – **Focus on the gap.** The measurements were taken with a different incident energy,  $E_i = 3.70$  meV to reach a higher resolution. (a) Measured excitation spectrum. (b)  $\omega$ -scan at the zone centre corresponding to  $Q = (1\ 0\ 0)$  and equivalent reflections.

To conclude this section, I remark that although beautiful, the present data do now permit a precise refinement of the interaction parameters for two reasons. First, the measured powder spectrum as well as the knowledge of (Ba; Ti) that I have built throughout this thesis implies that the richness of the high-energy region provides essential features in order to verify the validity of a model. A precise refinement of the parameters is then only possible on the basis of single crystal measurements. Secondly, the weak magnetic moment as well as specific heat and susceptibility measurements indicate the presence of a quantum singlet ground state with short range interactions. Such a situation cannot be described by the LSW theory, which is intrinsically suited for the modelling of quasi-classical systems, but the aforementioned plaquette-bond approach should provide significant insight on the physics in this system.

## 5.5 Summary

In this chapter, I reported the outcome of extensive inelastic neutron scattering measurements on three members of the  $A(BO)Cu_4(PO_4)_4$  cupola family. I extracted the relevant interactions in (Ba; Ti) based on high-resolution measurements at zero-field, and from fits based on the LSW approximation. Based on their hierarchy, I describe the magnetic lattice as coupled ( $J'_2$ ), weakly tetramerised plaquettes ( $J_1$ ). Additional weak intra- ( $J_2$ ) and inter- ( $J'_{1i}$ ) plaquettes interactions were necessary in order to explain the high-energy dynamics of the system. The large observed gap then emerges from the symmetrically allowed DM interaction placed on each plaquette bond. Although an accurate determination of its magnitude could be performed based on zero-field data only, knowledge of the field-induced evolution of the excitations was necessary in order to extract a precise estimate of its direction.

The analysis of the INS measurement on (Pb; Ti) was somewhat more complicated both because of the lower resolution of the data, and the high number of coupling parameters in the system. However, its excitation spectrum revealed many similarities with (Ba; Ti), a clear sign that its interaction strengths only slightly differ from those of its sister compound. The smaller bandwidth implies a weaker leading interaction. The relative configuration of a plaquette being exactly the same as in (Ba; Ti), suggesting that  $J_1$  and  $J_2$  remain unchanged, the spectrum should then be well-described by a smaller  $J'_2$  coupling strength. On these grounds, I firmly believe that a precise estimate of the coupling strength in (Pb; Ti) could be extracted from extra high-resolution INS data.

The case of (K; Nb) is slightly different, and definitely more interesting. Unlike for its sister compounds, specific heat data show that only little entropy is released during the low-temperature phase transition, and that the entropy is mainly built around 20 K. This behaviour is a strong sign of short range interactions, which indicates that the ground state of (K; Nb) could be of quantum origin. First measurements of the powder spectrum revealed an overall similar spectrum, which I characterised, although its bandwidth is twice as large as those of (Ba, Pb; Ti).

All in all, the strongly 2D nature of the  $A(BO)Cu_4(PO_4)_4$  family of compounds, combined with the clearly resolvable effects of all the different interaction parameters, makes them excellent candidates for investigating quantum phases in tetramerised and gapped square-lattice models, which are yet still unexplored. For this purpose, we started building a plaquette-operator theory based on a four-site unit with DM interactions. The analysis is ongoing, but will certainly provide great insight on the influence of the DM on the  $J$ - $J'$  phase diagram, which is always gapped but not necessarily ordered, as well as on the nature of the measured excitations.



## 6 Conclusion and outlook

In this thesis, I investigated static and dynamic properties of two different classes of magnetic compounds using neutron scattering techniques and basic numerical methods. I present a complete overview of my results as well as some remarks for future work below.

The dynamics of the spin- $\frac{1}{2}$  antiferromagnet  $\text{SeCuO}_3$  exhibit really rich physics. Inelastic neutron scattering measurements revealed the presence of two distinctive energy scales in the system.  $\text{Cu}_1$  dimers are responsible for singlet to triplet transitions, whose presence could be tracked at temperatures up to  $\sim 110$  K. Long range order emerges on a second lattice formed by interacting  $\text{Cu}_2$  ions, resulting in the presence of spin waves well-described by the semi-classical linear spin wave approximation. I consequently described associated magnetic sublattice as chains coupled in three dimensions. However, despite the effective decoupling of these two sublattices due to the energy scale difference, clear evidence of an entangled behaviour are observed in the weak dispersion of the triplon excitations, as well as in the surprising superexchange path of one of the excitations necessary in order to accurately describe the low-energy dynamics of the system. I extracted an upper estimate for the value of this interlattices interaction from perturbative theory on a four sites clusters, which is of the same order of magnitude as the chain-like coupling. Furthermore, I commented on the presence of a high-energy scattering intensity continuum above the one-magnon band along all measured directions. Having ruled out the possibility of two-magnon scattering events due to the absence of a gap between the spin wave and the continuum, and especially because of the strong continuum intensity, I attributed its origin to the presence of spinon excitations. These fractionalised excitations correspond to deconfined magnons above their binding energy given by the one-magnon band. It is the first observation of spinons in a purely 3D magnetic system.

In my opinion, future work on this system should follow three distinctive axes. First, the quantitative description of the energy continua was limited by the experimental

cut-off at high energy. It is then necessary to map out the entire reciprocal space with time-of-flight measurements in order to provide accurate benchmarks for future comparison. Secondly, following recent work on 2D systems, this work reveals that the existence of spinon-like excitations is not restricted to 1D chains. It provides supplementary information on their existence, such as frustration which enhances the quantum behaviour of the system. Finally, the outcome of this project extends the concepts of collective quantum spin excitations in a new direction, and mandates further, and combined, theoretical treatment of systems where the excitations show such a high degree of entanglement.

I then used spherical neutron polarimetry to refine the magnetic structure of three members of the  $A(BO)Cu_4(PO_4)_4$  family, denoted as  $(A; B)$ . The analysis of the single chiral domain  $\mathbf{k} = (0, 0, \frac{1}{2})$  compound (Sr; Ti) was straightforward and confirmed the existence of a highly non-collinear *two-in–two-out* magnetic structure, as previously proposed based on neutron powder diffraction measurements.

The analysis of (Ba; Ti), which also has  $\mathbf{k} = (0, 0, \frac{1}{2})$ , was more complicated because of the coexistence of two structural chiral domains called *levo* and *dextro*, which are related by spatial inversion. Two similar *irreps* provided an equally good description of the SNP data. However, the magnetic structure was extracted from a combined SNP and ND analysis, where the direction of the moments was determined by the best fit to the SNP data for each *irrep* and the neutron diffraction pattern was described in term of the norm of the moments only. The refined magnetic structure also corresponds to a *two-in–two-out* spin arrangement on each cupola. Additionally, the presence of a strong Dzyaloshinskii-Moriya interaction expected from the observed large gap in powder inelastic neutron scattering measurements is consistent with this magnetic structure. Indeed, the small angle between the presumed DM vector and the vector orthogonal to two neighbouring spins is the smallest for the *two-in–two-out* structure. The DM interaction then plays an important role in stabilising this highly non-collinear order. For both these compounds, a careful analysis of the chiral components of the polarisation matrix was the key of the analysis. I finally explored the case of (Pb; Ti), where the propagation vector has integer Miller indices. This implies the presence of both nuclear and magnetic scattering events at the same positions. Unfortunately, the complexity of the system, coupled with strong nuclear magnetic interference terms made a complete analysis not possible.

Motivated by their crystallographic structure that made them good realisations of the two dimensional spin- $\frac{1}{2}$  antiferromagnet model on the square lattice, the last chapter of my thesis was dedicated to an extensive investigation of the excitations spectrum of three members of the aforementioned  $(A; B)$  family, measured by means of inelastic neutron scattering. Using the LSW approximation, I modelled (Ba; Ti) as a network of interacting plaquettes, with weak intraplaquette couplings. This system is conse-



---

quently weakly plaquettised and the large measured gap comes essentially from the DM interaction which I quantified both in magnitude and direction.

I performed a qualitative description of the dynamics of its sister compound (Pb; Ti), whose excitations spectrum reveals extremely similar features. Due to its smaller measured bandwidth, the leading interplaquette interaction is probably downscaled, while the intraplaquette ones should remain unchanged. An accurate determination of the coupling parameters was impossible to carry due to the poor resolution of the data coupled to the large number of parameters. My opinion is that the extraction of these values could be greatly simplified by another five days of experiment on a high-resolution triple-axis spectrometer, both with and without magnetic field, in which the excitations would be collected along two inequivalent scattering directions, as well as their field-induced evolution at the zone centre.

The highly-symmetric compound (K; Nb) shows really interesting physics. Specific heat measurements indicate that most of the entropy is not released during the low-temperature phase transition but emerges at slightly higher temperature. I performed the first measurements of its dynamic properties on a powder sample, which reveals neat spin waves that form a spectrum similar to those of the other members of the family. However, its bandwidth is approximately twice larger, which rises the question of the effects of the symmetry on the magnetic properties. The next step is naturally to measure the same excitation spectrum on large single crystals. However, its growth has proven to be challenging.

Finally, efforts towards a deep understanding of the excitations spectrum as well as of the influence of the vector DM on plaquette phases on the square lattice have been put with the development of a plaquette-bond approach to describe the magnetic system. This method will provide significant help in the investigation of systems where a gap is always present, but its origin could be attributed both to an anisotropy or to quantum effects.

What makes the beauty of research is when the description of systems, which are thought to be simple at first glance, reveals the existence of very interesting phenomena, and of new mysteries to be solved. This was the case of  $\text{SeCuO}_3$ , which will certainly motivate new theoretical and experimental treatments of multi-type excitations and spinons. Sometimes, research faces a dead end, in which case the most sensible choice is sometimes to give up as in the SNP analysis of (Pb; Ti). At other times, research takes a sudden turn in another direction, and requires the development of new methods. Who would have thought that the last weeks of my thesis would be devoted to building a theoretical approach on cluster systems? This unpredictability, and capacity to situate phenomena in a global context are, in my humble opinion, what makes science so exciting. These remaining thoughts, dear reader, put an end to this thesis.



# Bibliography

- [1] J. Needham and C. Ronan, *The Shorter Science and Civilisation in China: Volume 3*, Shorter Science and Civilisation in China (Cambridge University Press, 1978).
- [2] J. Maxwell and J. Thompson, *A Treatise on Electricity and Magnetism*, A Treatise on Electricity and Magnetism No. vol. 2 (Clarendon, 1904).
- [3] E. Snider, N. Dasenbrock-Gammon, R. McBride, M. Debessai, H. Vindana, K. Venkatasamy, K. V. Lawler, A. Salamat, and R. P. Dias, *Nature* **586**, 373 (2020).
- [4] G. E. Moore, *IEEE Solid-State Circuits Society Newsletter* **11**, 33 (2006).
- [5] C. Kittel, *Introduction to Solid State Physics*, 8th ed. (Wiley, 2004).
- [6] D. I. Khomskii, *Transition Metal Compounds* (Cambridge University Press, 2014).
- [7] S. Blundell, *Magnetism in Condensed Matter*, Oxford Master Series in Condensed Matter Physics (OUP Oxford, 2001).
- [8] N. W. Ashcroft and N. D. Mermin, *Solid State Physics* (Holt-Saunders, 1976).
- [9] C. Lacroix, P. Mendels, and F. Mila, *Introduction to Frustrated Magnetism: Materials, Experiments, Theory*, Springer Series in Solid-State Sciences (Springer Berlin Heidelberg, 2011).
- [10] N. D. Mermin and H. Wagner, *Phys. Rev. Lett.* **17**, 1133 (1966).
- [11] G. Gatti, D. Gosálbez-Martínez, S. S. Tsirkin, M. Fanciulli, M. Puppini, S. Polishchuk, S. Moser, L. Testa, E. Martino, S. Roth, P. Bugnon, L. Moreschini, A. Bostwick, C. Jozwiak, E. Rotenberg, G. Di Santo, L. Petaccia, I. Vobornik, J. Fujii, J. Wong, D. Jariwala, H. A. Atwater, H. M. Rønnow, M. Chergui, O. V. Yazyev, M. Grioni, and A. Crepaldi, *Phys. Rev. Lett.* **125**, 216402 (2020).
- [12] G. L. Squires, *Introduction to the Theory of Thermal Neutron Scattering*, 3rd ed. (Cambridge University Press, 2012).
- [13] S. W. Lovesey, *Theory of neutron scattering from condensed matter. Vol. 1. Nuclear scattering* (1984).

## Bibliography

---

- [14] Furrer, A. and Mesot, J. and Strässle, T., *Neutron Scattering in Condensed Matter Physics* (WORLD SCIENTIFIC, 2009) <https://www.worldscientific.com/doi/pdf/10.1142/4870> .
- [15] Chatterji, Tapan, *Neutron Scattering from Magnetic Materials* (2005).
- [16] G. Shirane, S. M. Shapiro, and J. M. Tranquada, *Neutron Scattering with a Triple-Axis Spectrometer: Basic Techniques* (Cambridge University Press, 2002).
- [17] E. Rutherford, Proceedings of the Royal Society of London. Series A, Containing Papers of a Mathematical and Physical Character **97**, 374 (1920), <https://royalsocietypublishing.org/doi/pdf/10.1098/rspa.1920.0040> .
- [18] W. Bothe and H. Becker, Zeitschrift für Physik **66**, 289 (1930).
- [19] H. Becker and W. Bothe, Zeitschrift für Physik **76**, 421 (1932).
- [20] J. Chadwick, Proceedings of the Royal Society of London. Series A, Containing Papers of a Mathematical and Physical Character **136**, 692 (1932), <https://royalsocietypublishing.org/doi/pdf/10.1098/rspa.1932.0112> .
- [21] E. Amaldi, E. Fermi, F. Rasetti, and E. Segrè, **11**, 442 (1934).
- [22] L. Meitner and O. R. Frisch, Nature **143**, 239 (1939).
- [23] C. G. Shull, W. A. Strauser, and E. O. Wollan, Phys. Rev. **83**, 333 (1951).
- [24] Néel, M. Louis, Ann. Phys. **12**, 137 (1948).
- [25] A. Fetter and J. Walecka, *Quantum Theory of Many-particle Systems*, Dover Books on Physics (Dover Publications, 2003).
- [26] V. F. Sears, Neutron News **3**, 26 (1992), <https://doi.org/10.1080/10448639208218770> .
- [27] P. Brown, J. Forsyth, and F. Tasset, Physica B: Condensed Matter **267-268**, 215 (1999).
- [28] H. B. Callen and T. A. Welton, Phys. Rev. **83**, 34 (1951).
- [29] L. Van Hove, Phys. Rev. **95**, 1374 (1954).
- [30] A. Corney, *Atomic and Laser Spectroscopy*, Oxford science publications (Clarendon Press, 1977).
- [31] M. Blume, Phys. Rev. **130**, 1670 (1963).
- [32] Y. Izyumov and S. V. Maleev, JETP **14**, 1168 (1962).

- 
- [33] F. Tasset, P. Brown, E. Lelièvre-Berna, T. Roberts, S. Pujol, J. Allibon, and E. Bourgeat-Lami, *Physica B: Condensed Matter* **267-268**, 69 (1999).
- [34] F. Tasset, *Physica B: Condensed Matter* **297**, 1 (2001), proceeding of the Third International Workshop on Polarised Neutrons.
- [35] P. Brown, in *Neutron Scattering from Magnetic Materials*, edited by T. Chatterji (Elsevier Science, Amsterdam, 2006) pp. 215 – 244.
- [36] M. J. Cooper and R. Nathans, *Acta Crystallographica* **23**, 357 (1967).
- [37] M. Popovici, *Acta Crystallographica Section A* **31**, 507 (1975).
- [38] P. Babkevich, *Quantum materials explored by neutron scattering*, Ph.D. thesis, Oxford University, UK (2012).
- [39] M. Kempa, B. Janousova, J. Saroun, P. Flores, M. Boehm, F. Demmel, and J. Kulda, *Physica B: Condensed Matter* **385-386**, 1080 (2006).
- [40] F. Groitl, R. Toft-Petersen, D. L. Quintero-Castro, S. Meng, Z. Lu, Z. Huesges, M. D. Le, S. Alimov, T. Wilpert, K. Kiefer, S. Gerischer, A. Bertin, and K. Habicht, *Scientific Reports* **7**, 13637 (2017).
- [41] M. Markó, F. Groitl, J. O. Birk, P. G. Freeman, K. Lefmann, N. B. Christensen, C. Niedermayer, F. Jurányi, J. Lass, A. Hansen, and H. M. Rønnow, *Review of Scientific Instruments* **89**, 015105 (2018), <https://doi.org/10.1063/1.5018233>.
- [42] F. Groitl, D. Graf, J. O. Birk, M. Markó, M. Bartkowiak, U. Filges, C. Niedermayer, C. Rüegg, and H. M. Rønnow, *Review of Scientific Instruments* **87**, 035109 (2016), <https://aip.scitation.org/doi/pdf/10.1063/1.4943208>.
- [43] J. Lass, D. Graf, F. Groitl, C. Kägi, R. Müller, R. Bürge, M. Schild, M. S. Lehmann, A. Bollhalder, P. Keller, M. Bartkowiak, U. Filges, F. Herzog, U. Greuter, G. Theidel, L. Testa, V. Favre, H. M. Rønnow, and C. Niedermayer, “Design and performance of the multiplexing spectrometer CAMEA,” (2020), arXiv:2007.14796 [physics.ins-det].
- [44] F. Tasset, *Physica B: Condensed Matter* **156-157**, 627 (1989).
- [45] F. Tasset, E. Lelièvre-Berna, T. Roberts, E. Bourgeat-Lami, S. Pujol, and M. Thomas, *Physica B: Condensed Matter* **241-243**, 177 (1997), proceedings of the International Conference on Neutron Scattering.
- [46] M. Janoschek, S. Klimko, R. Gähler, B. Roessli, and P. Böni, *Physica B: Condensed Matter* **397**, 125 (2007).
- [47] R. Kubo, *Physical Review* **87**, 568 (1952).
- [48] P. W. Anderson, *Physical Review* **86**, 694 (1952).

## Bibliography

---

- [49] T. Holstein and H. Primakoff, Phys. Rev. **58**, 1098 (1940).
- [50] E. Manousakis, Rev. Mod. Phys. **63**, 1 (1991).
- [51] N. N. Bogoljubov, Il Nuovo Cimento (1955-1965) **7**, 794 (1958).
- [52] J. H. P. Colpa, Physica A: Statistical Mechanics and its Applications **93**, 327 (1978).
- [53] S. Toth and B. Lake, J. Phys. Condens. Matter **27**, 166002 (2015).
- [54] M. Tinkham, *Introduction to Superconductivity*, Dover Books on Physics Series (Dover Publications, 2004).
- [55] Romhányi, Judit and van den Brink, Jeroen and Rousochatzakis, Ioannis, Phys. Rev. B **90**, 140404 (2014).
- [56] S. Sachdev and R. N. Bhatt, Phys. Rev. B **41**, 9323 (1990).
- [57] T. Sommer, M. Vojta, and K. W. Becker, The European Physical Journal B - Condensed Matter and Complex Systems **23**, 329 (2001).
- [58] M. Moretti Sala, V. Schnells, S. Boseggia, L. Simonelli, A. Al-Zein, J. G. Vale, L. Paolasini, E. C. Hunter, R. S. Perry, D. Prabhakaran, A. T. Boothroyd, M. Krisch, G. Monaco, H. M. Rønnow, D. F. McMorrow, and F. Mila, Phys. Rev. B **92**, 024405 (2015).
- [59] K. Prša, H. M. Rønnow, O. Zaharko, N. B. Christensen, J. Jensen, J. Chang, S. Streule, M. Jiménez-Ruiz, H. Berger, M. Prester, and J. Mesot, Phys. Rev. Lett. **102**, 177202 (2009).
- [60] L. Testa, V. Šurija, K. Prša, P. Steffens, M. Boehm, P. Bourges, H. Berger, B. Normand, H. M. Rønnow, and I. Živković, Phys. Rev. B **103**, L020409 (2021).
- [61] N. Cavadini, G. Heigold, W. Henggeler, A. Furrer, H.-U. Güdel, K. Krämer, and H. Mutka, Phys. Rev. B **63**, 172414 (2001).
- [62] B. Thielemann, C. Rüegg, H. M. Rønnow, A. M. Läuchli, J.-S. Caux, B. Normand, D. Biner, K. W. Krämer, H.-U. Güdel, J. Stahn, K. Habicht, K. Kiefer, M. Boehm, D. F. McMorrow, and J. Mesot, Phys. Rev. Lett. **102**, 107204 (2009).
- [63] D. Schmidiger, S. Mühlbauer, A. Zheludev, P. Bouillot, T. Giamarchi, C. Kollath, G. Ehlers, and A. M. Tsvelik, Phys. Rev. B **88**, 094411 (2013).
- [64] B. D. Gaulin, S. H. Lee, S. Haravifard, J. P. Castellan, A. J. Berlinsky, H. A. Dabkowska, Y. Qiu, and J. R. D. Copley, Phys. Rev. Lett. **93**, 267202 (2004).
- [65] J. B. Torrance and M. Tinkham, Phys. Rev. **187**, 595 (1969).
- [66] G. S. Uhrig and H. J. Schulz, Phys. Rev. B **54**, R9624 (1996).

- 
- [67] S. Ward, M. Mena, P. Bouillot, C. Kollath, T. Giamarchi, K. P. Schmidt, B. Normand, K. W. Krämer, D. Biner, R. Bewley, T. Guidi, M. Boehm, D. F. McMorro, and C. Rüegg, *Phys. Rev. Lett.* **118**, 177202 (2017).
- [68] P. A. McClarty, F. Krüger, T. Guidi, S. F. Parker, K. Refson, A. W. Parker, D. Prabhakaran, and R. Coldea, *Nat. Phys.* **13**, 736 (2017).
- [69] P. R. Hammar, M. B. Stone, D. H. Reich, C. Broholm, P. J. Gibson, M. M. Turnbull, C. P. Landee, and M. Oshikawa, *Phys. Rev. B* **59**, 1008 (1999).
- [70] M. Mourigal, M. Enderle, A. Klöpperpieper, J.-S. Caux, A. Stunault, and H. M. Rønnow, *Nat. Phys.* **9**, 435 (2013).
- [71] S. E. Nagler, W. J. L. Buyers, R. L. Armstrong, and B. Briat, *Phys. Rev. B* **28**, 3873 (1983).
- [72] Q. Faure, S. Takayoshi, S. Petit, V. Simonet, S. Raymond, L.-P. Regnault, M. Boehm, J. S. White, M. Månsson, C. Rüegg, P. Lejay, B. Canals, T. Lorenz, S. C. Furuya, T. Giamarchi, and B. Grenier, *Nat. Phys.* **14**, 716 (2018).
- [73] A. Kitaev, *Ann. Phys.* **321**, 2 (2006).
- [74] J. Chaloupka, G. Jackeli, and G. Khaliullin, *Phys. Rev. Lett.* **105**, 027204 (2010).
- [75] J. Wang, B. Normand, and Z.-X. Liu, *Phys. Rev. Lett.* **123**, 197201 (2019).
- [76] C. Rüegg, N. Cavadini, A. Furrer, H.-U. Güdel, K. Krämer, H. Mutka, A. Wildes, K. Habicht, and P. Vorderwisch, *Nature* **423**, 62 (2003).
- [77] C. Rüegg, B. Normand, M. Matsumoto, A. Furrer, D. F. McMorro, K. W. Krämer, H. U. Güdel, S. N. Gvasaliya, H. Mutka, and M. Boehm, *Phys. Rev. Lett.* **100**, 205701 (2008).
- [78] B. Lake, D. A. Tennant, C. D. Frost, and S. E. Nagler, *Nat. Mater.* **4**, 329 (2005).
- [79] B. Dalla Piazza, M. Mourigal, N. B. Christensen, G. J. Nilsen, P. Tregenna-Piggott, T. G. Perring, M. Enderle, D. F. McMorro, D. A. Ivanov, and H. M. Rønnow, *Nat. Phys.* **11**, 62 (2015).
- [80] M. Skoulatos, M. Månsson, C. Fiolka, K. W. Krämer, J. Schefer, J. S. White, and C. Rüegg, *Phys. Rev. B* **96**, 020414 (2017).
- [81] M. Johnsson, K. W. Törnroos, F. Mila, and P. Millet, *Chem. Mater.* **12**, 2853 (2000).
- [82] V. N. Kotov, M. E. Zhitomirsky, M. Elhajal, and F. Mila, *Phys. Rev. B* **70**, 214401 (2004).
- [83] Z. Jagličić, S. El Shawish, A. Jeromen, A. Bilušić, A. Smontara, Z. Trontelj, J. Bonča, J. Dolinšek, and H. Berger, *Phys. Rev. B* **73**, 214408 (2006).

## Bibliography

---

- [84] O. Zaharko, A. Daoud-Aladine, S. Streule, J. Mesot, P.-J. Brown, and H. Berger, *Phys. Rev. Lett.* **93**, 217206 (2004).
- [85] K. Prsa, H. M. Rønnow, O. Zaharko, N. B. Christensen, J. Jensen, J. Chang, S. Streule, M. Jiménez-Ruiz, H. Berger, M. Prester, and J. Mesot, *Phys. Rev. Lett.* **102**, 177202 (2009).
- [86] R. Becker, M. Johnsson, R. K. Kremer, and P. Lemmens, *J. Solid State Chem.* **178**, 2024 (2005).
- [87] O. Zaharko, J. Mesot, L. A. Salguero, R. Valentí, M. Zbiri, M. Johnson, Y. Filinchuk, B. Klemke, K. Kiefer, M. Mys'kiv, T. Strässle, and H. Mutka, *Phys. Rev. B* **77**, 224408 (2008).
- [88] K.-Y. Choi, S. Do, P. Lemmens, J. van Tol, J. Shin, G. S. Jeon, Y. Skourski, J.-S. Rhyee, and H. Berger, *Phys. Rev. B* **90**, 184402 (2014).
- [89] H. Zhang, Z. Zhao, D. Gautreau, M. Raczkowski, A. Saha, V. Garlea, H. Cao, T. Hong, H. Jeschke, S. Mahanti, T. Birol, F. Assaad, and X. Ke, *Phys. Rev. Lett* **125**, 037204 (2020).
- [90] M. E. Zayed, C. Rüegg, T. Strässle, U. Stuhr, B. Roessli, M. Ay, J. Mesot, P. Link, E. Pomjakushina, M. Stingaciu, K. Conder, and H. M. Rønnow, *Phys. Rev. Lett.* **113**, 067201 (2014).
- [91] M. E. Zayed, C. Rüegg, J. Larrea J., A. M. Läuchli, C. Panagopoulos, S. S. Saxena, M. Ellerby, D. F. McMorrow, T. Strässle, S. Klotz, G. Hamel, R. A. Sadykov, V. Pomjakushin, M. Boehm, M. Jiménez-Ruiz, A. Schneidewind, E. Pomjakushina, M. Stingaciu, K. Conder, and H. M. Rønnow, *Nature Physics* **13**, 962 (2017).
- [92] J. T. Haraldsen, T. Barnes, and J. L. Musfeldt, *Phys. Rev. B* **71**, 064403 (2005).
- [93] J. Goldstone, A. Salam, and S. Weinberg, *Phys. Rev.* **127**, 965 (1962).
- [94] H. Bethe, *Zeitschrift für Physik* **71**, 205 (1931).
- [95] J. des Cloizeaux and J. J. Pearson, *Phys. Rev.* **128**, 2131 (1962).
- [96] L. Faddeev and L. Takhtajan, *Physics Letters A* **85**, 375 (1981).
- [97] G. Müller, H. Thomas, H. Beck, and J. C. Bonner, *Phys. Rev. B* **24**, 1429 (1981).
- [98] M. Karbach, G. Müller, A. H. Bougourzi, A. Fledderjohann, and K.-H. Mütter, *Phys. Rev. B* **55**, 12510 (1997).
- [99] J.-S. Caux, R. Hagemans, and J. M. Maillet, *Journal of Statistical Mechanics: Theory and Experiment* **2005**, P09003 (2005).
- [100] F. D. M. Haldane, *Phys. Rev. Lett.* **66**, 1529 (1991).



- 
- [101] D. A. Tennant, T. G. Perring, R. A. Cowley, and S. E. Nagler, Phys. Rev. Lett. **70**, 4003 (1993).
- [102] H. Effenberger, Z. Krist **175**, 61 (1986).
- [103] I. Živković, D. M. Djokić, M. Herak, D. Pajić, K. Prša, P. Pattison, D. Dominko, Z. Micković, D. Cinčić, L. Forró, H. Berger, and H. M. Rønnow, Phys. Rev. B **86**, 054405 (2012).
- [104] S. Emori, T. Tokii, and Y. Muto, Bulletin of the Chemical Society of Japan **48**, 1649 (1975), <https://doi.org/10.1246/bcsj.48.1649>.
- [105] N. Novosel, W. Lafargue-Dit-Hauret, Z. Rapljenović, M. Dragičević, H. Berger, D. Cinčić, X. Rocquefelte, and M. Herak, Phys. Rev. B **99**, 014434 (2019).
- [106] S. Lee, W.-J. Lee, J. van Tol, P. L. Kuhns, A. P. Reyes, H. Berger, and K.-Y. Choi, Phys. Rev. B **95**, 054405 (2017).
- [107] T. Cvitanić, V. Šurija, K. Prša, O. Zaharko, I. Kupčić, P. Babkevich, M. Frontzek, M. Požek, H. Berger, A. Magrez, H. M. Rønnow, M. S. Grbić, and I. Živković, Phys. Rev. B **98**, 054409 (2018).
- [108] V. Šurija, K. Prša, H. M. Rønnow, M. Boehm, and I. Živković, (2013), doi:10.5291/ILL-DATA.4-01-1295.
- [109] V. Šurija, K. Prša, H. M. Rønnow, P. Steffens, and I. Živković, (2015), doi:10.5291/ILL-DATA.4-01-1459.
- [110] M. Herak, A. Grubišić Čabo, D. Žilić, B. Rakvin, K. c. v. Salamon, O. Milat, and H. Berger, Phys. Rev. B **89**, 184411 (2014).
- [111] R. A. Cowley, W. J. L. Buyers, P. Martel, and R. W. H. Stevenson, Phys. Rev. Lett. **23**, 86 (1969).
- [112] D. A. Tennant, C. Broholm, D. H. Reich, S. E. Nagler, G. E. Granroth, T. Barnes, K. Damle, G. Xu, Y. Chen, and B. C. Sales, Phys. Rev. B **67**, 054414 (2003).
- [113] T. Huberman, R. Coldea, R. A. Cowley, D. A. Tennant, R. L. Leheny, R. J. Christianson, and C. D. Frost, Phys. Rev. B **72**, 014413 (2005).
- [114] Schweika, W., Maleyev, S. V., Brückel, Th., Plakhty, V. P., and Regnault, L.-P., Europhys. Lett. **60**, 446 (2002).
- [115] I. U. Heilmann, J. K. Kjems, Y. Endoh, G. F. Reiter, G. Shirane, and R. J. Birgeneau, Phys. Rev. B **24**, 3939 (1981).
- [116] R. Coldea, D. A. Tennant, A. M. Tsvelik, and Z. Tylczynski, Phys. Rev. Lett. **86**, 1335 (2001).

## Bibliography

---

- [117] R. Coldea, D. A. Tennant, and Z. Tylczynski, Phys. Rev. B **68**, 134424 (2003).
- [118] H. M. Rønnow, D. F. McMorrow, R. Coldea, A. Harrison, I. D. Youngson, T. G. Perring, G. Aeppli, O. Syljuåsen, K. Lefmann, and C. Rischel, Phys. Rev. Lett. **87**, 037202 (2001).
- [119] N. B. Christensen, H. M. Rønnow, D. F. McMorrow, A. Harrison, T. G. Perring, M. Enderle, R. Coldea, L. P. Regnault, and G. Aeppli, Proceedings of the National Academy of Sciences **104**, 15264 (2007), <https://www.pnas.org/content/104/39/15264.full.pdf>.
- [120] M. Kohno, O. A. Starykh, and L. Balents, Nature Physics **3**, 790 (2007).
- [121] A. W. Sandvik, Phys. Rev. B **56**, 11678 (1997).
- [122] A. Mezio, C. N. Sposetti, L. O. Manuel, and A. E. Trumper, Europhys. Lett. **94**, 47001 (2011).
- [123] H. Shao, Y. Q. Qin, S. Capponi, S. Chesi, Z. Y. Meng, and A. W. Sandvik, Phys. Rev. X **7**, 041072 (2017).
- [124] S.-L. Yu, W. Wang, Z.-Y. Dong, Z.-J. Yao, and J.-X. Li, Phys. Rev. B **98**, 134410 (2018).
- [125] E. A. Ghioldi, M. G. Gonzalez, S.-S. Zhang, Y. Kamiya, L. O. Manuel, A. E. Trumper, and C. D. Batista, Phys. Rev. B **98**, 184403 (2018).
- [126] F. Ferrari and F. Becca, Phys. Rev. X **9**, 031026 (2019).
- [127] J. Rodríguez-Carvajal, Physica B: Condensed Matter **192**, 55 (1993).
- [128] V. Petříček, M. Dušek, and L. Palatinus, Zeitschrift für Kristallographie - Crystalline Materials **229**, 345 (01 May. 2014).
- [129] P. Babkevich, L. Testa, K. Kimura, T. Kimura, G. S. Tucker, B. Roessli, and H. M. Rønnow, Phys. Rev. B **96**, 214436 (2017).
- [130] K. Kimura, M. Sera, and T. Kimura, Inorg. Chem. **55**, 1002 (2016).
- [131] Y. Kato, K. Kimura, A. Miyake, M. Tokunaga, A. Matsuo, K. Kindo, M. Akaki, M. Hagiwara, M. Sera, T. Kimura, and Y. Motome, Phys. Rev. Lett. **118**, 107601 (2017).
- [132] I. Dzyaloshinsky, J. Phys. Chem. Sol. **4**, 241 (1958).
- [133] T. Moriya, Phys. Rev. **120**, 91 (1960).
- [134] S. J. Joshua and S. Joshua, *Symmetry Principles and Magnetic Symmetry in Solid State Physics*, Graduate Student Series in Physics (Taylor & Francis, 1991).

- 
- [135] F. Cotton, *Chemical Applications of Group Theory*, A Wiley-Interscience publication (Wiley India, 2003).
- [136] A. Wills, *Physica B: Condensed Matter* **276-278**, 680 (2000).
- [137] W. Sikora, F. Białas, and L. Pytlik, *Journal of Applied Crystallography* **37**, 1015 (2004).
- [138] K. Kimura, P. Babkevich, M. Sera, M. Toyoda, K. Yamauchi, G. S. Tucker, J. Martius, T. Fennell, P. Manuel, D. D. Khalyavin, R. D. Johnson, T. Nakano, Y. Nozue, H. M. Rønnow, and T. Kimura, *Nat. Commun.* **7**, 13039 (2016).
- [139] A. C. Walters, T. G. Perring, J.-S. Caux, A. T. Savici, G. D. Gu, C.-C. Lee, W. Ku, and I. A. Zaliznyak, *Nature Physics* **5**, 867 (2009).
- [140] W. Fischer, *Physica B: Condensed Matter* **234-236**, 1202 (1997), proceedings of the First European Conference on Neutron Scattering.
- [141] F. Semadeni, B. Roessli, and P. Böni, *Physica B: Condensed Matter* **297**, 152 (2001), proceeding of the Third International Workshop on Polarised Neutrons.
- [142] K. Levenberg, *Quarterly of Applied Mathematics* **2**, 164 (1944).
- [143] D. W. Marquardt, *Journal of the Society for Industrial and Applied Mathematics* **11**, 431 (1963), <https://doi.org/10.1137/0111030>.
- [144] K. Kimura, D. Urushihara, T. Asaka, M. Toyoda, A. Miyake, M. Tokunaga, A. Matsuo, K. Kindo, K. Yamauchi, and T. Kimura, *Inorg. Chem.* **59**, 10986 (2020).
- [145] R. Råsta, I. Heinmaa, K. Kimura, T. Kimura, and R. Stern, *Phys. Rev. B* **101**, 054417 (2020).
- [146] J.-R. Soh, F. de Juan, N. Qureshi, H. Jacobsen, H.-Y. Wang, Y.-F. Guo, and A. T. Boothroyd, *Phys. Rev. B* **101**, 140411 (2020).
- [147] K. Kimura, M. Toyoda, P. Babkevich, K. Yamauchi, M. Sera, V. Nassif, H. M. Rønnow, and T. Kimura, *Phys. Rev. B* **97**, 134418 (2018).
- [148] K. Yamada, M. Matsuda, Y. Endoh, B. Keimer, R. J. Birgeneau, S. Onodera, J. Mizusaki, T. Matsuura, and G. Shirane, *Phys. Rev. B* **39**, 2336 (1989).
- [149] N. Qureshi, *Journal of Applied Crystallography* **52**, 175 (2019).
- [150] K. Kimura, M. Toyoda, P. Babkevich, K. Yamauchi, M. Sera, V. Nassif, H. M. Rønnow, and T. Kimura, *Phys. Rev. B* **97**, 134418 (2018).
- [151] S. S. Islam, K. M. Ranjith, M. Baenitz, Y. Skourski, A. A. Tsirlin, and R. Nath, *Phys. Rev. B* **97**, 174432 (2018).

## Bibliography

---

- [152] Y. Kato, K. Kimura, A. Miyake, M. Tokunaga, A. Matsuo, K. Kindo, M. Akaki, M. Hagiwara, S. Kimura, T. Kimura, and Y. Motome, Phys. Rev. B **99**, 024415 (2019).
- [153] K. Kimura, M. Sera, T. Nakano, Y. Nozue, and T. Kimura, Physica B **536**, 93 (2018).
- [154] K. Kimura, S. Kimura, and T. Kimura, J. Phys. Soc. Jpn. **88**, 093707 (2019).
- [155] H. Bethe, Z. Phys. **71**, 205 (1931).
- [156] L. D. Faddeev and L. A. Takhtajan, Phys. Lett. A **85**, 375 (1981).
- [157] G. Müller, H. Thomas, H. Beck, and J. C. Bonner, Phys. Rev. B **24**, 1429 (1981).
- [158] L. Isaev, G. Ortiz, and J. Dukelsky, Phys. Rev. B **79**, 024409 (2009).
- [159] O. Götze, S. E. Krüger, F. Fleck, J. Schulenburg, and J. Richter, Phys. Rev. B **85**, 224424 (2012).
- [160] R. L. Doretto, Phys. Rev. B **89**, 104415 (2014).
- [161] S.-S. Gong, W. Zhu, D. N. Sheng, O. I. Motrunich, and M. P. A. Fisher, Phys. Rev. Lett. **113**, 027201 (2014).
- [162] S. Morita, R. Kaneko, and M. Imada, J. Phys. Soc. Jpn. **84**, 024720 (2015).
- [163] L. Wang and A. W. Sandvik, Phys. Rev. Lett. **121**, 107202 (2018).
- [164] R. Haghshenas and D. N. Sheng, Phys. Rev. B **97**, 174408 (2018).
- [165] A. F. Albuquerque, M. Troyer, and J. Oitmaa, Phys. Rev. B **78**, 132402 (2008).
- [166] S. Wenzel, L. Bogacz, and W. Janke, Phys. Rev. Lett. **101**, 127202 (2008).
- [167] H. M. Rønnow, D. F. McMorrow, R. Coldea, A. Harrison, I. D. Youngson, T. G. Perring, G. Aeppli, O. Syljuåsen, K. Lefmann, and C. Rischel, Phys. Rev. Lett. **87**, 037202 (2001).
- [168] P. Babkevich, V. M. Katukuri, B. Fåk, S. Rols, T. Fennell, D. Pajić, H. Tanaka, T. Pardini, R. R. P. Singh, A. Mitrushchenkov, O. V. Yazyev, and H. M. Rønnow, Phys. Rev. Lett. **117**, 237203 (2016).
- [169] A. A. Tsirlin and H. Rosner, Phys. Rev. B **79**, 214417 (2009).
- [170] A. A. Tsirlin, R. Nath, A. M. Abakumov, Y. Furukawa, D. C. Johnston, M. Hemmida, H.-A. Krug von Nidda, A. Loidl, C. Geibel, and H. Rosner, Phys. Rev. B **84**, 014429 (2011).
- [171] J.-X. Zhu, R. Yu, H. Wang, L. L. Zhao, M. D. Jones, J. Dai, E. Abrahams, E. Morosan, M. Fang, and Q. Si, Phys. Rev. Lett. **104**, 216405 (2010).

- 
- [172] S. Miyahara, J.-B. Fouet, S. R. Manmana, R. M. Noack, H. Mayaffre, I. Sheikin, C. Berthier, and F. Mila, *Phys. Rev. B* **75**, 184402 (2007).
- [173] B. Xi, S. Hu, J. Zhao, G. Su, B. Normand, and X. Wang, *Phys. Rev. B* **84**, 134407 (2011).
- [174] S. Rufo, J. R. de Sousa, and J. A. Plascak, *Physica A* **518**, 349 (2019).
- [175] P. Babkevich, L. Testa, H. M. Rønnow, K. Kimura, and J. Ollivier, (2016), doi:10.5291/ILL-DATA.4-01-1528.
- [176] R. A. Ewings, A. Buts, M. D. Le, J. van Duijn, I. Bustinduy, and T. G. Perring, *Nucl. Instrum. Methods Phys. Res., Sect. A* **834**, 132 (2016).
- [177] L. Testa, H. M. Rønnow, and S. Raymond, (2019), doi:10.5291/ILL-DATA.CRG-2652.
- [178] A. V. Syromyatnikov, *Phys. Rev. B* **98**, 184421 (2018).
- [179] A. V. Syromyatnikov, *Phys. Rev. B* **102**, 014409 (2020).
- [180] M. Moretti Sala, V. Schnells, S. Boseggia, L. Simonelli, A. Al-Zein, J. G. Vale, L. Paolasini, E. C. Hunter, R. S. Perry, D. Prabhakaran, A. T. Boothroyd, M. Krisch, G. Monaco, H. M. Rønnow, D. F. McMorrow, and F. Mila, *Phys. Rev. B* **92**, 024405 (2015).
- [181] Habicht, Klaus, Quintero-Castro, Diana Lucía, Toft-Petersen, Rasmus, Kure, Mathias, Mäde, Lucas, Groitl, Felix, and Le, Manh Duc, *EPJ Web of Conferences* **83**, 03007 (2015).
- [182] Heinz Maier-Leibnitz Zentrum, *Journal of large-scale research facilities* **1** (2015), <http://dx.doi.org/10.17815/jlsrf-1-35>.
- [183] J. O. Birk, M. Markó, P. G. Freeman, J. Jacobsen, R. L. Hansen, N. B. Christensen, C. Niedermayer, M. Månsson, H. M. Rønnow, and K. Lefmann, *Review of Scientific Instruments* **85**, 113908 (2014), <https://doi.org/10.1063/1.4901160>.
- [184] R. Bewley, J. Taylor, and S. Bennington., *Nuclear Instruments and Methods in Physics Research Section A: Accelerators, Spectrometers, Detectors and Associated Equipment* **637**, 128 (2011).



# Luc Testa

Av. de Béthusy 26  
1005 Lausanne (CH)  
+41 78 872 76 34  
Skype : luc.testa

28 years old (27.06.1992)  
Swiss, Italian, French  
luc.testa@gmail.com  
ORCID : [0000-0002-6610-9282](https://orcid.org/0000-0002-6610-9282)



- **PhD in Quantum Magnetism at EPFL**
- **Strong expertise in material characterisation with the neutron scattering technique**

## PROFESSIONAL EXPERIENCE

**PhD in Physics** in the [Lab. for Quantum Magnetism](#), EPFL in Lausanne **Oct 2016 – Jan 2021**

- Research project in quantum properties of materials, aiming to confirm theoretical results
- Leading sensitive experiments on large scale facilities with international collaborators
- Skills in large data set analysis, project management, literature research, laboratory work
- Presentation of research results in international conferences (best poster award at ICM2018)
- Teaching assistant, responsible for the organisation of lectures
- PhD students representative

**Research intern** at Swiss Federal Inst. of Metrology (METAS) in Bern **Aug 2015 – Feb 2016**

- Implementation of numerical tools coupled with a Finite Element Modelling used in a full modal analysis of optical fibres
- Results comparable to in-lab measurements and professional softwares
- Led to the definition of new templates for a physical quantity and in the development of a new laboratory instrument

## EDUCATION

**Master of Science (MSc) in Applied Physics** at EPFL, Switzerland **2010 – 2016**

- Strong expertise in experimental physics thanks to the large amount of laboratory work
- Lectures followed both in theoretical and numerical physics
- Master's thesis done at SISSA, Trieste, Italy, on a numerical modelling and Variational Monte Carlo analysis of physical complex quantum systems

## COMPUTER AND TECHNICAL SKILLS

Computational science, data analysis, quantum physics, condensed matter, magnetism, neutron scattering, X-rays, crystallography  
Matlab, C++, Fortran, Python, L<sup>A</sup>T<sub>E</sub>X, Unix, SpinW, FullProf  
Laboratory work, vacuum and cold techniques, project leading

## LANGUAGES

<b>English:</b>	Fluent (level C1-C2)	First Certificate in English (2009)
<b>Italian:</b>	Good (level C1)	9 month stay in Trieste
<b>German:</b>	Intermediate (level B2)	6 months stay in Bern
<b>French:</b>	Mother tongue	

## ASSOCIATIVE EXPERIENCE

**Treasurer** of the Harmonie Municipale d'Epalinges **Aug 2017 – ...**  
Organisation of several concerts per year

**Webmaster** and organiser, PolyPhys **Jan 2017 – ...**  
Organisation of a yearly conference day (attended by two Nobel laureates) as well as monthly social seminars given by PhD students

## PERSONAL INTERESTS

Tennis – Ski (Jeunesse & Sport instructor), snowboard, ski touring – Mountaineering, climbing  
Flute and saxophone player – playing in two bands – blues, jazz and classical music

## PUBLICATIONS

- *Modelling of standard and specialty fibre-based systems using finite element methods*  
N. Castagna, J. Morel, L. Testa, S. Burger  
SPIE 10683, Fiber Lasers and Glass Photonics: Materials through Applications, 1068336 (2018)
- *Magnetic structure of  $Ba(TiO)Cu_4(PO_4)_4$  probed using spherical neutron polarimetry*  
P. Babkevich, L. Testa, K. Kimura, T. Kimura, G. S. Tucker, B. Roessli, and H. M. Rønnow  
Phys. Rev. B **96**, 214436 (2017)
- *Triplons, Magnons, and Spinons in a Single Quantum Spin System:  $SeCuO_3$*   
L. Testa *et. al.*  
Phys. Rev. B **103**, L020409
- *Radial Spin Texture of the Weyl Fermions in Chiral Tellurium*  
G. Gatti *et. al.*  
Phys. Rev. Lett. **125**, 216402 (2020)
- *Design and performance of the multiplexing spectrometer CAMEA*  
J. Lass *et. al.*  
arXiv:2007.14796 [physics.ins-det]
- *Spin dynamics in the square-lattice cupola system  $Ba(TiO)Cu_4(PO_4)_4$*   
L. Testa *et. al.*  
In preparation
- *Realization of a three-dimensional spin-1 quantum spin liquid in a trillium lattice compound*  
I. Zivkovic *et. al.*  
In preparation

## TALKS

- *Variational Monte-Carlo investigation of  $SU(N)$  Heisenberg systems* – 2016  
Host : Prof. Immanuel Bloch (Quantum Optics Group, LMU, Munich)
- *Effective magnetic decoupling in  $SeCuO_3$*  – 2020  
Host : Dr. Mingee Jung (Resonance Lab, University of Birmingham, Birmingham)
- *Coexistence of spinons, triplons and magnons in  $SeCuO_3$*  – 2020  
Host : Dr. Juraž Hašik (LFT, Université Toulouse III - Paul Sabatier, Toulouse)  
Host : ISIS Student meeting
- *Un voyage vers le magnétisme à petite échelle* – 2020  
Host : Les Irrationnels (EPFL, Lausanne)

## POSTERS

- *Excitation spectrum of the chiral cupola system  $Ba(TiO)Cu_4(PO_4)_4$*   
International Conference on Neutron Scattering – Daejeon, 2017
- *A neutron scattering journey of  $A(BO)Cu_4(PO_4)_4$*   
International Conference on Magnetism – San Francisco, 2018 – ★ **Best poster award**  
Trends in Quantum Magnetism – Bad Honnef, 2018  
Meeting of the Swiss Physical Society – Lausanne, 2018  
International Conference of Strongly Correlated Electron Systems – Okayama, 2019
- *A neutron diffraction investigation of  $A(BO)Cu_4(PO_4)_4$  using spherical neutron polarimetry*  
International School of Crystallography – Erice, 2019